UNIVERSITY OF COPENHAGEN
FACULTY OF SCIENCE

Department of Geosciences and Natural Resource Management
University of Copenhagen
&
Nordic Volcanological Center
Institute of Earth Sciences, University of Iceland

PhD Thesis

Johanne Schmith

Volcanology and hazards of phreatomagmatic basaltic eruptions

Eruption source parameters and fragmentation mechanism of large eruptions from Katla volcano, Iceland

Supervisor: Paul Martin Holm & Ármann Höskuldsson

Submitted on: 15 May 2017

Name of department: Department of Geosciences and Natural Resource Management

Author(s): Johanne Schmith

Title and subtitle: Volcanology and hazards of phreatomagmatic basaltic eruptions. Eruption source parameters and fragmentation mechanism of large eruptions from Katla volcano, Iceland

Topic description: The purpose of this study has been to produce the first set of eruption source parameters for Katla volcano. The second aim of this work has been to understand the eruption dynamics and particularly fragmentation mechanisms of large phreatomagmatic basaltic eruptions.

Supervisor: Paul Martin Holm & Ármann Höskuldsson (Nordic Volcanological Center)

Submitted on: 15 May 2017

Grade: PhD, double degree

Table of contents

Preface

The purpose of this study is to produce the first eruption source parameters for Katla volcano. Furthermore this study aims to understand the eruption dynamics and particularly fragmentation mechanisms of large phreatomagmatic basaltic eruptions. Two eruption deposits from the large basaltic explosive eruptions of Katla volcano in 1755 and 1625 were investigated to achieve these goals. Fragmentation mechanisms were studied to better understand the underlying processes of the large explosive eruptions and the distribution of the deposits were mapped, sampled and modeled to quantify their size. Furthermore studies of contemporary descriptions of the eruptions combined with detailed investigations of the temporal change in the deposits provided new insight into the evolution of these large eruptions.

Outline of thesis

The thesis is structured in 6 chapters. Chapter 1 is an introduction. Chapter 2 is an account of the methods used in this work. Chapter 3 is the published paper Schmith et al. (2017) presenting a new method for assessing the shape of ash grain bulk populations and a new way to interpret fragmentation mechanism from the shape data. This paper shows that the fragmentation mechanism of large basaltic explosive eruptions in Iceland must be viewed as a combination of magmatic and phreatomagmatic processes. Chapter 4 is a submitted manuscript, 2017 paper (Schmith et al. submitted manuscript, 2017) presenting the temporal evolution of the two Katla eruptions from 1755 and 1625 based on historical accounts, grain size modeling, and grain shape analysis of the deposits. This paper shows that while the apparent size, duration, geochemistry, and deposit distribution were similar for these two eruptions, they were different in terms of dominating fragmentation mechanisms and plume dynamics. Chapter 5 is a manuscript (Schmith et al. in prep), which presents the eruptive source parameters for the two Katla eruptions of 1755 and 1625. The parameters are derived from isopach maps, total grain size distribution-, volume-, inverse mass loading-, and plume height modeling. This final paper shows that both eruptions were subplinian to plinian and that most likely the 1625 eruption was the biggest Katla eruption in historical times. Chapter 6 presents the conclusive remarks and future perspectives of the study.

This work has contributed to the ICAO data collection and was co-funded by the Nordic Volcanological Center and University of Copenhagen.

Acknowledgements

There are many people to whom I am grateful for their involvement and support during this PhD-work. First I would like to thank my Icelandic supervisor and mentor Professor Ármann Höskuldson for inspiring, supporting and challenging me. I deeply appreciate the great faith you have shown in me and I have very much enjoyed all our field trips, crazy monitoring adventures and lively discussions about science and life in general. Thank you for showing me how amazing volcanology is and for always being available for idea bouncing, asking questions and … getting more lab keys. Likewise my grateful thanks are extended to my Danish supervisor Paul Martin Holm, who has helped and mentored me since I was an undergrad student dreaming about volcanoes. Your support and belief in me has made this project possible and I am very thankful that I can always come to you with my ideas, questions or concerns. Guðrun Larsen has provided invaluable help by sharing her knowledge of Icelandic tephra with me and by allowing me to benefit from her hard work collecting field data. I am grateful for the trust and kindness you have shown me and all the times you have helped me understand strange observations in the field or old Icelandic texts. I would also like to thank professor Costanza Bonnadonna for her guidance, helpful suggestions, openness and delightful energy. It's been a privilege working with you and thank you for making the CERG C course an unforgettable experience.

Without the help and lovely company of Eirik Gjerløw, Catherine Gallagher, Rob Askew, and William Moreland I would still be stuck in the field digging soil sections. I am grateful for all the hours we have spent together in and outside the field, for all our tephra talks and discussions and for your friendship. A special thanks to Eirik for an epic Gin-Tonic on Stromboli, for donating samples for me, for exploring SE Iceland, Vulcano, Suwanosejima and Geneva with me, for being patient with my jumping photos, and for always making me laugh ridiculously much. Also a heartfelt thanks to Kate and Rob for housing me, for divinely fluffy cuddles from Pipin the volcano dog, talks about everything important in life and for being two of the most amazing people I know. Jónas Guðnason and Bergrún Óladóttir has taught me how great (and absolutely crazy, Jónas!) Icelanders are – especially those who love tephra! Thank you for all the daily discussions of tephra data and possible new pet project, for crater jumping, for making EGU fun as hell (and getting me home) and for being so patient trying to teach me Icelandic. A special

thanks to you Jónas for spending time translating my abstract into Icelandic. Gro Birkefelt Møller Pedersen has been the best office mate ever and I am grateful for plank challenges, proofreading, girl talks, TED-talks, climbing introductions, and all the fun we've had along the way. I am also thankful to Paavo Nikkola, Stéphanie Dumont, Birgir Oskarsson and everyone else from the IES field monitoring team for making all the hard work so delightful. It was an experience for life and I am so happy that I got to share it with you lovely people.

Katrine Bruhn Holck and Liva Rønn Pedersen have been amazingly supportive and understanding and I sincerely appreciate all the consideration you have shown me during the final stages of the PhD.

I want to thank my family for standing by me through everything and for taking care of my boys, taking them on holidays and weekends, and for always being there. I am very lucky to have you by my side.

Mia Nielsen, I am so grateful for all our productive writing days at the Royal Library making this thesis happen, but I am especially thankful for having you in my life as a very dear and special friend.

Lastly a particularly heartfelt gratitude goes to my husband Johan Schmith and to my two boys Julius and Albert. Thank you for your love and support, patience and understanding and mostly just for embarking on this crazy and wonderful journey with me. I couldn't have done it without you!

Abstract

Iceland is one of the most active terrestrial volcanic regions on Earth with an average of more than 20 eruptions per century. Around 80% of all events are tephra generating explosive eruptions, but less than 10 % of all known tephra layers have been mapped. Recent hazard assessment models show that the two key parameters for hazard assessment modeling are total grain size distribution (TGSD) and eruptive style. These two parameters have been determined for even fewer eruptive events in Iceland. One of the most hazardous volcanoes in Iceland is Katla and no data set of TGSD or other eruptive parameters exist. Katla has not erupted for 99 years, but at least 2 of the 20 eruptions since the settlement of Iceland in 871 have reached Northern Europe as visible tephra fall. These eruptions occurred in 1755 and 1625 and remain enigmatic both in terms of actual size and eruption dynamics.

This work presents studies of these two far-reaching eruptions in terms of fragmentation and eruption dynamics as well as the first set of eruption source parameters for any Katla eruption. In order to provide detailed insight into the eruption dynamics a new method for classifying fragmentation mechanisms based on tephra grain morphology was developed and is presented in this work.

The deposits are estimated to cover 23400 km^2 and 23600 km^2 on land in Iceland for the 1755 and 1625 eruptions. Volumes calculated from the power-law integration method are 1.20-1.50 km^3 for the 1755 eruption and 1.12-1.36 km^3 for the 1625 eruptions. The total erupted mass converted from erupted volume of the 1755 eruption was $1.84\text{-}2.45 \cdot 10^{12}$ kg with a lower-bound mass eruption rate of $1.25\text{-}1.67 \cdot 10^{6}$ kg/s. In 1625 Katla erupted between $1.53\text{-}1.94 \cdot 10^{12}$ kg tephra as calculated from the erupted volume with a lower-bound mass eruption rate of $1.61\text{-}2.04 \cdot 10^{6}$ kg/s. The average 1755 plume height was 14.4 km based on mass loading data inversion with an empirical correlation estimate of paroxysmal peaks at 25± 6 km. The average 1625 plume height was 16.6 km based on mass loading data inversion with an empirical correlation estimate of paroxysmal peaks at 25± 6 km.

A new quantitative method producing grain shape data of bulk samples of volcanic ash was developed to correlate the bulk average grain shape with magma fragmentation mechanisms. The new shape index: the regularity index (RI) was developed from a manually classified reference morphology dataset using principal component analysis. The systematic change in RI

between wet and dry eruptions supports that the RI can be used to assess the relative roles of magmatic versus phreatomagmatic fragmentation. Surtseyan ash has an RI of 0.207-0.191 ± 0.002 (2σ), whereas Hawaiian ash has an RI of 0.134 ± 0.001 (2σ) and these samples represent the extremes of the fragmentation spectrum. Subglacial samples show intermediate RIs of 0.168 ± 0.002 (2σ), 0.175 ± 0.002 (2σ) and lacustrine samples have slightly higher RI of 0.187 ± 0.002 (2σ).

The method uses automated image analysis of 2D projections ash grains in the size range 125-63 μm. Loose bulk samples from the deposits of 6 different basaltic eruptions were analyzed and 20,000 shape measurements of 26 shape parameters for each were obtained within ~45 min using the Particle Insight^{TM} dynamic shape analyzer (PIdsa).

The RI modeling showed that subglacial eruptions were controlled by both magmatic and phreatomagmatic fragmentation processes. Further investigations determined the RI of consecutive depositional units of both the 1755 and 1625 eruptions. The detailed models showed that the fragmentation processes in the 1755 eruption was a stable combination of magmatic degassing and magma/water-interaction with only minor perturbations, whereas the 1625 eruption went progressively from predominantly phreatomagmatic to predominantly magmatic and back to phreatomagmatic. This study documents that the amount of and access to melt water can change significantly during subglacial eruptions and that magmatic processes play an important role in the fragmentation process.

The RI study was combined with field data on deposit stratigraphy, granulometric modeling, componentry, and written accounts of the eruptions and produced a coherent model of the evolution of the eruptions. The collective data set shows that the 1755 eruption was a continuous uprush eruption much like the recent 2011 Grímsvötn eruption. However, the 1755 Katla eruption had a longer duration of 17 days and a higher mass eruption rate. The 1625 eruption was a dynamic eruption less influenced by magma/melt-water interaction, which agrees well with the higher average plume height as compared to the 1755 eruption.

This work has contributed to the general understanding of the fragmentation dynamics of large subglacial eruptions. It has also provided much needed data for improvement of future hazard and risk assessments of one of the most hazardous volcanoes in Iceland. Furthermore the RI method is expected to be widely applicable to tephra morphology studies and to be helpful during the next volcanic ash crises.

Resumé (Danish summary)

Island er en af verdens mest aktive vulkanske regioner med gennemsnitligt mere end 20 udbrud pr. århundrede. Omkring 80% af alle eruptioner er eksplosive tephradannende udbrud, men under 10 % af alle kendte tephralag er kortlagt. Nye risikovurderingsmodeller viser at nøgleparametrene til modellering af udbrudsfarer er total kornstørrelsesfordeling (TGSD) og udbrudsstil, hvilket er blevet bestemt for endnu færre udbrud.

Katla er en af de farligste vulkaner på Island, og der findes ingen datasæt med TGSD eller andre udbrudsparametre for denne vulkan. Katla ikke har været i udbrud i 99 år, men mindst 2 ud af Katlas 20 historiske udbrud gennem de sidste 1100 år har nået Nordeuropa i form af synligt askefald. Disse udbrud fandt sted i 1755 og 1625 og er fortsat gådefulde både hvad angår faktisk størrelse og udbrudsdynamik.

Denne afhandling præsenterer studier af magmafragmentation og udbrudsdynamik for de to vidtrækkende 1755 and 1625 vulkanudbrud samt det første sæt af udbrudsparametre for Katla. For at give en mere detaljeret indsigt i udbrudsdynamikken er der derudover udviklet en ny metode baseret på askekornsmorfologi til klassificering af askefragmentation.

Aflejringerne fra udbruddene anslås at dække 23400 km^2 og 23600 km^2 på land i Island for henholdsvis 1755 og 1625 udbruddet. Volumener beregnet ud fra potensfunktionsmetoden er på 1,20-1,50 km^3 og 1,12-1,36 km^3 for henholdsvis 1755 og 1625 udbruddet. Den samlede udbrudsmasse af 1755-udbruddet er 1,84-2,45·10^{12} kg omregnet fra udbrudsvolumenet og det nedre estimat for en masseeruptionsrate er på 1,25-1,67·10^6 kg/s. I 1625 erupterede Katla 1,53-1,94·10^{12} kg beregnet ud fra udbrudsvolumenet med en masseeruptionsrate på 1,61-2,04·10^6 kg/s. Den gennemsnitlige askesøjlehøjde for 1755-udbruddet var 14,4 km baseret på inversion af massefordelinsdata. For 1625-udbruddet var denne højde 16,6 km. Den paroxysmale maximumhøjde anslås til 25 ± 6 km for begge udbrud ved beregning ud fra den empirisk korrelation af volumen og askesøjlehøjde for pliniske udbrud.

En ny kvantitativ metode til bestemmelse af askemorfologi blev udviklet for at korrelere den gennemsnitlige kornform i askeprøver med magmafragmentationsmekanismer. Det nye formindeks: Regularitetsindekset (RI) blev udviklet ved principal komponent analyse af et datasæt af manuelt klassificerede kornmorfologityper. Den systematiske ændring i RI mellem våde og tørre udbrud viser, at RI kan bruges til at vurdere de relative roller af magmatisk versus

phreatomagmatisk fragmentation. Surtseiske udbrud har et RI på 0,207-0,191 ± 0,002 (2σ), mens Hawaiianske udbrud har et RI på 0,134 ± 0,001 (2σ). Disse prøver repræsenterer ekstremerne af fragmentationsspektret. Prøver fra subglaciale udbrud analyseres til middelværdier af RI på 0,168 ± 0,002 (2σ) og 0,175 ± 0,002 (2σ) og prøver fra lakustrine udbrud har et lidt højere RI på 0,187 ± 0,002 (2σ).

Metoden bruger automatiseret billedanalyse af 2D-projektioner af askekorn i størrelsesområdet 125-63 μm. Løse askeprøver fra aflejringer af 6 forskellige basaltiske askeudbrud blev analyseret, og 20.000 kornmålinger af 26 formparametre blev opnået indenfor ~45 minutter ved anvendelse af Particle Insight ™ dynamic shape analyzer (PIdsa).

RI-modelleringen viste, at subglaciale udbrud blev styret af både magmatiske og phreatomagmatiske fragmentationsprocesser. Yderligere undersøgelser fastslog RI af de aflejrede udbrudsenheder i både 1755- og 1625-udbruddet. De detaljerede modeller viste, at fragmentationsprocesserne i 1755-udbruddet var en forholdsvis stabil kombination af magmatisk afgasning og magma/vand-interaktion. Fragmentationen under 1625-udbruddet gik gradvist fra overvejende phreatomagmatisk fragmentation til overvejende magmatisk og tilbage til phreatomagmatisk. Undersøgelsen dokumenterer, at mængden af og adgangen til smeltevand kan ændre sig signifikant under subglaciale udbrud, samt at magmatiske processer spiller en vigtig rolle i fragmentationsprocessen.

RI-studiet blev kombineret med stratigrafiske feltdata, granulometrisk modellering, komponentbestemmelse og skriftlige kilder med beskrivelser af udbruddene. Dette datasæt dannede baggrunden for en sammenhængende model for udbruddenes udvikling. Det samlede datasæt viser, at udbruddet i 1755 var et kontinuerligt opstrømsudbrud ligesom det seneste udbrud i 2011 fra Grímsvötnvulkanen. Dog havde Katla-udbruddet en længere varighed og en højere masseeruptionsrate. 1625-udbruddet var et dynamisk udbrud, som var mindre påvirket af magma/smeltevandsinteraktion, hvilket stemmer overens med den højere gennemsnitlige askesøjlehøjde sammenlignet med 1755-udbruddet.

Dette studie har bidraget til den generelle forståelse af fragmentationsdynamikken under store subglaciale udbrud. Det har også leveret nødvendige data til forbedring af fremtidige fare- og risikovurderinger af en af de mest farlige vulkaner i Island. Desuden forventes RI-metoden at være bredt anvendelig til tephra-morfologistudier og være et nyttigt værktøj under de næste vulkanske askekriser.

Ágrip (Icelandic summary)

Ísland er eitt af mestu jarðskjálftasvæðunum á jörðu, að meðaltali meira en 20 eldgos á öld. Um 80% allra atburða eru tephra sem veldur sprengifimum gosum, en minna en 10% allra þekktra tephra laganna hefur verið kortlagður. Nýlegar áhættumatsmyndir sýna að lykilatriði fyrir áhættumatsmat eru heildar kornstærð dreifingar (TGSD) og gosstíll, sem hefur verið ákvarðað fyrir jafnvel færri eldgos. Einn af hættulegustu eldfjöllunum á Íslandi er Katla og engin gögn um TGSD eða aðrar eldgosar eru til staðar. Þrátt fyrir að Katla hafi ekki gosið í 99 ár, hafa að minnsta kosti 2 af 20 eldgosum frá uppgjörinu á Íslandi árið 871 náð Norður-Evrópu sem sýnilegt tephra fall. Þessi gos átti sér stað árið 1755 og 1625 og haldist ótrúleg bæði hvað varðar raunverulegan stærð og gosdrif.

Þetta verk kynnir rannsóknir á þessum tveimur langt gosjum hvað varðar sundrungu og gosdrif og fyrstu eldgosgjafar fyrir eldgos frá Katla. Til að veita nákvæma innsýn í gosdrifið hefur verið þróað nýjar aðferðir til að flokka uppbrotsaðferðir sem byggjast á kornfræðilegri kenningu. Innlánin eru áætluð 23400 og 23600 km2 á landi á Íslandi fyrir 1755 og 1625 eldgos. Rúmmál reiknuð út frá samrunaaðferðinni fyrir orkuheimildir eru 1,20-1,50 km3 og 1,12-1,36 km3 fyrir 1755 og 1625 eldgos, í sömu röð. Heildar gosmassi 1755 gosið var 1,84-2,45·1012 kg breytt úr gosbindi með lægri bundnu gosshraða 1,25-1,67·106 kg / s. Árið 1625 gos Katla upp á milli 1,53-1,94·1012 kg tephra sem reiknað út frá gosinu með lægri bundnu massa gosinu á bilinu 1,61-2,04 kg / s. Að meðaltali 1755 plume hæð var 14,4 km byggt á massi hleðsla gagna innrennsli með empirical fylgni mat á paroxysmal tinda á 25 ± 6 km. Að meðaltali 1625 plume hæð var 16,6 km byggt á massi hleðsla gagna innrennsli með empirical fylgni mat á paroxysmal tinda á 25 ± 6 km.

Nýtt magn aðferð til að framleiða korn form gagna af magn sýni af eldfjallaösku var þróað til að tengja magn meðaltals korn lögun með magma sundrungu kerfi. Nýja formvísitalan: regluvísitalan (RI) var þróuð úr handvirkt flokkað tilvísunarformfræðilegu gagnasafni með því að nota meginhluta greiningu. Kerfisbundin breyting á RI milli blautra og þurra eldgos styður að hægt sé að nota RI til að meta hlutfallsleg hlutverk magmatískra versna gegn fitusýkingu. Surtseyanhas hefur RI 0,207-0,191 ± 0,002 (2σ), en Hawaiian aska hefur RI 0,134 ± 0,001 (2σ) og þessi sýni tákna öfgar brottsviðsins. Undirliggjandi sýni sýna millistig RIs 0,188 ± 0,002 (2σ), 0,175 ± 0,002 (2σ) og lacustrine sýni hafa aðeins hærra RI 0,187 ± 0,002 (2σ).

Aðferðin notar sjálfvirkan myndgreiningu á 2D vörpun á ösku korn á stærðarsvæðinu 125-63 µm. Losar lausnir í massa frá 6 mismunandi basaltgosum voru greindar og 20.000 formmælingar með 26 formbreytur fyrir hverja var fengin innan ~45 mín með því að nota Particle InsightTM dynamic formgreiningartækið (PIdsa).
RI líkanið sýndi að undirglacial var stjórnað af bæði magmatic og phreatomagmatic sundrunarferli. Frekari rannsóknir ákvarðu RI af samfelldri losunareiningum bæði í 1755 og 1625 gosinu. Nákvæmar gerðir sýndu að sundrunarferlið í 1755 eldgosið var nokkuð stöðugt blanda af magmatic degassing og magma / water-samskipti, en 1625 gosið fór smám saman úr aðallega phreatomagmatic að aðallega magmatic og aftur til phreatomagmatic. Þessi rannsókn lýsir því yfir að magn og aðgengi að bræðslumarki breytist verulega meðan á gosinu stendur og þessi magmatic ferli gegna mikilvægu hlutverki í sundrunarferlinu.
Rannsóknin í RI var sameinuð með gögnum um innsláttarskot, köfunarfræðilegan líkanagerð, componentry og skriflegar reikningar um gosið og framleitt samhengi fyrir þróun gosanna. Gagnaöflunin sýnir að 1755 gosið var samfellt gosgos, líkt og Grímsvötn 2011, en 17 daga lengur. Gosið 1625 var öflugt eldgos sem hefur minna áhrif á magma / bræðslu-vatn samskipti, sem er vel samhæft við hærri meðaltal plume hæð í samanburði við 1755 eldgosið.

Chapter 1

Introduction

In april 2010 the moderate VEI (Volcanic Explosivity Index) 4 explosive eruption of the Icelandic volcano Eyjafjallajökull caused the largest volcano-related aviation shutdown in history (Davies et al., 2010; Sammonds et al., 2010; Schumann et al., 2011; Langmann et al., 2012). The air traffic shutdown affected more than 4 million passengers and was estimated to have cost US$ 5.0 billion in lost global GDP (Oxford-Economics, 2010). No visible ash fall was detected over the European area, but a mass loading of 0.6 g/m^2, 40 μm modal grain size was measured in Tórshavn, Farao Islands (Stevenson et al., 2012). Air quality measurements also showed a small rise in the 24 h moving average concentrations of particles <10 μm (PM_{10}) at ground level in the UK (Stevenson et al., 2012). However, the plume height of the 2010 Eyjafjallajökull eruption never exceeded 10 km (Dellino et al., 2012).
Then in 2011 another VEI 4 eruption from Iceland produced an ash cloud that was detected in the Faeroe Islands, Scotland, Norway, Sweden, Finland and Denmark (Kerminen et al., 2011; Hreinsdottir et al., 2014). This was the largest eruption from Grimsvötn volcano since 1873, but the third eruption of this volcano since 1996 (Hreinsdottir et al., 2014). Once again air traffic was suspended on behalf of a moderate eruption with no visible ash fall, though the presence of ash was detected in air pollution levels (Kerminen et al, 2011).

In September 1625 black sand rained down over Bergen, Norway (Magnússon, 1627; Thorarinsson, 1981). It lay like snow and colored the sails black on ships in the harbor (Magnússon, 1625; Thorarinsson, 1981). This black sand was basaltic ash and it came from Katla volcano in Iceland. Again 130 years later basaltic ash from Katla colored hanging laundry black on the Farao Islands (Det Kongelige Danske Videnskabernes Selskab, 1758) in what in Icelandic records is known as the largest Katla eruption in historical times (Thorarinsson, 1958; Larsen, 2000, Larsen, 2010). It is clear even by qualitative comparison to the 2010 Eyjafjallajökull and 2011 Grímsvötn eruptions that events of such magnitude would have enormous consequences in modern times.

In the aftermath of the 2010 Eyjafjallajökull eruption European societies realized that hazards related to volcanic eruptions in Iceland were not restricted to the Icelandic territory. Analysis of the Icelandic tephra records show that these two examples of volcanic activity are neither extraordinary in magnitude nor frequency (Davies et al, 2010; Sammonds et al, 2010). Thus the 2010 Eyjafjallajökull eruption initiated a flurry of ash-related research on issues such as:

- **The volcanological characteristics of the Eyjafjallajökull and Grímsvötn eruptions** (e.g. Gislason et al., 2011; Dellino et al., 2012; Gudmundsson et al., 2012; Stevenson et al., 2012; Cioni et al., 2014, Hreinsdottir et al., 2014; Liu et al., 2015b; Wilkins et al., 2016)
- **The frequency of ash plumes over Northern Europe** (e.g. Swindels et al., 2011; Lawson et al., 2012; Biass et al., 2014; Sciani et al., 2014; Watson et al., 2016, Watson et al., 2017)
- **Modeling and detection of ash plumes over Northern Europe** (e.g. Bonadonna et al., 2011; Schumann et al., 2011; Bonadonna et al., 2012; Langmann et al., 2012; Biass et al., 2014; Sciani et al., 2014; Wilkins et al., 2016).

This increased focus on the distal hazard potential of Icelandic volcanoes has highlighted 3 unresolved issues in relation to explosive basaltic eruptions from Iceland:

First issue: Dynamics of phreatomagmatic subglacial explosive basaltic eruption are poorly understood.

There is a discrepancy between the known plume dynamics and associated expected impact of subglacial basaltic eruptions (e.g. Gudmundsson et al., 1997; Gudmundsson et al., 2008; Thordarson and Larsen, 2007; Thordarson and Höskuldsson, 2008; Jude-Eton et al., 2012) and the dynamics of the 2011 Grímsvötn eruption (Hreinsdöttir et al., 2014) as well as the recorded presence of large subglacial basaltic Katla eruptions (Einarson et al., 1980; Thorarinsson, 1981; Larsen, 2000; Larsen and Eiriksson, 2008; Thordarson and Höskuldsson, 2008, Larsen, 2010). Most knowledge about phreatomagmatic eruption dynamics comes from direct observations and deposit studies of Surtseyan eruptions (e.g. Thorarinsson, 1967; Walker and Croasdale, 1972; Wohletz, 1983; Dellino and LaVolpe, 1995, 1996; Mattson, 2010; Murtagh and White, 2013; Schipper et al., 2016). Fine-grained, poorly sorted deposits characterize these eruptions with fine lamination by surge deposits as well as accretionary lapilli (e.g. Walker and Croasdale, 1972, Wohletz, 1983, Murtagh and White, 2013). Surtseyan tephra grains are bound by breakage surfaces of the blocky, mostly equant, grains with planar to curvi-planar faces, smooth or stepped surfaces, and faces meeting at nearly right angles (Heiken 1972; Wohletz 1983; Büttner et al., 2002). Morphologies also include moss-like and platy textures (Wohletz, 1983) and vesicles are scarce and usually spherical (Heiken 1972, 1974). The plume dynamics as witnessed by Thorarinsson (1967) were “intermittent explosions” of debris, which were associated with vapor explosions. Thorarinsson (1967) also observed sustained plumes of few km in height feed by continuous uprush of vapor and tephra debris. This correlated with melt/water interaction experiments showing that the blocky shape could result from rapid vapor film generation, expansion and collapse (Wohletz, 1983; Wohletz, 1986; Zimanowski et al., 1997a,b; Büttner et al., 1999, 2002, 2006). In the industry this process is well-studied and known as molten fuel-coolant interaction (MFCI). Therefore much effort has been spent trying to classify ash grains as either blocky or vesicular to distinguish between phreatomagmatic and magmatic fragmentation and to support the MFCI theory experimentally (e.g. Dellino and LaVolpe, 1995, 1996; Büttner et al., 2002; Maria & Carey, 2002; 2007; Dürig et al., 2012; Murtaugh and White, 2013). However, tephra from large subglacial eruptions at Katla contain vesicular lapilli (Óladottir et al., 2005), and quantitative grain morphology studies show that the Grímsvötn 2011 tephra contained vesicular grains (Liu et al., 2015b). Thus the binary fragmentation classification related to the MFCI-framework is not well suited to classify fragmentation in subglacial eruptions. Nor does this eruption framework fully explain the subglacial fragmentation (Liu et al., 2015b).

Additional studies of phreatomagmatic basaltic eruptions have treated the fragmentation of deep submarine eruptions (Schipper et al., 2010), of littoral cones (Mastin, 2007) and of rootless cone environments (Hamilton et al., 2010; Fitch et al., 2017, Hamilton et al., 2017), but none of these environments provide a well-suited analog for large subglacial eruptions, as they do not produce any eruption plume.

The study of wet fissure eruptions suggests that high eruption rates associated with continuous uprush eruptions may produce an eruption plume (Mastin et al., 2004; Mattson and Höskuldsson, 2010) and this may be a better analog for explosive subglacial eruptions.

Another group of phreatomagmatic eruptions that provide information about phreatomagmatic eruption dynamics are phreatoplinian eruptions (e.g. Houghton et al., 2015). However, most phreatoplinian eruptions are associated with silicic melts and characterized by very fine fragmentation (e.g. Thordarson and Larsen, 2007; Carey et al., 2009, 2010, Avery et al., 2017), which do not correspond to the observed lapilli related to the large basaltic subglacial eruptions (Óladottir et al., 2005).

Wet plume dynamics are not straightforward to interpret and lack thermodynamic constraints (Houghton et al., 2015). Although eruption plume height is a function of thermal buoyancy (e.g. Sparks, 1986) and water act as a cooling factor on the system, water vaporization transfers great amount of energy into the gas phase (Houghton et al., 2015). Thus plume height cannot be directly correlated to water-content (Van Eaton et al., 2012). However, pre-eruptive water-temperatures do affect plume height (Houghton et al., 2015) suggesting that the meltingdynamics associated with subglacial eruptions lowers plume height. Woodcock et al. (2012) modeled heat loss in the Gjálp 1996 eruption and showed that 78 % of the initial magma heat could be lost to water boiling. This is consistent with the assumption of lower plume heights for subglacial eruptions. Based on 20th century observations of eruptions from Grímsvötn it was assumed that most eruption plumes of basaltic subglacial eruptions reached a height of 6-15 km (Thordarson and Höskuldsson, 2008). Thus the general evaluation has been that subglacial eruptions in Iceland didn't pose a significant distal hazard (Gudmundsson et al., 2008, Thordarson and Höskuldson, 2008).

However, the plume of the Grímsvötn eruption reached 15-20 km in the initial paroxysmal phase, where most of the tephra production occurred (Hreinsdottir et al., 2014). Furthermore, Mele et al. (2011) conducted at systematic study of the aerodynamics of ash particles using the Dellino et al. (2005) shape factor. They found that ash particles typically are highly irregular and that this irregularity results in a lower terminal velocity than for regularly shaped particles of similar grain size. This explains, why ash particles can be carried long distances in spite of a weak eruption plume, as seen in the Eyjafjallajökull eruption (Dellino et al, 2012).

Thus the dynamics of large basaltic subglacial eruptions cannot be equated to previously studied phreatomagmatic eruptions.

Second issue: Lack of basaltic tephra in European crypotephra record

Basaltic cryptotephras are hardy ever retrieved in the European tephrostratigraphy even though historical records document their presence in the European area (Larsen and Eiriksson, 2008a; Pyle-O'Donnell, 2011; Lowe, 2011, Swindles et al., 2011; Watson et al., 2016a). This has lead to the conclusion that basaltic eruptions don't produce ash clouds over Northern Europe (Watson et al., 2017) contrary to observations in 2011 (Kerminen et al., 2011) and historical accounts of tephra fall from historical eruptions (Thorarinsson, 1981, Larsen and Eiriksson, 2008). The reason for this discrepancy is still unknown (Watson et al., 2017), but traditional methods of extracting cryptotephra favour rhyolitic compositions (Pyle-O'Donnell, 2011; Lowe, 2011) and Larsen and Eiriksson (2008) suggested that acidity could affect the preservation of basaltic grains. Larsen & Eiriksson (2008) also noted that out of eight historical reports of tephra falls in NW Europe since 1600 AD, four silicic and four basaltic, only three silicic tephras have been recovered from the geological strata.

This causes an underestimate of the distal hazard of phreatomagmatic basaltic eruptions based on the distal cryptotephra record.

Third issue: No eruption source parameters for Katla

Katla has not erupted since 1918, but it is one of the most hazardous volcanoes in Iceland in terms of tephra fall and it is statistically overdue for an eruption (e.g. Larsen, 2000; Gudmundsson et al., 2008; Larsen, 2010; Budd et al., 2016). However, no eruption source parameters (ESPs) or observations exist to support a quantitative hazard and risk assessment of Katla (Biass et al., 2014, Scaini et al., 2014).

Problem and scope of thesis

The combination of an underestimate of the potential size of phreatomagmatic basaltic eruptions (1) with no findings of distal basaltic tephras (2) has lead to a low awareness of the tephra fall hazard of phreatomagmatic subglacial basaltic eruptions. This awareness has now changed with the 2010 and 2011 events and is continuously fueled by unrest at Katla (Budd et al., 2016). However, without the quantitative means to evaluate realistic hazard scenarios (3) mitigation steps are hard to take.

This work contributes to resolving these issues by the detailed study of eruption deposits from Katla volcano.

Geological setting

Iceland is one of the most active terrestrial volcanic regions on Earth with about 2400 eruptions during the last 11ka and an average of more than 20 eruptions per century (Gudmundsson et al., 2008; Thordarson and Höskuldsson, 2008). There are 30 active volcanic systems ranging from central volcanoes to fissure swarms and a combination of both (Sæmundsson, 1978) as shown in fig 1.1. The volcanic systems are structured in the neovolcanic zones (fig 1.1) of which the Eastern Volcanic Zone (EVZ) is the most active (Thordarson and Höskuldsson, 2008). Around 80% of all eruptions are tephra generating explosive eruptions and every 9 in 10 explosive eruption is basaltic (Larsen and Eiriksson, 2008; Thordarson and Höskuldsson, 2008). This unusually high amount of explosive basaltic eruptions is associated with a wet eruptive environment as most explosive eruptions are phreatomagmatic (86 %) (Larsen and Eiriksson, 2008; Thordarson and Höskuldsson, 2008; Larsen, 2010). Most explosive eruptions are assumed to be small producing on average 0.1 km^3 tephra (Thordarson and Höskuldsson, 2008) though the majority of estimated volumes are in the 0.1 km^3 - 1 km^3 range (Larsen and Eiriksson, 2008). However, less than 10 % of the known Holocene tephra layers had been mapped for dispersal in 2004 (Thordarson and Höskuldsson, 2008), so the statistics are not complete even though important work has been carried out since then (e.g Oladottir et al., 2008; Oladottir et al., 2011; Oladottir et al., 2014; Gudnason et al., 2017).

Subglacial phreatomagmatic eruptions from Katla, Grímsvötn and Bárðarbunga account for 60 % of the explosive eruptions with Grímsvötn being the most active volcano in historical times (since 870 AD), whereas Katla is the most productive in terms of volume (Thordarson and Larsen, 2007). Katla has also produced the highest amount of large basaltic eruptions in historical times with even bigger estimated volumes for prehistoric eruptions (Óladottir et al., 2014). It was selected as 1 of the 4 most dangerous volcanoes in Iceland in terms of tephra fall with a roughly estimated 5-10 % probability of producing ash clouds with an ash concentration of 2 mg/m^3 over Scandinavia, the UK and Northern Europe (Biass et al., 2014; Scaini et al., 2014).

Katla volcano

Katla is a 1450 m high, 30 km wide central volcano partly covered by the 600km^2 and 230 m thick Myrdalsjökull glacier (foto, front page) (Larsen, 2000, Björnsson et al., 2000; Óladottir et al., 2005; Larsen, 2010). Together with the 75 km SW-NE trending Eldgjá fissure swarm it forms the Katla volcanic system situated on the S part of the Eastern Volcanic Zone (EVZ) (Jakobson, 1979; Larsen, 2000). All the outcropping nunataks around the caldera are glassy rhyolites (Lacasse et al., 1995; Lacasse et al: 2007). The underlying magma chamber is estimated to be 5 km across and 10 km^3.

Myrdalsjökull has 3 outlet glaciers onto the lowlands, Sólheimajökull (S), Kötlujökull (E), and Entujökull (NW). They cut through deep breaches in the Katla caldera walls (Björnsson et al, 2000), which also function as pathways for jökulhlaups associated with the subglacial volcanism. Melt water and jökulhlaups drain onto the southern and eastern outwash plains (Sólheimasandur (S) and Myrdalssandur (E)) and the northern river of Markarfjót, but all documented jökulhlaups since 1179 AD has escaped at Kötlujökull onto Myrdalssandur with one minor exception in 1860 coming out at Sólheimajökull (Larsen, 2000). The jökulhlaups emerge in close temporal relation to the appearance of a visible eruption plume – either shortly before or after (Larsen, 2000) They discharge in pulses with the first ones usually being most voluminous, carrying melt-water, ice blocks and volcanic material with them (Larsen, 2000).

The closest farms are found at a distance of 13-14 km and the village Vík is about 20 km from the volcano (Larsen, 2000; Biass et al., 2014). Summer grazing fields are found on the east, south and west sides of the complex, a popular recreational area, Þórsmörk, lies on the western flanks, and crucial infrastructure, the highway 1, runs along the southern rim of the complex on the outwash plains to connect southern and eastern Iceland (Larsen, 2000).

Overall geochemistry

The geochemical characteristics of the Katla volcanic system are transitional-alkali Fe-Ti basalts, intermediate, and silicic products (Jakobsen, 1979; Larsen, 1999; Larsen, 2000; Larsen, 2001; Óladottir et al., 2005, 2008; Lacasse et al., 2007, Larsen, 2010). The basalts from

Katla volcanic system display a very narrow compositional range during the Pleistocene and Holocene (Lacasse et al., 2007) with consistently high TiO_2 content of about 4-5 wt % (Oladottir et al., 2005, 2008; Lacasse et al., 2007).

Eruption frequency and duration

The number of estimated basaltic eruptions during the last 8400 years is 300-350 eruptions (Óladottir et al., 2005) and 16-17 SILK layers have been identified in total, but a few more are expected to exist (Larsen, 2010, Larsen & Eiríksson, 2008). Eruptions in the system occurs about 1-3 times pr. century with a total of 20 eruptions in historical times (Larsen, 2000; Larsen, 2001; Larsen; 2010). The average repose time between eruptions is 48 years (since 1500 AD), but it ranges from 13-95 years (Larsen, 2000). The duration of recorded Katla eruptions has been between 2 weeks to 4 month (Larsen, 2000), but both shorter and longer eruption durations could be expected (Larsen, 2010). Silicic eruptions are generally expected to be short-lived event based on their narrow dispersal (Larsen, 2010), but there have been observations of silicic eruptions in historical times to verify this assumption.

Tephra volume estimates

Volume estimates of basaltic tephras have been made for the uncompacted land volumes of all historical eruptions (Larsen, 2000; Larsen, 2010) and for 9 prehistoric eruptions (ages between ~ 1860 BC – 870 AD) (Óladottir et al., 2014). Land volumes of the historic eruptions range one order of magnitude between 0.05 km^3-5km^3 (Larsen, 2010). However, the only deposit larger than 1 km^3 did not originate from the central volcano, but from the Eldgjá fissure swarm associated with the Katla volcanic system (Larsen, 2000; Larsen, 2010). Prehistoric volumes of basaltic tephras range from 0.2-2.7 km^3 with only two deposits smaller than 0.8 km^3, thus showing even larger eruptions in the past than what characterized the historical eruption record (Óladottir et al., 2014).

The volumes of silicic tephras are typically in the range of 0.05-0.3 km^3 of uncompacted material.

Icelandic tephra records traditionally distinguish between uncompacted volumes of freshly fallen tephra and volumes of older compacted tephra deposits. Thorarinsson (1958) found that compaction reduced deposit volumes by c. 40%, which is used as the conversion factor. Although uncompacted tephra volumes on land are useful for local hazard assessment and risk mitigation, they cannot be used to assess distal hazards for aviation and air quality.

Parameters of the large historical eruptions 1755 and 1625

An early determination of the 1755 tephra volume was a crude estimate of at least 1.5 km^3

freshly fallen tephra (Thorarinsson, 1975). Later volume calculations applied isopach maps (1625 map, Larsen, 2000) and estimated the uncompacted tephra volumes on land as 0.8 km^3 for the 1755 deposit and 0.5 km^3 for the 1625 deposit (Larsen, 2010).

Chapter 2

Field methods and field data processing

This chapter provides information on how field data and samples from the 1755 and 1625 eruption deposits were obtained. Methods directly involving sample measurements or field observations are also presented here. Methods used in subsequent modeling are introduced here, but described in further detail in the relevant chapters.

Field work

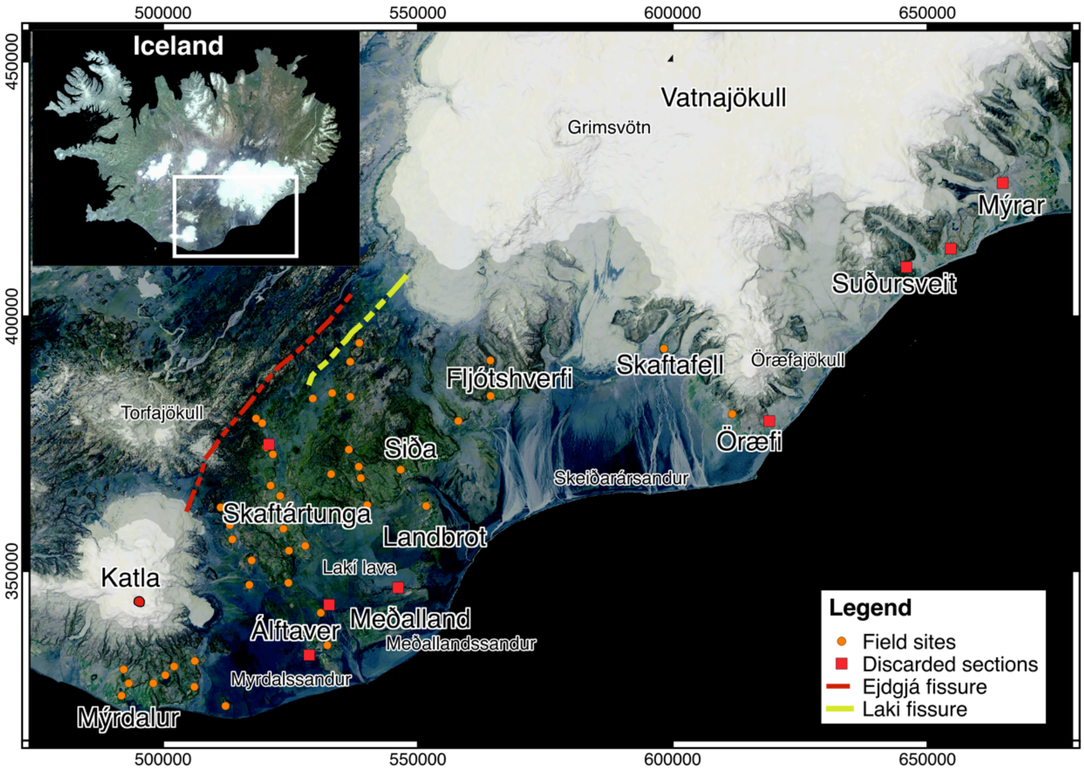

Figure 2.1. Map of the field area showing all 53 field sites. Eight sections were discarded after subsequent examination and overview of photos, observations, and in some cases geochemistry. Background maps are based on data from the National Land Survey of Iceland

Field surveys

Several field surveys were conducted in the SE of Iceland through the fall of 2012 and through the summer of 2014. Initial campaigns in the fall of 2012 focused on downwind areas 15-70 km from the vent, whereas later campaigns focused on tracing distal areas up to 200 km from the vent as well as the edges of the deposits. A final short field campaign in the summer of 2016 was used to revisit old sites that proved ambiguous or lacked sampling and to expand with a few new field sites in the Laki area (fig 2.1).

The main focus of the field surveys was to get widely distributed grain size samples along the main dispersal axis and on perpendicular cross sections of the deposits as well as to supplement previous observations and thickness measurements. The existing field observations (Larsen, personal communication, fig 5.2, and fig 5.3) were used to guide the search for good sections and to locate possible blank spots.

In total 53 sections were logged with thickness data, layer descriptions and field observations (fig 2.1, fig 5.2, fig 5.3, appendix A, appendix B).

Field observations are presented in the section logs and photos of appendix A. Thickness measurements were made with a 1 mm precision measuring stick and a measuring error of ± 2 mm. However, layer thickness is subjectively defined based on interpretation of primary layer features, section selection and spacing and natural thickness variation due to topographical changes (Engwell et al., 2013). An average measurement uncertainty of ~ 30% is therefore assumed following Engwell et al. (2013).

Section types

All data were collected from soil sections, as they were readily accessible, the layers were mostly well preserved, deformation and out washing of the layers was minimal compared to the glacial setting, and there are no complications from multiple flow depositions as in marine cores. Using a single section type also support a more coherent dataset, although local landscape factors, wind and water regimes still provide unique reworking and preservation conditions for each site.

Distribution of sampling sites

There are a few challenges related to finding soil sections in the SE of Iceland. The three large glacial outwash planes of Myrdalssandur, Meðallandssandur, and Skeiðarársandur dominate the lowland area of the SE and the vast lava fields from the 1783-84 Lakí eruption and the 934-37 Eldgjá eruption cover large parts of the lowlands as well (fig 2.1). Preservation conditions in the highland vary a lot and erosion of the tephra layers is common. Thus soil for preserving the tephra layers is not evenly distributed across the SE area and is completely absent close to the coast and on the sandurs. The most well preserved sections are found in the hilly grasslands such as Skaftártunga (fig 2.1), where the soil accumulation rate is high.

Thus the sampling of the deposits is biased in an E and NE direction with very few points to the SE and no proximal data. Below follows a description of the geographic areas of the field surveys. All areas are shown in figure 2.1 and all sections can be found in appendix A and appendix B.

The Rjupnafell section

The most proximal and detailed downwind section was found on the E side of Rjupnafell 22.5 km from the eruption site. Here the deposits consist of several sorted beds of lapilli to fine ash and the 1595 bluish Hekla deposit works as a stratigraphic marker. This section is used as a reference section for detailed studies of eruption evolution and dynamics in Chapter 4 and further details can be found there.

Skaftártunga and Síða

Plenty of soil was accessible in the areas of Skaftártunga and Síða providing good section coverage of these regions about 20-60 km from the eruption site. These areas were also rich in distinctive marker layers from the other volcanic systems in the EVZ and thus offered good stratigraphic control. In Skaftártunga many sections showed bedded deposits from the 1755 and 1625 eruptions, which were sampled and measured separately, but only one layer was distinctive enough to be correlated between sections. This was the white layer in the 1625 deposit, but to keep the dataset consistent both deposits were treated as whole eruption deposits.

Lakagígar and Eldgjá

The Lakagígar and Eldgjá areas about 25-70 km NE from the vent are still dominated by the lavas and tephras from the fissure eruptions as well as arid areas with little soil available. However, the stratigraphic control by marker layers is remarkably good in places with soil and therefore the trace of the 1755 deposit can be determined although the layer is too thin for sampling in most places. The 1625 deposit can be found and sampled throughout the region.

Alftaver, Meðalland, and Landbrot

The areas Alftaver, Meðalland, and Landbrot about 30-60 km SE-E of Katla were dominated by sandurs and lava fields from Eldgjá and Laki and many EVZ-eruptions never reached these areas. Thus soil sections are scarce, but the 1755 and 1625 deposits are distinct in terms of thickness here aiding the field recognition. Both deposits still show internal bedding in Alftaver, but no bedding in Landbrot further E.

Mýrdalur

The geographically most proximal sections are found in the Mýrdalur area S of the eruption site. They all lie within 14 to 21.5 km of the vent area, but in a crosswind direction. The Mýrdalur sections remain the most ambiguous since almost all tephra layers in this area are from Katla. The only available marker layers are the 1597, 1341 and 1300 Hekla deposits, which don’t cover the whole area, and then the 1357 Katla deposit, which is characteristically thick and coarse all over Mýrdalur (please refer to Chapter 5 for details on marker layers). Thicknesses of individual Katla layers can vary substantially between sections, and thin layers appear or disappear within short distances, which makes direct correlation between sections more difficult. The final interpretation of sections in this area was therefore reached by combining knowledge of eruption history from Katla (Larsen, 2010) and direction of historical eruptions (Larsen, 2000) and previous studies of the area (Buckland et al., 1986) with observations of marker layers and general rhythm and thickness of all layers in the sections. The 1625 deposit is missing in most sections in the area, while the 1755 deposit is found in all sections.

Fljótshverfi

In the Fljótshverfi region 70-90 km NE of the vent soil sections were less frequent and basaltic deposits from Grímsvötn volcano started to dominate the soils. Fortunately several stratigraphic markers still aid a field-based determination of stratigraphy. The 1755 and 1625 deposits show no internal structures marking the transition into the distal part of the deposits.

Skaftafell and Öræfi

Glaciers, steep topography and flooding planes dominate the Skaftafell and Öræfi areas around Vatnajökull and Öræfajökull volcano about 115-140 km ENE of the eruption site. Furthermore the 1362 Öræfajökull eruption deposit had destroyed soil production in the S-most parts of the Öræfi region. The thin Katla deposits cannot be uniquely distinguished in the field from the many other basaltic deposits from e.g. Grímsvötn and thus stratigraphic control was essential. This changed the field strategy in this area slightly, as more layers were sampled in the field for geochemical analysis.

Suðursveit and Mýrar

The most distal areas in the field surveys were the Suðursveit and Mýrar regions about 150-200 km NE of Katla. Situated on the edge of the Vatnajökull glacier these regions were also dominated by glacial landscapes with little undisturbed soil. A few soil sections were located, but there was no visual recognition of the Katla deposits. Several layers were sampled for geochemical analysis.

Modification of soil section dataset

In total 8 sections were discarded from the original dataset leaving 45 sections for the study (fig 2.1, Appendix B). In sections with limited stratigraphic control layers were analyzed geochemically to relate them to source volcanoes. The different volcanic systems in the EVZ are distinctive in terms of major element geochemistry (e.g. Óladottir et al., 2011) and therefore major element analysis of tephra samples can be used to assign the sampled layers to their volcanic system of origin. A total of 10 samples from 5 different sections in the Skaftafell, Öræfi, Suðursveit and Mýrar regions were analyzed (Appendix B, Appendix C). Two samples from the Skaftártunga region served as reference samples of the 1755 and 1625 deposits (Appendix C). Five tephra grains from each sample were mounted in a grid structure and cast into an epoxy plug. The plug was polished and carbon coated and run on a JEOL JXA-8200 Superprobe electron microprobe at University of Copenhagen for major element analysis. The acceleration voltage was 15 kV, the beam current was 10 nA and the beam diameter was 15 μm. Natural and synthetic minerals and glasses were used as standards (K22_ATHO and K15_KL5) and the standards were run for every 6th sample. Six to ten measurements were made on each sample and the average of the oxide total for the whole dataset was 99.01±0.94 with a single outlier below 95 % total oxides. The outlier was removed from the dataset.

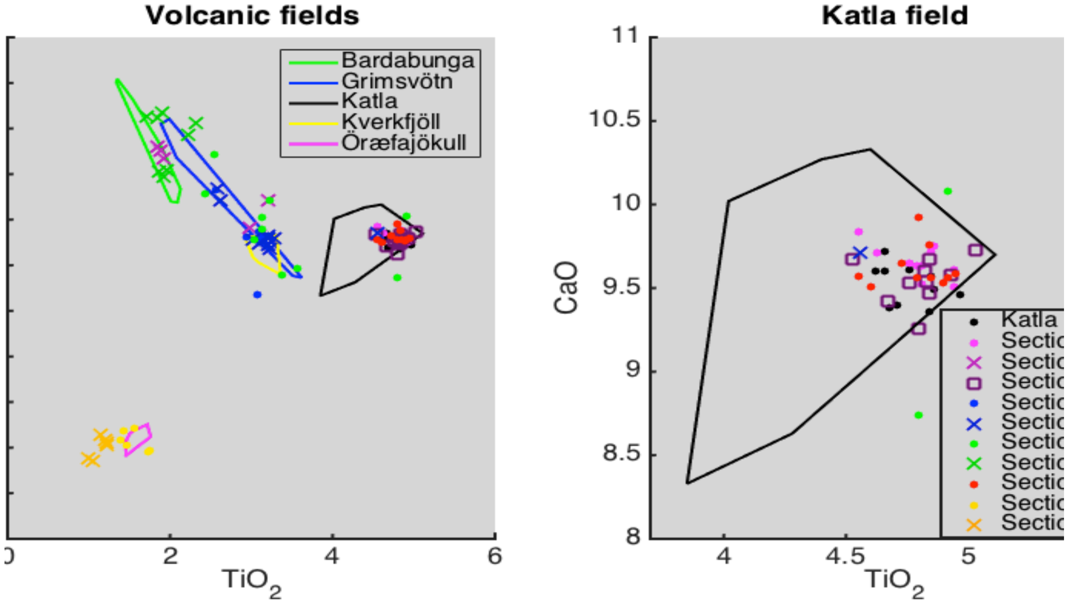

Figure 2.2. Major element variation diagrams showing the compositional fields of central volcanoes in the EVZ as well as the distribution of the analyzed samples. Section numbers refer to sections as presented in appendix A and B and a, b, and c refers to layers as outlined on the sections in appendix A. The right panel shows only the Katla field and shows that Gröf, section 21a, c and Skaftafell, section 25a are from Katla. Volcanic fields are based on data from Óladottir et al., 2008, Óladottir et al., 2011, and Larsen, 1999.

The geochemical variation diagram (fig 2.2) contains the compositional fields of the volcanoes closest to the sampled areas. In the CaO vs. TiO_2 variation diagram the compositional fields of the volcanoes hardly overlap and thus samples can be uniquely correlated to their source volcano. All analyses from each sample are included and the right panel shows that only 3 samples from 2 sections are related to Katla. One sample is from the Skaftafell section (section 25) and the other 2 are from the Öræfi section Gröf (section 21) (see fig 2.1, 2.2 appendix A and B). Sections 22 (Reynivellir) and 24 (Heinaberg) from Öræfi and Mýrar were removed from the dataset as no Katla deposits were found there (fig 2.1, 2.2, appendix A and B).

Other modifications were related to issues with separating homogeneous fall deposits from fine-grained jökulhlaup deposits. Qualitative comparison of photos and samples resulted in the subsequent removal of one Álftaver section (Hraunbær, section 12, appendix A and B) and one Meðalland section (Eldvatn, section 6, appendix A and B) from the original dataset, as the layers turned out to be water deposited.

Two sections in Suðursveit were also removed. One section was primarily measured for the Öræfajökull 1362 deposit, which left the upper part of the section including the Katla deposits poorly constrained (Steinadalur, section 19, appendix A and B). The other section showed signs of water deposition and was abandoned in the field after measuring (Borgarhafnarstadir, section 23, no photo). A section on Skaftártunga was withdrawn, as a better section was found very close by in a later campaign (Framri Tónfahringar, section 34, appendix A and B). Finally a section from Meðalland was removed from the dataset, as two stratigraphic markers were initially mixed up and all exposed soils in the area turned out to be prehistoric (Leidvellir, section 7, appendix A and B).

Isopach maps

When constructing the isopach maps additional thickness measurements from previous field campaigns in the 1970's by Gudrun Larsen (GL) were included in the dataset. In general the new and the old datasets showed good agreement, but a few outliers were excluded after examination of the stratigraphic control and field observations of the deposits. However, even with the addition of 59 sections the data point distribution was still highly skewed towards the Skaftártunga and Síða areas providing poor constraints on the E and SE shape of the isopachs. Therefore information on wind directions from contemporary descriptions was included to guide the interpretation of the thickness data distribution.

Wind analysis

A crude wind rose based on the wind data presented in table 4.4 was created for each eruption to quantitatively include information about wind conditions. The dataset was collected from weather descriptions in 3 contemporary texts (Magnússon, 1627; Det Kongelige Danske Videnskabernes Selskab, 1758; Hallgrímsson, 1870). However, observations had to be adjusted as people tended to align e.g. mountain ridges with E-W or N-S directions (Thordarson, 1991). Therefore the actual bearing trend of relevant ridges was measured and the wind directions were adjusted accordingly (Chapter 4, contemporary texts).

Time intervals have been binned by day/night and directions have been divided into 22.5° intervals. Intensities have been categorized into: No wind, wind, and strong wind/storm, which have in turn been translated into Beaufort scale intervals of 0 (0-0.3m/s), 1-6(0.3-13.9m/s) and ≥7 (≥13.9m/s) (figure 2.3). It should however be noted that wind data was collected from contemporary texts that are non-scientific and thus the interpretation has been done with great care.

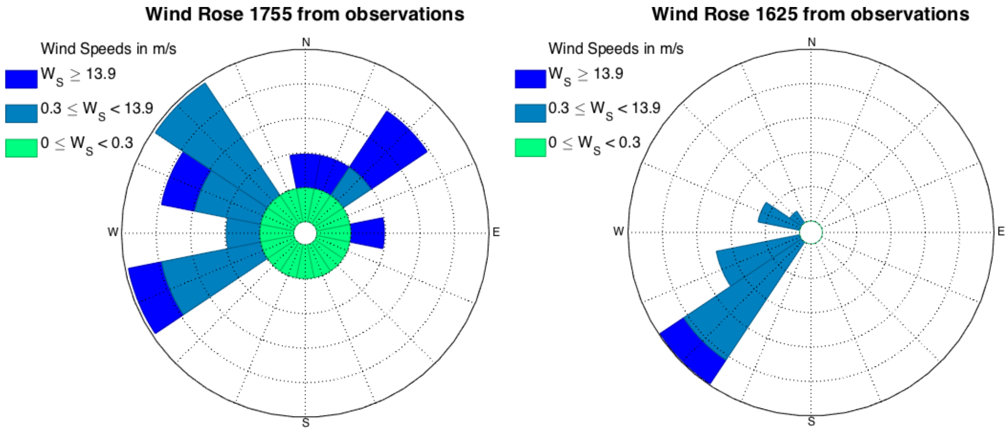

Figure 2.3 Wind roses showing the wind conditions during the 1755 and 1625 eruptions based on contemporary text data corrected (Magnússon, 1627; Det Kongelige Danske Videnskabernes Selskab, 1758; Hallgrímsson, 1870).

There are distinct differences between the wind conditions between the two eruptions. Wind conditions were dynamic and changing in strength and direction during the 1755 eruption, whereas the 1625 eruption had much more stable wind conditions.

1755 isopach map construction

The best-constrained isopach was the 10 cm line, which had an N, NE, E and SE constraint. The N extent was determined from the 8 cm (total 11 cm) measurement at Atley (fig 2.4ab). The top of the 1755 layer was eroded and mixed with soil, so the 8 cm is a min. thickness. The NE extent was determined by a cluster of measurements ranging from 9 cm (total thickness 20) at

Hemra to 7 cm in several places around Svinadalur (fig 2.4ab). Stratigraphy at Hemra was well-constrained, but the uppermost 11 cm of the total 20 cm were mixed with small amounts of soil. The E extension was constrained by the measurement at Skálmarbæjar (old farm, Skalmarbaeramaur fig 2.4a), where the stratigraphic constraint of the section was poor and thus the measurement of GL was followed (fig 2.4b).

The SW extent was estimated from a group of points on Alftaver converging around 12 cm (fig 2.4ab). Extent S-wards was estimated from the 6 cm measurement by GL (fig 2.4b). The wind rose was used to guide the final shape of the 10 cm isopach line, which was subsequently used to define the overall shape of the 1755 isopach map.

The 20 cm and 100 cm isopach were drawn afterwards reflecting the same shape as defined by the 10cm isopach, but with very few points as constraints (fig 2.4ab).

Then the 2 cm isopach was added with good constraints N and S, but has primarily relied on sections from this study as the stratigraphic control was well-known for all sections (fig 2.5a). The E extension was based on the measurement of 2 cm at Dalurfell from this study.

The 1 cm isopach was constrained in a similar way as the 2 cm isopach, but the E extent was estimated from several measurements W of Öræfajökull (fig 2.5a). A 0.1 line was based on GL indications of traces of 1755 (marked as (x), fig 2.5a).

The 0 line (to be used for total grain size distribution modeling) was drawn from the descriptions of the tephra fall. The ash fall reached all the way to the Eastfjords (Mjóifjördur) as well as Fljótshlid due to changing winds. This has been accounted for in the 0-line of the tephra map in figure 2.5b.

1625 isopach map construction

The 1625 thickness dataset required additional interpretation of local depositional effects as particularly medial points showed great diversity in thicknesses within very short distances. Some of the discrepancies could be explained by local preservation factors and landscape morphology, but the total variation could not. A few sections were therefore selected as key sections with good exposure and preservation as well as stratigraphic control from marker layers.

The 10 cm and 5 cm isopach lines have been used to define the overall shape of the isopach map (see fig 2.5) along with the wind rose (fig 2.3b).

Key sections for the 10 cm isopach of the 1625 map were Ingill, Þorláksfell, Hellnamyri (fig 2.6a) and these 3 sections define the NE extent of the 10cm isopach.

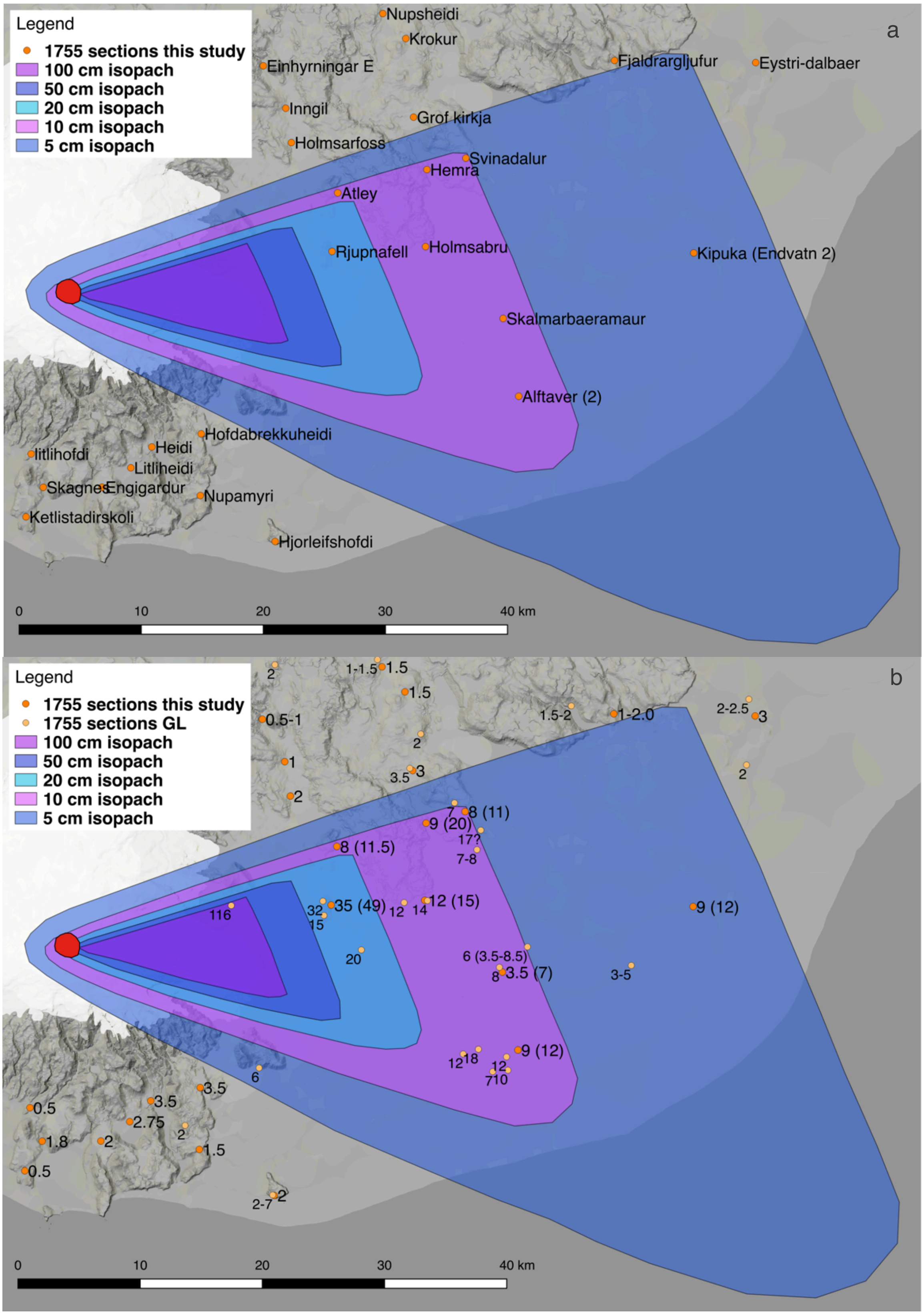

Figure 2.4 showing maps with 100 cm to 5 cm isopachs of the 1755 deposit. 2.4a shows section positions from this study with names while 2.4b shows the thickness measurements at these sections for the 1755 deposit together with sections measured previously by Gudrun Larsen (GL). At some sections ranges of thicknesses are reported, as no single thickness value was representative. In sections with primary internal layering of the 1755 deposit, the total layered thickness is given with the total thickness of the deposit in brackets. See text for additional comments.

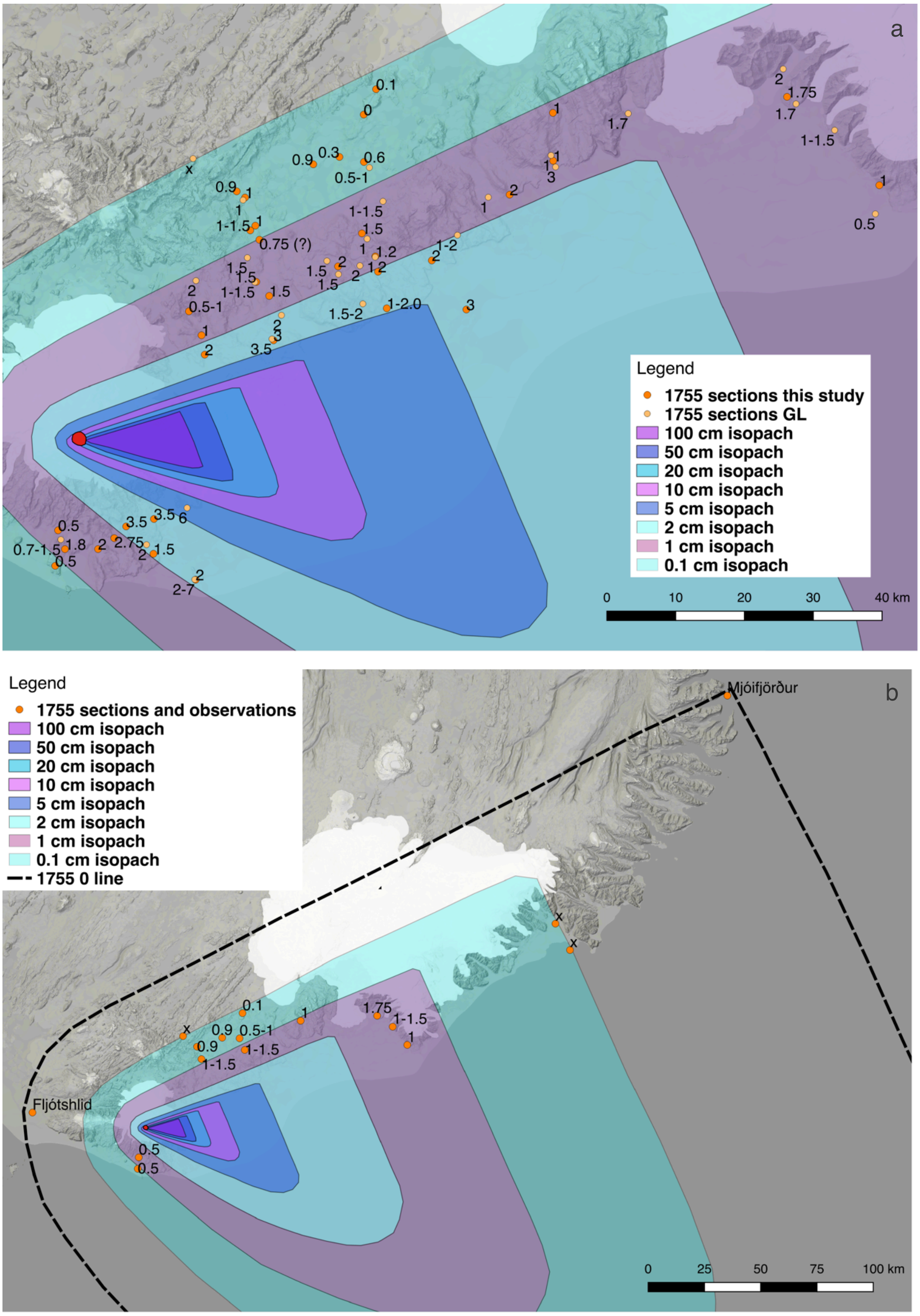

Fig 2.5a showing measurements used to constrain the 2-0.1 cm isopachs for the 1755 deposit. The map in 2.5b shows the information used to constrain the 0 line for the 1755 deposit. An x indicates a trace deposit was observed. See text for additional comments.

For the E and SE limits of the 10 cm isopach the sections of Svindalur, Holmsábru and E Eldvatn (GL) were considered (fig 2.6a). Svinadalur had a 7cm stratified deposit and about 12 cm of deposit in total with signs of reworked fine top. The primal thickness might be bigger than 7 cm, as the section was on a slight slope and thus could be thinned. The distinct 0.5 cm white dust layer was seen 1.5 cm from the deposit base and the section had a well-constrained stratigraphy. At Holmsabru (Hrifunes) there was a 12 cm stratified deposit with about 2 cm reworked top and 10 mm light-colored dust at the base. The total thickness was 14 cm and the stratigraphy was well constrained. At E Eldvath ~40 cm deposit with about 0.5 cm light colored dust at the base was found by GL with good stratigraphic control. A photograph shows reworking of the top of the deposit, but unfortunately there are no measurements of the stratified deposit and thus the primal thickness is unknown. Neither of these sections can be used to define the 10 cm isopach specifically, so instead the shape of the 5 cm isopach is used and these sections are then useful to estimate the extent of the 10 cm isopach in the E and SE directions.

For the E and SE extension of the 5 cm isopach line the key sections that are used to define the shape are the Eldvatn 2 section in a Kipuka in the Laki lava field as well as sections around Klaustur by GL and at Skalmarbaramaur (fig 2.6ab).

To the SE the Eldvatn 2 secion has a ~20 cm thick 1625 layer in a tilted section pushed up by the Laki lava forming a kipuka. The layer is still intact though cut by faults and slightly undulating at the top. The layer seems to be stratigraphically constrained by the Hekla 1597 layer and consists of 13 cm homogeneous tephra, where the top is undulating and disturbed (no exact measure) and 7 cm stratified. This point is placed within the 5 cm isopach area.

The E extent is constrained by measurements around Kirkjubæjarklaustur by GL. The section at Prestbakki from this study is considered a minimum thickness as all tephra layers in this section are fairly thin suggesting extensive remobilization of the tephra in this area.

Going S the Skalmarbaeramaur section shows a well-defined stratigraphy with 4-6 cm tephra and a reworked top and thus constrains the S extent of the 5 cm isopach. In addition to these three key sections a wind rose was used to construct the 5 cm isopach line. The N and NE shape followed that of the 10 cm isopach, but then the overall shape of the map was modified to both fit the three key sections as well as the wind rose.

The shape of the 20 cm isopach was given by the 10 cm isopach and the E extension was determined from the Hemra point with 18 cm stratified section and 19 cm 1625 tephra in total (fig 2.6ab). This point is placed just outside the 20 cm isopach.

The 50 cm isopach was drawn on the basis of the Rjupnafell (this study) and Moldir sections (GL) with Moldir showing ~50 cm of tephra (fig 2.6ab). In the lowermost 6-7 cm the black tephra is mixed with light colored dust which forms a ~0.5 cm clean light-grey layer at the top of the 6-7 cm layer as is in line with observations at Hemra and elsewhere for this layer. Thus min. 7 cm of the total 50 cm are stratified, but there is no reported primal thickness. There is also no stratigraphic control in terms of marker layers, so layer recognition is based on characteristics of the lower mixed and light units only. Although the primal thickness is unknown at Moldir the thickness at Rjupnafell and the overall shape of the isopachs suggests that the border of the 50 cm isopach lies close to this point and it has been included just within the 50 cm isopach as it is unknown whether erosion or secondary deposition have influenced the primal thickness of this section.

A suggestive 30 cm isopach was drawn based on the Hemra, Rjupnafell and Moldir sections (fig 2.6ab).

The 2 cm isopach was constrained N and NE by several points, but only approximated to the overall shape on the S part. Several measurements on Alftaver show thicknesses larger than 2 cm, but the Alftaver section shows a 2 cm thick unit with 2 cm medium ash on top (fig 2.7ab). The very top of the layer is reworked and so the primal thickness is most likely around 2 cm.

The N edge of the 1 cm isopach was well-constrained by several measurements in the Eldgjá and Laki area as was the most proximal S part measured in Myrdalur (fig 2.1, 2.7b). The E constrain was only given by a single point near Öræfajökull (fig 2.7ab).

The 0.5 cm isopach line was constrained S by measurements in the Myrdal-area as well as N from sections in the Eldgjá and Laki areas (fig 2.1, 2.7ab). The eastern extend was not constrained by direct measurements and was estimated based on the overall shape of the rest of the map.

The 0-line is suggestive and it was defined in order to model the total grain size distribution. The 0 line was based on measurements in Myrdalur (S) and near Eldgjá (N) (fig 2.7ab). Furthermore the description in Eldrit (Hallgrímsson, 1870) reported ashfall as far North as Langanes and over the entire South and East country. Ashfall over the sea NE of Iceland is also reported. Gudmundsdóttir et al., 2016 also found a thin 1625 deposit in lake Lögurinn (fig 2.7b)

White dust is found in several base units of the 1625 tephra deposit at multiple locations closest to Katla. It has not been possible to map out this deposit due to lack of points, and it is therefore included in the total 1625 deposit map.

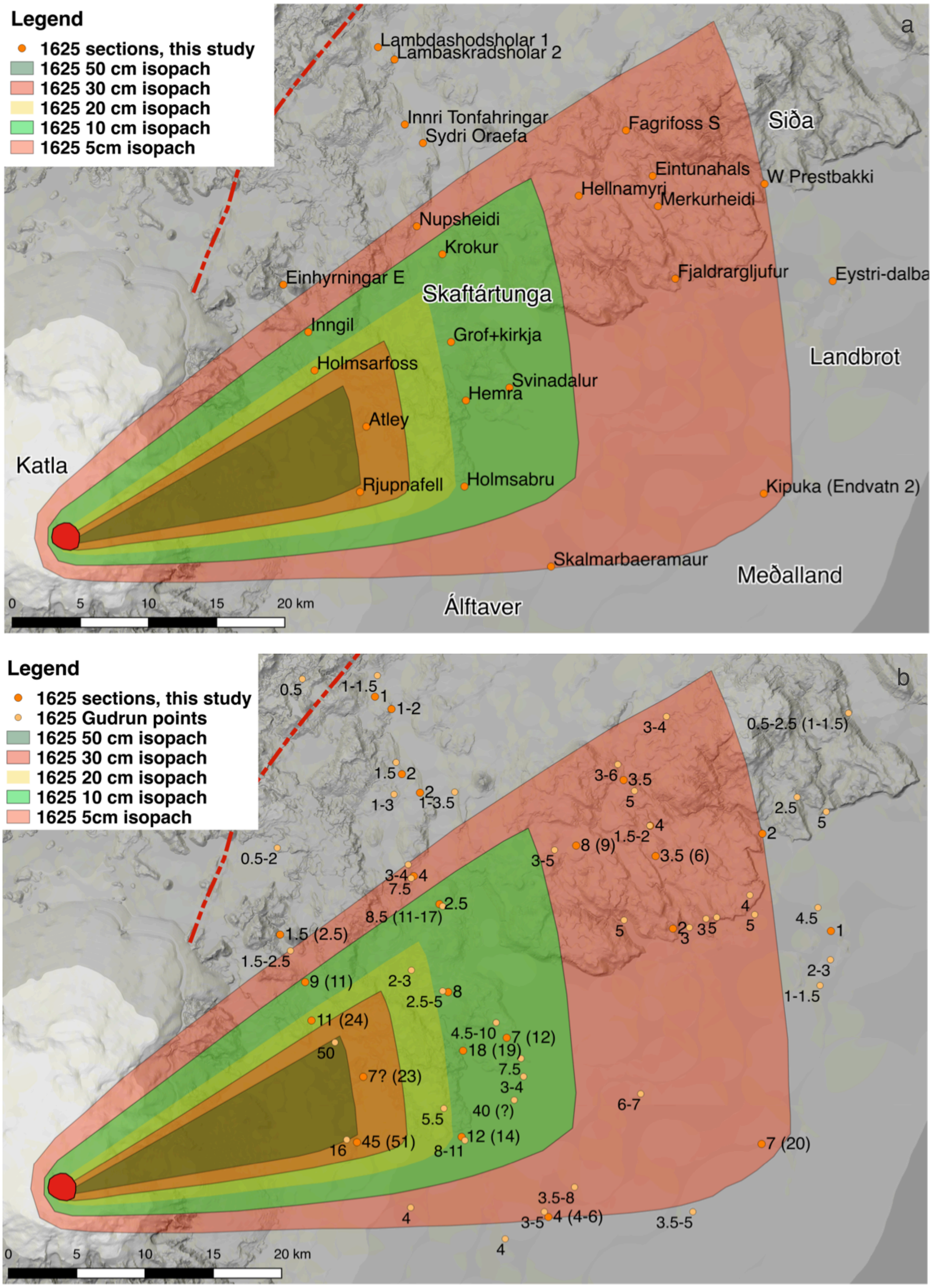

Figure 2.6 showing maps with 50 cm to 5 cm isopachs of the 1625 deposit. 2.6a shows section positions from this study with names while 2.6b shows the thickness measurements at these sections for the 1625 deposit together with sections measured previously by Gudrun Larsen (GL). At some sections ranges of thicknesses are reported, as no single thickness value was representative. In sections with primary internal layering of the 1625 deposit, the total layered thickness is given with the total thickness of the deposit in brackets. See text for additional comments.

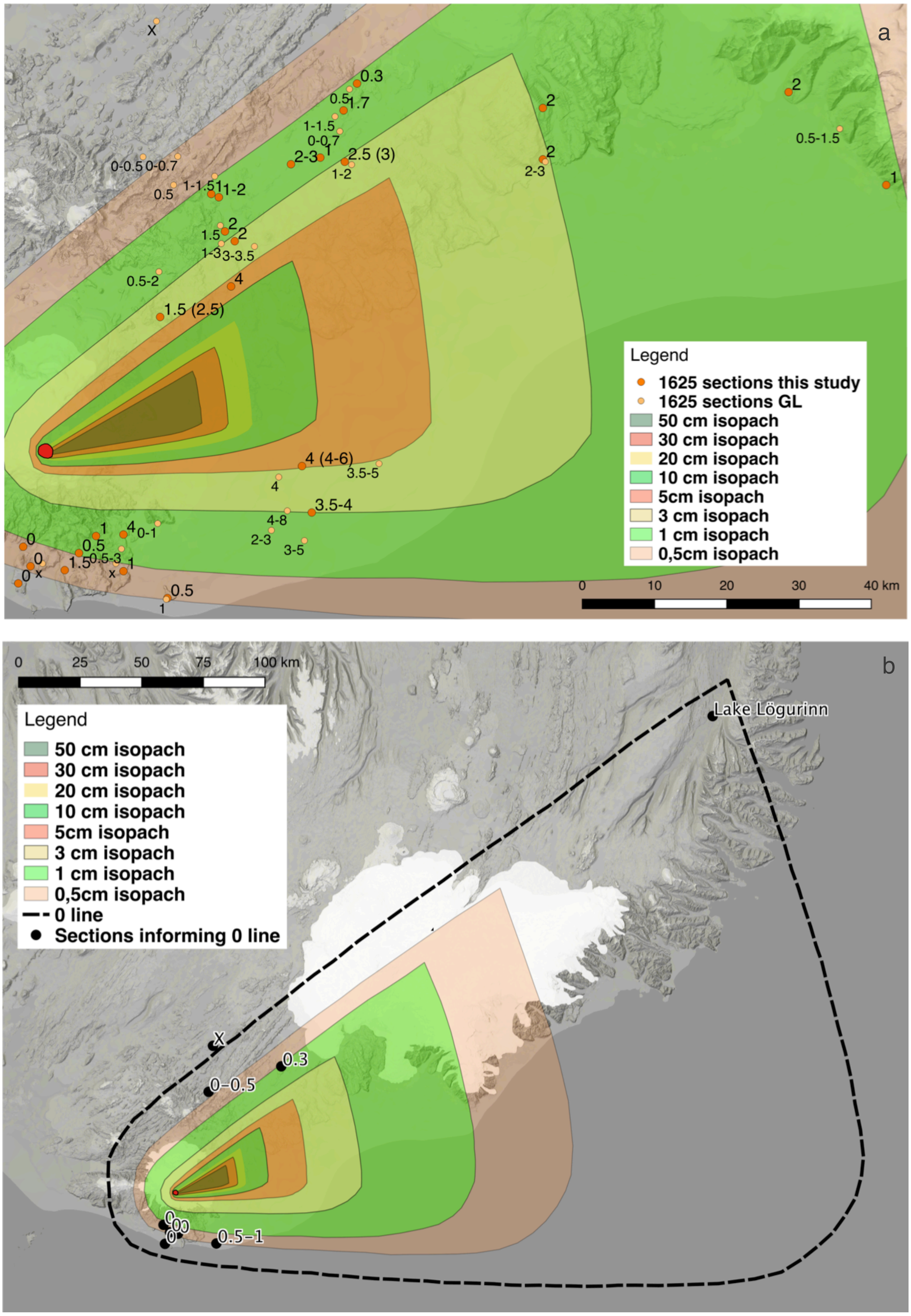

Fig 2.7a showing measurements used to constrain the 2-0.5 cm isopachs for the 1625 deposit. The map in 2.7b shows the information used to constrain the 0 line for the 1625 deposit. An x indicates a trace deposit was observed. See text for additional comments.

Grain size analysis

Grain size was measured on 34 1755 deposit samples and 33 1625 deposit samples (figure 5.2). However, a total of 128 samples were processes for grain size analysis, as all deposits were sampled by individual bedding units.

Sieving

Samples were dried at 50°C and samples > 15g were split in halves. All samples were hand sieved in 1φ steps down to 3φ, split at 3φ and one half was sieved down to 4φ, while the other half was run on the Sedigraph to obtain fine grain data down to 9-10φ. Sedigraph data were automatically binned into whole φ classes and merged with the sieving data using the 3-4 φ overlap to guide relative weights.

Fine grain size distributions on the SediGraph III 5120

The Sedigraph measures the grain size distribution by the sedimentation method, where particle mass and sedimentation fall rate is measured from x-ray absorption and related to an equivalent spherical diameter grain size by Stokes' law. This technique depends on laminar flow conditions during the sedimentation measurement, which required a liquid mixed of 50% glycerol and 50% demineralized water to ensure this condition even for the largest grains. However, increasing the viscosity of the liquid means much longer settling times for the fine particles. Thus the grain size variation should be as limited as possible to allow for as fluid a fall medium as possible so the fine end of the spectrum can settle within reasonable timescales. Therefore the overlap between hand sieving and Sedigraph grain sizes was kept at 1φ.

To optimize the procedure some initial test runs of various ash concentrations were made. Ash contents ranged from 0.5g to 3g. Each sample was run 3 consecutive times and the averages from each run were compared graphically (appendix D, fig D1). Furthermore x-ray intensity reduction feedback related to sample concentration was also logged for ash contents of 0.5 g – 4 g (appendix D, table D1).

The initial test runs showed that 2.5-3.5g of material with 60 ml mixed liquid was the acceptable amount of ash to produce stable results. Thus samples larger than 3 g were setup for a single measurement run with 3 g of sample in 60 ml liquid. Samples with less than 3 g available material were setup for 3 consecutive runs and results were reported as the average of the 3 runs. This procedure ensured good data quality for ash contents down to 1 g.

Density

The density of the ≤3φ grain size ash was measured by 100 ml pycnometer for use in tephra dispersal modeling and to obtain better accuracy on the Sedigraph grain sizes. Pycnometer measurements were carried out with demineralized water left on the lab counter overnight to obtain a stable water temperature for all measurements. Densities were calculated as the average of 4 samples from each deposit with standard deviations of 3.5 % and 5.4 % for the 1755 and 1625 deposit, respectively.

Average bulk density of field samples was also calculated based on mass loading measurements as presented in Chapter 5.

Componentry

Componentry was determined on the 3-4φ grain size range for all depositional units from the Rjupnafell deposit (please refer to appendix A and Chapter 4 for more information on the Rjupnafell units). Small subsamples were taken from the 3-4φ sieving portion of each unit after turning the sample bag slowly upside down 2-4 times to ensure proper mixing of the sample contents. Componentry counts were made on 100 grains/sample using binoculars.

Ash grain morphology

Descriptive ash grain morphology

A Hitachi TM 3000 Tabletop scanning electron microscope (SEM) was used to obtain images of ash grains in the 3-4φ size interval. The ash grains were mounted on a Hitachi 12.5 mm sample stub with carbon tape and were coated with gold. Twelve samples were selected to cover the most proximal down-wind deposits in the Rjupnafell section (appendix A, fig 2.1) as well as the distal section at Blomsturvallafjall (appendix A, fig 2.1) for both the 1755 and 1625 deposit. The images served as supportive imagery for the quantitative Particle Insight dynamic shape analyzer morphology study. Therefore the images were studied to get a qualitative overview of grain types, surface features and grain erosion, but no quantitative grain counts were attempted.

Quantitative grain morphology

A new method for quantitative grain morphology measurements was developed for the 3-4φ size interval of ash using the Particle Insight™ dynamic shape analyzer (PIdsa). Details of the method are presented in Schmith et al. (2017) in Chapter 3 and the reference grain dataset is presented in appendix F. All 128 grain size samples were also run on the shape analyzer and analyses from all the Rjupnafell units (appendix A) and presented in Chapter 4.

Modeling methodologies

Grain size modeling

Raw grain size distribution data have been described using the Inman (1952) parameters to describe the distributions (See appendix G for the complete raw grain size dataset). The deconvolution procedure allowed for tracking of subpopulations in a quantitative way and was carried out using the DECOLOG software (Borselli and Sarocchi, 2016).
Wohletz et al. (1989) developed the sequential fragmentation/transport theory (SFT-theory) for volcanic ash to demonstrate the correlation between a fragmentation and/or transport process and resulting grain size distribution. The basis of the theory is that mass distribution from fragmentation of a particle of mass m' is described by the function $f(m' \rightarrow m)$ as

$$f(m' \rightarrow m) = \left(\frac{m}{m_1}\right)^{\gamma}, \qquad \text{Eq. 1.1}$$

where m is the mass of the particles in the final population (m'>m) and $\left(\frac{m}{m_1}\right)^{\gamma}$ describes the sequential cascading mechanism similar to a chain reaction. The sequential mechanism relates the average mass m_1 to m by the free parameter γ, although γ is constrained by $\gamma \geq -1$ as particles have to break into smaller particles. Different fragmentation mechanisms have different distributions related to γ. Utilizing prior knowledge about fragmentation processes Wohletz et al., 1989 derived different equations for the resulting grain size distribution of both magmatic and phreatomagmatic fragmentation. They showed that γ was well suited to distinguish between magmatic and phreatomagmatic fragmentation. Values of -0.33 to -0.66 represented the full magmatic fragmentation process, whereas values between -0.5 and +0.33 were expected for phreatomagmatic fragmentation. This model was tested on the 1755 and 1625 deposit to explore the potential of an integrated shape and grain size interpretation of fragmentation mechanism.

Volume

Volume was calculated from isopach thickness and area using exponential (Fierstein and Nathenson, 1992), power law (Bonadonna and Houghton, 2005), and Weibull fits (Bonadonna and Costa, 2012) as standard procedure comparable to other studies (e.g. Daggit et al., 2014; Bonadonna et al., 2015). Isopach area was determined in QGIS and results are shown in appendix H. Volume was modeled in the AshCalc module (Daggit et al., 2014) and uncertainty was estimated using the TError package (Biass et al., 2014). AshCalc and uncertainty model inputs are described in chapter 5.

Recent studies have developed alternative volume calculation methods to overcome issues of poor field data coverage and the subjective process of selecting and constructing isopach/isomass maps (Burden et al., 2013; Engwell et al., 2013; Klawonn et al., 2014; Engwell et al., 2015; Green et al., 2016; Yang and Bursik, 2016). Some studies have aimed at automating the construction of isopach maps (Engwell et al., 2013; Engwell et al., 2015), while others suggest direct integration of field data to avoid the ambiguity of isopach/isomass map construction (Burden et al., 2013; Green et al., 2016; Yang and Bursik, 2016). Klawonn et al. (2014) showed that the derived volume discrepancy between different expert isopach maps is only 8% for well-constrained medial deposits irrespective of the expert's choice of isopachs. Therefore the main challenge of isopach/isomass maps is the poorly constrained proximal and distal area, but with much less influence on the total volume from the distal part (Klawonn et al., 2014). Thus the main challenge related to volume calculation by isopachs in this study is the lack of proximal data, which cannot be resolved using automatic isopach models. Instead the isopach-based volume estimates were compared to a statistical volume estimate. The Baysian statistical model of Green et al. (2016) use calibration against expert isopachs, which then leads back to the issue of the initial isopach map construction. The Yang and Bursik (2016) model required a "by hand" estimate of wind direction, which would introduce another unconstrained uncertainty unless compared to the isopach map. Thus the statistical model of Burden et al. (2013) was selected for the 1755 and 1625 deposits as it represented a direct integration of the thickness measurements.

Total grain size distribution (TGSD)

The total grain size distribution was calculated from the Voronoi tessellation standard method as recommended by Bonadonna et al. (2015). This model requires the estimate of a zero deposition line, which has been drawn onto the isopach maps based on field observations and descriptions of tephra fall in Iceland.

Total mass and mass eruption rate

The total erupted mass was derived from the total erupted volume using the density model described in chapter 5. Mass eruption rate was then calculated from eruption duration as estimated from the historical descriptions. The duration estimates were made based on observations of the presence of an eruption column.

Plume height

Plume height was derived using the empirical fits of Mastin et al. (2009) from both total dense rock equivalent (DRE) volume and MER:

$$H = 25.9 + 6.64 log_{10}(V)$$

$$H = 2.00 \cdot \dot{V}^{0.241},$$

where H is plume height, V is total DRE volume, and $\dot{V}$ is volumetric flow rate. The volumetric flow rate was calculated from the MER using a density conversion of 2700 kg/m^3 based on the density measurements of the 3-4φ ash fraction. Uncertainty of fits were made using the figures 1 and 2 of Mastin et al. (2009). Model implications are discussed in chapter 5.

Mass loading inversion

A new strategy to derive ESPs is to combine inverse problem algorithms with tephra dispersal models (Connor and Connor, 2006; Klawonn et al., 2012; White et al., 2017). These models use mass loading or grain size data as inputs and then use the inversion iteration algorithm to solve for the optimal parameter combination. Parameters are tested against the data distribution by forward modeling in the tephra dispersal models. Although the inversion algorithm uses the directly measured data the tephra dispersal model required assumptions about clast density, shape and total grain size distribution (Connor and Connor, 2006). The total grain size distribution can be problematic in the forward models, as the model cannot account for the deposition of accretionary lapilli (Mastin et al., 2016). However, corrections have not been made to the measured TGSD of the 1755 and 1625 deposits, as aggregation parameters could not be constrained. The Tephra2 based inversion method of Connor and Connor (2006) was applied here, as the inversion model of Klawonn et al. (2012) required actual observations of the plume shape, which are not available for these historical eruptions, and the model by White et al. (2017) was released too recently to be incorporated into this work. The Tephra2 inversion applies the simplex downhill method for optimal parameter solution. This method finds the local minima of the parameter function, which could result in several sets of parameter solutions. Therefore different starting plume heights ranging from 5 to 45 km were run to test the uniqueness of the solution in a realistic plume height parameter space. The extreme plume heights both converged on the same parameter outcome and thus the minima parameters are considered representative for realistic eruption source parameters. Other model inputs are presented and discussed in chapter 5.

Chapter 3

Grain shape of basaltic ash populations: implications for fragmentation

Johanne Schmith[1,3], Ármann Höskuldsson[1,2], and Paul Martin Holm[3]

[1]Nordic Volcanological Center, Earth Science institute, University of Iceland, johasch@hi.is, +4527121368
[2]Earth Science institute, University of Iceland
[3]Institute of Geoscience and Natural Resource Management, University of Copenhagen

Published in: Bulletin of Volcanology 24 January 2017

DOI: 10.1007/s00445-016-1093-5

Abstract

Here we introduce a new quantitative method to produce grain shape data of bulk samples of volcanic ash and we correlate the bulk average grain shape with magma fragmentation mechanisms. The method is based on automatic shape analysis of 2D projections ash grains in the size range 125-63 μm. Loose bulk samples from the deposits of 6 different basaltic eruptions were analyzed and 20,000 shape measurements for each were obtained within ~45 min using the Particle Insight™ dynamic shape analyzer (PIdsa). We used principal component analysis on a reference grain dataset to show that circularity, rectangularity, form factor, and elongation best discriminate between the grain shapes when combined. The grain population data show that the studied eruptive environments produce nearly the same range of grain shapes, although to different extents. Our new shape index (the regularity index (RI)) places an eruption on a spectrum between phreatomagmatic and dry magmatic fragmentation. Almost vesicle-free Surtseyan ash has an RI of 0.207 ± 0.002 (2σ), whereas vesiculated Hawaiian ash has an RI of 0.134 ± 0.001 (2σ). These two samples define the end-member RI, while two subglacial, one lacustrine, and another submarine ash sample show intermediate RIs of 0.168 ± 0.002 (2σ), 0.175 ± 0.002 (2σ), 0.187 ± 0.002 (2σ) and 0.191 ± 0.002 (2σ), respectively. The systematic change in RI between wet and dry eruptions suggests that the RI can be used to assess the relative roles of magmatic versus phreatomagmatic fragmentation. We infer that both magmatic and phreatomagmatic fragmentation processes played a role in the subglacial eruptions.

Introduction

Hazard evaluations of explosive eruptions are often based on information extracted from the geological tephra record. The significant differences between the hazards posed by magmatic and phreatomagmatic eruptions of basaltic magmas (e.g. Nemeth and Cronin 2011) mean that fragmentation is a key parameter, which is routinely studied on the basis of tephra grain morphology (e.g. Murtagh and White 2013; Dellino et al., 2012; Graettinger et al., 2013; Cioni et al., 2014; Miwa et al., 2015). To obtain interpreter independent results most methods are based on quantitative analysis of grain morphology (e.g. Leibrandt and Le Pennec 2015; Liu et al., 2015a; Genareau et al., 2013; Proussevitch et al., 2011; Büttner et al., 2002; Maria and Carey 2002), but current fragmentation classification methods cannot match observations of complex fragmentation events (e.g. Graettinger et al 2013; Jordan et al., 2014). Therefore we have developed a new quantitative method for studying the fragmentation processes of basaltic tephra deposits. It automates shape parameterization for ash in the size-range 125-63 µm for small samples with good reproducibility. The classification diagram models only the particles actively involved in the explosion and provides a quantitative spectrum between magmatic and phreatomagmatic fragmentation to allow for a more complex fragmentation evaluation.

Background of grain morphology and fragmentation

Tephra grain morphology has been linked to magma fragmentation by two different approaches. One is volcanological and combines grain morphology with eruption types and volcanic processes. It distinguishes between magma fragmentation by either magmatic volatile exsolution (magmatic) or by explosive interaction with external water (phreatomagmatic), thus focusing on fragmentation drivers (e.g. Heiken 1972; Dellino et al., 2012; Murtagh and White 2013). The other approach is mechanical and describes magma fragmentation in fluid dynamic terms as either brittle or ductile deformation (e.g. Büttner et al., 2002; Dürig et al., 2012). The volcanological approach is typically used in studies of field samples of tephra, while fluid dynamic approaches are often preferred in experimental studies.

The volcanological morphology framework

The systematic features that link tephra morphology to eruption types were based on overall grain shape and surface features derived from SEM imagery (Heiken 1972). For the magmatic fragmentation scheme it characterized ash from fire fountains as whole smooth-skinned rounded droplets, elongated strands (Pele's hairs), and broken, ragged, and irregular droplets (Heiken 1972). For magmatic Strombolian activity Heiken (1972) noted equant grains, which contained ovoid to spherical vesicles.

Another classification ties grain morphology to the magmatic volatile exsolution processes by defining simple and complex particles (Proussevitch et al., 2011). Simple ash particles have full-length curved sides representing bubble walls and represent the plateau border between three or more bubbles. Complex particles have indents from more bubbles on their surface and result from the breakage of larger bubbles. Complex particles are larger than the simple particles and for proximal basaltic samples they range in size from 50 μm and up (Genareau et al., 2013), while simple particles dominate the finer ash.

Phreatomagmatic eruptions produce blocky, mostly equant, grains with planar to curvi-planar faces, smooth or stepped surfaces, and faces meeting at nearly right angles (Heiken 1972; Wohletz 1983; Büttner et al., 2002). Vesicles are scarce and usually spherical (Heiken 1972, 1974). Other characteristic morphology traits include moss-like and platy textures, which are usually found in grains smaller than 63 μm (Wohletz 1983).

Graettinger et al., 2013 showed that magmatic gas-driven explosions could trigger phreatomagmatic ones and vice versa creating feedback loops between these two fragmentation types. This explosion facilitation creates highly complex deposits, which can be difficult to interpret in terms of a main fragmentation process (Jordan et al., 2014), though volcanological morphology studies of ash still characterizes deposits as either magmatic or phreatomagmatic (e.g. Murtagh & White 2013; Jordan et al., 2014).

The fluid dynamic morphology framework

This experimental perspective highlights the important distinction between passive and active particle formation (Zimanowski et al., 1997a; Büttner et al., 2002; Dürig et al., 2012). Active particles are produced directly in the explosion whereas passive particles are not. Molten fuel-coolant interaction (MFCI) experiments show that the active particles are angular (blocky) and crack-dominated particles less than 130 μm in size related to brittle fragmentation (Zimanowski et al., 1997a; Büttner et al., 2002). Passive particles are related to ductile fragmentation and consist of spherical and elongated drops and broken strands (Zimanowski et al., 1997a).

Connecting volcanological and experimental data

Phreatomagmatic eruption deposits have been associated with blocky grains inferred to represent the active MFCI particles (Wohletz 1983; Zimaowski et al., 1997a), but blocky particles can also be formed passively by quench granulation in a non-explosive interaction with water. Quench granulation is caused by brittle failure of the material as it contracts during cooling and produces grain sizes around coarse ash to fine lapilli (Mastin et al., 2009; Schipper et al., 2011; Graettinger et al., 2013). Furthermore natural brittle fragmentation involves fragmentation of pre-stressed material (Dürig et al., 2012) and cannot solely be attributed to MFCI.

Passive particles are placed in the magmatic morphology scheme although they are also created in MFCI explosions (Zimanowski et al., 1997a; Wohletz 1983). Thus active and passive particles classes cannot be directly equated to volcanological morphology suites.

For hazard assessment purposes the active particles generated by the explosion are the important ones. Therefore drops, hairs, and blocky passive shapes should be removed from the dataset, as they are passive particles. The data of Genareau et al. (2013), Graettinger et al. (2013), Büttner et al. (2002), and Wohletz (1983) suggests that the optimal size interval of volcanic ash particles for studying active eruption fragmentation is between 3 φ and 4 φ (125 – 63 μm).

Method background

Automatic shape analysis

Interpretation of qualitative grain morphology is largely subjective and interpreter-dependent (Sheridan and Marshall 1983) and therefore quantitative shape parameters were developed to remove interpreter bias. Leibrandt and Le Pennec (2015) and Lui et al. (2015) have given extensive reviews of both the history and nomenclature of shape parameters and only highlights will be repeated here.

Dellino and La Volpe (1996) used image parameter analysis (IPA) and constructed 4 dimensionless parameters, which were assigned to the 2D projection of the selected tephra particles on photographs and SEM images by automated image analysis software. Using multivariate data analysis the four parameters were combined to a 2D diagram to distinguish between ductile and brittle fragmentation (passive and active particles) (Büttner et al., 2002). Murtagh and White (2013) added a magmatic/phreatomagmatic fragmentation regime boundary to the diagram.

The IPA shape parameters relate to properties of the tephra particle as a whole such as length/width, area and perimeter. These metrics are measured in raster-based imagery counting pixels. To obtain stable bulk average results around 1000-1500 particles should be analyzed per sample (Leibrandt and Le Pennec 2015). The shape parameters are more or less sensitive to image sharpness, resolution and pixel classification model. The least sensitive parameters are area and length, which receive the largest contribution from the unambiguous pixels within the grain and converge towards a single best estimate value with increasing resolution. Liu et al. (2015a) have found a minimum resolution of 750 pixels/particle to get stable area and length parameters. Perimeter, however, is calculated from ambiguous edge pixels and thus highly resolution and pixel-smoothing dependent. Perimeter values of tephra increase with increased resolution (Maria and Carey 2002), which suggests a fractal/pseudo fractal behavior of the perimeter (e.g. Dellino et al., 2002; Maria and Carey 2002). This is used in the fractal method of morphology classification (e.g. Dellino et al., 2002; Maria and Carey 2002, 2007; Perugini and Kueppers 2012), but the method has not yet been automated for large grain capacities.

3D shape analysis is yet another branch of morphology studies currently being developed with promising results, but it remains laborious, costly, and can only produce data on a few grains at this stage (Bagheri et al., 2015).

Thus the 2D projection method remains the fastest, most cost effective, and widely used (Leibrandt & Le Pennec 2015).

The IPA shape parameters

To aid interpretation 2D particle metrics are mostly described by geometric shapes; i.e. circles, rectangles, ellipses or polygons. Directly constructed grain geometries include circumscribing circles, ellipses, rectangles or polygons. A group of model geometries translates some of the particle properties (length, width, area or perimeter) into simple shape models by constructing, for example, a circle with the same area or perimeter as the grain. The geometric shapes are intuitive to interpret and to compare to the measured particle metrics by the IPA parameter formulas (Table 3.1). To be able to compare different grain sizes IPA parameters are often constructed to be dimensionless and some have values between 0 and 1.

Unfortunately, due to differences in software and nomenclature in the literature, 2D shape parameters have no standard reference. Parameters with the same name can be defined differently in different studies and conversely parameters calculated in the same way may bear different names across different publications. The nomenclature in this paper follows the PIdsa software, but otherwise following Liu et al. (2015a).

Connecting tephra morphology and shape parameters

Complex tephra grain morphology cannot be uniquely captured by one single shape parameter (Liu et al., 2015a). Instead it can be divided into three main types of shape variation, which are captured by different groups of shape parameters (Liu et al., 2015a). One group deals with the dimensions of the grain in terms of elongation expressed as aspect ratio.

Table 3.1 previous page. Shape parameter overview and definitions from the PIdsa. The 25 parameters used in this study are described by shape model and shape name and equations are shown where relevant. See additional comments in text about shape models and parameters. Additional used parameters from other studies are shown beneath the relevant references.

Circle model

Equivalent area circle diameter

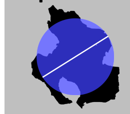

$$d_{EAC} = \sqrt{\frac{A_p}{\pi} \cdot 4}$$

Equivalent perimeter circle diameter

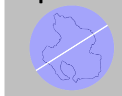

$$d_{EPC} = \frac{P_p}{\pi}$$

Bounding Circle Diameter

d_{BC} = Diameter of the smallest circle that encloses, but does not intersect the particle

Mean Radius Diameter

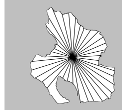

$$d_{MR} = \overline{r_p} \cdot 2$$

Particle radius from centeroid to perimeter measured at 36 equally spaced angles

Circularity

$$C = \frac{4A_p}{\pi d_{BC}^2}$$

Form Factor

$$FF = \frac{4\pi A_p}{P_p^2}$$

Compactness

$$CP_C = \frac{2 \cdot \sqrt{A_p}}{\sqrt{\pi d_{BC}^2}}$$

Rectangle model

Bounding Rectangle length & width

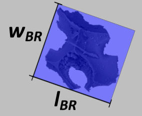

l_{BR} & w_{BR} are the length and width of the smallest area rectangle that encloses, but does not intersect the particle

Bounding Rectangle aspect ratio

$$AR_{BR} = \frac{l_{BR}}{w_{BR}}$$

Rectangularity

$$R = \frac{A_p}{l_{BR} \cdot w_{BR}}$$

Ellipse model

Equivalent elliptic area length & width

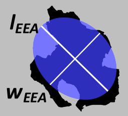

$$l_{EEA} = 2\sqrt{\frac{A_P \cdot AR_{BR}}{\pi}}$$

$$w_{EEA} = 2\sqrt{\frac{A_P}{\pi \cdot AR_{BR}}}$$

Ellipse aspect ratio

$$AR_{EEA} = \frac{l_{EEA}}{w_{EEA}} = \frac{l_{BR}}{w_{BR}}$$

Bounding ellipse length and width

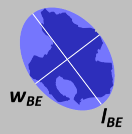

L_{BE} & w_{BE} = length and width of the smallest area ellipse that encloses, but does not intersect the particle

Ellipsicity

$$E_{BE} = \frac{4A_p}{\pi \cdot l_{BE} \cdot w_{BE}}$$

Polygon model

Polygon order

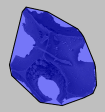

Number of sides in a convex polygon fitted to the particle

Convexity

$$CV_{CP} = \frac{A_p}{A_{CP}}$$

Irregular model

Feret length & width (caliper dimensions)

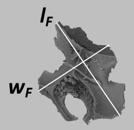

l_F = Smallest distance between two parallel lines that contact but do not intersect the particle

w_F = Largest distance between two parallel lines orthogonal to l_F that contact but do not intersect the particle

Feret aspect ratio

$$AR_F = \frac{l_F}{w_F}$$

Fiber model

Fiber length & width

$$D = \frac{P_p^2 - 16A_p}{4}, If\ D > 0\ then$$

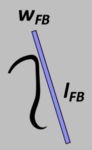

$$l_{FB} = \frac{P_p + 2\sqrt{D}}{4}$$

$$w_{FB} = \frac{A_p}{l_{FB}}$$

Fiber aspect ratio

$$AR_{FB} = \frac{l_{FB}}{w_{FB}}$$

Other parameters

Particle measures

A_p = Area of particle
P_P = Perimeter of particle
r_P = Radius of particle

Model measures

A_{CP} = Area of convex polygon

Dellino and LaVolpe 1996

Circularity

$$C_{DLV} = \frac{P_p}{2\pi^{0.5} A_p^{0.5}}$$

Elongation

$$E_{DLV} = \frac{\text{max intercept}}{\text{mean intercept perpendicular}}$$

Compactness = R

Rectangularity

$$R_{DLV} = \frac{P_p}{2l_{BR} + 2w_{BR}}$$

Leibrandt and LePennec 2015

Circularity

$$C_{LLP} = \frac{1}{C_{DLV}}$$

Convexity

$$CV_{LLP} = \frac{P_{CP}}{P_p},$$

P_{CP} = Perimeter of convex polygon

Liu et al., 2015

Convexity = CV_{LLP}
Solidity = CV_{CP}
Rectangularity = R_{DLV}

Another group (the morphology roughness of Liu et al., 2015a) deals with the overall geometric shape of the grain seen as either larger bubble walls or straight breakage faces defining the outline of the tephra grain. It is best evaluated by comparing the area of the particle to the area of a model geometric shape (circle, ellipse, rectangle or convex hull). The last group (textural roughness of Liu et al., 2015a) deals with surface perturbations, such as small vesicles or breaking steps on the grain surface, that do not change the overall geometry and is measured by perimeter parameters.

Tephra morphology can then be described by using a parameter from each group; elongation, morphology roughness and textural roughness. However, elongation and morphology roughness are determined from length and area measures, which are stable in high-resolution raster imagery, but textural roughness is perimeter derived and is thus dependent on sharpness and resolution (Leibrandt and Le Pennec 2015). The specific choice of parameters depends on the analytical settings, software output, particle orientation, and resolution, and should always be considered carefully for each experimental setup.

Method

Sample selection

Samples of five basaltic tephra fall deposits were collected from multiple different volcanic settings in Iceland (fig 1) and one sample site from Jan Mayen Island, Norway. Sample information is presented in Table 3.2. The deposits were carefully chosen to avoid samples that may have been altered by erosion or transport. The Katla and Grimsvötn tephra layers were sampled from the middle unit of a series of several consecutive fall units. The Karl sample was chosen from a cm thick fall unit in the deposit and the Hverfjall deposit was sampled on the crater rim to ensure that no flow transport had affected the grains. The tephras have similar SiO_2 contents ranging from 46.5–49.7 wt.% (Table 3.2) and contain only scarce phenocrysts and microlites. They are therefore ideal for comparing the tephra populations from different eruptive settings.

Sample preparation

Samples were dried at 50 °C and carefully hand sieved dry through a 125 µm (3 φ) and a 63 µm (4 φ) sieve. Small subsamples were mounted on carbon tape on a Hitachi 12.5 mm sample stub, were gold coated and then studied in a scanning electron microscope (SEM) to look for erosion features on the grains and get a qualitative overview of grain types (see appendix J). Erosion features were not observed.

Table 3.2 (left). Overview of the 6 tephra fall samples used in this study

Eruption	Fimmvörðuháls 2010	Eggoya 1732	Katla 1755	Grímsvötn 2011	Hverfjall 2500 BP	Karl 1210-40
Location	Iceland	Jan Mayen, Norway	Iceland	Iceland	Iceland	Iceland
Eruption type	Hawaiian	Surtseyan	Subplinian	Subplinian	Surtseyan	Surtseyan
Vent type	Fissure	Submarine vent	Subglacial vent	Subglacial vent	Lacustrine fissure	Submarine vent
Deposit type	Loose tephra deposit	Tuff cone fall unit	Tephra layer	Tephra layer	Tuff ring	Tuff cone fall unit
Fragmentation	Dry magmatic	Phreatomagmatic	Phreatomagmatic	Phreatomagmatic	Phreatomagmatic	Phreatomagmatic
Sampling	Few 100m from source during the eruption	~2 km from vent in costal section from second fall unit (P1-2)	~22 km from vent in soil section from fifth fall unit	~9 km from vent in glacial section from third fall unit	From crater of eruption phase III	~300 m from vent in costal section
Geochemistry	Alkali basalt 46.8 wt% SiO_2	Alkali basalt 46.5-48 wt % SiO_2	Transalkalic basalt 47.8 wt % SiO_2	Tholeiitic basalt 49.5 wt % SiO_2	Tholeiitic basalt 49.2 wt % SiO_2	Tholeiitic 49.67 wt% SiO_2
References	Sigmarsson et al. 2011; personal observation	Gjerløw et al. 2015	Oladottir et al. 2008; Oladottir et al. 2011	Sigmarsson et al. 2013	Mattsson and Höskuldsson 2011; personal comm.	Eiriksson et al. 1994; Jakobsson et al. 1978

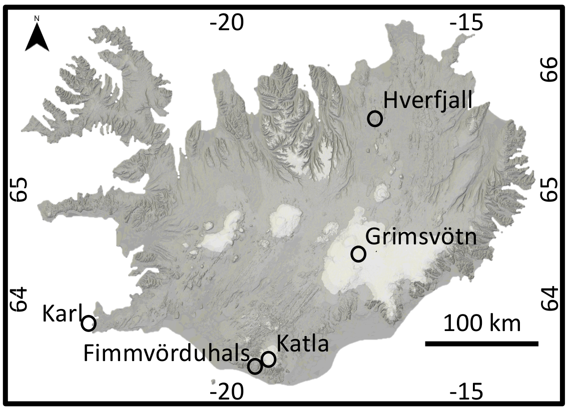

Figure 3.1. Map of Iceland showing the source locations of the sampled eruptions.

Image analysis

50-90 mg of sieved bulk sample was run on the Particle Insight™ dynamic shape analyzer (PIdsa). The analyzer circulates a fluid containing the suspended grains though a lens in front of a camera, which captures 30 frames/second. Images have a resolution of 0.858 µm/pixel, which translates to a resolution range of 16600 to 4200 pixels/particle for the chosen grain size.

The images are processed as binary images and analyzed automatically by the PIdsa software. Predefined grain rejection criteria such as size, shape, darkness and focus can be used to ensure data quality. We used a darkness threshold of 0.8 for grain detection and a circularity rejection of 0.98 to reject air bubbles created in the fluid from the dataset. Up to 28 shape parameters are reported on each analyzed grain and sample photos with grain data are available as well as general sample average statistics. For more information on the general setup we refer to the PIdsa website.

We used a setup that generated 25 parameters on 20,000 grains for each sample (see Table 3.1). Many particle images are out of focus because the photos are taken while the grains are flowing, and samples were run with 90 % focus rejection in order to ensure high image quality. Individual grain data were exported for grains with an equivalent area circle diameter (see Table 3.1) larger than 63 µm. The area-based size cut-off is also used to ensure a minimum of 4000 pixels/particles, which is much larger than the minimum of 750 pixels/particle recommended by Liu et al. (2015a).

Shape parameters

The shape parameters are grouped into 5 overall shape models: circular, rectangular, ellipsoid, convex polygonal shape and fiber (see Table 3.1). A short overview of each is given here.

The circular model converts the irregular grain into an equi-axis model, which is intuitive to interpret and easy to compare to other grains in terms of size, for example. This may also be convenient for tephra fall models that assume all particles are spheres. Different circle models are constructed either using equal area or perimeter of the grain or as a shape-bounding circle. All models are rotation independent.

The rectangular model is a single model based on the bounding rectangle yielding a length, width and aspect ratio. A smallest rectangle is fit to the particle regardless of rotation and it is thus orientation independent.

An ellipsoid model is built to better take particle shape irregularity into account. Analogous to the circular model, the ellipse has an equal area and a bounding model. The challenge of the ellipsoid model is that many major and minor axes can be defined from a specific area. To guide the choice of axes the software chooses the axes with the same aspect ratio as the bounding rectangle and the actual amount of new information is thus very limited. This model is rotation dependent.

The polygon model is based on the convex hull shape and measures polygon order (i.e. number of sides on the fitted polygon) and convexity based on convex hull area. This model is also rotation independent.

The irregular model provides the caliper measures of Feret length and width, which are the smallest and largest possible distance between two parallel lines, and are thus by this definition rotation invariant (as opposed to other definitions in the literature of maximum and minimum pixel distances).

The fiber model is mostly intended for industrial use and uses a simple algorithm to straighten out long thin curved particles to rectangles.

We only discuss dimensionless parameters such as aspect ratio, form factor, and circularity (Table 3.1) because we are interested in the parameter changes between irregular magmatic grains and regular blocky phreatomagmatic grains and not the size diversity. However, because each dimensionless parameter only captures a limited amount of shape change, it is useful to analyze and combine the shape parameters to obtain as much shape information as possible while keeping it graphically simple.

Building a reference grain dataset and modeling shape parameters

Thumbnail images from the 6 samples were used to identify and define a reference grain dataset. Initial qualitative observations indicate that the grains could not be divided into strictly blocky or vesicular grains. Some grains were blocky with no visible vesicles, but other grains had overall blocky shapes with bubbles disrupting the outline to a greater or lesser extent. Thus, grains with greater numbers of bubbles, or fewer larger bubbles, grew progressively more irregular (also observed by Liu et al., 2015a). There was no clear cut-off at which the grains went from generally blocky to generally irregular. Grains were therefore divided into four different classes: blocky, blocky-vesicular, vesicular and elongate, based on their projection outlines (see Table 3.3). Blocky grains have a clearly regular outline. Vesicular grains have a clearly irregular outline. Blocky-vesicular grains have an overall blocky shape with a more or less irregular outline. The elongated grain class has a clear elongated appearance.

We assigned 75 grains to each class and then used the standard deviation normalized reference grain dataset for principal component analysis to identify the most important variation parameters for separating different grain types. Variation diagrams for the eruption bulk samples were subsequently generated based on the principal component analysis results.

The principal component analysis was run with a 6-non-dimensional parameter setup. Twenty of the reported parameters were relating to the grain size variation between 63 and 125 µm (lengths, widths, and diameters, see Table 3.1) or redundant aspect ratio measures. They were therefore removed from the initial 26-parameter setup before the principal component analysis. The six parameters used were circularity, form factor, rectangularity, polygonal order, convexity, and Feret aspect ratio (see Table 3.1).

	Blocky		Blocky-vesicular		Vesicular		Elongated	
PIdsa images of representative grains	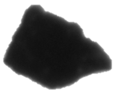		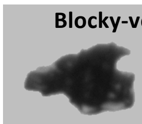	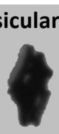	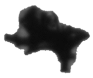	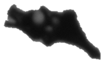		
Regularity parameter	0.29	0.29	0.21	0.18	0.15	0.06	0.02	0.05
Feret aspect ratio	1.33	1.93	1.53	1.87	1.65	1.88	6.88	4.31
Convexity	0.92	0.91	0.88	0.90	0.84	0.84	0.97	0.89
Mean radius diameter	113 μm	106 μm	112 μm	111 μm	109 μm	99μm	75 μm	105 μm
SEM images of same grain type at comparable size	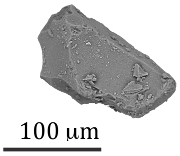		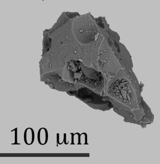		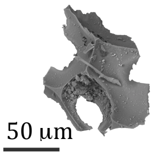		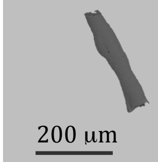	
Characteristics	Straight perpendicular faces, rectangular outline		Straight perpendicular faces with few concavities, overall rectangular outline		Curved faces, irregular outline		Long thin grains, rectangular outline	
Grain type group data								
Regularity parameter (RP)	> 0.2		0.09-0.33		< 0.2		< 0.14	
RP arithmetic mean	0.30		0.20		0.12		0.05	
Feret aspect ratio (FAR)	< 2.6		< 2.6		< 2.6		> 2.6	
FAR arithmetic mean	1.59		1.82		1.94		4.98	
Convexity (CV)	> 0.85		> 0.83		> 0.79		> 0.81	
CV arithmetic mean	0.91		0.89		0.86		0.91	

Table 3.3. Grain type morphology overview. PIsda and SEM images are shown of a typical grain from each grain type and the descriptive characteristics are given. For the PIsda grains the regularity parameter, Feret aspect ratio and convexity measures are given for the shown grains. The mean radius diameter is given for size comparison. Finally an overview of the parameters for the reference grain type groups is given stating the range of the given parameters as well as the arithmetic average for the grain type.

	Comp 1	Comp 2	Comp 3	Comp 4	Comp 5	Comp 6
Circularity	0.487	-0.0066	-0.2922	-0.1814	-0.0146	0.8027
Form Factor	0.4726	0.1214	-0.2011	-0.2891	0.6843	-0.4118
Rectangu-larity	0.1627	0.9023	0.1778	-0.1445	-0.3204	-0.065
Polygonal order	0.4168	0.0837	0.0201	0.902	0.0601	-0.04
Convexity	0.3583	-0.2496	0.8822	-0.161	0.0277	0.0659
Aspect ratio	-0.4592	0.3189	0.2527	0.1522	0.6515	0.4195
Percent of variance	62.2421	17.4474	9.5186	6.8809	2.3823	1.5287

Table 3.4. Principal component coefficients for all variables and *percent of variance for each principal component. 96 % of the reference grain variation is described by components 1 to 4.

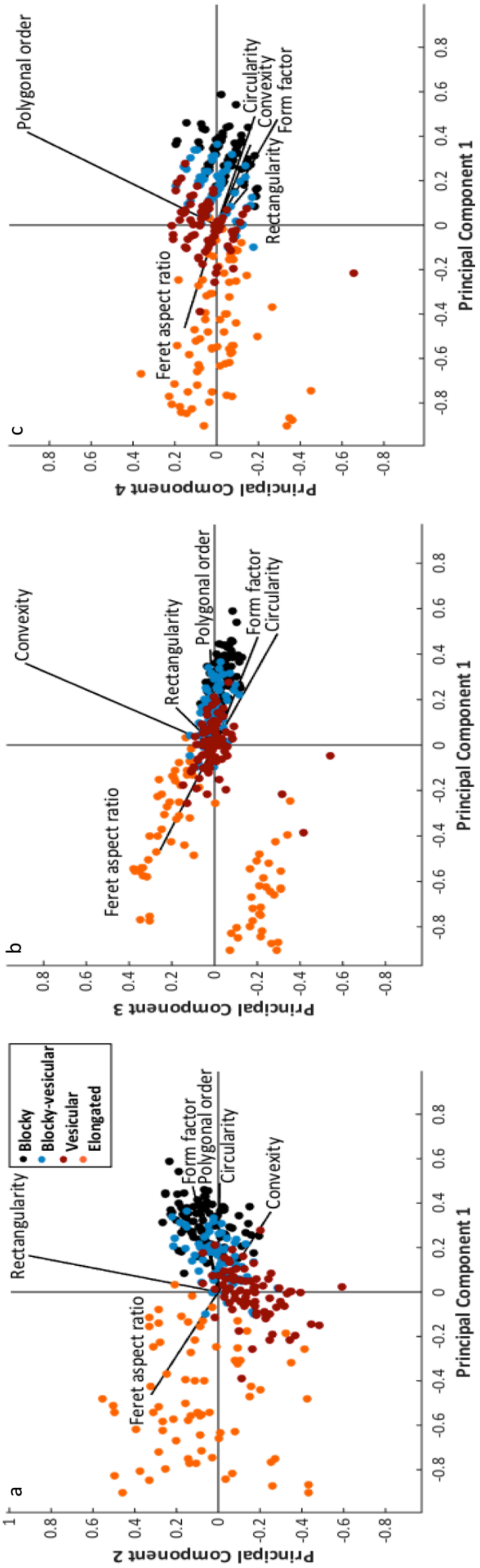

Figure 3.2. Principal component analysis for 6 variables on the reference grain dataset. 3.2a: Principal component 2 vs. 1. 3.2b: Principal component 3 vs. 1. 3.2c: Principal component 4 vs. 1. See text and Table 3.4 for additional comments.

Results

Principal component analysis and parameter selection

The principal component analysis (PCA) shows that 96 % of the data variance could be expressed by 4 components (Table 3.4). The first component, particle elongation, captures 62.24 % of the variance. As particles get more elongated the area to perimeter ratio changes, as does the length to width ratio. The area to perimeter ratio change is tracked by form factor and circularity, while the length to width ratio change is found in the changing aspect ratio. Therefore, form factor, circularity, and aspect ratio contribute most to the first component (Table 3.4). However, elongation is best expressed by the particle aspect ratio, as form factor and circularity are also very sensitive to roughness changes, for example. We used the Feret aspect ratio because it is directly measured on the particle and is rotation invariant as measured by the PIdsa. This parameter alone efficiently separates the elongated grains from the rest (Fig 3.2a).

The second most prominent variation (17.45 %) was the change from regular to irregular morphology—or blocky to vesicular morphology (Fig 3.2a). Rectangularity stands out as the primary contributor to this second component (Table 3.4) and it is one of the parameters that measures the overall shape of the grain by comparing the area of the particle to the area of the smallest bounding rectangle. This fits with the observed component trend in Figure 3.2a. Convexity, commonly known as solidity (Cioni et al., 2014; Liu et al., 2015a), and polygonal order describe the remaining shape variation of the reference grain population as the third component (9.52 %) and the fourth component (6.88 %) (Fig. 3.2b,c). Both parameters are related to the convex-hull shape of the particles and express the complexity of the overall grain geometry. However, the convexity variation is caused by a group of elongated grain outliers with very low convexities. This grouping cannot be correlated with other parameters or visual specifics. We interpret it as an image analysis error with regard to this specific parameter. Furthermore, when taking components 3 and 4 into account it becomes clear that they do not reflect a morphology change from blocky to vesicular grains and instead their variation is perpendicular to the blocky-vesicular trend as seen on Fig 3.2b and c.

Other parameters contribute essential information about irregularity shown by the trend from blocky to vesicular grains. Both circularity and form factor make important contributions as mentioned in the discussion of component 1. Figure 3.2 shows that both form factor and circularity follow the blocky to vesicular grain trend in all diagrams. Circularity, like rectangularity, evaluates the overall morphology by comparing the area of the particle to the area of the bounding circle. The more regular, compact and equant a particle is the closer both circularity and rectangularity are to 1. The form factor takes the smaller irregularities of the outline into account by comparing the particle's perimeter to the perimeter of a circle with the same area as the particle. Notice that elongated particles will have a very low form factor in spite of their smooth, regular outline. This is because by definition they are not equant. Following the examples of others (e.g. Dellino and La Volpe 1996) we combined the three parameters into a single factor to contain all the information in a simple 2D diagram. We call it the regularity parameter, because it accounts for both the outline and overall shape aspects of regularity variation. It is defined as:

$$\text{Regularity parameter} = \text{Circularity} \cdot \text{Rectangularity} \cdot \text{Form Factor} \qquad \text{Eq. 3.1}$$

$$\text{Circularity} = \frac{4A_{particle}}{\pi d_{BC}^2} \qquad \text{Eq. 3.2}$$

$$\text{Rectangularity} = \frac{A_{particle}}{l_{BR} w_{BR}} \qquad \text{Eq. 3.3}$$

$$\text{Form Factor} = \frac{4\pi A_{particle}}{P_{particle}^2} \qquad \text{Eq. 3.4}$$

$$\text{Regularity parameter} = \frac{4A_{particle}}{\pi d_{BC}^2} \; \frac{A_{particle}}{l_{BR} w_{BR}} \; \frac{4\pi A_{particle}}{P_{particle}^2} = \frac{16 A_{particle}^3}{d_{BC}^2 l_{BR} w_{BR} P_{particle}^2} \qquad \text{Eq. 3.5}$$

Reproducibility and dissimilarity	Circularity	Form Factor	Rectangularity	Convexity	Feret aspect Ratio	Regularity factor	Regularity index
Mean of sample means	0.642045427	0.68149016	0.703576096	0.893492635	1.466746758	0.289339024	0.19615*
Standard deviation, all runs	0.000770942	0.001555488	0.000473191	0.000607576	0.002284821	0.002224955	0.000992891
Standard deviation	**0.120%**	**0.228%**	**0.067%**	**0.068%**	**0.156%**	**0.769%**	**0.506%**
t test 2-2, 2-3	0.598571526	0.000128061	0.859760127	0.268307558	0.541316593	0.027402511	
t test 2-3, 2-4	0.806764454	0.658252344	0.396769053	0.898315488	0.482365366	0.816127473	
t test 2-4, 2-5	0.636078303	0.791632872	0.548264641	0.24455235	0.974518866	0.816502623	
t test 2-5, 2-6	0.24897216	0.484885537	0.995892164	0.474223264	0.291492419	0.340340108	
t test 2-6, 2-7	0.045237502	0.122738053	0.044922286	0.679838823	0.026149296	0.043885719	
t test between samples with largest difference in mean	0.045237502 (2-6, 2-7)	7.58856E-05 (2-2, 2-7)	0.046570228 (2-5, 2-7)	0.150868397 (2-4, 2-7)	0.026149296 (2-6, 2-7)	0.199501127 (2-2, 2-6)	

* Mean of the regularity index of all runs

Table 3.5. Reproducibility tested by running the same subsample consecutively 6 times. The low standard deviations all below 1% show a good precision of the method. T-tests were also performed on consecutive runs and on runs with the largest difference in the mean of the parameter. Only two tests show dissimilarity of a single parameter (< 0.005) (Johnson 2013).

where $A_{particle}$ = area of the particle projection, $P_{particle}$ = perimeter of the particle projection, d_{BC}= diameter of the circle bounding, but not intersecting the particle projection, l_{BR}= length of the rectangle bounding, but not intersecting the projection, w_{BR}= width of the rectangle bounding, but not intersecting the projection. All components of the regularity parameter are ratios from 0 to 1 and thus the regularity parameter is also a ratio ranging between 0 and 1. Regular, equant particles with smooth edges score close to 1 whereas irregularly shaped particles score close to 0.

The change from regular to irregular tephra grains reflects a change from blocky to vesicular and then to elongated grains. The form factor is very sensitive to the jagged irregular outline of vesicular grains and the high perimeter to area ratio of elongated grains. All three parameters are sensitive to the overall morphology change from compact blocky equant grains to irregular vesicular and elongated grains. The regularity parameter is therefore good for distinguishing between blocky and vesicular particles (Table 3.3, Fig 3.3a).

Particle Insight shape analyzer data reproducibility

The PIdsa was not specifically designed to run tephra samples and the stability of the shape parameter output was tested by 6 runs of the same sample under the same conditions. Standard deviations on the means of the dimensionless parameters of circularity, rectangularity, form factor, convexity, and Feret aspect ratio range from 0.07% to 0.23% (Table 3.5). This translates into a standard deviation of 0.77% for the regularity parameter (Table 3.5). The same parameters were tested for normality with normal probability plots and all show normal distributions for minimum 99% of the distribution (Appendix K). T tests were used to test for dissimilarity between adjacent sample runs as well as sample runs with the largest difference in parameter mean value. P-value recommendations of Johnson (2013) were followed, so p-values < 0.005 reject the null hypothesis (Table 3.5). Only 2 of the 36 t tests resulted in a rejection of the null hypothesis. Based on the low standard deviations and the t test results the data are considered reproducible.

Statistical verification of grain types

T tests between all reference grain types were performed to test if the grain types are statistically significantly different (Table 3.6). All results of regularity parameter, form factor and circularity reject the null hypothesis and are thus successful in distinguishing between shape types. Rectangularity for blocky-vesicular and vesicular grains is not statistically dissimilar. This is also true of the Feret aspect ratio T-test of blocky-vesicular and elongated distributions. However, the overall result of the t tests show that the regularity parameter combined with the Feret aspect ratio is effective in separating the grain types.

Reference grain types	Circularity	Form Factor	Rectangularity	Feret aspect ratio	Regularity factor
Blocky vs. blocky-vesicular	7.28633E-13	1.79975E-21	0.001206307	3.23483E-07	1.97618E-20
Blocky vs. Vesicular	4.40146E-28	1.77909E-48	4.11322E-22	3.81556E-09	4.72646E-05
Blocky vs. Elongated	4.37849E-70	4.61729E-57	0.001312259	8.01789E-29	6.14298E-59
Blocky-vesicular vs. Vesicular	8.65214E-10	5.1706E-13	1.37356E-15	0.035989286	4.24739E-18
Blocky-vesicular vs. Elongated	2.19939E-59	2.95902E-36	0.137023985	5.23038E-27	6.97522E-43
Vesicular vs. Elongated	4.62724E-42	5.1776E-20	0.000120391	2.71972E-26	3.73693E-25

Table 3.6. T tests of the dissimilarity between the shape parameters of the different grain types. All but two parameters are shown to be dissimilar by the p<0.005 criterion (Johnson 2013). Only the Feret aspect ratio of the blocky-vesicular vs. vesicular distributions and the rectangularity of blocky-vesicular vs. elongated distributions do not reject the null hypothesis. This shows that the grain types display well-defined distributions compared to one another.

Statistical significance of different deposits

Finally, all the samples were compared to each other by t-tests of the shape parameters circularity, rectangularity, form factor, Feret aspect ratio, and regularity parameter. Only 6 of the

75 t tests reject the null hypothesis and the 6 eruption samples are considered significantly different in terms of their shape parameters.

The regularity index

Based on the results of the PCA we constructed a classification diagram using the Feret aspect ratio and the regularity parameter (Fig 3.3a).

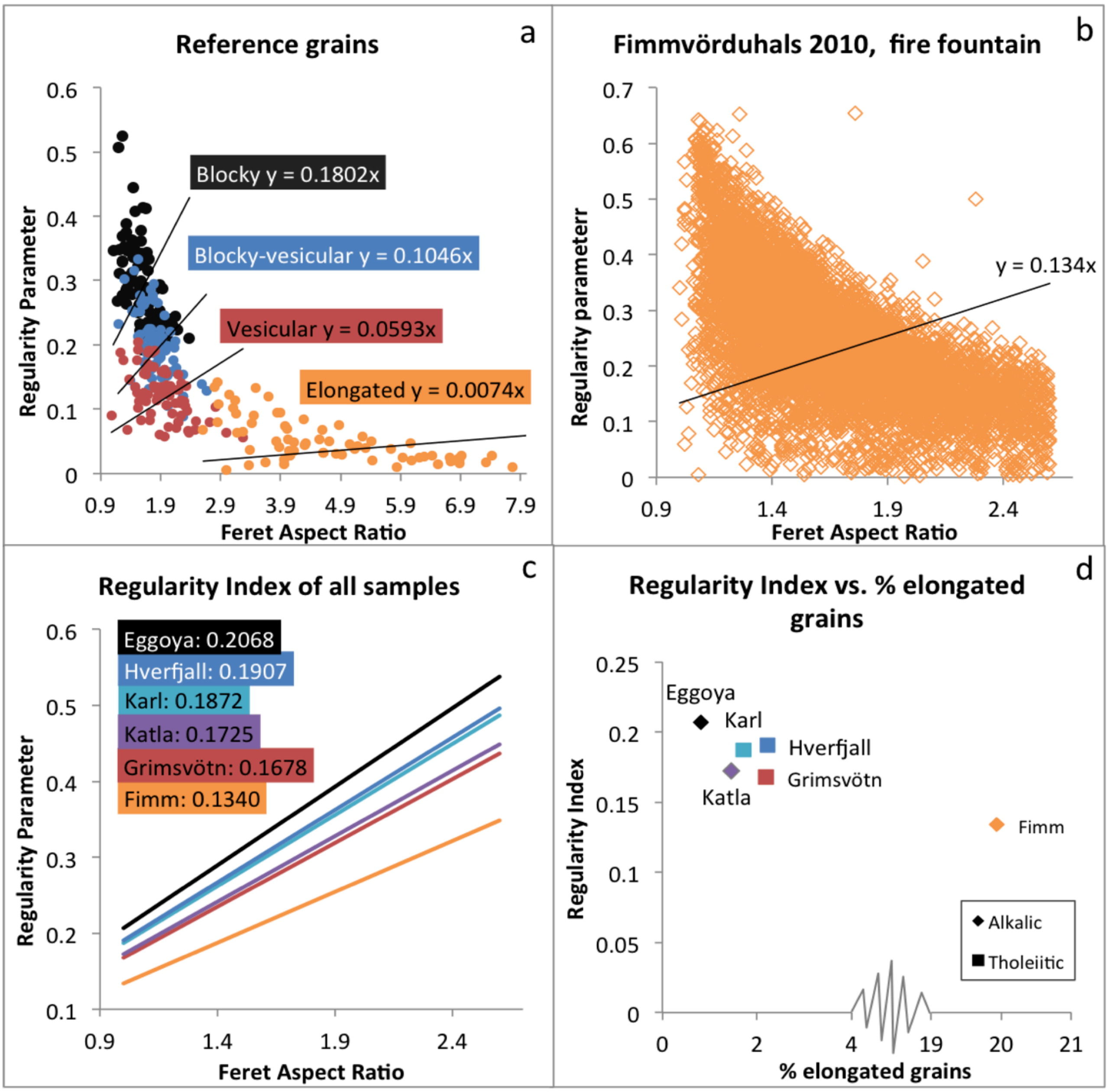

Figure 3.3. 3.3a: All reference grains plotted with regularity against elongation. Graphical average lines through (0.0) show the difference between grain types as inclinations of the slope. 3.3b: Showing grains from the Fimmvördurhals sample in a “regularity against elongation” plot. Elongated grains have been removed. A graphical average line with manipulated starting point is shown to illustrate the average regularity of the whole population. 3.3c: All sample average lines plotted in a plot similar to 3b and showing the regularity index of each eruption deposit. 3.3d: Correlating regularity index, percentage of elongated grains and geochemistry. See text for additional comments.

The plot quantitatively characterizes the ash from the different eruption environments. It is possible to separate blocky, vesicular and elongated reference grains (Fig 3.3a), although adjacent shape groups overlap due to transitional grains. These transitional grains become important when the whole sample grain morphologies are plotted (Fig 3.3b) and individual grain types cannot be distinguished. Cut-off values for grain types are given in Table 3.3 based on the 300 reference grains.

In order to focus the quantitative study on the active ash particles generated by the explosion, elongated grains generated by ductile fragmentation (Büttner et al., 2002) were removed by the cut-off values in Table 3.3. An important observation is that all eruption deposits contain the whole spectrum of grain types within the measured grain size interval (see appendix L). Therefore the sheer amount of data points in each plot (around 15,000–17000 points) makes any visual distinction impossible. To quantify the difference we have projected the points onto a line through (0.0) using a linear regression. The line serves as a graphical average of the distribution and the slope is a measure of the average regularity of the grains. The (0.0) constraint has been invoked so all the lines have the same starting point and the slope of the lines are directly comparable. We also prefer to have a positive slope, so it follows the same logic as the shape change. The higher the regularity parameter of a grain the higher it plots in the diagram. Thus, the more regular and blocky a grain population is the steeper the slope is and the higher the slope value is. Conversely, a population with very jagged, elongated and irregular grains will have a much flatter regression line and a lower slope value. We have termed the slope value the regularity index (RI) and we note the slope is strictly a modeling tool that is used to quantify the relative amounts of blocky vs. vesicular and elongated grains. Values of the RI of the 6 samples are given in Figure 3.3c. The sample with the most irregular grains is the Fimmvörduhals fire fountain sample, which has the lowest RI of 0.134 ± 0.001 (2σ). Then follows the subglacial tephra samples from the Grimsvötn and the Katla eruptions, which have intermediate RIs of 0.168 ± 0.002 (2σ) and 0.173 ± 0.002 (2σ), respectively. The highest RI (0.207 ± 0.002 (2σ)) is exhibited by the sample of the Surtseyan eruption in Eggoya, Jan Mayen, whereas the sample from other Surtseyan eruption of Karl shows a slightly lower RI of 0.187 ± 0.002 (2σ). The latter is comparable to the tephra from the wet fissure eruption sample from Hverfjall, which has a RI of 0.191 ± 0.002 (2σ). There is no apparent correlation between the fraction of elongated grains and the RI (Fig 3.3d). However, there is a tentative correlation between geochemistry and RI for same eruption environments. In the submarine environment the alkalic Eggoya sample has a higher index than the tholeiitic Karl sample. Between the subglacial samples the trans-alkalic Katla sample has a slightly higher index than the tholeittic Grimsvötn sample.

Discussion

Points of awareness using the PIdsa method

The sheer rapidity (20,000 grains in about 30-45 min) makes this method attractive and useable. The equipment is small, easy to run, and requires only simple sample preparation. Its main advantage is that it characterizes many grains from random angles, which allows for more accurate and complex grain shape models. However, it is clear upon examining results and thumbnail images that the use of a moving medium involves some challenges. Firstly each sample should run for a limited time only. Small grains may start to wash out from the larger grains and thereby change the optical properties of the fluid slightly. Using wet sieving methods or prewashing the dry-sieved samples can resolve the issue to some extent, so samples can run for longer if needed.

Another challenge is defining the dark threshold and the camera gain. There is a balance between detecting clear grains and getting a well-defined dark-grain outline. This will mostly be a challenge for samples with transparent tephra grains such as silicic ash. Finally, high focus rejection is important to ensure data quality (90 % is recommended). High focus rejection, however, limits the analyzed grain size to the larger part of the dispersed grains. Reruns on the same < 125 µm grain size sample with 90 % focus rejection and then 30 % focus rejection show a shift in average mean radius diameter from 81.6 µm to 46.1 µm.

Resolution and the perimeter value issue revisited

The resolution of the OPA imagery determines the baseline data quality. Outline irregularity is one of the key features that distinguish magmatic tephra from phreatomagmatic tephra, and the perimeter is the central parameter in gaining this information. Therefore most studies use parameters highly sensitive to perimeter changes (e.g. Dellino and La Volpe 1996; Büttner et al., 2002; Jordan et al., 2014; Leibrandt and Le Pennec 2015; Lui et al., 2015), but as previously discussed perimeter measurements are resolution dependent. This becomes an issue when dealing with a stationary imaging setup for a range of grain sizes. While some studies have overcome this obstacle by manually normalizing the OPA imagery to a specific resolution (e.g. Liu et al., 2015a; Dürig et al., 2012), this option defies the objective of automated bulk analysis. As the imaging setup is usually stationary and the pixel/area is constant for all images, the resolution effectively drops significantly for smaller grains, thus decreasing the perimeter value. This means that smaller grains will seem smoother compared to larger grains of similar shape. This effect is evident in the dataset of by Leibrandt and Le Pennec (2015). They provide average convexity (see Table 1 for definition) data of 1500 particles in 0.5 φ sieving intervals.

They show grain sizes ranging from 0.5 φ to 5.5 φ (0.710 mm to 0.023 mm) from one bulk sample at a fixed magnification. Including data using different magnifications makes it possible to evaluate whether the parameter change is a real shape change or an artifact of the resolution. When comparing the constant magnification data with higher magnifications it is evident that the change is indeed an artifact of perimeter resolution (Leibrandt and Le Pennec 2015). Based on the published diagram of the Leibrandt and Le Pennec (2015) dataset we have found a quantitative change in bulk average of the convexity parameter of less than 2 % in the 3 to 4 φ size range. Liu et al. (2015a) finds that changing the resolution from 10^6 to 10^2 pixels/particle increases convexity of a single grain by a factor of 2–3 depending on the grain morphology. However, that would correspond to a size range from e.g. 3 to 10 φ (0.125 to 0.00125 mm) or about -2.5 to 4 φ (6.3 to 0.063 mm), which are orders of magnitude from the grain size range of current automated morphology studies. Thus the resolution difference in the limited size range of 3 to 4 φ should not pose problems for the data quality.

Additionally, perimeter parameter values from different studies with different image resolution/grain sizes cannot be compared. Unfortunately most of the IPA studies reported in the literature are focused on perimeter parameters and thus comparing results between different studies remains difficult.

Applicability of established classification diagrams to PIdsa data and automated bulk analysis

When comparing the different classification diagrams of Büttner et al. (2002), Murtagh and White (2013), and Liu et al. (2015a) it is apparent that these authors have shown no quantitative way to deal with bulk samples containing a broad mix of all morphologies and only quantify shape changes of single grains. Liu et al. (2015a, b) presents a bulk analysis of tephra from Grimsvötn, 2011, which plots all across the classification diagram—as observed in our study. Leibrandt and Le Pennec (2015) treat bulk datasets and deal with bulk averages in their classification diagram, but a lot of morphology distribution information is lost in this way. Many different morphology distributions may result in the same average value, although the generic implications may be vastly different. Therefore, we encourage the use of what we term a graphical average model instead, so that the overall point distribution may be visually inspected. For comparison we plotted our reference grains and samples onto the classification diagrams of Büttner et al. (2002), Murtagh and White (2013), Leibrandt and Le Pennec (2015), and Liu et al. (2015a) (Fig. 4). For the Büttner et al. (2002) and Murtagh & White (2013) diagrams we had to recalculate our data to reflect circularity, rectangularity and compactness as defined in these diagrams (Table 1, Dellino and LaVolpe 1996). Unfortunately elongation cannot be obtained

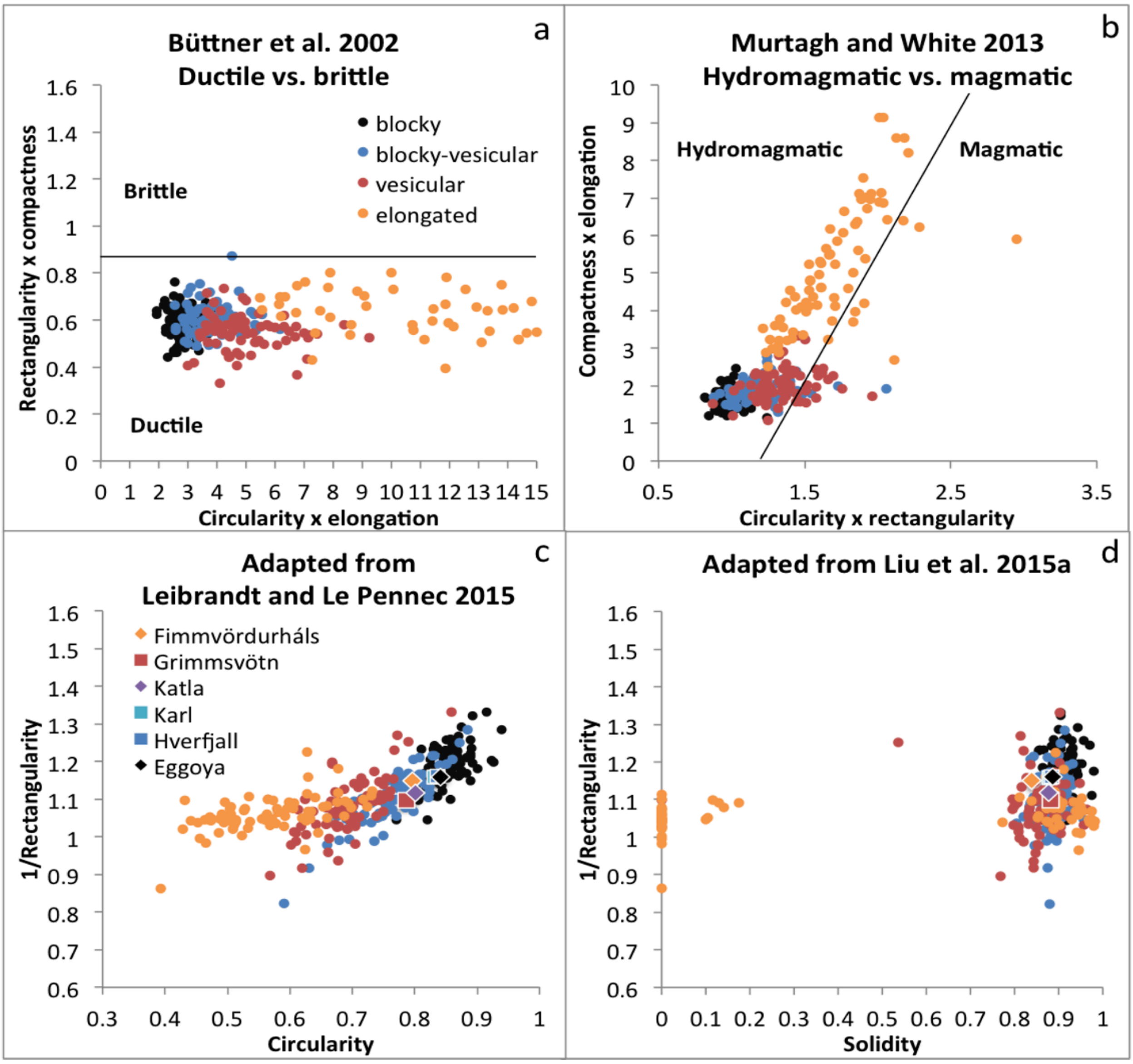

Figure 3.4. PIdsa data plotted in the most commonly used classification diagrams related to tephra grain morphology. 3.4a: Diagram first presented by Dellino and La Volpe (1996), and Büttner et al. (2002) subsequently added the ductile/brittle fields based on MFCI experiments. The parameters used in this diagram can be recalculated from PIdsa data except for elongation. We have defined a substitute elongation. All parameter calculations are shown in Table 1, Dellino and LaVolpe (1996). 3.4b: Diagram from Murtagh and White (2013). Parameters are the same as used by Dellino and La Volpe (1996), but they are combined in a different way on the two axis. 3.4c: Adopted from Leibrandt and Le Pennec (2015). Parameter definitions are shown in Table 1, Leibrandt and Le Pennec (2015). As the convexity parameter of Leibrandt and Le Pennec (2015) could not be obtained from the PIdsa, we have used rectangularity as defined by Dellino and La Volpe (1996) (Table 1). See text for additional comments. 3.4d: Diagram adopted from a. Parameter definitions are shown in Table 1. Again convexity has been replaced by rectangularity. See text for further comments.

from our dataset in the exact same way, so instead we have used the Feret length as the long axis and calculated a perpendicular mean based on the particle area (Table 3.1). For the Leibrandt and Le Pennec (2015) and Liu et al. (2015a) diagrams we have used circularity and solidity as defined. Both diagrams use convexity, which cannot be obtained from our dataset and thus leaves these diagrams ill-suited for the interpretation of the PIdsa-dataset. However, in an attempt to revise the diagrams to accommodate the PIdsa data, we have followed the recommendations of Liu et al. (2015a) and chosen a shape parameter from the same cluster analysis parameter group as convexity. In three out of four cluster analyses rectangularity (of Dellino and LaVolpe 1996) follows convexity in the same position in the diagram (Liu et al., 2015a) and it is therefore chosen as the best replacement parameter. The major difference between the two parameters is that rectangularity is not bound between 1 and 0 because the bounding rectangle does not define the shortest perimeter of the grain. Additionally, to follow the same graphical logic as the original diagrams we have inverted the Dellino and LaVolpe (1996) rectangularity (1/rectangularity), but it should be kept in mind that the grain distribution does not approach (1,1).

The four comparative plots are shown in Fig 4. In the Büttner et al. (2002) diagram (Fig 3.4a) all reference grains are classified as ductile, while the Murtagh and White (2013) diagram (Fig 3.4b) classifies almost all reference grains as phreatomagmatic. None of these obscure classifications can be explained by our slight adaptation of the elongation equation, and so these two diagrams do not represent our dataset well. Nemeth and Cronin (2011) used light microscopy, scanning electron microscopy and backscatter electron microscopy to obtain images of tephra grains, which were subsequently turned into binary images and analyzed by the ImageJ software package. Their study shows that the data distribution is controlled by the imaging method. Both light microscopy and scanning electron microscopy data plot in the ductile field of Büttner et al. (2002), while all backscatter electron data falls in the brittle field for the same samples. Thus the distribution of our reference grains might be controlled by the imaging method. Either way the diagrams are not appropriate for interpretation of our PIdsa data.

In the diagram adapted from Leibrandt and Le Pennec (2015) (Fig 3.4c) the reference particles are spread out and blocky and vesicular particles rarely overlap. However, when applying the method of averages to our samples the distinction between different bulk samples from different eruptions sites is not well defined. The six bulk samples fall in two groups consisting of (1) Fimmvörduhals, Grimsvötn, and Katla, and (2) Karl, Hverfjall, and Eggoya. Thus the overall division is the same as shown in Figure 3 by using the RI, but the averages do not provide a quantitative comparable measure and this makes it hard to interpret the differences between bulk samples. So, although it is useful to differentiate between our reference grains, it is less effective for bulk samples of similar chemical composition using the proposed method of bulk averages.

In the diagram adopted from Liu et al. (2015a) (Fig 3.4d) the instability issue of our solidity parameter for elongated grains is evident. The rest of the reference grains plot with the blocky grains in the upper left part and vesicular and elongated grains plot in the lower part. But the groups overlap significantly and are not as well-defined and systematic as reflected in the Leibrandt and Le Pennec (2015) plot. The same can be said for the eruption bulk sample averages. Thus the adapted version of the Liu et al. (2015a) diagram is not helpful in interpreting our dataset.

Our overall conclusion is that the existing diagrams and discrimination methods are not adequate to characterize our dataset. This may be due to different imaging set-ups, where our setup is the only dynamic one, or it could be related to different image processing conditions and differences in grain sizes. However, it may also be explained as an artifact of diagrams created on the basis of very different reference grains. The Büttner et al. (2002) diagram was based on experimental grains of MFCI without any vesiculation taking place. All our samples show evidence of some vesiculation and they might not be appropriate for the Büttner et al. (2002) plot.

The magmatic/phreatomagmatic fields in the Murtagh and White (2013) diagram were drawn from an equation from a study comparing end-member products of Kilauea Iki ash and Loi’hi seamount ash. Thus the reference grains are very similar to this study as they are basaltic and include similar environments with similar grain types (except for quench granulation grains from seamounts). But the means of deriving the equation is not published and the classification differences remain unresolved.

The Leibrandt and Le Pennec (2015) diagram was constructed from andesitic reference samples with comparable geochemical compositions but different eruption styles (Strombolian and subplinian, Leibrandt and Le Pennec 2015). Thus, the sample setup resembles our study and might explain why this diagram is the most useful for our dataset as depicted by the plotted systematics of our reference grains (Fig 3.4c).

The diagram of Liu et al. (2015a) builds on convex hull shape parameters. We have previously shown that our analysis provides ambiguous solidity results particularly for elongated grains. Therefore, this diagram cannot be used to accurately evaluate our dataset. Furthermore, the diagram was made to illustrate different grain types and is therefore based on reference samples from vastly different eruption styles. Samples also range from mafic to silicic compositions. Blocky reference particles are taken from submarine quench granulation of basalt, while the vesicular grains are from basaltic to dacitic eruptions. There is no ambiguity in telling these particles apart even without shape parameters, so it is not surprising that shape parameters do a good job of separating them. Our reference grains were picked out from a much narrower variation interval as all samples share approximately the same geochemistry and crystal content. This could also limit the applicability of the Liu et al. (2015a) diagram to our dataset.

In summary we suggest the use of a diagram for the PIdsa dataset based mostly on area- and dimension ratio parameters in which grain shape changes continuously and where the whole bulk dataset is shown.

Volcanological implications of the grain type distribution

The presence of all grain types in all eruption deposits suggest that brittle fragmentation is more complex than traditionally reflected in classification diagrams. This is probably related to the studied grain size, which supports the detection of both blocky and vesicular (irregular) grains. Liu et al. (2015b) recognized that the grain size and morphology of tephra from the Grimsvötn 2011 eruption was related to pre-fragmentation bubble size and distribution. They showed that the proportion of dense fragments (without vesicles) grew to up to 80% as the grain size approached that of the modal vesicle diameter (15–25 µm). At 63–91 µm 60% of the grains were dense and the rest vesicular, whereas about only 25–10 % of the grains were dense in the 91–125 grain size fraction. Thus, the choice of studied grain size is critical to volcanological interpretations. An example of this is the work of Honnorez and Kirst (1975): their results are most probably an artifact of comparing particles from grain sizes two orders of magnitude apart. The particles in their quench-fields (Fig. 3.4) are primarily in the range of 0.08 to 0.05 mm, whereas the grains in their explosive granulation fields (Fig. 3.4) all range from few mm up to cm in size. The fields are set apart by the number of corners or inflexion points in the grain perimeter and the planarity fields (percentage of plain grain perimeter). Thus, the distribution of samples is readily explained as pertaining to larger vesicle-populations being preserved in the larger grains—or the change from a simple particle-dominated sample to a complex particle-dominated sample (Genareau et al., 2013).

However, the grain type diversity in all deposits needs an explanation and therefore the fragmentation dynamics must be considered. The eruption style of fire fountaining has been attributed to volatile-coupled ascent of basaltic magma, with mono-modal or bimodal vesicle size distributions found in fire fountain clasts (e.g. Parfitt and Wilson 1995; Mangan and Cashman 1996; Stovall et al., 2011; Jutzeler et al., 2016). Pre-fragmentation heterogeneity in vesicle size for fire fountains has been observed (Stovall et al., 2011) spanning as much as 3 orders of magnitude, which can thus produce different sizes of simple ash grains (Genareau et al., 2013). Large dense simple ash grains would settle out close to the fountains, which is where the sampling of Fimmvörduhals was done. These simple ash grains could, in some orientations, be characterized as blocky or blocky-vesicular grains by the PIdsa analysis.

Another possible process might relate to post-fragmentation alteration. Post-fragmentation vesicle size heterogeneity is very commonly observed in fire fountain clasts (e.g. Mangan and Cashman 1996; Schipper et al., 2010; Stovall et al., 2011). However, the post-fragmentation bubble expansion and coalescence process usually produces thin bubble walls and small plateaus (Mangan and Cashman 1996; Parfitt and Wilson 1995; Jutzeler et al., 2016) and it is likely not the cause of the blocky grains observed in the analyzed size range. Other explanations could be brittle fragmentation of degassed recycled clasts, but this is mostly a concern in pulsatory eruptions such as Strombolian or Surtseyan and probably not a valid explanation in fire fountains (d'Oriano et al., 2014). We suggest that the presence of blocky and blocky-vesicular grains in the fire fountain deposit is related to the pre-fragmentation vesicle size distribution.

Genareau et al. (2013) found that complex ash particles (bubbly ash grains preserving more than one vesicle indentation) preserve pre-fragmentation vesicle sizes with no post-fragmentation expansion features complicating the analysis. They also showed a method for determining the vesicle size distribution for complex ash-sized particles in the 50–125 µm size range. It would be interesting to compare the results from vesicle size studies like Genareau et al. (2013) with a PIdsa dataset for the same samples.

The presence of irregular vesicular grains in the phreatomagmatic eruptive settings can be explained by pre-fragmentation vesiculation (Liu et al., 2015b). Other recent studies have reported on the pre-fragmentation vesicle size and volume distributions in subaqueous environments, such as submarine (e.g. Schipper et al., 2010, 2011; Jutzeler et al., 2016), glacial lake (Graettinger et al., 2013), and Surtseyan eruptions (e.g. Murtagh and White 2013; Schipper and White 2016). They conclude that the eruption style is related to the pre-fragmentation volatile-coupled or de-coupled ascent of the magma. Thus the pre-fragmentation vesiculation processes play a vital role in the phreatomagmatic eruptions and can explain the presence of vesicular grains.

Volcanological implications of the regularity index results

Our classification scheme allows for quantitative comparison of the morphology of populations of ash grains generated in different eruptive settings. The general systematics of the RI conforms to the established shape interpretation scheme by showing that wet eruptions have blockier and more equant particles than dry eruptions. The advantage of using a grain population-based index is that the rigid binary classification of magmatic/phreatomagmatic can be transformed into a fragmentation spectrum. The spectrum end-members represent the phreatomagmatic fragmentation (high RI) and the dry magmatic fragmentation (low RI). Intermediate RI values represent mixed fragmentation processes. Interestingly, the intermediate RI values in this study are related to eruptions of subglacial central volcanoes, where magmatic degassing have been shown to play a significant role in the fragmentation process for silicic melts (Owen et al., 2013) as well as for the Grimsvötn 2011 eruption (Liu et al., 2015b). Data from Hreinsdottir et al. (2014) shows that the height of the Grimsvötn 2011 eruption column correlated with the rate of pressure change in the underlying magma chamber. This observation supports the influence of pre-fragmentation volatile exsolution on the eruption style. Liu et al. (2015b) suggests that thermal stresses play a role in the fragmentation process and argue that their data supports an initial fluidal (ductile) magmatic fragmentation followed by brittle thermal granulation of thermally stressed vesicular particles. Graettinger et al. (2013) also report a tephra sequence from a subaqueous glacier lake eruption at Askja volcano, Iceland, with fluidal textures. However their deposit sequence changes from fluidal-dominated textures to a fine blocky ash deposit indicating that the more effective brittle fragmentation mechanism of MFCI takes over. Considering the plume heights of the Grimsvötn 2011 eruption of 20 km we consider the brittle thermal granulation to be a secondary fragmentation mechanism to MFCI in this eruption as well.

Schipper and White (2016) looked at fragmentation in Surtseyan eruptions and found that it is the mingling of magma and water in MFCIs that drives them. Graettinger et al. (2013) suggests that the magmatic ductile fragmentation can enable the fuel-coolant premix that leads to MFCI-explosions. Conversely, the shockwave from MFCI explosions can cause rapid depressurization of the magma and trigger magmatic explosions. This feedback mechanism could explain the varying content of vesicular grains between our two Surtseyan deposit samples and relate it to differences in the volatile exsolution history of each eruption.

The findings from Hreinsdottir et al. (2014) and Schipper and White (2016) can also explain a part of our quantitative dataset. They suggest that the higher the RI gets the more the MFCI has controlled the fragmentation process. This is supported by the data from Liu et al. (2015b), where our intermediate RI for Grimsvötn 2011 deposit correlates with 60% – 25 % blocky grains in our analyzed size range.

The above fragmentation interpretation of our RI is based on the assumption that the irregular grains are related to magmatic degassing and vesiculation, whereas blocky grains are related to phreatomagmatic explosions. Such an interpretation should be used carefully, as grain shapes are highly influenced by phenocryst and microlite content (Schipper et al., 2010; Jutzeler et al., 2016). Therefore our fragmentation spectrum can only be directly applied to phenocryst- and microlite-poor tephras of basaltic composition at present.

Conclusion

Our analysis of grain populations shows that both Surtseyan, subglacial and fire fountain eruptions produce a similar range of shapes from blocky to vesicular as well as elongated grains. We suggest that the analyzed particle morphologies are directly related to the fragmentation mechanisms. We have tested our dataset in four different published classification diagrams for tephra grains. This test shows that while other diagrams are successful at classifying the grain shape they are not useful for interpreting our bulk datasets and they do not provide a means for quantitatively comparing bulk samples.

To deal with the lack of comparability among existing classifications, we have defined a regularity parameter and demonstrate how the regularity of grain shape can be used to distinguish between blocky and vesicular grains. Then we designed a diagram plotting regularity against elongation, which shows a systematic change from blocky grains to vesicular grains and which allows for graphic averaging of the shape of an entire grain population. This average is a measure of the overall grain regularity and can be used as an index of regularity of the population. Our results show that the RI differs for different eruptive settings. Submarine and lacustrine eruptions produce the most regular grains with regularity indices of 0.207–0.187. A fissure eruption produces mostly irregular grains with an index of 0.134, whereas subglacial eruptions produce intermediate averages with indices of 0.168–0.173. If the RI is used as a fragmentation proxy, then our initial results suggest that both phreatomagmatic explosions as well as magmatic degassing play a significant role in the active subglacial eruption fragmentation.

The systematic change in indices between wet and dry eruptions suggests that the RI can be used to assess the role of magmatic versus phreatomagmatic fragmentation. This could be very helpful in active eruption scenarios and hazard studies. Other interesting perspectives could arise from looking at changes in RI with increased microlite content, increased silica content or systematically varying volatile content.

Future work should consider combining PIdsa analysis with thorough vesicle size distribution studies on the same samples and adding samples from Strombolian and Plinian eruptions.

Acknowledgements

Our sincere gratitude goes to Eirik Gjerløw and Jónas Guðnason for providing samples from Jan Mayen and Grímsvötn. Our grateful thanks are also extended to Guðrún Larsen for advice and assistance with fieldwork and to Tobias Dürig, Bergrun Óladottir, Tinna Jónsdottir, Agnes Magnúsdottir, Emma Liu and Kathy Cashman for the many interesting discussions. Finally we warmly acknowledge the helpful comments and suggestions of P. Dellino, K. Cashman and 3 anonymous reviewers.

Chapter 4

Large explosive basaltic eruptions at Katla volcano, Iceland: fragmentation, grain size and eruption dynamics

Johanne Schmith[1,3], Ármann Höskuldsson[1,2], Paul Martin Holm[3], and Guðrún Larsen[2]

[1]Nordic Volcanological Center, Earth Science institute, University of Iceland, johannes@ign.ku.dk, +4527121368
[2]Earth Science institute, University of Iceland
[3]Institute of Geoscience and Natural Resource Management, University of Copenhagen

Submitted manuscript, 2017 to Journal of Volcanology and Geothermal Research april 2017

Abstract

Katla volcano in Iceland produces hazardous large explosive basaltic eruptions on a regular basis, but very little quantitative data for future hazard assessments exist. Here details on fragmentation mechanism and eruption dynamics are presented for the first time. We show that magma/water interaction is important in the ash generation process, but to a variable extend. By investigating the large explosive basaltic eruptions from 1755 and 1625, we document that eruptions of similar size and magma geochemistry can have very different fragmentation dynamics. Our models show that fragmentation in the 1755 eruption was a combination of magmatic degassing and magma/water-interaction with the most magma/water-interaction at the beginning of the eruption. The fragmentation of the 1625 eruption was initially also a combination of both magmatic and phreatomagmatic processes, but magma/water-interaction diminished progressively during the next stages of the eruption. However, intense magma/water interaction was reintroduced during the final stages of the eruption dominating the fine fragmentation at the end. This detailed study of fragmentation changes documents that subglacial eruptions have highly variable interaction with the melt water showing that the amount and access to melt water changes significantly during eruptions.

Our study is based on a detailed deposit stratigraphy, granulometric modeling, componentry and the new quantitative regularity index model of fragmentation mechanism. While it is often difficult to reconstruct the progression of eruptions that have no quantitative observational

record, this study shows that integrating field observations and granulometry with the new regularity index can form a coherent model of eruption evolution.

Introduction

Katla volcano in the SE part of Iceland is one of the most prominent and hazardous Icelandic volcanoes known to produce major explosive eruptions (Thordarsson and Larsen, 2007; Thordarsson and Höskuldsson, 2008; Biass et al., 2014; Budd et al., 2016). During the last millennium at least two major basaltic eruptions from Katla has reached Europe (Det Kongelige Danske Videnskabernes Selskab, 1758; Thorarinsson, 1981) with observed tephra fall in 1625 and 1755, respectively. Even though Katla is a bimodal system (Larsen, 2000, 2010; Óladottir et al., 2005, 2008), explosive basaltic eruptions by far outnumber silicic ones by 300 to 20 within the Holocene (Larsen, 2000; Óladottir et al., 2005). Katla has not produced an eruption since 1918, but recent seismic unrest suggests another eruption might be imminent (Budd et al., 2016). It is therefore very important to understand the mechanisms responsible for creating these potent basaltic explosive eruptions.

The explosivity of the basaltic eruptions is usually attributed to interaction of the magma with glacial melt water creating phreatomagmatic explosions (e.g. Óladottir et al., 2005, 2008; Larsen 2010 and references therein). However, the tephra fall deposits of many Katla tephras including those of the 1625 and 1755 eruptions consist of vesicular ash and lapilli and they hardly contain any lithics (Óladottir et al., 2005), which is atypical for phreatomagmatic deposits (e.g. Wohletz, 1983). As fragmentation mechanism has a great influence on the hazard assessment of future eruptions (Nemeth and Cronin, 2011) it is of key importance to sort out the details of the fragmentation process driving large explosive basaltic Katla eruptions.
Therefore this study aims to frame the fragmentation mechanism(s) of the 1755 and 1625 eruptions through detailed studies of the deposits with detailed stratigraphy, granulometric analysis, contemporary descriptions and the fragmentation index of the ash component. In terms of the general Katla tephra record these two eruptions fit into the group of large Katla eruptions, but they are not uncharacteristically large compared to other historical eruptions (Larsen, 2010) or compared to the Holocene tephra record (Óladottir et al., 2008; Thordarsson and Höskuldsson, 2008). With Katla being a very active system and overdue for the next explosive eruptions, this information could in turn influence hazards assessments of past and future Katla eruptions.

Geological background

The Katla volcanic system

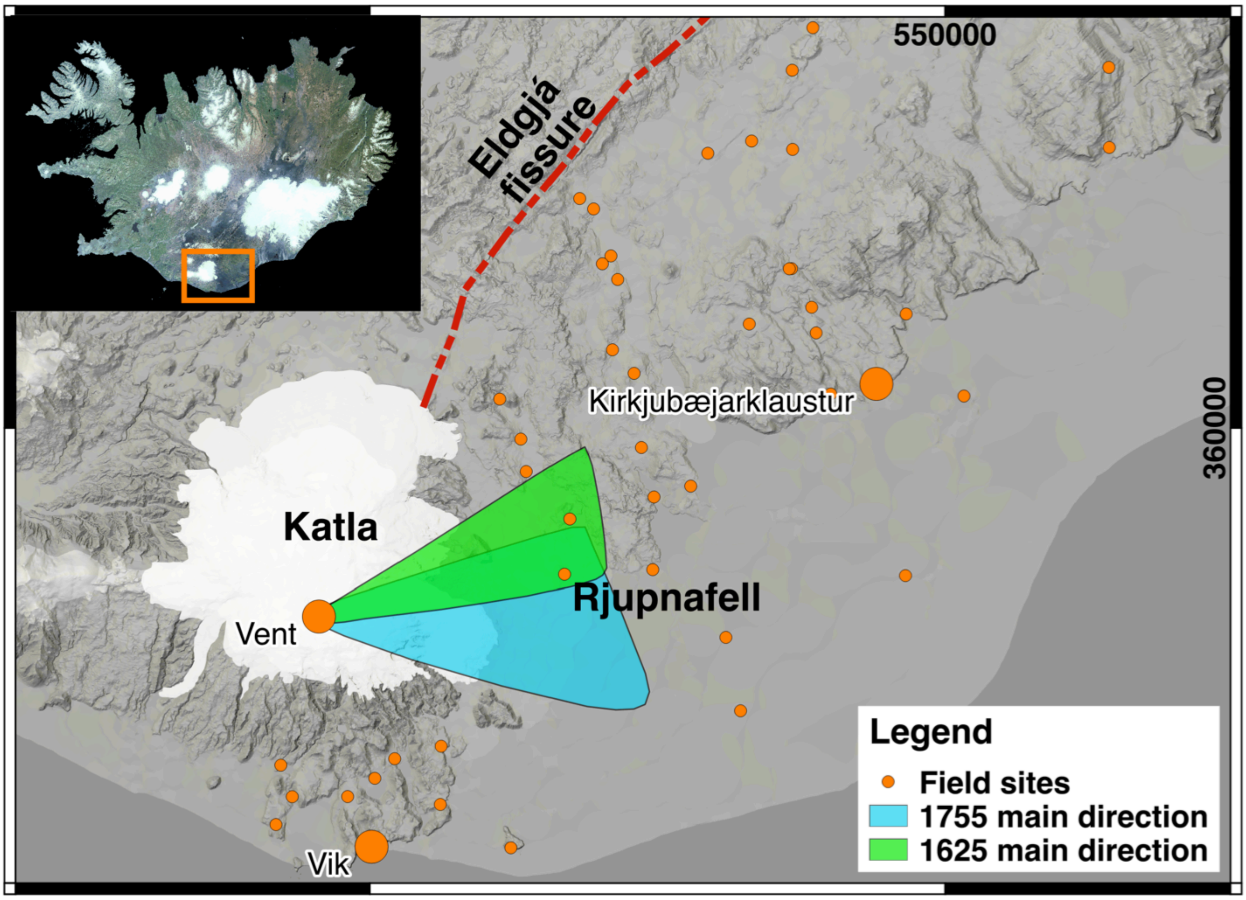

Figure 4.1. Map of field area showing Katla volcanic system and field sections. The main mapped directions of the 1755 and 1625 deposits are indicated with isopach fields. Background maps are based on data from National Land Survey of Iceland.

The Katla volcanic system is ~80 km long and situated on the Southern part (Southern Transgressive Zone) of the Eastern Volcanic Zone (EVZ) in Iceland. It consists of the 30 km wide Katla central volcano and the 75 km southwest-northeast trending Eldgjá fissure swarm. Katla central volcano is partly covered by the 600km^2 Myrdalsjökull glacier, which reaches an average thickness of 230 m (Björnsson et al., 2000). The central volcano is situated on the SW part of the Katla volcanic system, while the Eldgjá fissure swarm propagates from the Myrdalsjökull ice cap almost reaching the Vatnajökull ice cap (fig 4.1).

The hyaloclastite massif of the central volcano reaches 1380m a.s.l (Larsen, 2010) and the volcano reaches a total height of 1450 m a.s.l. (Òladottir et al, 2005). The summit caldera is a 10 x 14 km, 110 km^2 ice filled structure with a depth of 650-750 m (Björnsson et al., 2000).

All the outcropping nunataks around the caldera are silicic (Lacasse et al., 1995; Lacasse et al., 2007) and consists of glassy rhyolites. The age of the caldera is unknown, but some authors have linked it to the formation of the Vedde ashes around ~12.1 ka cal. years BP (Lacasse et al., 1995; Birks et al., 1996; Lacasse and Garbe-Schönberg, 2001).

A seismic undershooting study (Gudmundsson et al., 1994) revealed a S-wave slow anomaly beneath the caldera. It was about 5 km across and terminating at 3 km's depth (1500 m below sea level). The resolution did not allow for an estimate of the top of the anomaly, but the volume was estimated to be about 10 km^3. This depth correlates to the neutral buoyancy of basaltic melts in the crust (Gudmundsson et al., 1994).

Tephra characteristics and geochemistry

Basaltic tephra from the Katla volcanic system is coal-black fine ash to lapilli (e.g. Larsen, 2000; Óladottir, 2005). The geochemical characteristics of the Katla volcanic system are transitional-alkali Fe-Ti basalt with a very narrow compositional range and consistently high TiO_2 content of about 4-5 wt % during the Pleistocene and Holocene (Lacasse et al., 2007).

It is estimated that the tephra contains about 1-5 modal% phenocrysts and groundmass crystals of plagioclase, olivine, clinopyroxene, and rarely magnetite (Óladottir et al., 2005; Óladottir et al., 2008). The lithic component includes greyish white felsic rock fragments of rhyolite, brownish hyaloclastites and greyish basalts (Óladottir et al., 2005). Accessory crystal fragments of plagioclase and olivine crystals and lithics constitute less than 1 modal %. Microcrysts consists of needle-like plagioclase and rare sub-rounded clinopyroxene.

Lacasse et al. (2007) estimated the vesicularity of lapilli and coarse ash to be 30-50 %. Vesicles were sub-rounded <1-2mm. Pipe-vesicles were also present (Lacasse et al., 2007).

Holocene eruption summary

The Katla volcanic system has probably been active for several hundred thousand years (Björnsson et al., 2000). The duration of recorded Katla eruptions has been between 2 weeks to 4 month (Larsen, 2000), but both shorter and longer eruption durations could be expected (Larsen, 2010).

The Holocene eruptions are mostly confined to the 700 m deep Katla caldera beneath the Myrdalsjökull glacier. Conventional opinion is that the dominant explosive eruption style is caused by the presence of the ice, which interacts with the magma in phreatomagmatic eruptions (Thorarinsson, 1975). Basaltic tephra layers outside the ice cap represents supposedly more than 300 eruptions during the Holocene (Oladottir et al., 2005, 2008; Larsen and Eiriksson, 2008; Larsen 2010). There are 20 known silicic eruptions from Katla volcanic system in the corresponding period. There are 8-10 known lava-producing eruptions from the volcanic system (Larsen, 2010), including the Eldgjá eruption 934-40 and the 7700 years old Holmsá fires.

Soil sections in SE Iceland have recorded 20 historic eruption since 870 AD of which 16 have been mentioned in historical documents. Eighteen of the tephra layers have been chemically analysed to verify their origin from the Katla Volcanic System (Larsen, 2000; Óladottir et al., 2005). The volume of the 20 historical tephra deposits ranges 0.02-1.5 km^3 uncompacted volume (Larsen, 2000). Isopach maps have been made of several prehistoric basaltic eruptions to estimate volume of the eruptions (Óladottir et al., 2014). Volumes of the biggest prehistoric eruptions may exceed 2 km^3 (the K-E and K-N of Róbortsdóttir, 1992).

Methods

Selection of key section and field sampling

Key section

To make a good characterization of the fragmentation pattern for the two large eruptions in this study, we needed a well-preserved detailed deposit. However, due to the presence of the Myrdalsjökull glacier the most proximal undisturbed tephra sections are located more than 14 km from the suspected vent area outside the glacier itself (fig 4.1). Work on the main axis of historical Katla eruptions of Larsen et al. (2009) show that downwind sections are found in the areas E/NE of Katla (fig 4.1), and we have selected a single key section for both deposits in this area. Dealing with only one key section ensures that parameters influencing the deposit such as distance from vent, preservation conditions, and landscape factors do not change. However, the challenge of using a single key section is that changing wind directions would change the part of the plume being deposited over the area or even blow the plume away from the area of the section. To account for changing wind directions we have compared the section’s bearing from the eruption site with the prevalent wind directions for the eruptions as provided in contemporary descriptions. Assuming the main axis of dispersal is controlled by wind, this provides information about the position of the Rjupnafell section relative to the plume.

The most proximal and best preserved section found was the Rjupnafell section 22-23 km from the source area (fig 4.1). The section lies close to the estimated major deposition axis of Larsen et al. (2009) (fig 4.1) with an azimuth angle of ~80° from the source area (fig 4.1).

Our selection criteria were well-preserved stratified fall deposit(s) with internal units, which show minimal reworking by wind. We have used the Hekla 1597 bluish/grey deposit as a stratigraphic marker (see figure 4.2) as well as historic information on number and timing of Katla eruptions (Hallgrímsson, 1870).

Field sampling

The deposits are divided into fall units based on abrupt grain size changes, where vesicular lapilli tops of the lower unit and a fine ash bottom of the next unit define most unit boundaries. Both deposits are loose and therefore sampling was done by carefully taking out the loose material with a knife and spatula. The open framework structure of the lapilli layers permitted secondary deposition of ash from the fall unit above into the lower unit and it was not practically possible to make a clean break between the units for sampling. Therefore we chose to sample the top of one unit with the fine bottom from the next, which is accounted for in the interpretations of different types of data. The dimensions of the hole left after sampling were measured to obtain sample volume, and all samples have been carefully bagged and transported in order to keep the grains as intact as possible.

Granulometry methods

Grain size measurements

All samples have been dried at 50°C and split in halves. One half was carefully hand-sieved for grain size in whole φ steps down to 3φ (125μm) following Wohletz et al. (1995). The sieved sample was split again at 3φ (125μm) and one half was run on a Micrometrics Sedigraph III grain size analyzer to obtain data for the fine ash granulometry. The other half was hand sieved through the 4φ (63μm) sieve to allow calibration of the Sedigraph data. Sieve- and Sedigraph data were merged to produce whole grain size distributions for each sample.

Deconvolution and modeling of subpopulations

The granulometry data of each unit was treated with the deconvolution program DECOLOG 5.6 to obtain data on grain size subpopulations. Inman parameters (Inman 1952) of arithmetic mean, sorting, and skewness were evaluated using the logarithmic method of moments scale (Blott and Pye, 2001). The subpopulation data were then modeled using the approach of Wohletz et al. (1989), (1995), and Eychenne et al. (2012).

Morphology analysis

Qualitative grain morphology

Photos of 3-4φ (125-63 µm) sized ash grains were obtained from a Hitachi TM 3000 Tabletop Microscope scanning electron microscope (SEM) for manual inspection. The ash grains were mounted on carbon tape on a Hitachi 12.5 mm sample stub, were gold coated and studied to get a qualitative overview of grain types, surface features and grain erosion.

Quantitative grain morphology

To characterize the bulk grain morphology of small subsamples of ash from each eruption deposit sample, we analyzed the samples by the method recommended by Schmith et al. (2017). We used a Particle Insight™ dynamic shape analyzer (PIdsa) to run about 50-90 mg of bulk sample of 3-4φ (125-63 µm) to characterize the morphology of the ash grains by shape parameters. We used this grain size, because it allows for the best discrimination between magmatic and phreatomagmatic fragmentation mechanisms (Wohletz, 1983; Schmith et al., 2017 and references therein). The image resolution for this grain size is in the range of 16600 to 4200 pixels/grain, which ensures good 2D shape parameters (Schmith et al., 2017). We used a darkness threshold of 0.8 for grain detection, 90% focus rejection, circularity rejection of 0.98 to remove air bubbles and ensure high data quality. We measured 25 shape parameters and collected data from 20,000 grains for each sample. Individual grain data were exported for grains with an equivalent area circle diameter larger than 63 µm.

Componentry methods

100 grains were counted in each sample for ash componentry in the 3-4φ (125-63 µm) grain size range using binoculars. This grain size was chosen to support the morphology data.

Treatment of contemporary texts

Contemporary descriptions of both eruptions can be found in the Icelandic and Danish litterature (e.g. Det Kongelige Danske Videnskabernes Selskab, 1758; Hallgrímsson 1870; Magnússon, 1627). We have used information about weather conditions, wind directions, tephra fall areas, and the apparent activity during each eruption.

Eruptive activity

Information about eruptive activity is provided indirectly as descriptions of loud thunders or bangs, visual observations of smoke, fire and tephra fall, and earth movements. We interpret the loud thunders and bangs to be explosions and base eruption intensity on the experienced loudness or frequency as provided. The smoke column rising from Katla is taken represent the eruption column. Fires are often mentioned as well and we interpret these to be either activity at the main vent or independent fire fountains based on the context.

Weather conditions

Weather information about precipitation was used directly from the texts as provided. Thordarson (1991) found that people tended to align topographic directions with E-W or N-S directions in the 18th century. We have therefore corrected the provided directions accordingly using bearings of the local topography. When only areas of tephra fall is provided these have been used to infer the wind direction. If the provided wind directions do not correlate with inferred wind directions from fall area, then emphasis has been given to the direction inferred by fall area, as we deem fall information more reliable.

Analysis of 1755 and 1625 deposits

The 1755 Rjupnafell field deposit and componentry

The 1755 tephra deposit at Rjupnafell consists of ash to lapilli sized juvenile grains. Componentry of the 3-4φ (125-63 µm) ash shows that brown sideromelane glass dominates this grain size making up 67-75 %, while opaque tachylite represents 23-33% (fig 4.3a). Crystal fragments are scarce as are lithics, which combined make up 0-4% of the deposit (fig 4.3a) with unit 4 showing the highest contents of lithics of 2% and unit 6 showing the highest crystal content of 3%. The deposit is classified as a mono-component juvenile tephra deposit (Walker, 1971) and therefore grain size and morphology data can be directly related to eruption processes and ambient conditions for this fall deposit.

The 1755 deposit can be divided into 7 units (fig 4.2a,b), where each unit consists of a poorly consolidated ash layer overlain by loose lapilli. The lack of flow structures and textures in any of the beds support that this is a primary fall deposit. The beds show different degrees of sorting and grading (fig 4.2a,b). Unit 1 and 2 are poorly sorted, but unit 2 tends towards inverse grading. Unit 3 is well sorted and inversely graded, whereas unit 4 is poorly sorted though also tending towards inverse grading. Unit 5 is moderately sorted with invers grading and unit 6 and 7 are both poorly sorted. The fine bed of unit 6 shows a slightly undulating top, suggesting slight erosion (fig 4.2a). The coarse bed of unit 6 and 7 shows no grading and the transition is defined by a higher content of fines in the deposit, but no proper fine unit (fig 4.2a,b).

The 1625 Rjupnafell deposit

The 1625 tephra consists of fine ash to lapilli sized juvenile grains. The lapilli contain scoria as well as reticulite up to 1.7 cm on longest axis. This ash is also dominated by juvenile fragments consisting of 61-76 % sideromelane glass and 21-36 % tachylite (fig 4.3b). Crystal fragments and lithics combined make up 1-4% of the deposit (fig 4.3b).

The 1625 deposit can be divided into 9 bedded units shown in (fig 4.2e,f). All units consist of black tephra, but the base of the deposit has fine white-ish dust mixed in with the black tephra (fig 2e). The 1625 beds show different degrees of sorting and grading (fig 4.2e,f).

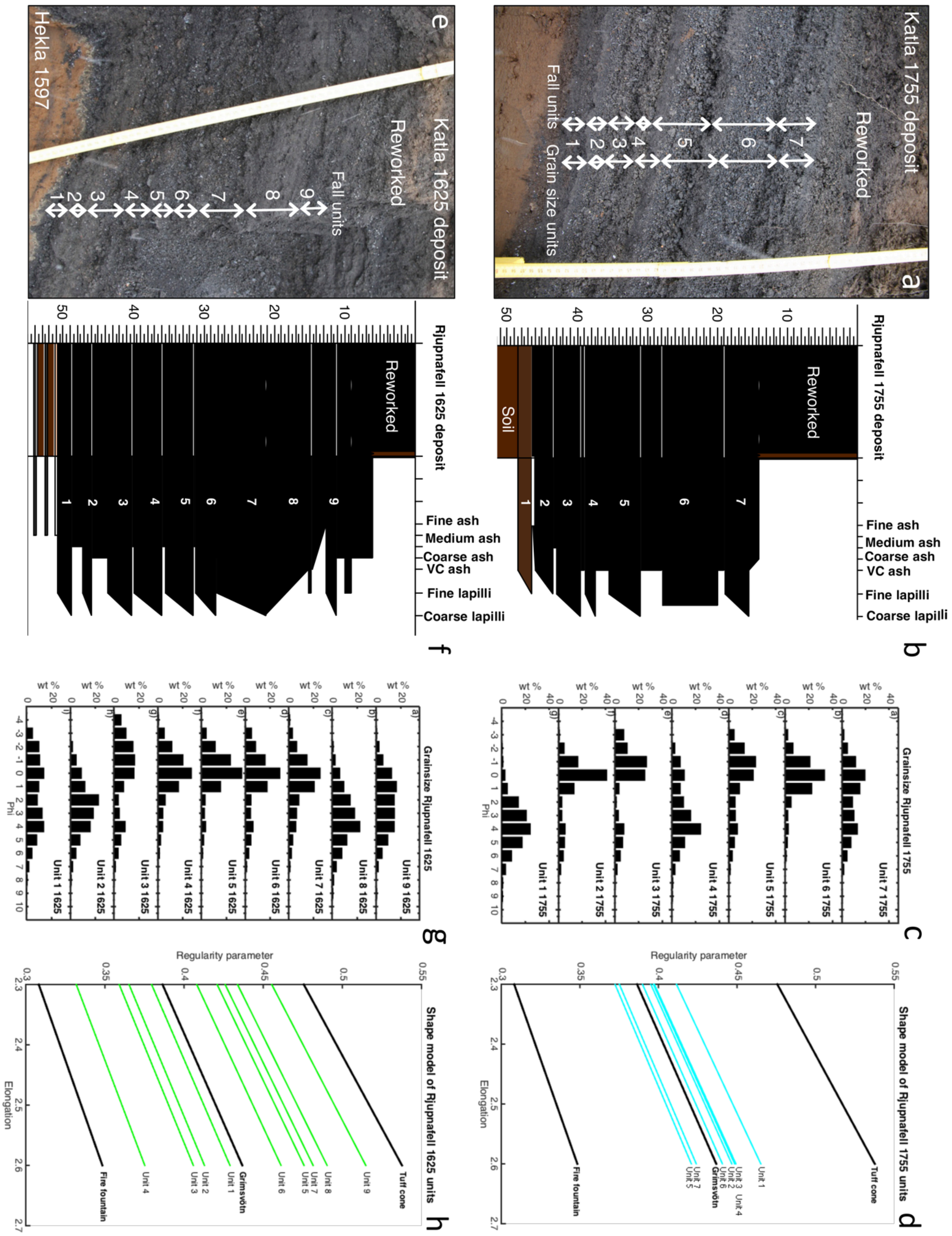

Figure 4.2. 4.2a: Photo of the 1755 deposit at Rjupnafell and 4.2e photo of the 1625 deposit at Rjupnafell. 7 units are indicated for the 1755 deposit, while 9 units are indicated for the 1625 deposit. Interpreted fall units vs. sampled units are indicated by numbers and arrows. 4.2b: Interpreted log of the 1755 Rjupnafell section and 4.2f interpreted log of the 1625 Rjupnafell section show qualitative grain size variation and grading as observed in the field. 4.2c: Grain size variation for each sample unit of the 1755 deposit and 4.2g grain size variation for each sample unit of the 1625 deposit. 4.2d: Plot of regularity index for the 1755 sample units fell and 4.2h) plot of regularity index for the 1625 sample units.

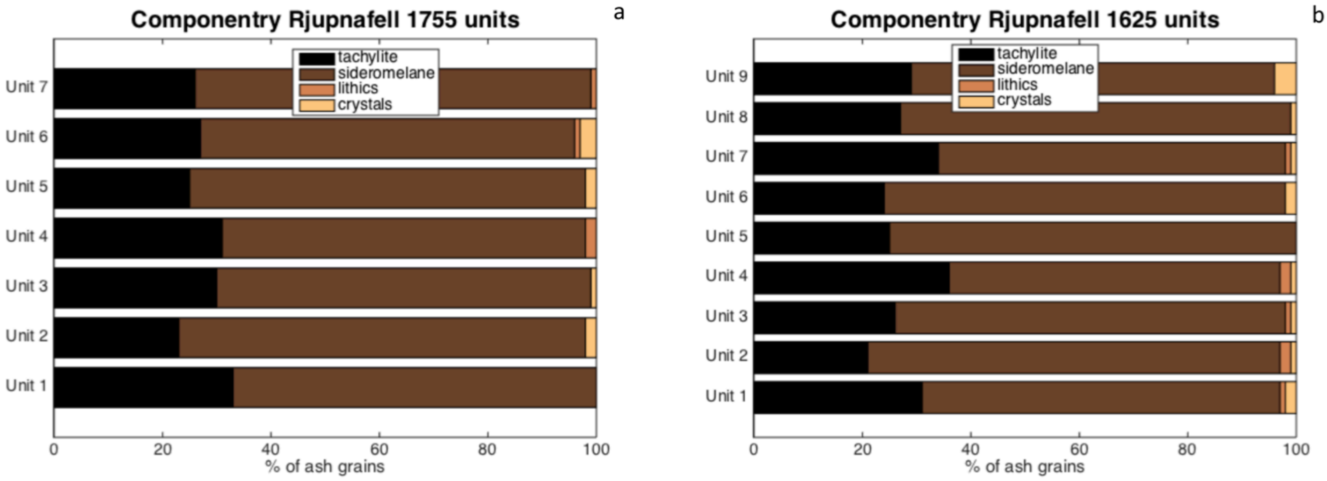

Figure 4.3. 4.3a: the ash componentry of the 1755 unit. 4.3b: the ash componentry of the 1625 units

Unit 1 is inversely graded and contains up to 0.5 cm lithics, unit 2 is normally graded, and unit 3 is inversely graded with vesicular lapilli defining the very top. A very thin ash layer starts unit 4, which is poorly sorted, but with a top defined by vesicular lapilli. Unit 5 and 6 are the same as 4. Unit 7 is also poorly sorted, but with a tendency to normal grading. Unit 8 is a normally graded fine-grained unit with a single truncation of coarse grains 2 cm from the top. The last well-defined unit (unit 9) is again inversely graded and poorly sorted.

Granulometric analysis

Grain size for the 1755 deposit

Grain size variation charts for each unit of the deposit are shown in figure 4.2c. For the 1755 deposit all units except 1 and 6 are clearly bimodal in the frequency plots and very poorly sorted (σ_ϕ >2, table 4.1). Unit 1 and 6 are close to unimodal with only small 2nd modes and classify as poorly sorted (2> σ_ϕ >1, table 4.1). All units except units 1 and 4 are skewed towards fines, with units 2, 3, and 5 being very fine skewed (α_ϕ > 1.30, table 4.1) and units 6 and 7 being fine skewed (1.30 > α_ϕ > 0.43, table 4.1). Unit 4 and 1 are coarse skewed (-1.30 > α_ϕ > -0.43, table 4.1).

Grain size for the 1625 deposit

Grain size variation charts for each unit of the deposit are shown in figure 4.2g. In this deposit all units except 8 are bimodal in the frequency plots and all units except unit 5 are very poorly sorted (σ_ϕ >2, table 4.1). Unit 8 is unimodal with a broad mode and very poor sorting (σ_ϕ >2, table 4.1). Units 1, 2, 8, and 9 are symmetrical (0.43 > α_ϕ > -0.43, table 4.1), while units 3 to 6 are fine skewed (1.30 > α_ϕ > 0.43, table 4.1) with unit 5 being very fine skewed (α_ϕ > 1.30, table 4.1).

Grain size units	Mean $M\phi$	Median Md_ϕ	Sorting σ_ϕ	Skewness α_ϕ	Coarse mode ϕ_c	Coarse mean M_c	Coarse median $Md_{\phi c}$	Coarse sorting σ_c	Coarse skewness α_c	Coarse γ_c	Fine mode ϕ_f	Fine mean M_f	Fine median $Md_{\phi f}$	Fine sorting σ_f	Fine skewness α_f	Fine γ_f	Coarse FF* (ϕ_c/γ_c)	Fine FF* (ϕ_f/γ_f)
1755																		
Unit 7	1.19	0.76	2.35	0.29	-0.26	-0.55	-0.46	1.13	-0.45	-0.92	3.22	3.51	3.42	1.32	0.39	-0.95	0.29	-3.41
Unit 6	-0.22	-0.05	1.67	1.43	-0.45	-0.60	-0.55	0.99	-0.30	-0.90	2.31	1.41	1.69	2.71	-0.56	-0.99	0.31	-1.89
Unit 5	0.07	2.88	2.52	0.83	-1.19	-1.41	-1.34	1.10	-0.38	-0.92	3.08	2.98	3.00	1.91	-0.02	-0.98	1.29	-3.16
Unit 4	2.47	2.80	2.47	-0.55	0.28	1.88	1.41	2.84	0.88	-0.99	3.29	3.56	3.47	0.79	0.64	-0.83	-0.28	-3.97
Unit 3	0.20	-0.88	2.71	0.95	-1.06	-1.30	-1.22	0.98	-0.39	-0.89	4.00	4.28	4.20	1.38	0.30	-0.95	1.18	-4.21
Unit 2	0.45	-0.86	2.25	1.33	-0.42	-0.67	-0.59	0.77	-0.60	-0.81	4.13	3.94	4.01	1.71	-0.25	-0.97	0.52	-4.27
Unit 1	3.15	3.22	1.76	-0.44	1.15	0.29	0.53	1.34	-1.00	-0.95	3.25	3.53	3.45	1.44	0.27	-0.95	-1.21	-3.41
1625	**$M\phi$**	**Md_ϕ**	**$\sigma\phi$**	**α_ϕ**	**ϕ_c**	**M_c**	**$Md_{\phi c}$**	**σ_c**	**α_c**	**γ_c**	**ϕ_f**	**M_f**	**$Md_{\phi f}$**	**σ_f**	**α_c**	**γ_f**	**FF**	**FF**
Unit 9	1.88	1.81	2.22	0.14	0.76	0.56	0.63	1.44	-0.28	-0.96	3.45	4.20	3.99	1.22	0.96	-0.93	-0.79	-3.70
Unit 8	2.77	2.88	2.05	-0.08	2.67	2.72	2.69	2.15	0.11	-0.98	3.20	3.27	3.25	0.44	0.18	-0.28	-2.73	-11.39
Unit 7	0.29	-0.05	2.19	0.84	-0.28	-0.56	-0.47	1.04	-0.44	-0.91	1.87	1.32	1.50	2.70	-0.38	-0.99	0.31	-1.89
Unit 6	0.14	-0.29	2.36	0.91	0.02	-1.05	-0.75	1.24	-1.40	-0.94	3.17	2.54	2.74	2.26	-0.48	-0.98	-0.02	-3.23
Unit 5	-0.44	1.81	1.92	1.32	-0.52	-1.11	-0.94	1.09	-0.85	-0.92	1.90	2.04	1.99	2.28	0.17	-0.98	0.57	-1.93
Unit 4	-0.30	-0.56	2.08	0.88	-0.81	-1.25	-1.12	1.19	-0.61	-0.93	0.79	1.89	1.57	2.02	0.85	-0.98	0.87	-0.81
Unit 3	-0.25	-0.86	2.98	0.60	-1.56	-1.67	-1.63	1.66	-0.18	-0.97	3.16	4.22	3.92	1.31	1.27	-0.94	1.61	-3.35
Unit 2	2.02	1.99	2.01	-0.14	0.67	0.12	0.28	1.29	-0.68	-0.94	2.47	3.19	2.98	1.37	0.83	-0.95	-0.71	-2.60
Unit 1	1.23	1.08	2.77	-0.35	-0.98	0.53	0.10	2.73	0.87	-0.99	3.36	3.65	3.56	1.03	0.51	-0.90	0.99	-3.71

Table 4.1. Granulometric Inman parameters for each unit as well as Inman parameters for coarse and fine subpopulations in each unit derived by deconvolution modeling. γ is the free parameter of the sequential fragmentation/transport-theory of Wohletz et al. (1989). *FF = Fragmentation factor (Wohletz et al., 1995).

Deconvolution modeling

Based on the bimodal nature of the grain size distributions as well as field observations of the bedding of all units, we have modeled the presence of two subpopulations of grain sizes in all units using the deconvolution method (modified from Wohletz et al., 1989) to obtain Inman parameters for each subpopulation (see table 4.1). Fits between observed data and the model function used for the deconvolution are very good as shown by the fit values in table 4.2.

For the 1755 deposit the coarse subpopulation modes fall between -1.19 ϕ and 1.15 ϕ with means ranging from -1.41 ϕ to 1.88 ϕ with unit 1 and 4 being the finest grained of the coarse subpopulations (table 4.1). Unit 4 is the only very poorly sorted and very fine skewed coarse unit. All other coarse units are moderately to poorly sorted and unit 3, 5, and 6 are symmetrical, while unit 1, 2 and 7 are coarse skewed (table 4.1).

The fine subpopulation modes of the 1755 deposit fall between 2.31 ϕ and 4.13 ϕ and means ranging 1.41 ϕ to 4.28 ϕ and thus show the same range of spread as the coarse subpopulations (table 4.1). However 2 subpopulations stand out. The fine subpopulation of unit 4 is fine skewed and moderately sorted, while that of unit 6 is coarse skewed and very poorly sorted (table 4.1). The remaining subpopulations 1,2,3,5,and 7 are symmetrical and poorly sorted (table 4.1).

17555	**CDF fit R^2**	**PDF fit R^2**	**1625**	**CDF fit R^2**	**PDF fit R^2**
Unit 7	0.9999542	0.9968378	**Unit 9**	0.9999794	0.9992018
Unit 6	0.9999671	0.9988244	**Unit 8**	0.9999793	0.9989606
Unit 5	0.9999793	0.9989606	**Unit 7**	0.9999671	0.9988244
Unit 4	0.9998893	0.9912369	**Unit 6**	0.9999289	0.9960601
Unit 3	0.9996597	0.9881978	**Unit 5**	0.9999794	0.9992018
Unit 2	0.9999056	0.9917086	**Unit 4**	0.9999786	0.9990741
Unit 1	0.9999766	0.9990752	**Unit 3**	0.9999497	0.9932051
			Unit 2	0.9999692	0.9986175
			Unit 1	0.9999392	0.9931204

Table 4.2. Deconvolution R^2-fit values for each unit for a two-component deconvolution. The R^2-fits are reported between observed and modeled cumulative distribution functions (CDF)s as well as for observed and modeled probability density functions (PDF)s.

The 1625 deposit has coarse subpopulation modes between -1.56 ϕ and 0.76 ϕ with means ranging from -1.67 ϕ and 0.56 ϕ with unit 8 as a clear outlier with a coarse mode at 2.67 ϕ and a mean at 2.72 ϕ (table 4.1). Unit 1 is the only very poorly sorted and fine skewed coarse unit, though unit 8 is also very poorly sorted but symmetrical (table 4.1). All other coarse units are poorly sorted and coarse skewed except for unit 3 and 9, which are symmetrical (table 4.1).

Fine subpopulation modes range from 0.79 ϕ to 3.45 ϕ and means ranging 1.32 ϕ to 4.22 ϕ (table 4.1). The range of spread of the fine subpopulations is thus wider range than the coarse subpopulations. The units are divided into two groups based on mean grain size and sorting. Group 1 consists of units 4 to 7, which have the coarsest modes with means ranging 1.32 ϕ to 2.54 ϕ and all are very poorly sorted (table 4.1). In the frequency diagrams in figure 2h these units have very similar grain size distribution patterns with a pronounced coarse mode and minor fine mode. Group 2 consists of units 1, 2, 3, and 9, which have finer means ranging 3.19 ϕ to 4.22 ϕ and they are all poorly sorted (table 4.1). Unit 8 stands out as the only moderately well sorted unit (table 4.1).

Interpreting granulometric results

A plot of sorting versus median diameter can be used to assess the relative roles of eruption intensity (i.e. column height) or changing wind directions against changes in fragmentation intensity with e.g. magma/water interaction or ash aggregation processes. For decreases in column height or wind changing from primary axis to the edge of the plume the resulting deposit will be finer and better sorted (Eychenne et al., 2012; Pardini et al., 2016). For increases in fragmentation intensity with magma/water interaction or increased ash aggregation and premature settling from the plume, the deposit will also decrease in grain size, but the sorting will decrease showing higher values of σ.

The total units of the 1755 deposit shows no distinct pattern with fining, whereas the 1625 show a better sorting with fining except for unit 1 and 3 (fig 4.4a). This suggests that the grain size of the 1755 deposit is primarily controlled by water/magma interaction and/or ash aggregation processes. Conversely the 1625 eruption seems to primarily be controlled by eruption intensity or changing wind directions.

Further details can be obtained if we assume that coarse and fine modes of the deconvolution roughly represent the coarse and fine beds of the deposit.

We have therefore plotted these modes in a sorting vs. median diagram as well (fig 4.4b and c). The coarse modes of the 1755 deposit form a fairly well-defined group with unit 4 as a distinct outlier in terms of lower grain size and much poorer sorting (fig 4.4b). The fine units form a group of slightly poorer sorting than the coarse modes with the two outliers of unit 6 with very poor sorting and unit 4 with moderate sorting. The grouping of the coarse unit modes suggests a relatively stable eruption process only disrupted for unit 4. The main grouping of the fine unit modes is towards slightly poorer sorting suggesting that increased magma/water interaction processes are responsible for the cyclic grain size change. However, premature settling of fines by aggregation processes would also decrease the sorting of only the fine part of the deposit and could also contribute to poorer sorting of the fine unit.

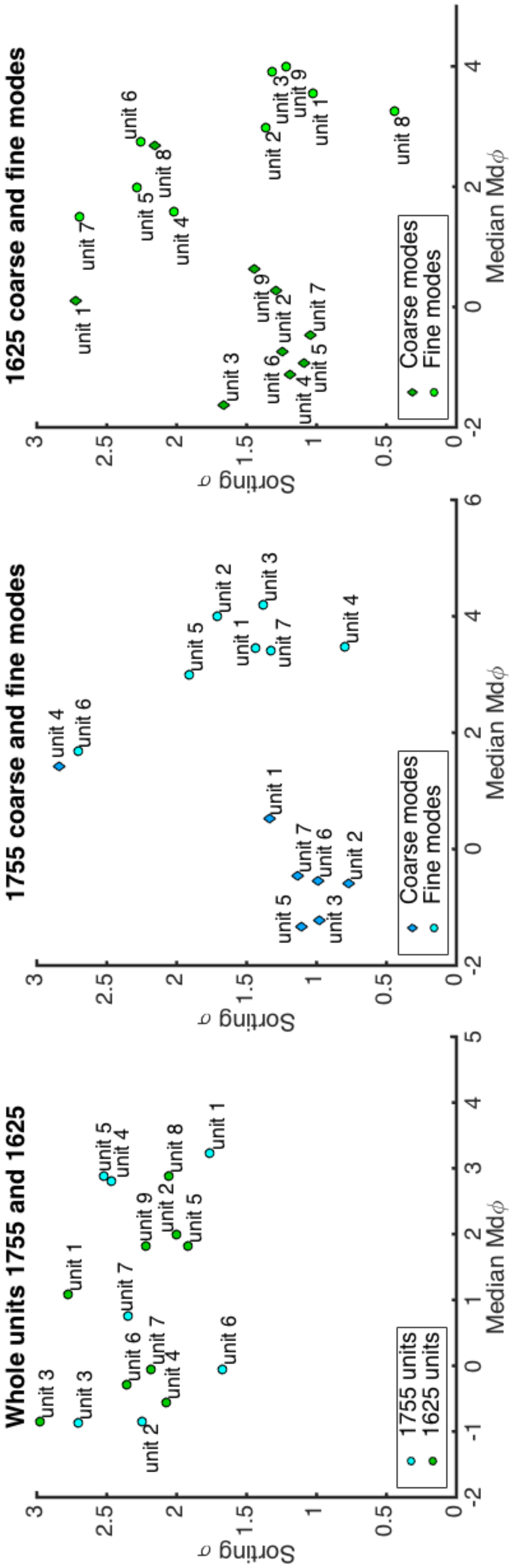

Figure 4.4. 4.4a: Sorting vs. median diameter for whole unit grain size distributions, 4.4b: 1755 fine and coarse modes, 4.4c: 1625 fine and coarse modes.

The significantly better sorting of unit 4 suggests that eruption intensity variation or changing winds are responsible for this unit. Coarse unit 4 and fine unit 6 form a distinct group of very poor sorting. Thus a significant change in fragmentation intensity or aggregation processes should be considered for these two units. Such changes might have been recorded as either extremely intense explosions or heavy precipitation in the contemporary accounts. However, unit 6 is close to being unimodal with a long fine tail and therefore the deconvolution algorithm might not resolve the fine subpopulation efficiently. The observations of the almost uniform ash deposit that make up unit 8 (fig 4.2a) could similarly explain why the coarse subpopulation of unit 8 is an outlier.

In the 1625 diagram all coarse units except 1 and 8 are grouped at approximately same to slightly poorer sorting values at the same median range (fig 4.4c). The fine modes are divided with one group of unit 1, 2, 3, and 9 of similar to slightly better sorting than the coarse modes suggesting eruption intensity or wind changes to be the controlling processes (fig 4.4c). The other group consists of units 4, 5, 6, and 7, which are coarser and very poorly sorted units (fig 4c). This group points to increased fragmentation intensity or ash aggregation as the controlling process for these grain size changes. However, like unit 6 of the 1755 deposit, the coarser medians and poorer sorting might also be an artifact of the deconvolution process due to small amounts of fines.

γ and the fragmentation factor

According to the sequential fragmentation/transport-theory (SFT-theory) the free parameter γ can be used to assess the fragmentation mechanism related to the different subpopulations by means of estimating the sequential size distribution of different fragmentation processes (Wohletz et al., 1989). Values of -0.33 to -0.66 are expected for magmatic fragmentation, whereas values between -0.5 and +0.33 are expected for phreatomagmatic fragmentation (Wohletz et al., 1989). However, if the fragmentation mechanism does not fully evolve, values will remain close to -1. γ-values for all subpopulations of the two deposits are shown in table 4.1. For the 1755 deposit all values lie close to -1 and no single fragmentation mechanism can be pinpointed. The 1625 deposit shows the same pattern except for the fine subpopulation of unit 8, which has a γ-value of -0.28. This points to a well-developed phreatomagmatic fragmentation for this unit.

The fragmentation factor was developed to account for the increased dispersal (and decreased sorting) of phreatomagmatic deposits (Wohletz et al., 1995). A plot of fragmentation factor against subpopulation mode can be used to discriminate between magmatic and phreatomagmatic deposits (Wohletz et al., 1995).

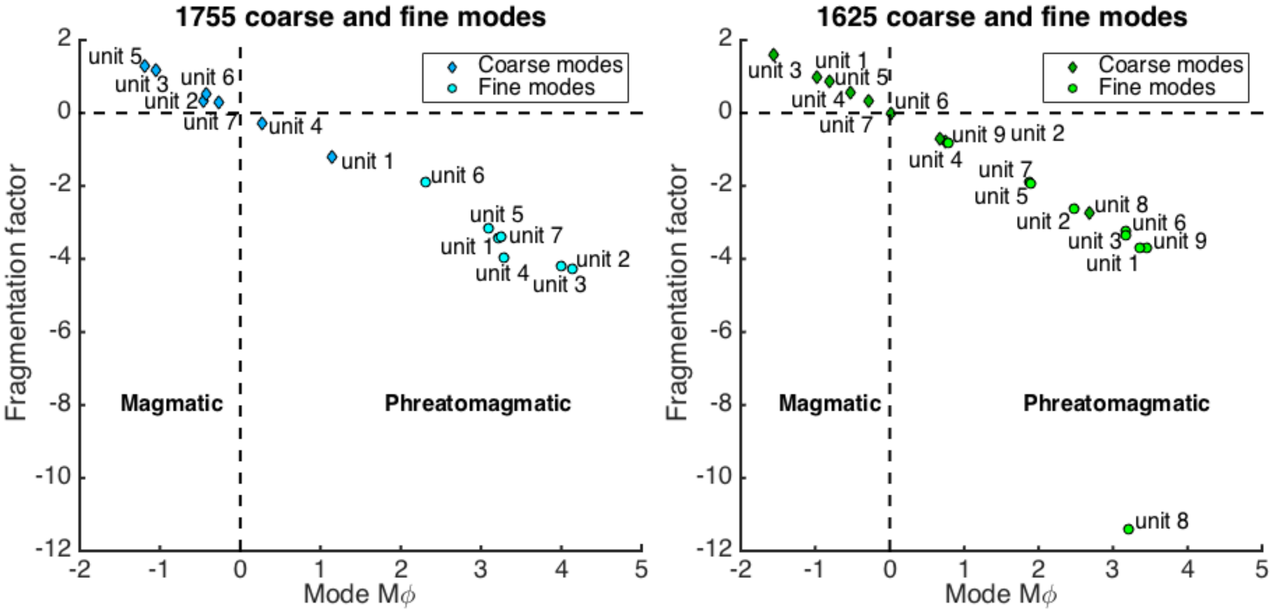

Figure 4.5. Plots of fragmentation factor against subpopulation mode. 4.5a: The 1755 units and 4.5b the 1625 units. Magmatic and phreatomagmatic fields are separated at (0.0) on both axis. After Wohletz et al. (1995).

For the 1755 deposit all the fine-grained subpopulations as well as coarse subpopulation of unit 4 and 1 are classified as phreatomagmatic (fig 4.5a). The remaining coarse subpopulation units are magmatic (fig 4.5a). For the 1625 deposit all the fine-grained subpopulations as well as coarse subpopulation of unit 2, 8, and 9 are classified as phreatomagmatic (fig 4.5b). The coarse subpopulation of unit 6 fall on the boarder between magmatic and phreatomagmatic, while the remaining coarse subpopulation units are magmatic (fig 4.5b).

However, the SFT-model does not consider the influence of ash aggregation, which would undermine the size distribution assumptions used for calculating the bounds of the magmatic and phreatomagmatic γ-value.

Morphology of grains and bulk population morphology

Qualitative ash grain morphology

Ash grains from both eruption deposits have been inspected visually on the SEM and show a wide range of morphologies. We have observed: blocky and aggregate morphologies associated with phreatomagmatic explosions (fig 4.6a,b,c) as well as vesicular and curved grains from breakage of bubble foam related to magmatic fragmentation (fig 4.6e,f,g), blocky-vesicular grains showing some degree of gas exsolution taking place (fig 6d), and smooth skinned achneliths from ductile melt deformation (fig 4.6h,i). All morphologies are observed within the same deposit and it is not possible to pinpoint the dominant grain shape from general visual inspection for either eruption deposit. Nor is it possible to identify general morphology changes between units within each deposit. Therefore we have used the regularity index of Schmith et al. (2017) to quantify any bulk morphology changes.

Morphology modeling and interpretations

To obtain quantitative information about fragmentation we have used a plot of regularity parameter vs. grain elongation for all the grains in each unit. A straight trendline was then fitted to each unit through (0,0) to obtain the regularity index for all sampled units (fig 4.2d,h, table 4.3). The regularity index is represented by the inclination of the sample trend line and can therefore also be interpreted from the plots. We also included the regularity indicies of a phreatomagmatic tuff cone, Grimsvötn 2011 and a magmatic fire fountain for comparison (after Schmith et al., 2017, table 4.3).

Ash morphology of the 1755 deposit

The 1755 deposit show a moderate variation in regularity index between different units of 0.162 and 0.179, which indicate both phreatomagmatic and magmatic fragmentation for all units (fig 4.2d, table 4.3). The narrow variation suggests a fairly stable cyclic behavior of the eruption. Unit 1 has the steepest line with the highest index value of 0.179 (fig 4.2d, table 4.3), which would indicate that magma/water contact dominated the initial fragmentation generating ash. The fragmentation process generating ash shows no systematic variation with stratigraphy, but the indices get slightly lower to around 0.162-0.170 in the last part of the eruption for units 5-7 (fig 4.2d, table 4.3) indicating less magma/water contact towards the end.

Ash morphology of the 1625 deposit

The regularity indices of the 1625 deposit show large variations throughout the units (table 4.3). The base of the deposit is not included in the analysis, so the initial trigger of the eruption is unknown. The regularity index unit 1 falls in the middle of the spectrum at 0.165 (fig 4.2h, table 4.3), which indicates that both gas exsolution and magma/water-interaction played a role. Through units 2,3, and 4 the lines flatten and index values decrease all the way to 0.144 for unit 4 (fig 4.2h, table 4.3), which indicate that the role of magma/water-interaction diminishes.

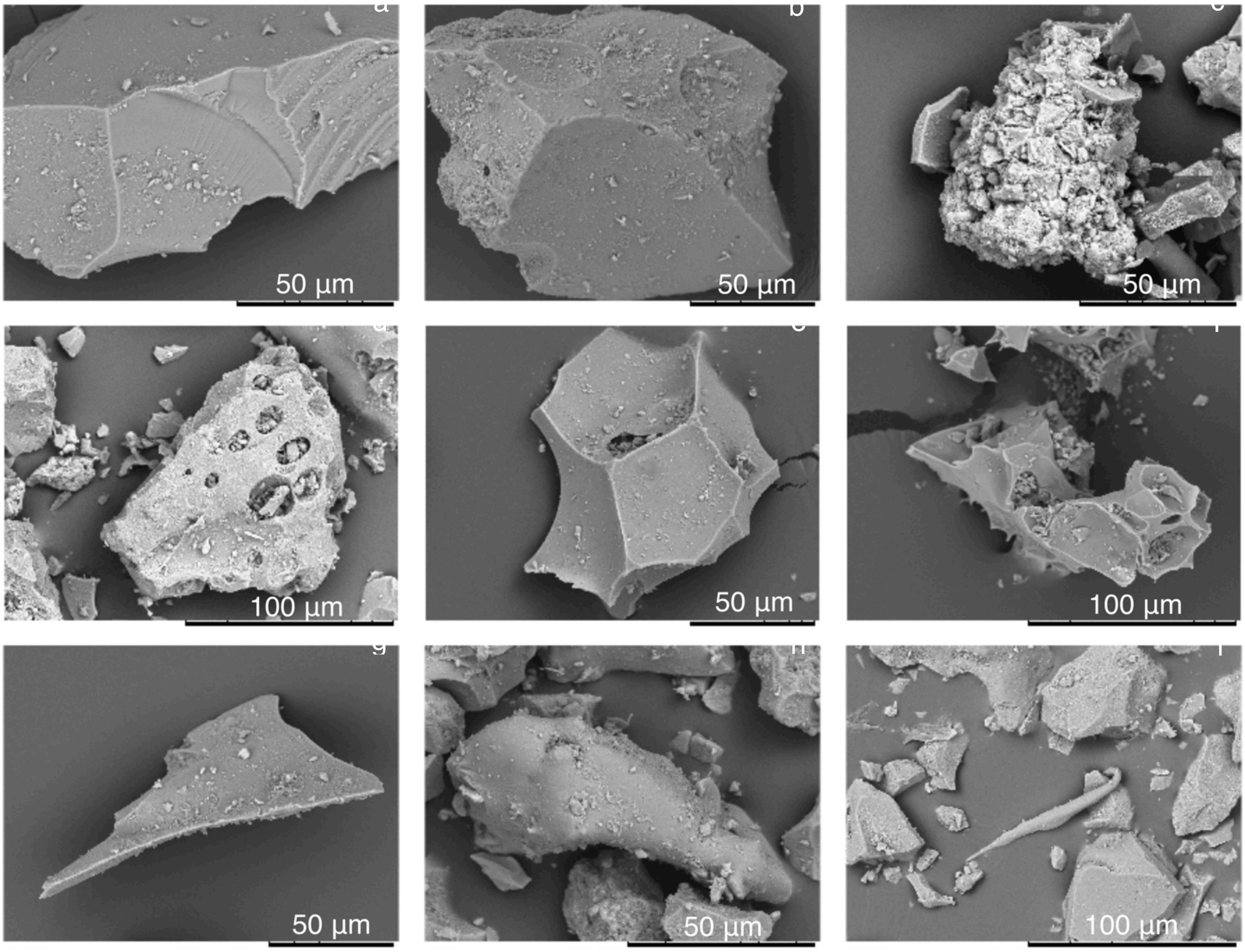

Figure 4.6. SEM images showing the variety of ash grain morphologies from the 1755 deposit. 4.6a: Blocky equant ash grain. 4.6b: Blocky ash grain with small dents from bubbles. 4.6c: Ash aggregate. 4.6d: Blocky ash with several separated near-spherical vesicles. 4.6e: Vesicular ash grain from bubble foam. 4.6f: Vesicular ash grain with deformed and coalesced vesicles. 4.6g: Platy grain from bubble wall. 4.6h: Smooth-skinned tear shaped achnelith. 4.6i: Elongated achnelith surrounded by blocky grains.

Samples	1755 regularity index values	1625 regularity index values
Unit 1	0.179	0.165
Unit 2	0.172	0.159
Unit 3	0.173	0.156
Unit 4	0.173	0.144
Unit 5	0.162	0.183
Unit 6	0.170	0.177
Unit 7	0.163	0.185
Unit 8		0.189
Unit 9		0.198
Phreatomagmatic tuff cone Eggoya		0.207
Fire fountain Fimmvörduháls		0.134
Subglacial eruption Grímsvötn		0.168

Table 4.3. Regularity index values for all units of the 1755 and 1625 deposits as well as reference values from a tuff cone, a fire fountain and a subglacial eruption from Schmith et al. (2017). Regularity index values refer to figures 4.2d and 4.2h.

Unit 4 has an index line close to that of the magmatic fire fountain (fig 4.2h), which shows that the fragmentation style creating the ash of this unit was predominantly magmatic. Then indices increase for units 5-8 to 0.177-0.189 (fig 4.2h, table 4.3), reflecting changes of the dominating fragmentation style towards phreatomagmatic processes. The sampled deposit ends with unit 9 showing the highest regularity index of 0.198 (fig 4.2h, table 4.3) suggesting the fragmentation being mostly related to magma/water-interaction in the end of the eruption.

Contemporary descriptions

Eruption activity and weather information

Data on weather conditions and eruptive activity are presented in table 4.4. The local topography by Holt in Myrdalur, where the 1755 observations were made, have a bearing of N114°E, which is close to the overall bearing trend of N110°E from Eyjafjallajökull to the Holt area (fig 4.1). As this topographic trend was most likely considered e-w at the time, then that would have influenced the reported directions by approximately +20°. This discrepancy has been accounted for in the wind directions in table 4.4.

A written summary of the course of each eruption is given in the following sections.

Table 4.4 (right). Activity levels as interpreted from descriptions of the 1755 and 1625 eruptions in Magnússon, 1627; Det Kongelige Danske Videnskabernes Selskab, 1758; and Hallgrímsson, 1870 (Eldrit). Dates in the duration column refer to dates in October and then November for the 1755 eruption. The 1625 eruption dates all refer to September.

Duration	Activity level 1755	Wind	Precipitation	Special events
17th – 18th	Intense explosive activity	Calm 17th W-wind 17th night Calm 18th	Clear 17th Rain 18th	3 vents and one eruption column observed
19th-20th	Increased explosive activity	WNW wind 19th-20th	Clear 19th Rain 19th night Rain 20th	2 vents mentioned on the 19th
20th	Very intense explosions	Strong WSW wind	Rain	2 especially large bangs and dense rock fall noted
20th-21st	Intense explosive activity	Strong WSW wind 20th-21st	Rain + snow 20th-21st	
21st – 24th	Explosive activity	Strong NNE wind 21st night Strong WNW wind 22nd Strong E wind 22nd night Strong NE wind 23rd Low WSW wind 23rd night Strong N wind 24th	Dry 21st-22nd Snow 22nd night Dry 23rd+24th	
25th – 26th	Decreased explosive activity	WNW-NW-NNW wind	Dry	
27th	Increased explosive activity	Strong NE wind	Snow	
28th – 2nd	Decreased explosive activity	Calm	Rain 28th	
3rd	Incandescence at vent	Calm		No eruption column. Eruption stopped

Duration	Activity level 1625	Wind	Precipitation	Special events
2nd noon – 2nd midnight	Intense explosive activity	WSW wind	Dry	
3rd midnight – 3rd sunrise	Decreased activity	WSW wind	Dry	
3rd sunrise – 7th 8-9 AM	Intense explosive activity	WSW wind 3rd SW wind 4th-6th WNW wind 7th	Dry	
7th 8-9 AM – 7th 3 PM	Very intense explosive activity	WNW wind	Dry	Incandescent fall, very loud explosions, “lightning” colors and collisions
7th 3 PM – 8th noon	Intense explosive activity	WNW wind 7th WSW wind 8th	Dry	
8th noon – 9th morning	Very intense explosive activity	WSW wind 8th Storm SW 9th	Dry 8th Rain 9th	Opening of several fissures E of vent. Earth movement felt N of Katla
9th morning – 9th evening	Quiet eruption	Storm SW 9th	Rain	
9th night – 11th noon	Decreased explosive activity	Storm SW 9th WSW wind 10th Calm 11th	Rain 9th Dry 10th-11th	Fountains visible and continuous tremors N of Katla
11th noon – 11th afternoon	Increased explosive activity	Calm	Dry	
11th afternoon – 13th evening	Decreasing explosive activity	Calm 11th WNW wind 11th night SW wind 12th NW wind 13th	Dry 11th Rain 11th night Dry 12th-13th	Eruption stops on the 13th

Summary of the interpretation of the 1755 eruption

The 1755 eruption began around 10AM on the 17th of October 1755. It was initiated by a felt earthquake and a violent jökulhlaup all over Myrdalssandur with an eruption column rising from the central volcano (Katlagjá). The eruption column lasted for 17 consecutive days and was reported gone on the 3rd of November (table 4.4). Based on the description of continuous noise from the mountain the activity seems to have been relatively stable for the first 8 days of the eruption except for two particularly violent explosions on the 20th of October. These explosions caused dense rocks of 1-5 kg and a single one on 7.25 kg to fall up to 30km from the volcano according to Det Kongelige Danske Videnskabernes Selskab (1758). For the last 9 days the intensity waxed and waned a little, but is mostly described as a steady decrease in activity (table 4.4).

The initial fall was reported to consist of firm and dense hot rocks followed by a pumice fall and then hail with “sand”-grains in the middle of the ice. This suggests an initial phreatomagmatic phase.

The South country suffered some damage, but especially Skaftártunga was damaged. Tephra fall was reported all the way to the East Fjords (Mjóifjörður) on the 20th of October and on the 19th it fell on ships close to the Faroe Islands.

Summary of the interpretation of the 1625 eruption

The 1625 eruption began early in the morning on the 2nd of September 1625 with a loud explosion and a Jökulhlaup at 8 AM (Magnússon, 1627). Throughout the eruption the activity was waxing and waning with 9 different phases (table 4.4) until it ended in the evening of the 13th of September. The eruption column lasted ~11 days, but additional small vents of fountaining were opened on the 8th-9th of September (Magnússon, 1627). There are reports of continuous ground movement in the Skaftártunga area during the last 3-4 days of the eruption (Magnússon, 1627). We suggest that they are related to tremor.

The ash in Skaftártunga ended up covering the forest and ash fall was reported over the entire S and E country as far N as Langanes (Magnússon, 1627). Ships in the sea were covered by ash and ash also fell in several villages in Norway (Magnússon, 1627; Thorarinsson, 1981).

Implications of the contemporary descriptions for eruption dynamics

The traditional length of the 1755 eruption according to the literature is ~120 days, but this interval is based on including jökulhlaup events in mid January 1756, which are not relevant for the tephra modeling. Such a significant change in eruption duration would have profound impact on the estimated mass eruption rate (MER) and thus on the estimated intensity and hazard potential of the eruption.

An integrated interpretation of eruption dynamics

Since the Rjupnafell section is at a medial distance of 22-23 km from the vent area we assume that only substantial changes in the eruption dynamics or local weather would be recorded in the tephra deposit. We have therefore aimed at relating major changes in the deposit to changes in eruption activity and weather conditions.

The 1755 eruption

For the 1755 deposit the combination of initially intense activity, calm conditions and clear weather (table 4) should result in a poorly sorted deposit at Rjupnafell. The presence of the glacier and the initial jökulhlaups suggest that the initial energy at least partly goes into water/magma interaction. Therefore the overall grain size is expected to be fine and the regularity index to be high. This is observed in unit 1 (table 4.1, figure 4.2a,b,c, and figure 4.4a,b) with the lowest mean and the ash bulk morphology showing the highest phreatomagmatic contribution of all eruption units at Rjupnafell (figure 4.2d, table 4.5).

Then the weather changes to W-wind (table 4.4), which places Rjupnafell close to the main dispersal and we expect a sorted bed of increased grain size to be deposited, which fits with the coarse bed of unit 2 (figure 4.2a, 4.4b).

The weather changes again to calm conditions with rain and a poorly sorted fine dominated deposit is expected as the result of increased ash aggregation. This is seen in the fine part of sample unit 2 (table 4.1, figure 4.2a,b,c, and figure 4.4a,b) (fine lower bed of fall unit 3).

Then the wind changes to WNW with apparently increased explosive activity and no precipitation. This should result in a poorly sorted, tending to inversely graded deposit, but with an increased fine component as rain sets in (table 4.4). This fits well with the observations of sample unit 3 with an inversely graded lower part overlain by a very poorly sorted top with a higher content of fines (table 4.1, figure 4.2a,b,c, and figure 4.4a,b). The coarse bed grain size increase compared to coarse unit 2 (table 4.1, fig 4.4b), which fits with the increased eruption intensity.

The wind then turns WSW and increases in strength, which should result in a light increase in grain size being deposited at Rjupnafell. This is observed in the lower part of unit 4 (figure 4.2, a,b). Then two very strong explosions are mentioned along with a fall of dense blocks. This fall suggests violent fragmentation and a widening of the vent, which indicates that most of the explosive energy went into fine fragmentation in these events.

	Regularity index	Fragmentation factor		Sorting vs median		
1755		**Coarse**	**Fine**	**Global**	**Coarse**	**Fine**
Unit 7	P*0.40	P	P	?	Column/wind	FI/accretion
Unit 6	P*0.49	M	P	?	Column/wind	FI/accretion
Unit 5	P*0.38	M	P	?	Column/wind	FI/accretion
Unit 4	P*0.53	P	P	?	FI/accretion	Column/wind
Unit 3	P*0.53	M	P	?	Column/wind	FI/accretion
Unit 2	P*0.52	M	P	?	Column/wind	FI/accretion
Unit 1	P*0.62	M	P	?	Column/wind	FI/accretion
1625						
Unit 9	P*0.88	M	P	FI/accretion	FI/accretion	Column/wind
Unit 8	P*0.75	P	P	Column/wind	Column/wind	Column/wind
Unit 7	P*0.70	M	P	Column/wind	Column/wind	Column/wind
Unit 6	P*0.60	M	P	Column/wind	Column/wind	FI/accretion
Unit 5	P*0.67	M	P	Column/wind	Column/wind	FI/accretion
Unit 4	P*0.14	P/M	P	Column/wind	Column/wind	FI/accretion
Unit 3	P*0.30	M	P	Column/wind	Column/wind	FI/accretion
Unit 2	P*0.34	P	P	Column/wind	FI/accretion	Column/wind
Unit 1	P*0.43	P	P	Column/wind	Column/wind	Column/wind

Table 4.5. Summary of classification of units based on figures 4.3, 4.4, 4.2d,h, and table 4.3. Regularity indices have been recalculated to as fractions of the scale between the phreatomagmatic tuff cone and the magmatic fire fountain. P=phreatomagmatic, M=Magmatic, Column/Wind=decreased column height/wind changing direction, FI/Accretion=increased fragmentation intensity from water/magma interaction/accretion of ash and premature fallout.

It would therefore be expected to leave a deposit rich in fines, which show an increased content of lithics. Both features fit well with the fine part of unit 4 (table 4.1, figure 4.2a,b,c, figure 4.3a). Interestingly the increased fragmentation intensity is not connected to increased magma/water interaction by either the regularity index (table 4.5, figure 4.2d), or by the position of fine sample unit 4 in figure 4.4b.

The apparent eruption intensity remains very high, and with the strong WSW-wind and rain/snow falling we would expect an inversely graded deposit with large scoracious lapilli, but with a significant content of fines washed out from the plume, which is seen in the coarse bed of unit 5 (table 4.1, figure 4.2a,b,c, figure 4.4b).

The wind then changes to NNE with clear weather leaving Rjupnafell on the edge of the plume. This accompanied by an apparent decrease in the eruption intensity with little tephra fall for a few hours. Next the sources disagree about the wind direction. One mentions a drop in activity and little fall in the morning, with increased fall and strong WNW wind in the afternoon. The royal Danish scientific society report mentions tephra fall across Myrdalur, which would result in a N-NE directed wind during this period. Thus the wind has probably been unstable with low eruption intensity. Thus a change for a fine very poorly sorted deposit is expected as seen at the top of sample unit 5 (table 4.1, figure 4.2a,b,c, figure 4.4b). The regularity index indicates a decrease in magma/water interaction might explain the perception of decreased activity.

Then both sources agree that the wind then changes to E and ENE combined with lower explosive intensity suggesting no deposition at Rjupnafell. This might explain the undulating top of the fine bed of sampled unit 5 (fine lower bed of fall unit 6) as seen in figure 4.2a.

From here on the descriptions of the eruption becomes less detailed making direct links to the deposit more difficult. However this also suggests that the remaining part of the eruption was less intense and eventful.

The next period is described as dry weather and at first a low WSW wind, which quickly turns to a strong N wind, followed by a period of NW winds and decreased activity, leaving Rjupnafell off the main depositional axis. A moderately sorted though not graded deposit of relative fine grain size would be expected from this description. This fits with unit 6 (fig 4.2a,b, table 4.1) except the grain size indicates that the activity decrease might not have been that substantial, but explained by less magma/water interaction. The dry conditions also fits well with small amount of fines in this unit (fig 4.2c, table 4.1, table 4.4).

A short activity increase coupled with strong NE winds on the 27th should mark a change in the deposit towards fining, which might be the cause of the transition from unit 6 to unit 7 (fig 4.2a). The regularity index of the ash of sample unit 6 (the fine transition to unit 7) increases from unit 5 (table 4.5, fig 4.2d), which indicates increased water-magma interaction, and could explain the perceived increase in activity. The rest of the activity in calm conditions should produce a poorly sorted top for the rest of the eruption probably representing unit 7 (table 4.4, fig 4.4a).

The 1625 eruption

The description of the 1625 eruption is not as detailed as that of the 1755 eruption. Thus the amount of information available for the 1625 eruption does not allow as detailed a correlation between the described eruptive activity, wind directions and the Rjupnafell deposits.

From a section at Hemra as well as other sections further N of Myrdalssandur we know that the white base of the Rjupnafell deposit is not the first part of the eruption. At least one additional phase is observed below the fine-grained white deposit (field observation). The initial activity also remains unknown in the contemporary descriptions as most of the observations are focused on the jökulhlaup and consequences of tephra fall. However, there was a seemingly stable WSW wind and dry weather. The activity of the opening was sustained for only a day and then at night the activity decreased. Based on grain size means (table 4.1) unit 1 and 2 might be related to this initial decreased activity.

The next three days the only information is that the wind remained in SW placing Rjupnafell in the main fall direction, the weather stayed dry, and the activity level remained the same (table 4). We suggest that the part of the Rjupnafell deposit, containing unit 3 to 7 represents this part. These units are dominated by lapilli with large scoracious pieces found in all units. The regularity index of sampled unit 2 represents the fine part of fall unit 3 and it decreases significantly (table 4.5, fig 4.2h) showing decreasing influence of magma/water-interaction in the fine fragmentation. This fits with fine unit 2 being better sorted than coarse unit 3 in figure 4.4c suggesting eruption intensity controls the deposition. This would also explain the increase in scoracious lapilli for unit 3 (figure 4.2e, f). This trend continues with sample unit 3 (fine base of fall unit 4) and culminated with the lowest regularity index in sample unit 4 (lower fine base of fall unit 5). Thus the influence of magma/water-interaction decreases, which correlates with an increased mean grain size from unit 3 to 5 (table 4.1) and a decreasing amount of fines (figure 4.2f). Thus there is nothing to suggest that there is an increase in magma/water-interaction or in ash aggregation as suggested by the position of the fine subpopulations of unit 4-7 in figure 4.4c. This distinct group of fine subpopulations instead shows that the deconvolution algorithm cannot resolve the fine subpopulations properly.

Then suddenly the fragmentation style changes for the fine fragmentation in the fine top sample of unit 5 (fine base of fall unit 6, figure 4.2e). A much higher regularity index (table 4.5, fig 4.2h) points to a marked increase in magma/water-interaction, which correlates with a more than 1φ decrease in mean grain size for unit 6 (table 4.1). For the fine base of fall unit 7 the magma/water-interaction decreases slightly as the regularity index drops a little (table 4.5, fig 4.2h), which correlates with a slight increase in the mean grain size of unit 7 (table 4.1).

After this steady period the wind turned WNW (table 4.4) leaving Rjupnafell on the edge of the plume. At the same time the intensity of the explosions increased considerably with heavy ash fall reported (table 4.4). This suggests that eruption intensity increased and a fine-grained deposit would then be deposited at Rjupnafell, which probably corresponds to unit 8. This continued for another day with the wind turning WSW, briefly interrupted by a massive explosion/earthquake that might have opened up several fire fountains as the description report new fires on the mountain (table 4.4). At Rjupnafell a small lapilli interval is seen in the otherwise fine-grained unit (fig 4.2 e,f), which could correspond to this event. The otherwise fine deposit suggests intense fragmentation at the vent supported by the high unit 8 regularity index (table 4.5, fig 4.2h) showing large influence on fine fragmentation by water/magma interaction. Then the wind turned SW and rain set in coinciding with a quite period in the eruption (table 4.4) and this change might correspond to the very fine thin top of unit 8 (fig 4.2e,f). Then eruptive activity picked up again though not as intense as previously with a WSW wind (table 4.4).

Therefore a lapilli-dominated bed is expected at Rjupnafell though with finer lapilli size than previously seen. This corresponds with the coarse bed of unit 9 (table 4.1). Continuous earthquake activity is described for the whole period as well. We infer this to be related to shallow intense explosions causing tremor and the high regularity index of unit 9 (table 4.5, fig 4.2h) indicates a fragmentation dominated by water/magma interaction.

A short burst of increased activity coupled with calm conditions is then described (table 4.4) followed by an activity decrease with changing wind conditions until the end of the eruption. However, as the top of the deposit was reworked, we do not have any data for this last part of the eruption.

Implications for fragmentation modeling of basaltic eruptions

Recent studies have shown that fragmentation in subglacial eruptions is not solely driven by magma/water-interaction (Graettinger et al., 2013; Jude-eton et al., 2012; Cioni et al., 2014; Liu et al., 2015). Graettinger et al. (2013) reported feedback loops between decoupled gas magma eruption and phreatomagmatic explosions, which are in line with our observations.

Heap et al. (2014) showed that large vesicles in low porosity magma could decrease the brittle strength of the magma more than small vesicles at the same porosities. Furthermore coalescence of bubbles in low porosity magmas would also reduce the brittle strength (Heap et al., 2014). In a complex fragmentation setting of subglacial basaltic eruptions, this is likely to have implications for the feedback between magmatic and phreatomagmatic explosions. In such a fragmentation framework the findings of multi stage bubble nucleation and thus highly variable size distribution of Genereau et al. (2013), could explain the morphology variation seen in figure 4.6.

The study of the dynamics of the two large subglacial Katla eruptions contributes another perspective that even though the geological setting, geochemistry, duration, estimated areal distribution, and overall deposit type are comparable (Larsen, 2010), subglacial eruptions can still differ in essential ways.

The 1755 eruption deposition is mainly controlled by weather-processes of wind and precipitation changing throughout the eruption. In contrast the wind remains fairly stable and the weather dry during the 1625 eruption and eruptive processes mainly control the 1625 deposition.

This has major implications for the treatment of the eruption deposits.

The grain size variations can to some extent be used to sort out eruption dynamics information, but the variations of sorting with median are not straightforward and require a lot of supplementary information about weather. The fragmentation factor shows no correlation with any of the changes in the eruption (table 4.5) and cannot be used to constrain the fragmentation mechanism according to our dataset. This shows that the assumptions about grain size and sorting as a proxy for fragmentation as in the method by Wohletz et al. (1995) is to heavily influenced by other processes such as ash aggregation.

The morphology data from the quantitative shape analysis show good correlations with grain size variations for the 1625 eruption, where steady weather conditions do not affect the deposition. The correlation is not as good for the 1755 deposit, where frequent showers and changing winds are the main controls of the grain size distribution.

The morphology population modeling clearly shows the distinction between the two eruptions and is a very effective way to distinguish between different fragmentation mechanisms. We therefore recommend that assessment of fragmentation mechanism should be based on quantitative morphology models and not on grain size distributions accompanied by qualitative morphology observations.

Conclusion

We have studies the eruptive processes of the two large basaltic explosive eruptions of 1755 and 1625 from Katla from 3 different datasets. The field data show that the eruptions are comparable in terms of total thickness, a cyclic eruptive behavior, and componentry. However, there are differences in grading, apparent vesicularities of lapilli, and thicknesses of units. Grain size variations show a similar range of grain sizes and an overall bimodal grain size distribution for both deposits, and for units of significant bimodality, deconvolution modeling can be used assess the Inman parameters for each mode. Correlating mode sorting with mode median cannot be used as a fragmentation type proxy as depositional processes modify the distribution. However, the new regularity index can be used to assess fragmentation processes of complex eruptive settings. Therefore we recommend combining granulometric analysis with quantitative morphology modeling to better constrain complex fragmentation mechanisms.

In the 1755 eruption ash was generated by a combination of magmatic degassing and magma/water-interaction with magma/water-interaction being more dominant in the beginning of the eruption.

Ash fragmentation in the 1625 eruption was also initially a combination magmatic degassing and magma/water-interaction, but magma/water-interaction became progressively less important during the next phases. In the final phases magma/water-interaction dominated the fragmentation process.

Acknowledgements

This project is part of a PhD-project conducted on the 1755 and 1625 eruptions from Katla and part of the ICAO data collection. We would like to extend our grateful thanks to Eirik Gjerløw, Cathrine Gallagher, William Moreland, and Rob Askew for assisting with and making fieldwork in SE Iceland most enjoyable. Our sincere gratitude also goes to Bergrún Óladottír for your helpful input and comments. Finally we would also like to acknowledge the financial support of the Nordic Volcanological Center.

Chapter 5

Eruption source parameters of large explosive basaltic eruptions at Katla volcano, Iceland.

Johanne Schmith[1,4], Costanza Bonadonna[2], Ármann Höskuldsson[1,3], Guðrún Larsen[3], and Paul Martin Holm[4]

[1]Nordic Volcanological Center, Earth Science institute, University of Iceland, Iceland,
johannes@ign.ku.dk, +4527121368
2 Department of Earth Sciences, University of Geneva, Switzerland
[3]Earth Science institute, University of Iceland, Iceland
[4]Institute of Geoscience and Natural Resource Management, University of Copenhagen, Denmark

Abstract

Katla volcano has not erupted for 99 years. However, a history of numerous past eruptions can be found in tephra records and contemporary accounts from historical chronicles. At least 2 of the 20 historical eruptions have reached Northern Europe as visible tephra fall, even though all historical eruptions were basaltic. These eruptions occurred in 1755 and 1625 and they show the hazard potential of subglacial basaltic explosive eruptions from Katla. We have studied these two far-reaching eruptions based on the Icelandic tephra record in soil sections in SE Iceland and have produced the first eruption source parameters for any Katla eruption.

We have projected the deposits to cover 23400 and 23600 km^2 on land in Iceland for the 1755 and 1625 eruptions, respectively. The volume of the 1755 eruption was 1.34 km^3 with a 99 % confidence interval of 1.20-1.50 km^3 based on power-law integration. The 1625 eruption volume was 1.24 km^3 with a 99 % confidence interval of 1.12-1.36 km^3. The total erupted mass of the 1755 eruption was $2.13 \cdot 10^{12}$ kg (99 % confidence interval of (1.84-2.45)·1012) based on a conversion from eruption volume with a lower-bound mass eruption rate of $1.45 \cdot 10^6$ kg/s (99 % confidence interval of $(1.25\text{-}1.67) \cdot 10^6$). In 1625 Katla erupted a total of $1.73 \cdot 10^{12}$ kg (99 % confidence interval of $(1.53\text{-}1.94) \cdot 10^{12}$) tephra as calculated from the erupted volume. However, due to shorter duration of the 1625 eruption it had the higher lower-bound mass eruption rate of the two eruptions extruding tephra at $1.82 \cdot 10^6$ kg/s (99 % confidence interval of $(1.61\text{-}2.04) \cdot 10^6$). Plume height estimates for the 1755 eruption range from 9± 2 km to 25± 6 km based on empirical correlation methods, but with a most likely average at 14.4 km from mass loading data

inversion. Empirical correlation estimates brackets the plume height of the 1625 eruption between 10± 2 km and 25± 6 km with an inversion-based plume height of 16.6 km. Comparison with the recent Grímsvötn 2011 eruption plume dynamics suggest that average plume heights for the whole eruption is given by the inversion plume height, whereas most tephra was emplaced from a peak plume height at 25 km.

We recommend that the reported eruption source parameters are implemented in future hazard models for Katla volcano.

Introduction

Katla is one of the most prominent Icelandic volcanoes known to produce major explosive eruptions (Thorarinsson, 1981; Larsen, 2010; Biass et al., 2014; Schmith et al. submitted manuscript, 2017). Volume wise Katla volcanic system is the most productive volcanic system in Iceland in historical times counted from 870 AD (Thordarson and Larsen, 2007; Thordarson and Höskuldsson, 2008) and recent unrest suggests that another Katla eruption may be imminent (Budd et al., 2016). Hazard assessment of Icelandic volcanoes shows that Katla is one of the most important volcanic systems to constrain in terms of hazards (Gudmundsson et al., 2008; Biass et al., 2014). Past basaltic eruptions have been studied for volume (e.g. Larsen, 2000, 2010; Thordarsson and Larsen, 2007) and a statistical approach estimating hazard potential has also been used (Biass et al., 2014; Scaini et al., 2014), yet there exists no dataset of eruption source parameters (ESP) for explosive eruptions of this volcanic system (Biass et al., 2014). Therefore this study combines field studies with numerical modelling to obtain values of total grain size distributions, erupted volumes, erupted mass, mass eruption rate and plume height for two large explosive basaltic Katla eruptions.

Explosive eruptions from Katla in 1755 and 1625 both have left large deposits on SE Iceland and are therefore well suited for detailed study. They are also described in contemporary texts, which yield information on weather conditions and eruption (Schmith et al. submitted manuscript, 2017). Both eruptions have reached far outside Iceland and have been reported to leave visible fall deposits in e.g. Bergen (1625, Thorarinsson, 1981), Shetland Islands (1755, Thorarinsson, 1981) and on the Faroe Islands (both erutions, Det Kongelige Danske Videnskabernes Selskab, 1758; Thorarinsson, 1981). In terms of the general Katla tephra record these eruptions fit into the group of large Katla eruptions, but they are not uncharacteristically large compared to other historical eruptions (Larsen, 2010; submitted manuscript, 2017) or compared to the Holocene tephra record (Óladottir et al., 2008). They are therefore an attractive choice for constraining the first Katla eruption source parameters.

Geological background

Katla volcano is situated in the SW of Iceland on the very active Eastern Volcanic Zone (EVZ) (fig 5.1). The area is dominated by 9 large volcanic structures with associated fissure swarms making up active volcanic systems of which the 6 most notorious are Bárðarbunga-Veiðivötn, Grímsvötn, Hekla, Törfajökull, Eyjafjallajökull, and Katla (fig 5.1) (Thordarson and Höskuldsson, 2008). In historical times the EVZ has been responsible for about 87 % of all volcanic activity in Iceland and has covered the SE area of Iceland with tephra at least 57 times as documented in the surrounding soils (Thordarson and Höskuldsson, 2008). The lowland in the area contains several large glacial outwash plains such a Myrdalssandur, Sólheimasandur, Meðallandssandur, and Skeiðarársandur as well as the wide lava fields from the Eldgjá and Lakí eruptions. The highland area is a largely arid rock desert with few lush valleys.

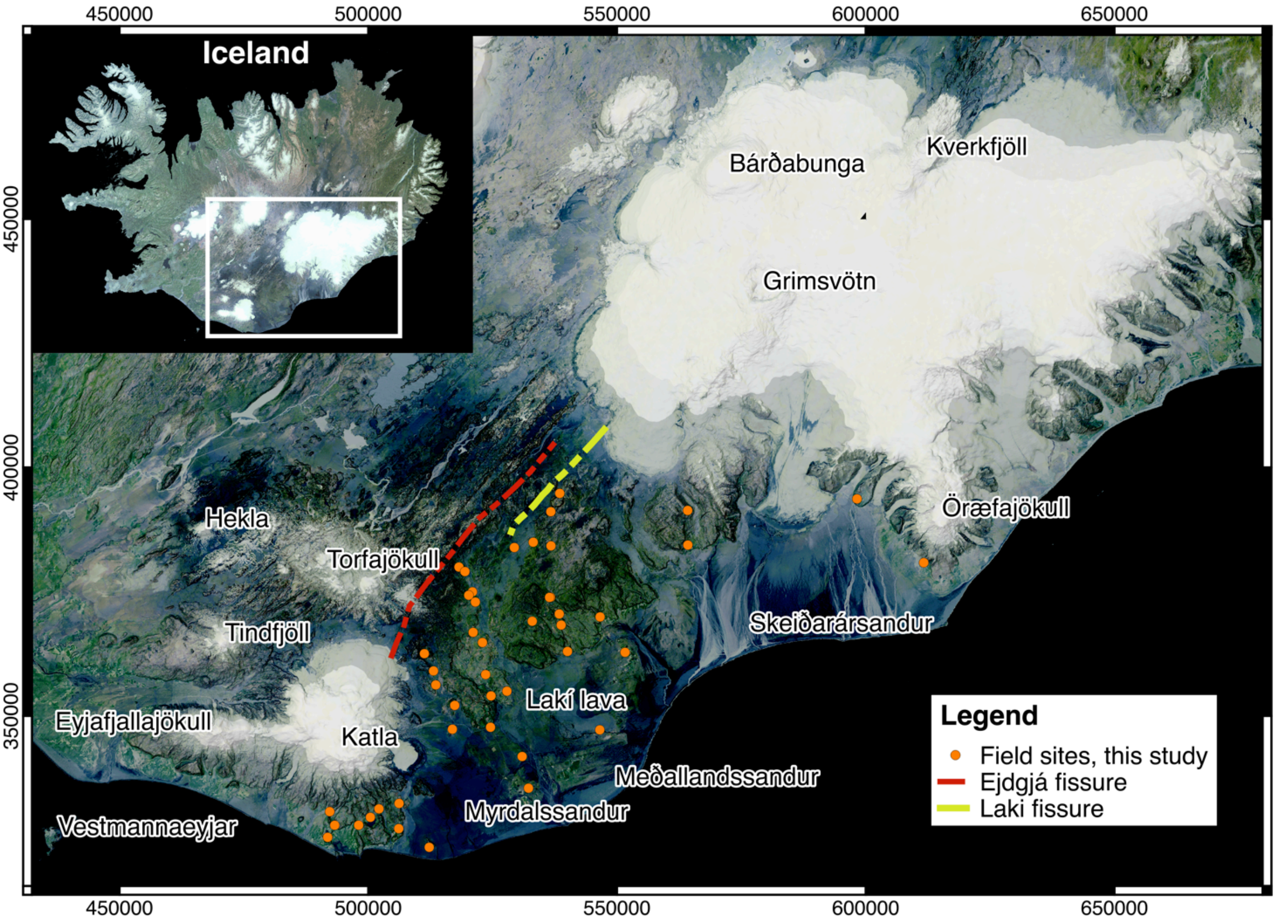

Figure 5.1. Overview map of field area in SE Iceland. Place names represent volcanoes of the Eastern Volcanic Zone, the larger glacial outwash planes (sandurs) and the Laki lava flow in the low-land area. The glacial outwash planes and the Laki lava flow mark soil free areas and thus show the limitations to the soil section distribution.

Katla volcanic system

Katla volcanic system consists of the central volcano of Katla as well as the 75 km SW-NE trending Eldgjá fissure swarm propagating from the Myrdalsjökull ice cap almost reaching the Vatnajökull ice cap (fig 5.1).

Katla volcano is a 30 km wide hyaloclastite massif reaching 1380m a.s.l (Larsen, 2010) with outcrops of rhyolitic nunataks around the summit (Lacasse et al., 1995; Lacasse et al., 2007). The summit caldera is 10 x 14 km and has a depth of 650-750 m (Björnsson et al., 2000). The age of the caldera could date back to the Vedde ash formation ~12.1 ka cal. years BP (Lacasse et al., 1995; Birks et al., 1996; Lacasse & Garbe-Schönberg, 2001) and studies show that all eruptions during the past millennium has been confined to the caldera (Thorarinsson, 1975; Larsen, 2010). The magma chamber beneath Katla is suggested to be at about 3 km's depth with a 10km^3 volume containing basaltic magma (Gudmundsson et al., 1994).

Katla is partly covered by the 600km^2 Myrdalsjökull glacier, which reaches an average thickness of 230 m (Óladottir et al., 2008) giving the volcano a total height of 1450 m a.s.l. (Òladottir et al., 2005). Myrdalsjökull has 3 outlet glaciers onto the lowlands, Sólheimajökull (south), Kötlujökull (east), and Entujökull (northwest) (fig 5.1). They cut through deep breaches in the Katla caldera walls (Björnsson et al., 2000), which also function as pathways for jökulhlaups associated with the volcanism. Melt water and jökulhlaups drain onto the southern and eastern outwash plains (Sólheimasandur (south) and Myrdalssandur (east)) and the northern river of Markarfjót and Björnsson et al. (2000) calculated the water divides as shown in fig 5.1. Since 1179 AD all documented jökulhlaus except one (a minor jökulhlaup below Sólheimajökull in 1860) have gone through the Kötlujökull passage and down to Myrdalssandur carrying meltwater, ice blocks and volcanic material with them (Larsen, 2010). The jökulhlaups are reported to emerge in close temporal relation to the appearance of a visible eruption plume – either shortly before or after (Larsen, 2010). The jökulhlaups discharge in pulses with the first ones usually being most voluminous (Larsen, 2010).

Like other Icelandic volcanoes Katla mainly produces basaltic tephra although the system is bimodal (Larsen, 2000, 2010, Óladottir et al., 2005, 2008). The basalts from Katla are transitional-alkali Fe-Ti basalts and they displayed a very narrow compositional range during the Pleistocene and Holocene (Lacasse et al., 2007) with consistently high TiO_2 content of about 4-5 wt %. Therefore they can be uniquely identified in major element geochemical analysis (Óladottir et al., 2005, 2008, and 2011).

Holocene eruption summary

Deposits from more than 300 explosive basaltic eruptions and 20 silicic eruptions have been found in soil sections from the Holocene period (Oladottir et al., 2005, 2008; Larsen & Eiriksson, 2008; Larsen 2010). Furthermore 8-10 lava eruptions have covered the SW of Iceland with a few km^2 and up to 780 km^2 of basaltic lava fields. This includes the Eldgjá eruption from 934-40 AD and the 7700 years old Holmsá fires (Larsen, 2010).

The settlement of Iceland in 870AD marks the beginning of the historic period in Iceland. In this period Katla has produced 20 tephra layers and 16 has been mentioned in historical documents (Larsen, 2000). Their volume range from 0.02-1.5 km^3 uncompacted volume (Larsen, 2000). Explosive eruptions in the system occur 1-3 times pr. century and the average repose time between eruptions is 48 years (since 1500 AD), but it ranges from 13 to 95 years (Larsen, 2000).

Isopach maps have also been made of several prehistoric basaltic eruptions to estimate volume and magnitude of the eruptions (Thorarinsson, 1975; Larsen, 2010). Volumes of the biggest prehistoric eruptions may exceed 2 km^3 (the K-E and K-N of Róbortsdóttir, 1992).

The 1755 eruption

An earthquake and a jökulhlaup initiated the 1755 eruption on the 17th of October 1755 (Det Kongelige Danske Videnskabernes Selskab, 1758, Schmith et al. submitted manuscript, 2017). Shortly after an eruption column rose from the central volcano lasting for 17 consecutive days and it was reported gone on the 3rd of November (Det Kongelige Danske Videnskabernes Selskab, 1758, Schmith et al. submitted manuscript, 2017). Schmith et al. (submitted manuscript, 2017) showed that the activity was stable from the 17th to the 23rd though deposited in different directions due to changing wind directions. However, two violent explosions took place on the 20th of October according to Det Kongelige Danske Videnskabernes Selskab (1758). Then between the 24th October and the end of the eruption the intensity waxed and waned a little before decreasing steadily (Schmith et al. submitted manuscript, 2017).

The 1755 deposit can be divided into 7 units. The 1755 tephra deposit consists of ash to lapilli sized juvenile grains with 67-75 % brown sideromelane glass, 23-33% opaque tachylite and 0-4% crystals and lithics in the 3-4φ (125-63 µm) ash component (Schmith et al. submitted manuscript, 2017).

The fine fragmentation generating ash during the eruption was related to both magmatic gas exsolution as well as phreatomagmatic processes (Schmith et al. submitted manuscript, 2017) and changed little during the eruption.

Tephra fall across Skaftártunga was reported as 30-90 cm on flat fields, but 125-190 cm on sheltered locations and the tephra thickness across the 300 km long Eastern country all the way to Mjóifjörður in the East Fjords was reported to have been 8 cm even after some wind and water erosion (Det Kongelige Danske Videnskabernes Selskab, 1758). Tephra fall reached ships close to the Faroe Islands on the 3rd day of the eruption (Det Kongelige Danske Videnskabernes Selskab, 1758).

The 1625 eruption

The 1625 eruption started with a loud explosion, a Jökulhlaup and an eruption column at 8 AM on the 2nd of September 1625 (Magnússon, 1627). The eruption column lasted ~11 days until the evening of the 13th of September (Magnússon, 1627; Schmith et al. submitted manuscript, 2017). Contrary to the 1755 eruption dynamics the activity of the 1625 eruption was waxing and waning with 9 different phases throughout the eruption (Schmith et al. submitted manuscript, 2017). The fine ash fragmentation also changed significantly during the eruption from a mixture of magmatic and phreatomagmatic processes to dominantly magmatic processes and ending with mostly phreatomagmatic processes (Schmith et al. submitted manuscript, 2017).

On the 7th-8th day of the eruption additional small vents were opened displaying fountaining activity (Magnússon, 1627; Schmith et al. submitted manuscript, 2017).

The 1625 tephra deposit can be divided into 9 fall unit of ash to lapilli sized juvenile grains with 61-76 % brown sideromelane glass, 21-36% opaque tachylite and 1-4% crystals and lithics in the 3-4φ (125-63 µm) ash component (Schmith et al. submitted manuscript, 2017).

The fine fragmentation generating ash during the eruption was related to both magmatic gas exsolution as well as phreatomagmatic processes and varied significantly over the course of the eruption (Schmith et al. submitted manuscript, 2017).

Also for this eruption the area of Skaftártunga was buried deep in ash, which covered the birch forest and reached depths of ~50 cm (Magnússon, 1627). The ash fall was reported as far N as Langaneset (Magnússon, 1627) and covered the entire S and E country as well as ships in the sea off the Icelandic coast (Magnússon, 1627; Schmith et al. submitted manuscript, 2017). The ash fell on ships in Bergen in Norway 1000 km from Katla covering the deck as snow and ash fall was reported in several villages in Norway (Thorarinsson, 1981).

Field studies of the tephra deposits

Field surveys

We have conducted a series of field surveys from 2012 to 2016 and identified the 1755 and 1625 tephra fall layers in 53 soil sections (outcrops and pits) across the SE area of Iceland (fig 5.1, 5.2, and 5.3). We used previous studies and descriptions of the 1755 and 1625 deposits (e.g. Magnússon, 1627; Det kongelige danske videnskabernes selskab, 1758; Hallgrímsson, 1870; Thorarinsson, 1958; Buckland et al., 1986; Larsen, 2000, 2010) to guide the search for

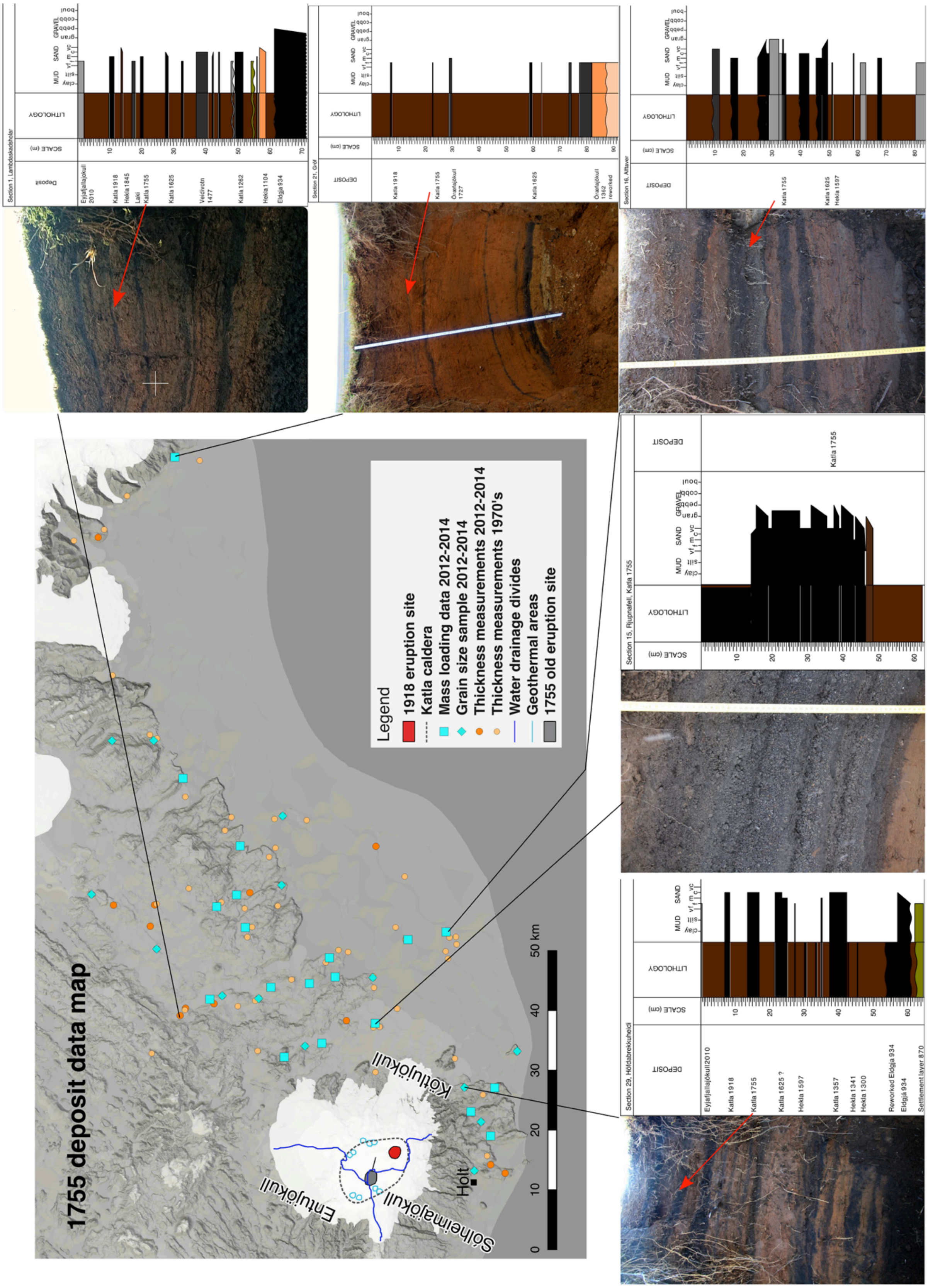

Figure 5.2. Map of data points on the 1755 deposit, where each point represents a logged soil section. Sections with mass loading data were also sampled for grain size and thickness and sections with grain size samples were sampled and measured for thickness. Sections logged for thickness include sections from previous field campaigns in the 1970's. The 1918 eruption site is shown and we have also chosen this as the 1625 vent site. The old placement of the 1755 eruption site by Björnsson et al. (2000) is also shown along with the water drainage divides of the Myrdalur glacier. The old 1755 eruption site lies in the S drainage area, whereas the new 1755 eruption site is situated in the E drainage area correlating with observed jökulhlaups on the Myrdalssandur. Five representative soil sections are presented as well. They show the diversity between medial down-wind (Rjupnafell) and medial off-axis (Höfdubrekkuheidi) sections as well as the differences in the 1755 deposit and stratigraphic markers in various areas.

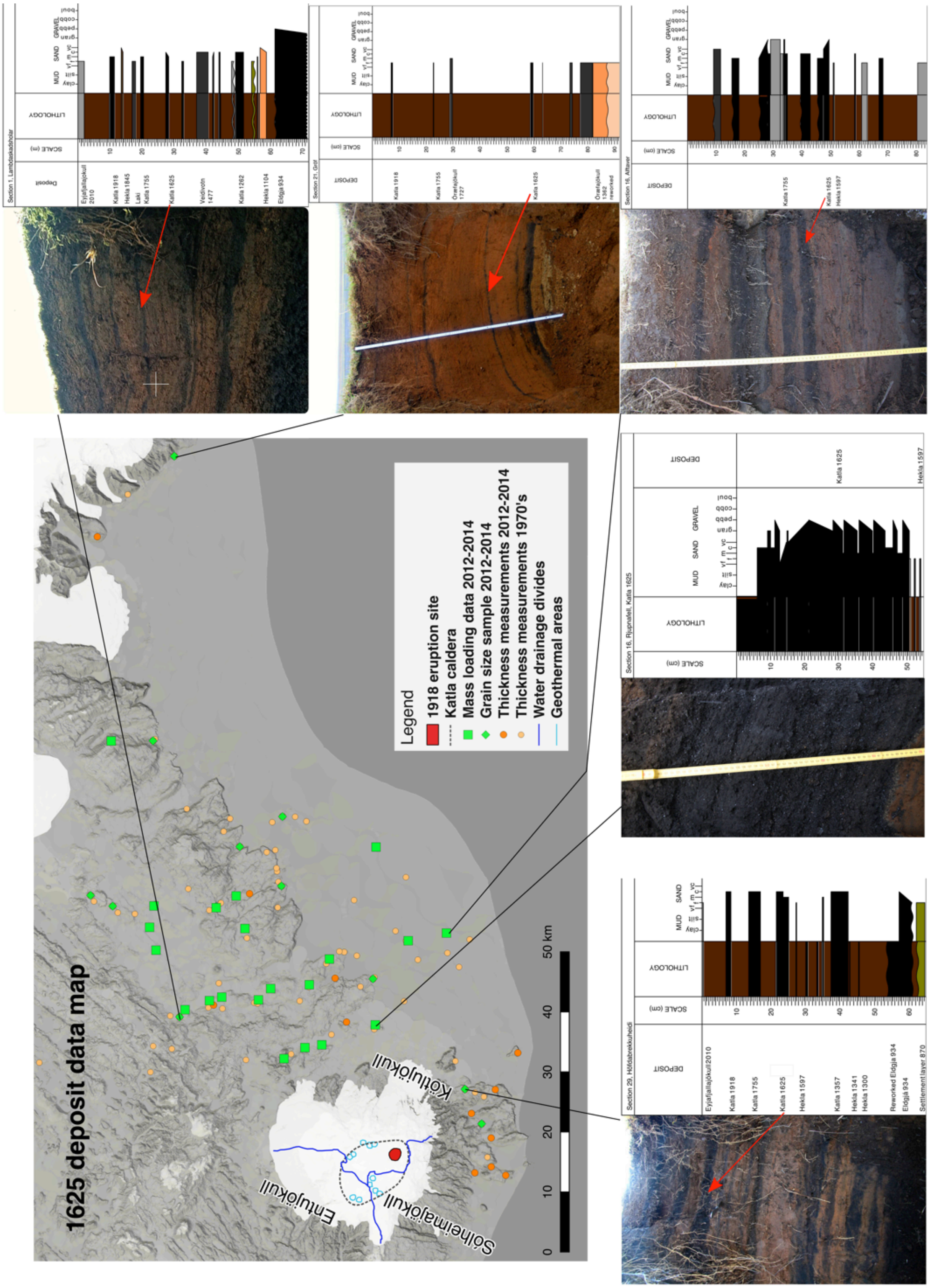

Figure 5.3. Map of data points on the 1625 deposit, where each point represents a logged soil section. Sections with mass loading data were also sampled for grain size and thickness and sections with grain size samples were sampled and measured for thickness. Sections logged for thickness include sections from previous field campaigns in the 1970's.
The 1918 eruption site is shown and we have chosen this as the vent site of the 1625 eruption based on jökulhlaup directions.
Five representative soil sections are presented as well. They show the diversity between medial down-wind (Rjupnafell) and medial off-axis (Höfdubrekkuheidi) sections as well as the differences in the 1625 deposit and stratigraphic markers in various areas.

sections mainly in the E and NE directions from Katla volcano. The aim was to sample the deposits in cross sections as well as along the main dispersal axis. However, lack of available soil on the glaciers, glacial outwash planes and in the lava fields (fig 5.1) limited the distribution of sections to an area between 15 km to 70 km from the caldera with a few distal sections along the direction of dispersal reaching up to 120 km from source (fig 5.1, 2, and 5.3).

1755 and 1625 tephra layer identification

Basaltic tephra deposits from Katla are recognized as coal-black layers of ash to lapilli in the field (fig 5.2 and 5.3) and they are usually distinguishable from other basaltic tephras from the EVZ based on macroscopic characteristics (Óladottir et al., 2005). However, as there are about 300 different basaltic layers from Katla in the SE Icelandic soils, we used distinct stratigraphic marker layers to obtain stratigraphic control of each section. Among the important marker layers are the brown coarse ash deposit from the Hekla 1845 eruption, the bluish-black tephra from Lakí 1783-84 and the fine grey ash layer from the 1597 Hekla eruption. Other historic marker layers include the yellow fine ash layer from the 1362 Öræfajökull eruption, the coarse yellow ash trace from the Hekla 1104 eruption, the fine grey ash layer from Veidivötn 1477 and Hekla 1200 and the fine grey-green Settlement-layer from about 871 (fig 5.2 and 5.3).

In distal areas with more than 100 km distance to the vent the fine ash grain size causes the Katla deposits to change to a more grey-black color, which resembles that of other basaltic tephras from the EVZ. Therefore we have sampled all likely candidates of the 1755 and 1625 Katla deposits for major element geochemical analysis in distal sections with ambiguous stratigraphy.

Sections in the Myrdal area had few stratigraphic markers (fig 5.2 and 5.3, Höfdubrekkuheidi). Instead the rhythm of the layers, their relative distances, and the work by Larsen et al. (2009) on the main axis of historical Katla eruptions aided interpretation of the stratigraphy.

Measurements and sampling

All 53 sections have been measured for layer thicknesses and layers of 1 cm or more were sampled for grain size. In stratified deposits the internal layers were sampled separately as units where possible. Sampling of layers of a few cm was done by cutting out regular pieces with a small knife and carefully scraping out the loose material. The dimensions of the sample were measured for mass loading and bulk density information in sections where the layer thickness and preservation permitted a regular shape of the sample to follow recommendations on types of field data by Bonadonna (2006). Thin layers were sampled by gently scraping out the loose material with a knife. Great care was taken to bag and transport all samples in order to keep the grains as intact as possible.

Soil sections

The 1755 layer was identified in 45 soil sections in the field area, whereas the 1625 layer was identified in 44 sections. Eight of the initial 53 sections were discarded due to lack of stratigraphic control or because the deposits turned out to be contaminated with flooding deposits. The position of the final 45 soil sections is shown in fig 5.2 and 5.3 as well as a sedimentary log and photos of representative sections. The most proximal section downwind was the Rjupnafell section, which has been extensively described in Schmith et al. (submitted manuscript, 2017). This section contains the most detailed deposit, though the medial 1625 deposit sections further N contain a distinct deposit component of white dust, which is absent in the Rjupnafell deposit.

Isopach maps

New model for vent areas

We have made a new model of the vent area based on water divides of the Myrdal glacier (Björnsson et al., 2000), information about directions of jökulhlaups (Larsen, 2000, 2010) and new interpretations of the contemporary vent descriptions (Hallgrímsson, 1870) accounting for direction bias caused by topography (Thordarson, 1991).

1755 vent position

The 1755 vent was observed almost due north of the farm Holt in Myrdalur (fig 5.2), but with no observations of the specific area (Hallgrímsson, 1870). However, Thordarson, 1991 found that people in the 18th century tended to align topographic directions with E-W or N-S directions. The cliffs by Holt have a bearing of N114°E, which is close to the overall bearing trend of N110°E from Eyjafjallajökull to the Holt area (fig 5.2), though this topographic trend is shown as an E-W trend in 16th-18th century maps of Iceland. Thus N would be perceived at about 20°E and the 1755 eruption site should be found at a bearing around 20°E from the farm Holt. Further constraints from the E outlet of all the jökulhlaups of the 1755 eruption, frame the position of the vent in the E drainage area by the water drainage divides modeled by Björnsson et al. (2000) (fig 5.2). There are several active geothermal areas in this region, but the bearing of 20°E from Holt correlates only with the 1918/1823 eruption site and the 1955 geothermal area (fig 5.2) and we consider the 1918/1823 eruption site the best candidate for the 1755 eruption vent. This area has produced several explosive eruptions, while the 1955 geothermal area falls on the caldera rim along with many other geothermal areas not know to have produced explosive eruptions. Thus our 1755 vent area model suggests that recent major explosive eruptions from Katla had the same vent area within the caldera.

Vent position of 1625 eruption

There are no observations relating to the specific position of the 1625 eruption site, but the jökulhlaup directions are the same as for the 1755 and 1918 eruptions. Following the vent model of the 1755 eruption, we have placed the 1625 vent at the site of the 1918 vent (fig 5.3).

Isopach map construction

The isopach maps were constructed based on thicknesses from the soil sections as well as 59 and 52 thickness measurements from previous surveys (Larsen, unpublished data) of 1625 and 1755 deposits, respectively (fig 5.4 and 5.5).

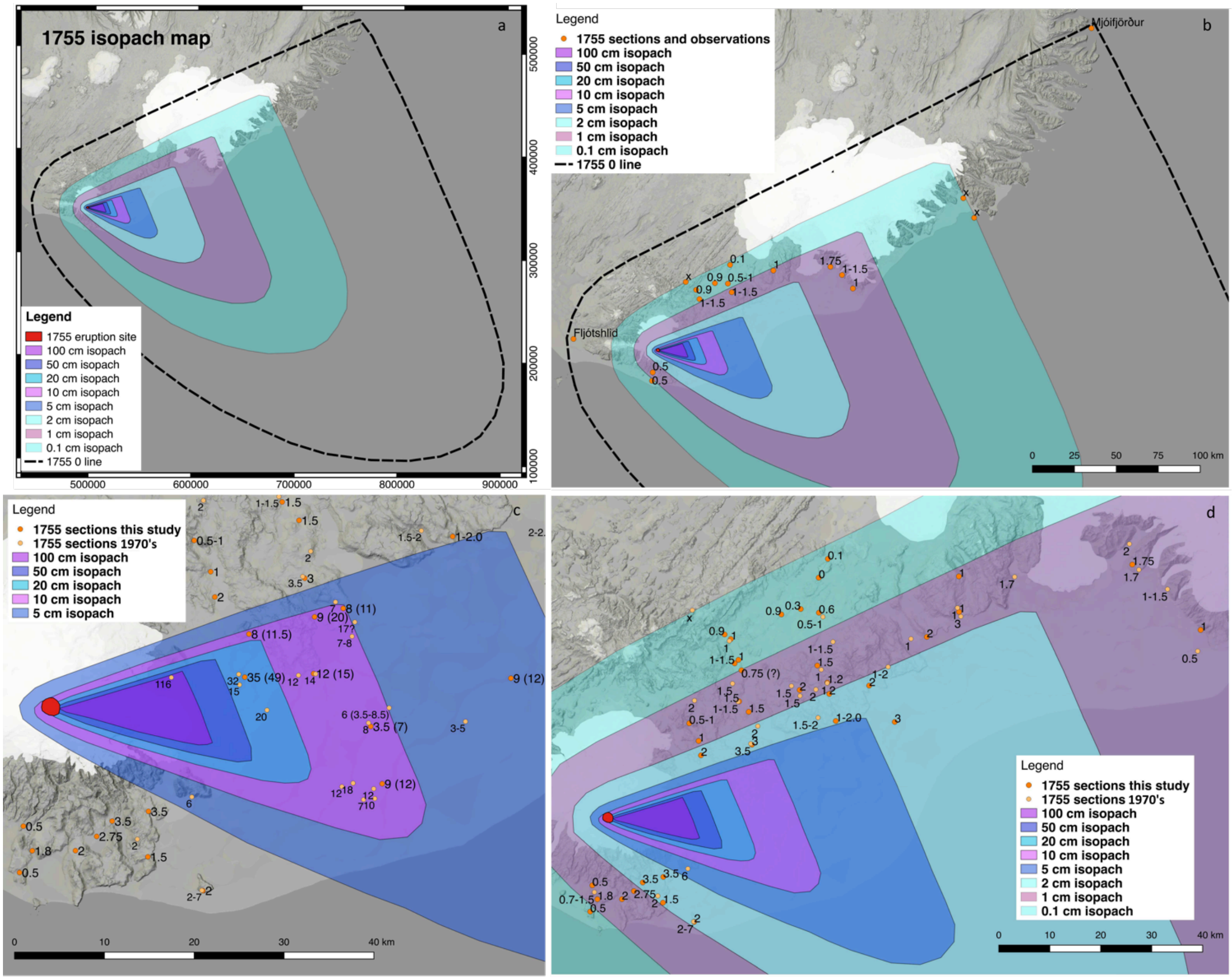

Figure 5.4. Isopach map for the 1755 deposit. 5.4a: The overall isopach map of 1755 deposit, where each point represents a logged soil section. Sections logged for thickness include sections from previous field campaigns in the 1970's.
5.4b-d: Subsections of the isopach map at different scales with deposit thicknesses. An x indicates a trace of the deposit. Indications of Fljótshlid and Mjóifjörður on 5.4b are areas of tephra fall named in the contemporary sources (Det Kongelige Danske Videnskabernes Selskab, 1758).

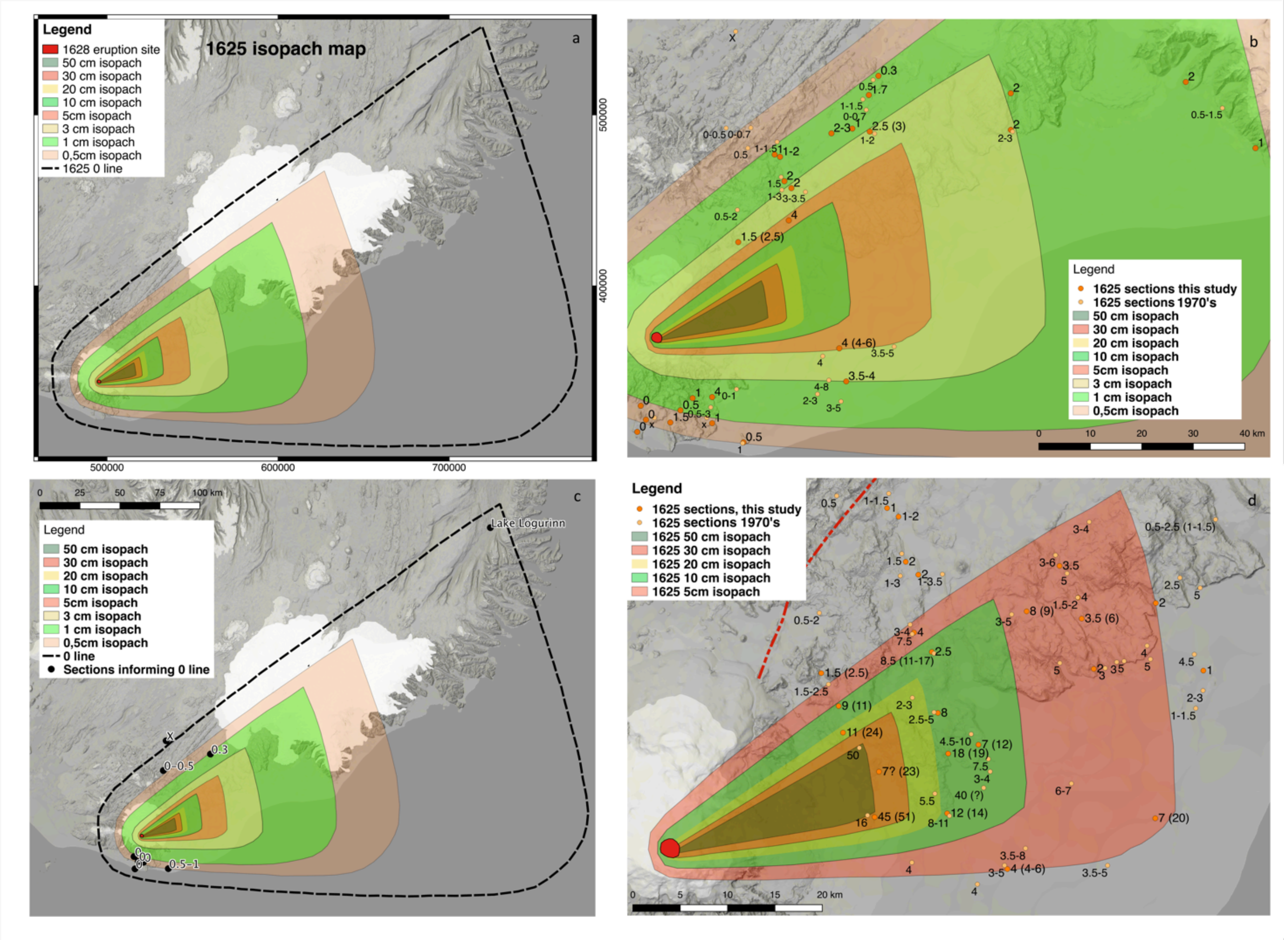

Figure 5.5. Isopach map for the 1625 deposit. 5.5a: The overall isopach map of 1625 deposit, where each point represents a logged soil section. Sections with mass loading data were also sampled for grain size and thickness and sections with grain size samples were sampled and measured for thickness. Sections logged for thickness include sections from previous field campaigns in the 1970's.
5.5b-d: Subsections of the isopach map at different scales with deposit thicknesses. An x indicates a trace of the deposit. Indication of Lake Lögurinn on 5.5b marks the position of a lake core containing deposit of the 1625 eruption (Gudmundsdottir et al., 2016).

We have mapped whole deposits as single layers as individual black units could not be traced between sections. The only units that can be traced independently are the white and mixed lowermost units of the 1625 deposit, but to keep the mapping consistent we have included these units in the total isopach map.

1755 and 1625 isopach maps

The 1755 isopach map (fig 5.4) contains 8 isopachs from 100 cm to 0.1 cm as well as a 0-line and covers around 23400 km^2 on land. There is a main axis of deposition towards ENE and a secondary axis towards ESE.
The 1625 isopach map (fig 5.5) contains 9 isopachs from 50 cm to 0.1 cm and covers around 23600 km^2 on land. There is one main axis of deposition towards ENE.

The land coverage of the 10 cm and 1 cm isopachs for each eruption as well as the maximum distance from vent to isopach are shown in table 5.1.

Comparison with previous estimates from Larsen (2010) shows that the 1755 1 cm isopach has extended significantly (59%) in distance from vent, but not in land area coverage (0.5%). The 1755 10 cm isopach has increased in lateral extent (20% increase), but shows a substantially smaller area-coverage (-30%). For the 1625 1 cm isopach there is only a 5% increase in distance from vent, but a 30% increase in land area coverage. The 1625 10 cm isopach has also increased 5% in lateral extent and only 4% in land area coverage. Thus the most significant changes are related to significantly smaller areas of the medial isopachs for the 1755 deposit, whereas the significant area coverage changes for the 1625 deposit are related to the distal isopachs.

Eruption source parameters (ESP)

Total grain size distribution method (TGSD)

Samples from 34 of the 1755 sections and from 33 of the 1625 sections (fig 5.2 and 5.3, grain size sample points) have been dried at 50°C and carefully hand-sieved for grain size in whole φ step down to 3φ (125μm). At 3φ (125μm) the sample was split and one half was run on a Micrometrics Sedigraph III grain size analyzer in a 50% glycerin solution to measure the fine ash grain size distribution. The other half was hand sieved through the 4φ (63μm) sieve to achieve an overlap between sieve- and Sedigraph data.

Sieve- and Sedigraph data were merged using sieve overlap as scaling to produce grain size distributions from -4φ (16 mm) to 10φ (1μm). For sections with multiple units both unit grain size and whole deposit grain size were calculated.

VORONOI_TOTGS (Bonadonna and Houghton, 2005; Biass and Bonadonna, 2014) was used to model the total grain size distribution of each eruption deposit with the zero-line defined as in the isopach maps (fig 5.4 and 5.5). We only used input from samples with mass loading estimates in this model (fig 5.2 and 5.3, mass loading data points).

Total grain size distribution results

The TGSD model results are shown in fig 5.6 and table 5.1 and shows different distribution for the two deposits. The 1755 distribution has a mean at 2.03φ, a median at 2.27φ reflecting a fine skewed very poorly sorted bimodal deposit (fig 5.6) with more than one third (38 wt%) of the

Parameters	1755	1625	Parameters	1755	1625
TGSD (φ)			**Isopach distance (km)**		
Mφ:	2.03	1.92	d_{10cm}	42	42
Mdφ	2.27	1.86	$d_{Larsen,\ 2010\ 10cm}$	35	40
σφ	2.04	1.94	δd_{10cm}	+20 %	+5 %
Skφ	-0.13	0.02	d_{1cm}	191	137
Kφ	0.83	1.15	$d_{Larsen,\ 2010\ 1cm}$	120	130
% ≥ 3φ	37.4	27.8	δd_{1cm}	+59 %	+5 %
Volume (km³)			**Area of isopachs (km²)**		
$\mathbf{V}_{\mathbf{Powerlaw,}\ total}$	**1.34** (1.20-1.50)	**1.24** (1.12-1.36)	A	**126000**	**46100**
$V_{Powerlaw,\ medial\text{-}distal}$	0.63 (0.56-0.70)	0.42 (0.38-0.46)	A_{land}	**23400**	**23600**
$V_{Exponential,\ 1\ segment}$	1.04	0.52	$A_{Land\ 10cm}$	6027	594
$V_{Exponential,\ 2\ segments}$	0.81 (0.72-0.91)	0.53	$A_{Larsen,\ 2010\ Land\ 10cm}$	6000	570
$V_{Exponential,\ 3\ segments}$	0.86	0.48 (0.43-0.50)	$\delta A_{Land,10cm}$	+0.5 %	+4%
$V_{Weibull}$	0.66 (0.58-0.72)	0.44 (0.38-0.48)	$A_{Land\ 1cm}$	625	7172
$V_{Statistical,\ min}$	0.94±0.004	1.24±0.009	$A_{Larsen,\ 2010\ Land\ 1cm}$	900	5500
$V_{Statistical,\ max}$	0.97±0.003	2.76±0.032	$\delta A_{Land\ 1cm}$	-30 %	+30%
Volume model error			**Plume height (km)**		
$\mathbf{V}_{\mathbf{Powerlaw,\ total}}$	**0.97**	**3.62**	$H_{MER,Powerlaw,\ total}$	**9± 2**	**10± 2**
$V_{Powerlaw,\ medial\text{-}distal}$	0.97	3.62	$H_{MER,Powerlaw,\ medial\text{-}distal}$	8± 2	7± 2
$V_{Exponential,\ 1\ segment}$	0.52	0.18	$H_{MER,\ Exponential,\ 2\ segments}$	8± 2	8± 2
$V_{Exponential,\ 2\ segments}$	0.06	0.11	$H_{MER,Weibull}$	8± 2	7± 2
$V_{Exponential,\ 3\ segments}$	0.103	1.9E-3	$H_{MER,Statistical,\ min}$	8± 2	10± 2
$V_{Weibull}$	0.08	0.08	$H_{MER,Statistical,\ max}$	8± 2	12± 2
Total mass (kg)			**Plume height (km)**		
$\mathbf{M}_{\mathbf{Powerlaw,\ total}}$	$\mathbf{2.13\cdot10^{12}}$ $\mathbf{(1.84\text{-}2.45)\cdot10^{12}}$	$\mathbf{1.73\cdot10^{12}}$ $\mathbf{(1.53\text{-}1.94)\cdot10^{12}}$	$\mathbf{H}_{\mathbf{V,\ Powerlaw,\ total}}$	**25± 6**	**25± 6**
$M_{Powerlaw,\ medial\text{-}distal}$	$1.00\cdot10^{12}$ $(8.66\cdot10^{11}\text{-}1.15\cdot10^{12})$	$5.86\cdot10^{11}$ $(5.17\text{-}6.58)\cdot10^{11}$	$H_{V,\ Powerlaw,\ medial\text{-}distal}$	23± 6	22± 6
$M_{Exponential,\ 2\ segments}$	$1.29\cdot10^{12}$ $(1.1\text{-}1.5)\cdot10^{12}$	$6.70\cdot10^{11}$ $(5.8\text{-}7.2)\cdot10^{11}$	$H_{V,\ Exponential,\ 2\ segments}$	24± 6	22± 6
$M_{Weibull}$	$1.05\cdot10^{12}$ $(8.9\cdot10^{11}\text{-}1.2\cdot10^{12})$	$6.14\cdot10^{11}$ $(5.2\text{-}6.8)\cdot10^{11}$	$H_{V,Weibull}$	23± 6	22± 6
$M_{Stat,min}$:	$1.49\cdot10^{12}$	$1.70\cdot10^{12}$	$H_{V,Statistical,\ min}$	24± 6	25± 6
$M_{Stat,max}$:	$1.54\cdot10^{12}$	$3.85\cdot10^{12}$	$H_{V,Statistical,\ max}$	24± 6	27± 6
MER (kg/s)			**Inversion model**		
$\mathbf{MER}_{\mathbf{Powerlaw,}\ total}$	$\mathbf{1.45\cdot10^{6}}$ $\mathbf{(1.25\text{-}1.67)\cdot10^{6}}$	$\mathbf{1.82\cdot10^{6}}$ $\mathbf{(1.61\text{-}2.04)\cdot10^{6}}$	Fit	16.77	22.60
$MER_{Powerlaw,\ medial\text{-}distal}$	$6.82\cdot10^{5}$ $(5.89\text{-}7.85)\cdot10^{5}$	$6.17\cdot10^{5}$ $(5.44\text{-}6.92)\cdot10^{5}$	$Md\varphi_{inversion}$	1.60	1.50
$MER_{Exponential,\ 2\ segments}$	$8.77\cdot10^{5}$ $(7.5\cdot10^{5}\text{-}1.0\cdot10^{6})$	$7.05\cdot10^{5}$ $(6.1\text{-}7.6)\cdot10^{5}$	$M_{inversion}$ (kg)	$9.92\cdot10^{12}$	$4.52\cdot10^{11}$
$MER_{Weibull}$	$7.15\cdot10^{5}$ $(6.1\text{-}8.3)\cdot10^{5}$	$6.46\cdot10^{5}$ $(5.5\text{-}7.2)\cdot10^{5}$	$MER_{inversion}$ (kg/s)	$6.75\cdot10^{6}$	$4.76\cdot10^{5}$
$MER_{Statistical,\ min}$	$1.02\cdot10^{6}$	$1.79\cdot10^{6}$	$H_{inversion}$ (km)	**14.4**	**16.6**
$MER_{Statistical,\ max}$	$1.05\cdot10^{6}$	$4.05\cdot10^{6}$			
Density (kg/m³)			**Volume DRE (km³)**		
$\boldsymbol{\rho}_{\mathbf{ash}}$	**2756**±97	**2789**±151			
$\boldsymbol{\rho}_{\mathbf{field}}$	**870**±250	**860**±158	$V_{DRE,\ powerlaw,\ total}$	0.79	0.64
$\boldsymbol{\rho}_{\mathbf{bulk}}$	**1590**±210	**1396**±156			

Table 5.1 (left): Overview of characteristic eruption- and deposit parameters for the 1755 and 1625 tephra deposits. Parameters used: d is the maximum distance of the isopach from vent. A is the area of the isopach. Subscripts of 10cm and 1cm refers to the 10cm and 1 cm isopach lines, respectively. Subscript Land refers to land coverage and subscripts Larsen, 2010 refers to values in Larsen (2010). δd and δA show the change in percent from Larsen (2010)-values to values of the present study.
TGSD gives total grain size distribution parameters, where Mφ is mean φ, Mdφ is median φ, σφ is the standard deviation (sorting), Skφ is distribution skewness, Kφ is kurtosis, and % ≥ 3φ gives the percentage of the distribution of ash of 3φ or smaller.
For density ρ_{ash} is the density of 3-4φ ash, ρ_{field} is average measured bulk field density and ρ_{bulk} is bulk density of the deposit as calculated by equation 5.2 in the text. Volume estimates from all volume models are reported as calculated in the AshCalc module (Daggit et al., 2014) with 99 % confidence interval in brackets estimated by TError (Biass et al., 2014). V is volume, M is total mass, and MER is mass eruption rate. Model error is the mean relative squared error for the model fit of all isopach based volume models. Error for the statistical model is the standard deviation for the solution distribution.
The dense rock equivalent (DRE) volume was calculated only for the power-law using a DRE density of 2700 kg/m^3.
Plume height (H) is calculated by empirical relations defined by Mastin et al., 2009, where subscripts beginning with MER refer to equation 5.3 in the text and subscripts with V refer to equation 5.4 in the text. The Mastin et al. (2009)-estimates are given with a 50 % confidence interval.
Inversion model refers to the method outlined in Connor and Connor (2006) and presents median φ ($Md\varphi_{inversion}$), mass ($M_{inversion}$), mass eruption rate ($MER_{inversion}$), and plume height ($H_{inversion}$). The model fit is the chi-squared fit.

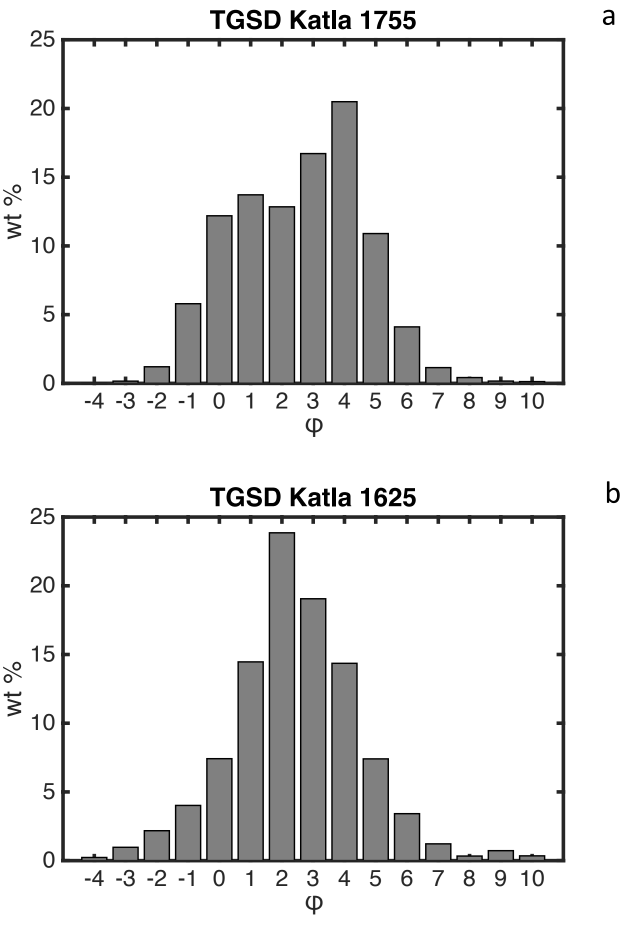

Figure 5.6. Total grain size distribution (TGSD) for the 1755 deposit (a) and the 1625 deposit (b). Grain sizes are binned in whole φ steps in both distributions and span -4 to 10 φ for both deposits.

Discussion of the TGSD models

The similar mean of the TGSD of the two deposits supports the finding by Schmith et al. (submitted manuscript, 2017) that both eruptions had a similar degassing history, while the difference in distributions and content of fines supports differences in surface water/magma interaction modifying the grain size distribution as also indicated by Schmith et al. (in submitted manuscript, 2017). The symmetric 1625 TGSD supports an eruption dominated by eruption plume processes with relatively stable wind and dry weather conditions and low influence of ash aggregation. The high fines content of the 1755 deposit shows the higher degree of fragmentation from water/magma interaction and also wet weather conditions leading to washout of fines from the plume as found by Schmith et al. (submitted manuscript, 2017). Thus fewer fines would reach very distal regions from the 1755 plume and this could explain why the 1625 ash fall was observed further from the source than the slightly bigger 1755 eruption.

Volume (V)

Methods to determine volume

Volume has been calculated from exponential segment models, power law models and weibull models of thickness vs. isopach area fits using AshCalc (Daggit et al., 2014). The statistical approach suggested by Burden et al. (2013) has also been used for both deposits.

The Weibull model was applied to both eruptions and a single minimum on the Kappa vs. Lambda error-surface was found in both cases. The exponential models were applied to both eruptions and resulted in 1-3 segments. The power law fitting was integrated to find a total volume between 0.2 km and 1300 km from the vent for the 1625 eruption and between 0.2 km and 1000 km from the vent for the 1755 eruption. The proximal limit of both eruptions was based on proximal limits suggested by Bonadonna & Houghton (2005) based on the proximal exponential thinning, as we do not have any observations of the proximal thicknesses. The distal limit was based on observed ash fall in Bergen in 1625 (1317 km from Katla) and in the Shetland Islands in 1755 (992 km from Katla) (Thorarinsson, 1981).

The statistical model of Burden et al. (2013) was also applied, but as the thickness showed high variability in several field sites, we ran a minimum and maximum scenario using respectively the minimum thicknesses and maximum thicknesses measured for each site.

Errors on all isopach-based volumes were reported as the 99% confidence intervals of each volume model and were estimated using the TError package (Biass et al., 2014). It is beyond the scope of this study to assess our own isopach thickness and area uncertainty, and therefore we adopted uncertainty estimates following results of Klawonn et al. (2014).

Errors of the statistical volume model were calculated as the standard deviation of the volume distribution.

We subsequently explored the significant difference between the volume results of the exponential and Weibull models compared to the power-law and statistical models. A partial power-law volume was constructed using the same model parameters as for the total volume power-law model. However, we equated the proximal integration limit to the nearest medial data point, to investigate whether the volume difference was related to the lack of proximal thickness data. As the power law model assumes a symmetric circular distribution, the same area circle radius of the nearest isopach served as the nearest medial data point. For the 1755 deposit the partial volume proximal limit was moved to 4.5 km from vent and for the 1625 deposit the partial volume proximal limit was 5 km.

Volume results of the 1755 deposit

The results from the 4 different strategies for calculating the total erupted tephra volume are shown in table 5.1 and figure 5.7. All results are presented with the 99 % confidence interval as determined by the TError-package in parenthesis. Of the isopach-based volume calculation strategies the Weibull model yields the lowest volume of 0.66 (0.58-0.72) km^3, while the power-law yields the highest value of 1.34 (1.20-1.50) km^3. The exponential model shows intermediate values ranging from 0.81 (0.72-0.91) km^3 to 1.04 km^3, with the best fit at the two-segment model of 0.81 km^3 volume. The strategy of Burden et al. (2013) shows little variation between the minimum and maximum thickness scenarios and results in model volumes of 0.94±0.004 km^3 and 0.97±0.003 km^3, respectively. The power law model restricted to the medial-distal data coverage estimates a medial-distal volume of 0.63 (0.56-0.70) km^3.

Discussion of 1755 volume results

The Weibull model volume and the medial-distal power law volumes are in the same range suggesting that the Weibull model does not take the proximal deposition effectively into account without any proximal deposition data. This is supported by findings that the Weibull model underestimates the volume by ~50-60%, when proximal data input are missing (Bonadonna and Costa, 2012). This also fits well with the observation that the total volume estimate by the power law model doubles the Weibull model volume. The exponential strategy accounts for the whole deposit, but underestimates the proximal deposit contribution as the 1st segment decay is based on the more moderate medial decay value. Thus the best-fit model of two segments yields the lowest volume estimate. Model sensitivity evaluations show that the exponential model tends to underestimate the total volume with about 60%, when based only on medial and distal data (Bonadonna and Houghton, 2005). The strategy of Burden et al. (2013) suggests a total volume close to 1 km^3 and is less sensitive to the lack of proximal data points, but may still underestimate to total volume as the thickness measurement distribution is skewed due to the lack of soil sections in many areas and because it does not extrapolate to distal areas. The power-law model shows a reasonable fit and thus we infer this model to be the best representation of the min. volume of the 1755 deposit. This is in line with sensitivity estimates showing that power law model based on medial and distal data only underestimated the total volume by ~25% (Bonadonna and Houghton, 2005). Furthermore Bonadonna et al. (2015)

found that the power law was more appropriate for deposits with exponent m >2 (m=2.164 and m=2.292 for the 1755 and 1625 fits, respectively) and well-constrained distal deposits. Previous volume estimates were based on freshly fallen tephra thickness estimates and range from 1.5 km^3 total uncompacted volume (Thorarinsson, 1975) to 0.8 km^3 uncompacted volume on land (Larsen, 2010). The volume is reduced by at least 38% from the freshly fallen deposit to the compacted tephra layers found in soil sections (Thorarinsson, 1958). Thus the current volume estimates would range from 1.02 to 2.12 km^3 uncompacted tephra with the estimate by Thorarinsson (1975) well within this range.

Volume results of the 1625 deposit

The results from the 4 different strategies for the calculation of the total tephra volume are shown in table 5.1 and figure 5.8. The Weibull model yields the lowest volume of 0.44 (0.38-0.48) km^3 and then the exponential model shows intermediate values ranging from 0.48 (0.43-0.50) km^3 to 0.53 km^3 with the best fit at the three-segment model of 0.48 km^3 volume. The total distribution power-law again shows the highest isopach based volume of 1.24 (1.12-1.36) km^3. The strategy of Burden et al. (2013) shows significant variation between the minimum and maximum thickness scenarios and model volumes are 1.24±0.009 km^3 and 2.76±0.032 km^3, respectively. The power law model restricted to the medial-distal area yields a partial volume of 0.42 (0.38-0.46) km^3.

Discussion of 1625 volume results

The volume results of the 1625 deposit show the same patterns as the 1755 volume results, though with an even larger value range. The power law model restricted to the medial-distal data coverage models a medial-distal volume of 0.42 km^3 consistent with the observation from the 1755 deposit that the Weibull and exponential fits do not account for the proximal volume contribution without any proximal data. Again the total power-law volume correlates with the minimum statistical volume estimate and thus it is again considered the best total volume estimate. The lack of a thickness measurement at the most proximal location of Sandfell is probably the cause of the much larger discrepancy between what is effectively medial-distal volume estimates and the total deposit estimates. For the statistical model the measured thicknesses vary by 50-100% in several places causing a high maximum scenario estimate. Previous estimates of the 1625 volume were 0.5 km^3 of uncompacted tephra on land by Larsen (2010) and therefore a direct comparison yields no new information. However, the previous volume estimate is contained within all of the current volume estimates with the lowest being recalculated to 0.71 km^3 uncompacted tephra. Thus the present estimates do not contradict the previous one.

1755 volume models

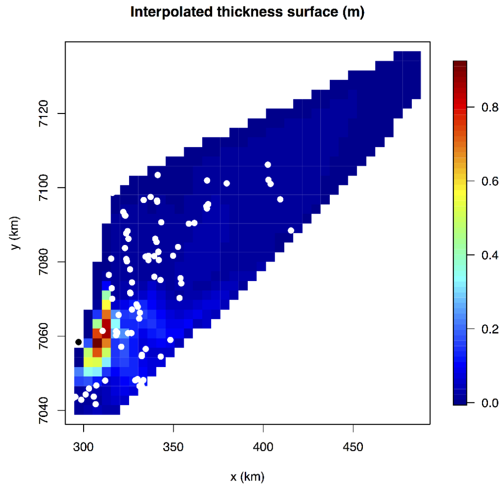

Burden statistical interpolation max

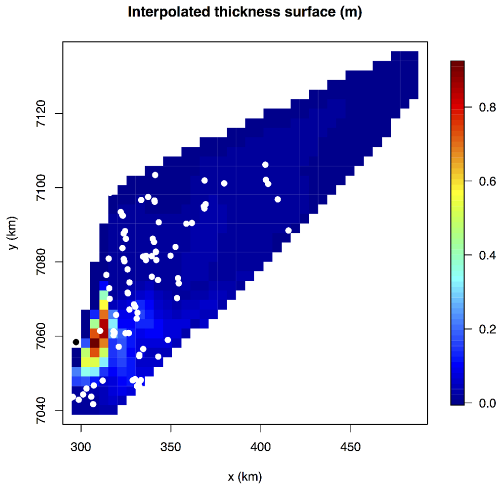

Burden statistical interpolation min

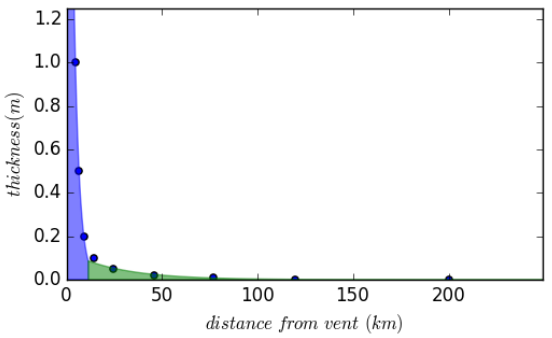

Exponential fit, 2 segments

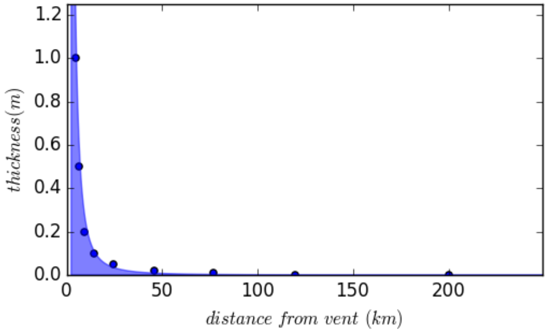

Power law fit, medial + distal

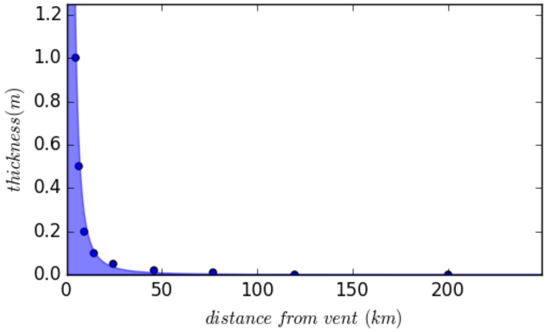

Power law fit, total

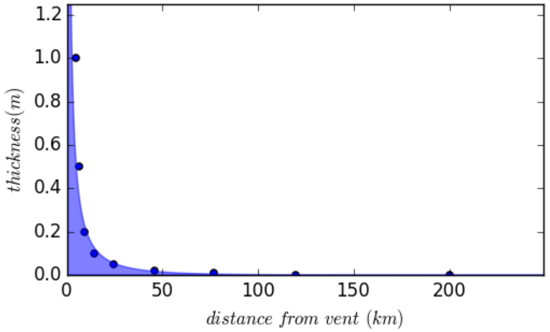

Weibull fit

Figure 5.7. Volume models for the 1755 eruption. All plots show modeled thickness with distance from vent, but the Burden interpolation plots show the interpolated thickness in 2D, whereas the exponential. powerlaw and Weibull fits show 1D correlations.

1625 volume models

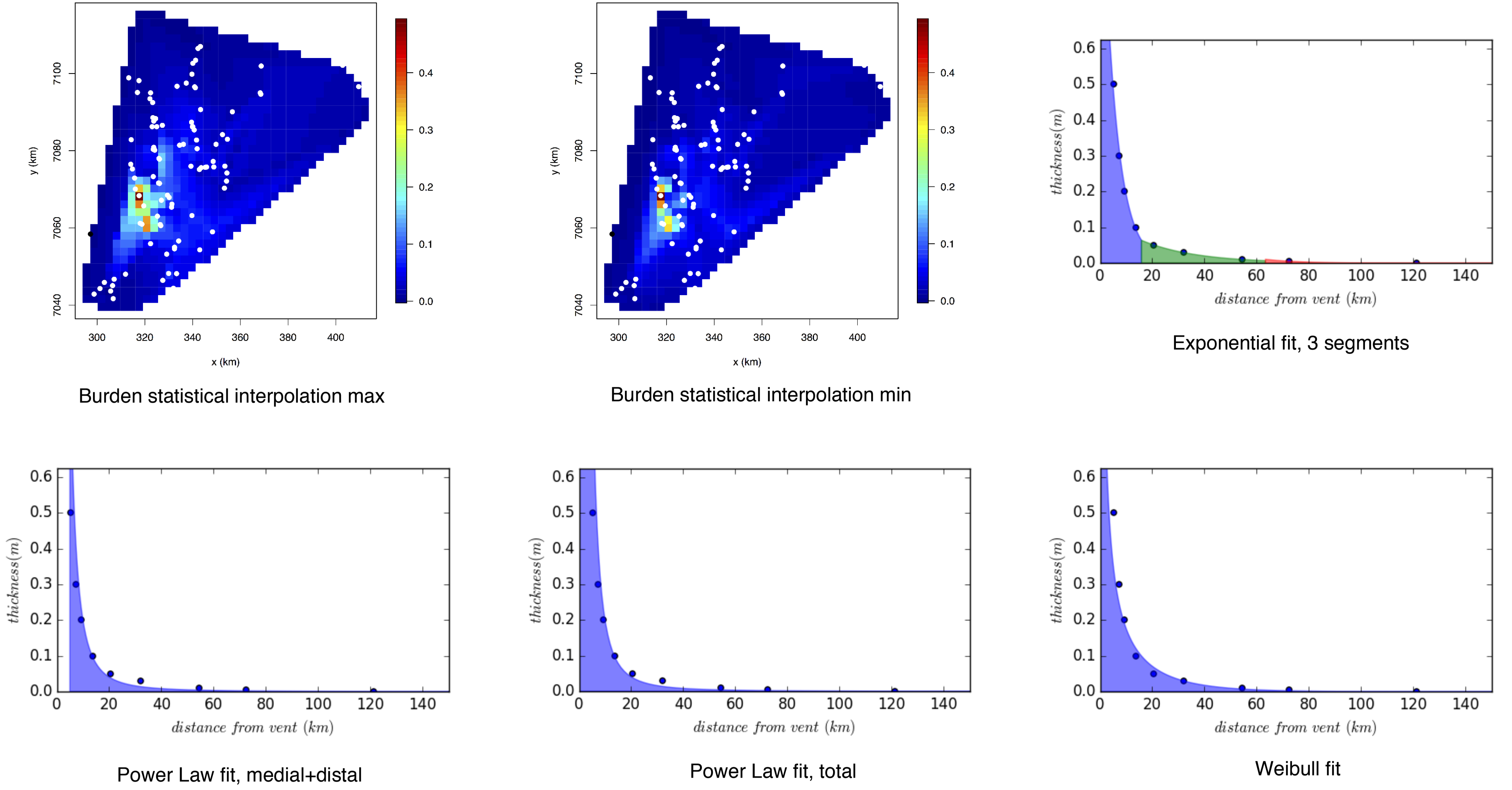

Burden statistical interpolation max

Burden statistical interpolation min

Exponential fit, 3 segments

Power Law fit, medial+distal

Power Law fit, total

Weibull fit

Figure 5.8. Volume models for the 1625 eruption. All plots show modeled thickness with distance from vent, but the Burden interpolation plots show the interpolated thickness in 2D, whereas the exponential. powerlaw and Weibull fits show 1D correlations.

Total mass (M), mass eruption rate (MER) and plume height (H)

Methods

Total erupted mass

There are no previous estimates of the total mass of the 1755 and 1625 Katla eruptions and no observations of the plume heights. Therefore we have used two different approaches based on independent datasets to constrain the total erupted mass and plume height.

The first approach was based on conversion of the isopach-based volume to mass and then using empirical relations between volume and plume height as well as volume flow rate and plume height from Mastin et al. (2009) to estimate the plume height. In addition, we also used the Tephra2 inversion strategy proposed by Connor and Connor (2006) to derive the erupted mass and plume height based on a mass loading dataset.

We converted volume to mass by equation 5.1, where ρ is the bulk density modeled for each whole eruption deposit as shown in equation 5.2:

$$M = \rho \cdot V, \qquad \text{Eq 5.1}$$

$$\rho = dm_{<3\varphi} \cdot \rho_{field} + dm_{\geq 3\varphi} \cdot \rho_{ash}, \qquad \text{Eq 5.2}$$

where M is the total mass, V is the total volume (here as calculated by the power law model), dm is the mass fraction of the specified grain size interval according to the TGSD-model, ρ_{ash} is the ash density of the 3-4φ (125-63μm) ash grain size measured with a pycnometer, and ρ_{field} is the field bulk density average for 20 samples in the area ~15-65 km from the vent (fig 5.2 and 5.3). For the field density estimates the sample volume was measured in situ in the field and the bulk density of each sample was calculated from equation 5.1 using the dry sample weight. The field-based medial bulk density is assumed to be an average of the density of clasts larger than 3φ (125μm). We have used this density model to account for the density variation from coarse to fine grains (e.g. White et al., 2017), but this density model does not account for varying degrees of compaction and variable amounts of fine ash between sections. However, sections are scattered across most of the medial deposit and is considered a better estimate than an average reference table value.

MER

To turn the total mass into an average mass eruption rate, we have used the timespan of eruption column, which was 17 consecutive days for the 1755 eruption, whereas the 1625 column lasted 11 days (Schmith et al. submitted manuscript, 2017).

Plume height

We estimated the volume-based plume height from the empirical relationship between volumetric flow rate $\dot{V}$ of dense rock equivalent (DRE) and plume height H (equation 5.3) and between total DRE volume (V_{DRE}) and plume height (equation 5.4) as found by Mastin et al. (2009). We converted MER to $\dot{V}$ and M to V_{DRE} using a DRE density of 2700 kg/m^3.

$$H = 2.00 \cdot \dot{V}^{0.241} \qquad \text{Eq 5.3}$$

$$H = 25.9 + 6.64 \cdot Log_{10}(V_{DRE}) \qquad \text{Eq 5.4}$$

Inversion approach

The inversion was run on 20 mass/area values for the 1755 deposit and 21 for the 1625 deposit distributed primarily between 15-65 km from source (fig 5.2 and 5.3). Input parameters are shown in table 5.1. Grain size parameters are closely constrained by the TGSD model and diffusion ranges follow Connor and Connor (2006). Densities are as calculated from field bulk density of medial deposits for juvenile clasts and as pycnometer ash density used for the lithic density, as there are only very small amounts of lithics. Plume height is constrained by the volume-based plume height estimates, which will be discussed in the next section. The total mass ranges were calculated using lowest bulk density and volume estimate for the lower bound and highest volume estimate and ash density for maximum boundary.

Results of total mass and MER from volume

The ρ_{ash} was determined as 2756±97 kg/m^3 for the 1755 ash and 2789±151 kg/m^3 for the 1625 ash. Arithmetic average of the field densities resulted in a field bulk density of 870±254 kg/m^3 for the 1755 deposit and 860±158 kg/m^3 for the 1625 deposit. The uncertainty of the field bulk density is the standard deviation for the measurements and thus relate to measurement and sample size uncertainty, but not uncertainty due to difference in compaction. The deposit bulk density of the whole deposit then becomes 1590±210 kg/m^3 for the 1755 deposit and 1395±156 kg/m^3 for the 1625 deposit.

The total mass is calculated as $2.13 \cdot 10^{12}$ $(1.84\text{-}2.45) \cdot 10^{12}$ kg for the 1755 eruption and as $1.73 \cdot 10^{12}$ $(1.53\text{-}1.94) \cdot 10^{12}$ kg for the 1625 eruption (table 5.1), when using the power-law integration as the best volume estimate. In terms of average MER the 1755 has a slightly lower value of $1.45 \cdot 10^{6}$ $(1.25\text{-}1.67) \cdot 10^{6}$ kg/s compared to the $1.82 \cdot 10^{6}$ $(1.61\text{-}2.04) \cdot 10^{6}$ kg/s of the 1625 eruption.

Discussion of erupted mass and MER results

Both eruptions are comparable both in volume and erupted mass suggesting that the estimate of the 1755 eruption being the largest eruption of historical times (Thorarinsson, 1975) is not correct.

The higher average MER of the 1625 eruption fits well with the interpretation of lower water/magma ratio evident from field observations and shape analysis of Schmith et al. (submitted manuscript, 2017). This suggests that the melt water could not get access to as much of the column for part of the eruption.

The traditional length of the 1755 eruption according to the literature is ~120 days, but this interval is based on including jökulhlaup events in mid January 1756, which are not relevant for the tephra modeling. Such a significant change in eruption duration has profound impact on the estimated mass eruption rate (MER) and thus on the estimated intensity of the eruption.

Results of plume height estimates from MER and volume

The plume height estimates are listed in table 5.1 and show that the volume based plume height estimate yields the higher values of 25.22 km for the 1755 eruption and 24.62 km for the 1625 eruption. The MER based estimates yields much lower values of 9.10 km and 9.61 km for the 1755 and 1625 eruptions respectively. Errors corresponding to the 50% confidence interval on the fits are about ± 6km for the volume fits (fig 2 of Mastin et al., 2009) and ± 2km for the MER fits (fig 1 of Mastin et al., 2009).

Discussion of plume height estimates from MER and volume

Previous estimates of moderate to large explosive Katla eruptions suggest that plume heights between 10-25 km would be reasonable (Biass et al., 2014), but with no direct relation to the 1755 and 1625 eruptions. Although both plume height estimates are based on rough empirical best-fit relations (Mastin et al., 2009), they outline the same range as the previous estimates. However, they do not overlap within the 50% confidence interval. This might be related to the MER being a minimum average estimate for the entire eruption and thus the derived plume height is a lower bound average. The volume-based plume height model is primarily based on Plinian eruptions and is thus suitable to estimate peak eruption plume height.

Results of plume height and total mass by inversion

The results of the inversion models are reposted in table 5.2. The plume height of the 1755 eruption was modeled as 14.4 km with a chi-squared fit of 16.8. The associated total mass was modeled to be $9.92 \cdot 10^{12}$ kg and grain size parameter estimates a median grain size of 1.60φ with a standard deviation of 1.43φ.

The plume height of the 1625 eruption was modeled to reach 16.6 km with a chi-squared fit of 22.6. The associated total mass was modeled to be $4.52 \cdot 10^{11}$ kg. The modeled median grain size was reported as 1.50φ with a 1.85σ.

Discussion of inversion results

TGSD

The grain size distribution of the inversion compares well with the TGSD of the two deposits. The median values are shifted towards coarser grain sizes, which are to be expected, as the inversion models cannot take fine ash aggregation into account (Mastin et al., 2016). Therefore the inversion standard deviations are also smaller reflecting the smaller grain size interval of the total grain size distribution. However, when comparing the inversion median grain size between the two deposits the 1755 median is still shifted towards finer values than the 1625 median as seen in the deposit TGSD. When comparing the sorting values of the inversions, they do not reflect the TGSD of the deposits. This may also be related to the fine ash cut-off of the inversion model.

Total erupted mass

The total mass values of the inversions are both within a factor 5 of the volume-derived total mass estimate for both deposits, although not within the TError confidence interval. The 1755 inversion has overestimated the total erupted mass, while the 1625 inversion underestimates the total erupted mass compared to volume based values. This discrepancy might also be explained by differences in fine ash aggregation between the two eruptions. In the 1755 eruption much of the ash settled prematurely by aggregation processes (Schmith et al. submitted manuscript, 2017). This was not the case in the 1625 eruption. Thus average mass loading values of the 1755 eruption in the medial area are increased by aggregation, which is not accounted for in the inversion.

Plume height

The plume heights of the inversions fall within the minimum and maximum estimates made by using the Mastin et al. (2009) conversion of MER and V to plume height. This is consistent with recent findings of Bonadonna et al. (2015) that inversion of mass/area results in an average value for the plume height of the whole duration of the eruption. The inversion plume heights are also within previous assumptions about Katla plume heights (Biass et al., 2014).

The 1755 plume height is about 2 km lower than the 1625 plume height. This fits well with the volume based estimates of higher MER of the 1625 eruption compared to the 1755 eruption. It also fits with previous studies finding a higher water/magma-ratio involved in the fragmentation process of the 1755 eruption compared to the 1625 eruption. Thus the inversion model results successfully described the main features of the two eruption deposits.

The issues of using an inversion model are related to the limited description of the complex column deposition processes in the most proximal areas, medial and distal aggregation processes, and the assumption of a single wind profile (Bonadonna and Costa, 2012). The single wind profile is particularly of concern in long-lasting eruptions, where wind conditions are prone to significant changes. Schmith et al. (submitted manuscript, 2017) estimated substantial changes in wind conditions especially during the 1755 eruption, which are not reflected in the wind sampling of the inversion. However, in cases where isopleth data is difficult to collect and other parameters can be constrained by other means, it provides a useful alternative to Plinian plume derived empirical parameterizations of plume height.

Classification of the eruptions

The most accurate way to characterize explosive eruptions is probably by reporting ESPs (Bonadonna et al., 2016). However, traditional nomenclature supports a process-based characterization of eruption, though there is not yet a fully satisfactory classification model that can be used to adequately compare all explosive eruptions (Bonadonna et al., 2016). Walker, 1973 used the Fragmentation index (F) defined as the percentage of ash finer than 1mm at the point of the dispersal axis corresponding to 1/10 of the max thickness of the deposit to classify eruptions. However, ash aggregation strongly affects the fragmentation index (F) (Bonadonna and Costa, 2013; Bonadonna et al., 2016). Thus this classification method is deemed unsuitable, as we have not been able to account quantitatively for the amount of aggregation in these two deposits.

The volcanic explosivity index (VEI) (Newhall and Self, 1982) is widely used and based on our total volume estimate the 1755 and 1625 eruption would both be classified as VEI 5 eruptions. However, this index does not take the much longer duration of these eruptions into account and therefore a characterization combined with the inversion plume height might be more suitable. The inversion plume height of 14.4 km for the 1755 eruption and 16.6 km for the 1625 eruption would place both eruptions in the VEI 4 category and thus these eruptions are either way characterized as large eruptions.

The description of basaltic volcanism by Valentine and Gregg (2008) does not include eruption styles beyond Strombolian and cannot be used for a more detailed classification.

A simplified new classification based on the MER and H empirical relationship as described by Mastin et al. (2009) was recently introduced (fig 5.9) (Bonadonna and Costa, 2013). Using the MER-derived plume height both eruptions are classified as moderate/small (fig 5.9), but as previously discussed, the calculated average MER is too low to provide a meaningful plume height for the eruptions. The volume-derived plume height parameter classifies the 1755and 1625 eruptions as Plinian (fig 5.9), whereas both eruptions are classified as subplinian eruptions based on the inversion parameters (fig 5.9).

From this discussion it is evident that the 1755 and 1625 eruptions represent a class of large eruptions that has yet to be properly included in future classification models.

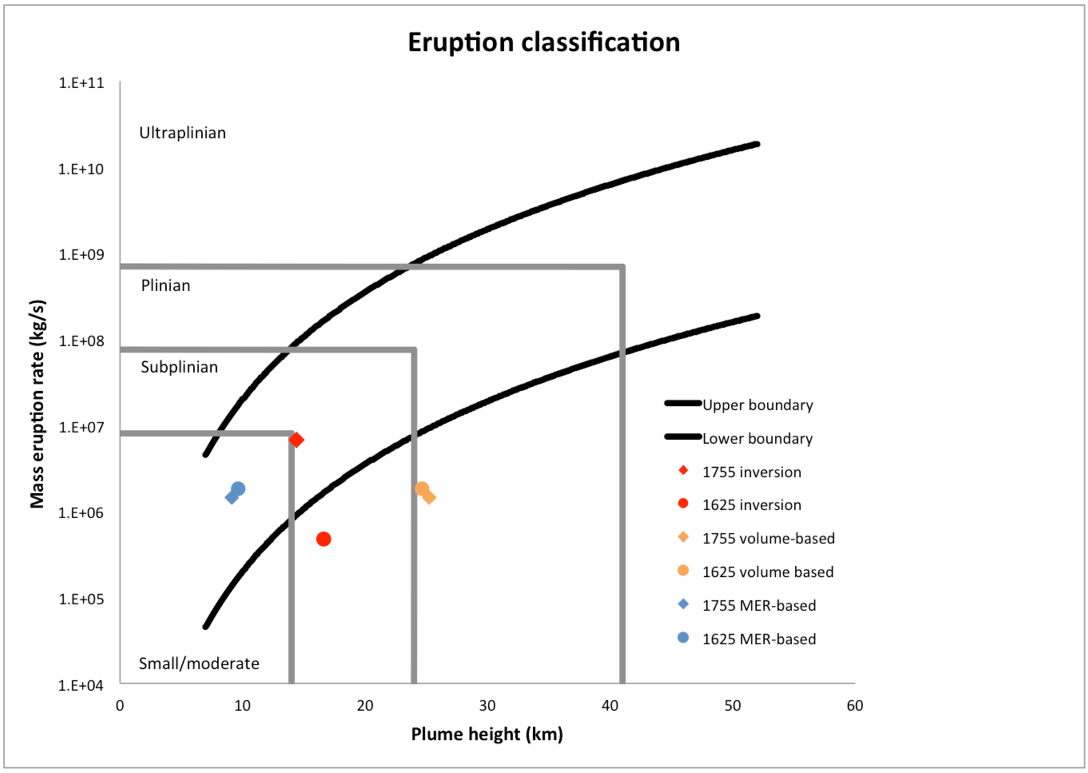

Figure 5.9. Eruption classification diagram based on mass eruption rate (MER) and plume height (H) from Bonnadonna and Costa (2013) of both the 1755 and 1625 eruptions. Classifications for each plume height model for each eruption are shown. Plume height models based on mass eruption rate classifies both eruptions as small to moderate although the 1755 eruption is bordering subplinian. The plume height model based on mass loading inversion classifies both eruptions as subplinian with the 1755 eruption bordering the moderate to small field. The highest plume heights are obtained in the volume-based plume height model, which classifies the 1755 eruption as Plinian and the 1625 eruption as Plinian bordering subplinian.

Discussion

The characterization of eruption in terms of quantifiable parameters is important for evaluating future eruption scenarios and for informing hazard- and risk assessments. These two large basaltic Katla eruptions within a timeframe of about a century show the hazard potential of this volcanic system. Both eruptions are larger in terms of volume and erupted mass than previously estimates for any explosive Katla eruptions (Larsen, 2010; Biass et al., 2014; Scaini et al., 2014).

The ESPs are consistent the recent findings by Schmith et al. (submitted manuscript, 2017) related to the eruption dynamics of the two eruptions. The 1755 eruption was characterized by phreatomagmatic activity with stable amounts of accessible water at the vent, but very unstable and wet weather (Schmith et al. submitted manuscript, 2017). This is consistent with the bimodal TGSD of the 1755 deposit. The 1625 eruption started out with phreatomagmatic activity like the 1755 eruption, but the amount of water decreased progressively during the peak of the eruption, although it came back to dominate the late stages of the eruption (Schmith et al. submitted manuscript, 2017). During this eruption the weather remained stable and mostly dry. The lower magma-water interaction as well as the stable dry weather could explain the single mode of the 1625 TGSD. The lower bulk density of the 1625 deposit compared to the 1755 deposit is also in line with a more vesiculated 1625 tephra due to less magma-water interaction during the peak of the eruption.

The stronger influence of melt water on the 1755 fragmentation compared to the 1625 eruption could also explain the slightly lower average plume height as estimated from the direct inversion of deposit data. This is explained as plume height is related to heat-based buoyancy (e.g. Sparks, 1986) and heat transfer studies for subglacial eruptions show that ash-size particles loose 70-80 % of their heat to boiling water in magma-melt-water interaction (Woodcock et al., 2012). The higher magma-water interaction of the 1755 eruption would thus on average produce a colder and hence lower plume.

To evaluate the ESPs qualitatively we compare the 1755 and 1625 Katla eruptions to the recent 2011 Grímsvötn eruption. The subglacial setting is very similar and the phreatomagmatic fragmentation is comparable particularly to the 1755 eruption (Schmith et al., 2017). The 2011 Grímsvötn eruption lasted for 7 days and produced 0.27 km^3 DRE based on fall out integration (Hreinsdottir et al., 2014). This compares to a 17-day duration and 0.79 km^3 DRE of the 1755 eruption and 11-day duration and 0.64 km^3 DRE production of the 1625 eruption. Thus the Katla eruptions had a 1.2 times (1755) and 1.5 times (1625) higher average tephra production rate than Grímsvötn eruption. This suggests that plume heights of the 1755 and 1625 eruptions should be comparable and higher than observed for Grímsvötn 2011. Most of the tephra from Grímsvötn was extruded during the first 24 h with a peak MER of ~8□10^6 kg/s correlating with plume heights of 15-20 km, which decreased to 5-10 km for the remainder of the eruption (Hreinsdottir et al., 2014). The dynamics of the Grímsvötn 2011 eruption supports the inference that the inversion plume heights of the Katla eruptions are averages of the whole eruption and that most of the tephra was emplaced from a much higher plume at the initial peak of the eruption. Thus plume heights of the volume-based model of about 25 km seem reasonable for the bulk of the tephra emplacement.

Field data show that the Katla volcanic system has produced more than 300 explosive basaltic eruptions during the Holocene (e.g. Óladottir et al., 2008). Field indications of deposit thicknesses suggest that the 1755 and 1625 deposits are among the larger eruptions, but certainly not abnormally large. It is therefore reasonable to think that large basaltic explosive eruptions from Katla are to be expected in the future. However, further investigations of deposit sizes would be required to estimate the frequency and recurrence interval of such large events.

Conclusion

The 1755 and 1625 Katla eruption deposits result from two large subplinian historical eruptions. Both eruptions are very similar in size and our new isopach maps and isopach derived volume estimates show that 1.20-1.50 km^3 of tephra was deposited from the 1755 eruption, while 1.12-1.35 km^3 was deposited from the 1625 eruption. These are larger than previous estimates.

The 1755 deposit covered 23400 km^2 on land and was observed settling as far as 1000 km from vent. The 1625 deposit covered 23600 km^2 on land and settled as far as 1300 km from Katla. We determined the total erupted mass of the 1755 eruption as 1.84-2.45$\cdot10^{12}$ kg with a mass eruption rate of 1.25-1.67$\cdot10^{6}$ kg/s. The 1625 eruption total mass was 1.53-1.94$\cdot10^{12}$ kg tephra with a mass eruption rate of 1.61-2.04$\cdot10^{6}$ kg/s. Plume height estimates for the 1755 eruption range from 9± 2 km to 25± 6 km with an inversion plume height at 14.4, whereas the 1625 eruption plume height falls between 10± 2 km and 25± 6 km with an inversion plume height of 16.6 km.

Comparison with the recent Grímsvötn 2011 eruption plume dynamics suggest that average plume heights for the whole eruption is given by the inversion plume height, and that most tephra was emplaced from a peak plume height at 25 km.

We conclude that the lower average plume height of the 1755 eruption by comparison to the 1625 average plume height is partly related to differences in fragmentation mechanism between the two eruptions and partly due to the longer duration of the 1755 eruption.

We recommend that this new information on large Katla eruptions should be included in future assessments of Icelandic tephra hazards.

Chapter 6

Concluding remarks

The demand for quantitative constraints on volcanological phenomena is rising along with growing computational capacities of modern society. Conclusions that previously relied on subjective expert evaluation are now being informed by statistical inputs and large quantities of raw data. This trend applies to classification schemes and process modeling as well as forecasts and real-time monitoring (Bonadonna et al., 2016). A good example of this transformation is the field of tephra grain morphology. The original morphology classification scheme and tephra catalog was based on visible inspection of qualitative grain features (Heiken, 1972, 1974), whereas current shape analysis is defined by quantitative shape parameters and statistical analysis (e.g. Dellino and LaVolpe, 1996; Büttner et al., 1999; Maria and Carey, 2002, 2007; Riley et al., 2003; Alfano et al., 2011; Murtagh and White, 2013; Jordan et al., 2014; Bagheri et al., 2015; Leibrandt and LePennec, 2015; Liu et al., 2015a, b; Miwa et al., 2015; Schmith et al., 2017; White et al., 2017). In the field of fragmentation assessment one of the main challenges was to produce a meaningful classification system for the eruption deposits. The initial binary classification between magmatic and phreatomagmatic fragmentation (Heiken, 1972) has been adapted to shape analysis (Büttner et al., 2002 and Murtagh and White, 2013). However, recent understanding of interactions between fragmentation mechanisms show fragmentation is much more dynamic (e.g. Graettinger et al., 2013, Jordan et al., 2014) and thus a more dynamic classification model is needed. The RI-classification provides a fragmentation spectrum to accommodate this need for a flexible fragmentation classification. The method was developed for basaltic tephras from different eruptive settings in Iceland. However, recent studies of silicic tephras from Antartica, Alaska and New Zealand used a similar approach of PCA analysis showing results of a fragmentation spectrum in line with the RI-method (Avery et al., 2017). This supports the universal applicability of the RI-method to other eruptive settings, geological regions, and chemical compositions. However, the interpretive setup of Avery et al. (2017) relies on SEM-imaging and separate image analysis software, which increases the time and effort used on data processing considerably. Other automated grain shape methods have focused on single grain morphology classification (e.g. Liu et al., 2015b) or average bulk morphology classification (Leibrandt and LePennec, 2015). These studies have proved successful in providing high quality morphology data, but have not presented a quantitative method for comparing different morphologies in terms of fragmentation interpretation (Schmith et al., 2017). Thus the new RI-classification is currently the only flexible fragmentation model based on shape parameters.

Previous quantitative fragmentation models primarily relied on grain size modeling. However, the application of both the RI morphology classification and the grain size model of Wohletz et al. (1989, 1995) show that grain size is modified by many other processes such as ash aggregation and thus doesn't provide reliable results in relation to fragmentation. The modifications of grain size distributions are currently a topic of intense study (e.g. Alfano et al., 2016; Costa et al., 2016a; Mastin et al., 2016; Pardini et al., 2016; Mueller et al., 2017) and recent findings show that the ash aggregation process mainly produces a narrow size range of aggregates (Mastin et al., 2016). Thus parameterization and possible correction procedures might be available in the future.
However, even without grain size constraints, the RI method shows that the large Katla eruptions are a result of mixed fragmentation. A vesiculation study of deep submarine, shallow submarine, phreatomagmatic (on land), and dry magmatic eruptions showed that shallow submarine and phreatomagmatic land eruptions more closely mimic bubble distribution characteristics of more evolved and more explosive eruptions (Jutzeler et al., 2016). This suggests that the most explosive basaltic magma-water interaction happen at low confining pressures as in the Katla setting. The findings

The need for quantification also applies to eruption size and dispersal as seen by the demand for better ESPs and size classification (Bonadonna et al., 2015; Bonadonna et al., 2016). The ESP modeling of the 1755 and 1625 eruption was necessitated by the urgent need for quantitative hazard assessment of Katla (Biass et al., 2014, Budd et al., 2016), but it points to several unresolved issues with the ESP modeling process. Firstly, the optimal characterization of past eruptions is by direct mass/area measurements to avoid density complications when obtaining a range of total erupted mass (Bonadonna et al., 2015). However, for medial-distal deposits it is a challenge to obtain enough and widely distributed mass/area measurements for isomass maps as shown by this work. Furthermore total mass estimates based on isomass maps do not resolve the issues of underestimating proximal and distal contributions as well as the subjectivity of drawing isomass lines. These issues are currently intensely studied for volume estimates (Burden et al., 2013; Engwell et al., 2013; Daggit et al., 2014; Klawonn et al., 2014; Engwell et al., 2015; Green et al., 2016; Yang and Bursik, 2016), but they also apply to total mass estimates based on isomass maps (e.g. Bonadonna et al., 2015).

Secondly, the number and distribution of thickness measurement made the construction of isopach maps possible. However, with the issues of volume determination in mind this work has followed recent recommendations of Bonadonna et al. (2015) to combine several approached. The most obvious combination is the 3 well-established area vs. thickness fitting techniques assuming either exponential, power law or Weibull thinning (Pyle, 1989; Fierstein and Nathenson, 1992; Bonadonna and Houghton, 2005; Bonadonna and Costa, 2012). All 3 are based on the dataset of the isopach map and thus directly comparable. Also the new modeling interfaces and algorithms of Ash-calc (Daggit et al., 2014) and TError (Biass et al., 2014) will surely make this standard procedure for isopach based mass- and/or volume estimates. Furthermore the combination of the 3 fitting estimates and the new statistical volume integration (Burden et al., 2013) shows that multiple methods contribute to better interpretation of the results of each model. In the case of this Katla modeling the underestimation of particularly the proximal volume became evident from model comparison. The interpretation of volume model results was also aided by the use of two comparable deposits. The thickness distributions varied slightly between the deposits, but the general distribution of sample points was similar. Thus the systematic underestimate of the proximal volume was highlighted.

Thirdly, this Katla study also shows that as older ESP estimates are likely to be volume estimates, this parameter continues to be important for inter-study comparison. Another interesting aspect is that Icelandic tephra volumes are traditionally reported as uncompacted volumes on land after Thorarinsson (1958, 1967) (Larsen, 2010; Óladottir et al., 2014). The sentiment was that farmers and civil authorities had to deal with volumes and thicknesses of freshly fallen tephra. Thus the current focus on modeling mass loading estimates for hazard and risk analysis (e.g. Biass et al., 2014, Scaini et al., 2014) might overlook an important aspect of the mitigation process.

Fourthly, this work on Katla deposits demonstrates some of the issues related to inversion approaches for generating ESPs. Although inversion of grain size data works well for average plume height estimates (Volentik et al., 2010), the inversion of mass/area data is sensitive to the lack of data points and is likely underestimate the total mass if the dataset is too small (Bonadonna et al., 2015) as supported by the inversion of Katla data. The inversion is also very sensitive to the choice of ash dispersal model (White et al., 2017). The Connor and Connor (2006) method applied to the Katla deposits is integrated with the Tephra2 dispersal model, and thus best suited for strong plumes with vertical mass release (Connor and Connor, 2006; Klawonn et al., 2012). This is probably a good model for the initial paroxysmal phase of the two Katla eruptions, but might not apply to later stages of the eruptions. The weak plume can be dealt with using the Klawonn et al. (2012)-method, but it requires observations of the actual position of the plume to provide the model with ash release points and cannot be applied to the Katla eruptions. However, this issue might be resolved by a new flexible inversion approach using a model-independent inversion interface (White et al., 2017). Furthermore this approach also provides much needed uncertainty estimates on the output parameters (White et al., 2017) and is thus in line with other ESP approaches (Biass et al., 2014, Bonadonna et al., 2015).

Future perspectives

First and foremost this work shows that we are only beginning to understand the nature of explosive phreatomagmatic basaltic eruptions in Iceland and thus the hazard they represent. The new RI-methods shows great potential to reveal much more detail about eruption dynamics in many more eruptive environments. The recent focus on standardized quantitative tephra morphology analysis (e.g. Jordan et al., 2014; Leibrandt and LePennec, 2015; Liu et al., 2015a, b) is a testimony to the demand for such a method. Detailed studies of many more eruption deposits could contribute to a more nuanced classification of phreatomagmatic eruptions. Furthermore the RI-method was developed to cope with fragmentation classification within short timeframes and with minimal manual effort. It can therefore also play a vital role in real-time eruption monitoring of future explosive eruptions.

In relation to tephra dispersal studies and hazard assessments, previous assumptions of low dispersal potential of phreatomagmatic eruptions (e.g. Thordarson and Höskuldson, 2008) are shown by the 2011 Grímsvötn eruption and findings in this work to be too simplistic. Thus a future effort to make a detailed mapping of phreatomagmatic fragmentation processes of subglacial eruptions would be vital to evaluate the hazard potential of future Icelandic phreatomagmatic eruptions.

With regard to tephra dispersal models there is a need for a reliable real-time method to determine grain morphology for terminal velocity estimates (e.g. Coini et al., 2014; Bonnadonna et al., 2015). Alfano et al. (2011) showed that 2D morphological characterization of sphericity could be used for calculating terminal fall velocity of ash grains and the PIdsa could provide such morphology data on a routinely basis. Thus future work directed at integrating the shape parameters of the automated image analysis software with terminal velocity models would be highly valuable.

The RI fragmentation model applies to ash-sized tephra grains and the PIdsa limits the grain size. This grain size is optimal for fragmentation studies of phreatomagmatic and mixed fragmentation eruptions, but a combination of the RI method with classical vesicularity studies of larger clasts (e.g. Shea et al., 2010) could provide new insights about particularly magmatic ash generation.

The findings of complex fragmentation mechanisms of the large Katla eruptions (Schmith et al. submitted manuscript, 2017) coupled with recent observations of paroxysmal plume heights around 15-20 km in the subglacial 2011-Grímsvötn eruption (Hreinsdottir et al., 2014) it would be important to obtain a more complete cryptotephra record for Northern Europe that focuses on extraction of basaltic cryptotephras. Currently very few basaltic cryptotephras have been recovered (Watson et al., 2017), but this work, recent ash plume observations (Kerminen et al., 2011), and historical records (Thorarinsson et al., 1981) provide clear indications that more basaltic tephras are to be found and included in future hazard assessments.

Another important aspect revolves around the determination of eruption source parameters derived from deposits. There are three main considerations.

Firstly, this work presents the first set of eruption source parameters for Katla, which is an important contribution as it will now be possible to do quantitative hazard and risk assessments for Katla. Furthermore the studied eruptions provide a good starting point for hazard assessments as they represent characteristically large eruptions from this volcano. However, with such a diverse eruption record much more work is needed to adequately account for different eruption types and scenarios. Therefore future

Secondly, field campaigns are costly, time consuming, weather and season dependent, and they rely on knowledge and understanding of the field area. The subsequent processing of field data in laboratories is also a costly and time-consuming process. Current practice is to collect individual datasets for each study as different types of studies requires different field observations and measurements. However, this is an ineffective use of time and funding and the tephra community is increasingly aware of this. Thus collective efforts at workshops in e.g. Portland, 2014 and Portland 2017 (planned) are aiming at creating common collection standards and databases (Kuehn et al., 2014). At the same time the dispersal and hazard modeling community also aims at creating standards for field measurements as to best support the subsequent parameter modeling (e.g. Biass and Bonadonna, 2011; Bonadonna et al., 2012). This work supports future data sharing by contributing data to the ICAO project and by attending the tephra community workshop.

Thirdly, the determination of eruption source parameters relies increasingly on integrated methods combining field data with rigorous computer modeling. As shown in this work it is essential that field data be collected to best support the subsequent modeling by e.g. making mass loading measurements. Furthermore it is important that model interpretations are in line with constraints and limitations of the field data (Biass and Bonadonna, 2011, Biass et al., 2014). Thus multidisciplinary research groups would provide the best future research environment for integrated tephra studies.

Main conclusion

This work has contributed to the continued progression of tephra science by providing a new quantitative method for shape analysis and fragmentation classification. The method assigns a Regularity Index (RI) to the deposit and data shows that Surtseyan ash has an RI of 0.207-0.191 ± 0.002 (2σ) and Hawaiian ash has an RI of 0.134 ± 0.001 (2σ) and these samples currently represent the extremes of the fragmentation spectrum. Subglacial and lacustrine samples show intermediate RIs of 0.168-0.175 ± 0.002 (2σ) and of 0.187 ± 0.002 (2σ).
This new method has been successfully applied to the 1755 and 1625 Katla eruption deposits and has demonstrated its usefulness as well as the complex dynamics of subglacial explosive basaltic eruptions.
The 1755 Katla deposit shows a RI range of 0.162-0.179 ± 0.002 (2σ), whereas the 1625 deposit shows a RI range of 0.144-0.198 ± 0.002 (2σ). Thus the fragmentation in the 1755 eruption is characterized by a relatively steady magma/water-interaction in contrast to the dynamic changes in water/magma-interaction during the 1625 eruption. The fragmentation difference between the two eruptions cannot be recognized by visual investigation or grain size modeling of the deposits. This discrepancy can be explained by other factors acting on the deposition during the eruptions such as weather conditions.

The two large Katla eruptions from 1755 and 1625 have also been quantified in terms of erupted volume, mass, MER, TGSD and plume height parameters given as intervals to account for the inherent uncertainty pertaining to preservation conditions, field observations, and various modeling approaches.
Volumes are 1.20-1.50 km^3 for the 1755 eruption and 1.12-1.36 km^3 for the 1625 eruption. The total erupted mass of the 1755 eruption is 1.84-2.45·10^{12} kg with a minimum MER of 1.25-1.67·10^6 kg/s. In 1625 Katla erupted 1.53-1.94·10^{12} kg tephra with a minimum MER of 1.61-2.04·10^6 kg/s. The average 1755 plume height was 14.4 km with paroxysmal peaks at 25± 6 km. The average 1625 plume height was 16.6 km with paroxysmal peaks at 25± 6 km.
These are the first eruption source parameters for Katla volcano and thus provide a significant contribution for future hazard and risk assessments of Icelandic volcanism and Katla in particular.
The lower average plume height of the 1755 eruption reflects the higher influence of magma/water-interaction on this eruption compared to the 1625 eruption.

The collective effort of this work shows that studies of eruption dynamics as well as determination of eruption source parameters are needed to fully characterize explosive eruptions.

References

Alfano F, Bonadonna C, Delmelle P, Costantini L (2011) Insights on tephra settling velocity from morphological observations. Journal of Volcanology and Geothermal Research 208(3-4):86-98

Alfano F, Bonadonna C, Watt S, Connor C, Volentik A, Pyle DM (2016) Reconstruction of total grain size distribution of the climactic phase of a long-lasting eruption: the example of the 2008-2013 Chaiten eruption. Bulletin of Volcanology 78(7)

Avery MR, Panter KS, Gorsevski PV (2017) Distinguishing styles of explosive eruptions at Erebus, Redoubt and Taupo volcanoes using multivariate analysis of ash morphometrics. Journal of Volcanology and Geothermal Research 332:1-13

Bagheri GH, Bonadonna C, Manzella I, Vonlanthen P (2015) On the characterization of size and shape of irregular particles. Powder Technology 270:141-153

Biass S, Bonadonna C (2011) A quantitative uncertainty assessment of eruptive parameters derived from tephra deposits: the example of two large eruptions of Cotopaxi volcano, Ecuador. Bulletin of Volcanology 73(1):73-90

Biass S, Bonadonna, C. (2014) TOTGS: Total grainsize distribution of tephra fallout.

Biass S, Scaini C, Bonadonna C, Folch A, Smith K, Hoskuldsson A (2014) A multi-scale risk assessment for tephra fallout and airborne concentration from multiple Icelandic volcanoes - Part 1: Hazard assessment. Natural Hazards and Earth System Sciences 14(8):2265-2287

Biass S, Bagheri, GH, Gholamhossein; Aeberhard, William H, Bonadonna, C (2014) TError: towards a better quantification of the uncertainty propagated during the characterization of tephra deposits. Statistics in Volcanology 1:1-27

Birks HH, Gulliksen S, Haflidason H, Mangerud J, Possnert G (1996) New radiocarbon dates for the Vedde ash and the Saksunarvatn ash from western Norway. Quaternary Research 45(2):119-127

Björnsson H, Pálsson F, Guðmundsson MT (2000) Surface and bedrock topography of the Mýrdalsjökull ice cap. Jokull 49:29-46

Blott SJ, Pye K (2001) GRADISTAT: A grain size distribution and statistics package for the analysis of unconsolidated sediments. Earth Surface Processes and Landforms 26(11):1237-1248

Bonadonna C (2006) Probabilistic modelling of tephra dispersion. In: Mader HM, Coles, S. G., Connor, C. B. & Connor, L. J. (ed) Statistics in volcanology. IAVCEI, Geological Society, London, pp 243-259

Bonadonna C, Scollo, S., Cioni, R., Pioli, L., Pistolesi, M. (2011) Determination of the largest clast of tephra deposits for the characterization of explosive volcanic eruptions: Report of the IAVCEI Commission on Tephra Hazard Modelling. In: IAVCEI, p 48

Bonadonna C, Biass S, Costa A (2015) Physical characterization of explosive volcanic eruptions based on tephra deposits: Propagation of uncertainties and sensitivity analysis. Journal of Volcanology and Geothermal Research 296:80-100

Bonadonna C, Cioni R, Costa A, Druitt T, Phillips J, Pioli L, Andronico D, Harris A, Scollo S, Bachmann O, Bagheri G, Biass S, Brogi F, Cashman K, Dominguez L, Dürig T, Galland O, Giordano G, Gudmundsson M, Hort M, Höskuldsson A, Houghton B, Komorowski JC, Küppers U, Lacanna G, Le Pennec JL, Macedonio G, Manga M, Manzella I, Vitturi MdM, Neri A, Pistolesi M, Polacci M, Ripepe M, Rossi E, Scheu B, Sulpizio R, Tripoli B, Valade S, Valentine G, Vidal C, Wallenstein N (2016) MeMoVolc report on classification and dynamics of volcanic explosive eruptions. Bulletin of Volcanology 78(11):84

Bonadonna C, Costa A (2012) Estimating the volume of tephra deposits: A new simple strategy. Geology 40(5):415-418

Bonadonna C, Costa A (2013) Plume height, volume, and classification of explosive volcanic eruptions based on the Weibull function. Bull Volcanol 75

Bonadonna C, Folch A, Loughlin S, Puempel H (2012) Future developments in modelling and monitoring of volcanic ash clouds: outcomes from the first IAVCEI-WMO workshop on Ash Dispersal Forecast and Civil Aviation. Bulletin of Volcanology 74(1):1-10

Bonadonna C, Genco R, Gouhier M, Pistolesi M, Cioni R, Alfano F, Hoskuldsson A, Ripepe M (2011) Tephra sedimentation during the 2010 Eyjafjallajokull eruption (Iceland) from deposit, radar, and satellite observations. Journal of Geophysical Research-Solid Earth 116

Bonadonna C, Houghton BF (2005) Total grain-size distribution and volume of tephra-fall deposits. Bulletin of Volcanology 67(5):441-456

Borselli L, Sarocchi, D. (2016) DECOLOG software. www.decolog.org

Buckland PCG, A.J.; Larsen, G.; Perry, D.W.; Savory, D.R.; Sveinbjarnadóttir, G. (1986) Late Holocene palaeoecology at Ketilsstadir in Myrdalur, South Iceland. Jökull (3):41-55

Budd DA, Troll VR, Dahren B, Burchardt S (2016) Persistent multitiered magma plumbing beneath Katla volcano, Iceland. Geochemistry Geophysics Geosystems 17(3):966-980

Burden RE, Chen L, Phillips CJ (2013) A statistical method for determining the volume of volcanic fall deposits. Bull Volcanol 75

Buttner R, Dellino P, La Volpe L, Lorenz V, Zimanowski B (2002) Thermohydraulic explosions in phreatomagmatic eruptions as evidenced by the comparison between pyroclasts and products from Molten Fuel Coolant Interaction experiments. Journal of Geophysical Research-Solid Earth 107(B11)

Buttner R, Dellino P, Raue H, Sonder I, Zimanowski B (2006) Stress-induced brittle fragmentation of magmatic melts: Theory and experiments. Journal of Geophysical Research-Solid Earth 111(B8)

Buttner R, Dellino P, Zimanowski B (1999) Identifying magma-water interaction from the surface features of ash particles. Nature 401(6754):688-690

Buttner R, Zimanowski B (1998) Physics of thermohydraulic explosions. Physical Review E 57(5):5726-5729

Carey RJ, Houghton BF, Thordarson T (2009) Abrupt shifts between wet and dry phases of the 1875 eruption of Askja Volcano: Microscopic evidence for macroscopic dynamics. Journal of Volcanology and Geothermal Research 184(3-4):256-270

Carey RJ, Houghton BF, Thordarson T (2010) Tephra dispersal and eruption dynamics of wet and dry phases of the 1875 eruption of Askja Volcano, Iceland. Bulletin of Volcanology 72(3):259-278

Carey S, Sparks, RSJ (1986) Quantitative models of the fallout and dispersal of tephra from volcanic eruption columns. Bulletin of Volcanology 48:109-125

Cioni R, Pistolesi M, Bertagnini A, Bonadonna C, Hoskuldsson A, Scateni B (2014) Insights into the dynamics and evolution of the 2010 Eyjafjallajokull summit eruption (Iceland) provided by volcanic ash textures. Earth Planet. Sci. Lett. 394:111-123

Connor L, Connor CB (2006) Inversion is the key to dispersion: understanding eruption dynamics by inverting tephra fallout. Statistics in volcanology 1:231242

Costa A, Pioli L, Bonadonna C (2016) Assessing tephra total grain-size distribution: Insights from field data analysis. Earth Planet. Sci. Lett. 443:90-107

Costa A, Suzuki YJ, Cerminara M, Devenish BJ, Ongaro TE, Herzog M, Van Eaton AR, Denby LC, Bursik M, de' Michieli Vitturi M, Engwell S, Neri A, Barsotti S, Folch A, Macedonio G, Girault F, Carazzo G, Tait S, Kaminski E, Mastin LG, Woodhouse MJ, Phillips JC, Hogg AJ, Degruyter W, Bonadonna C (2016) Results of the eruptive column model inter-comparison study. Journal of Volcanology and Geothermal Research

D'Oriano C, Bertagnini A, Cioni R, Pompilio M (2014) Identifying recycled ash in basaltic eruptions. Scientific Reports 4

Daggitt ML, Mather TA, Pyle DM, Page S (2014) AshCalc–a new tool for the comparison of the exponential, power-law and Weibull models of tephra deposition. Journal of Applied Volcanology 3(1):1-8

Davies SM, Larsen G, Wastegard S, Turney CSM, Hall VA, Coyle L, Thordarson T (2010) Widespread dispersal of Icelandic tephra: how does the Eyjafjoll eruption of 2010 compare to past Icelandic events? Journal of Quaternary Science 25(5):605-611

Dellino P, Gudmundsson MT, Larsen G, Mele D, Stevenson JA, Thordarson T, Zimanowski B (2012) Ash from the Eyjafjallajokull eruption (Iceland): Fragmentation processes and aerodynamic behavior. Journal of Geophysical Research-Solid Earth 117

Dellino P, Lavolpe L (1995) Fragmentation versus transportation mechanisms in the pyroclastic sequence of Monte-Pilato Rocche-Rosse (Lipari, Italy). Journal of Volcanology and Geothermal Research 64(3-4):211-231

Dellino P, LaVolpe L (1996) Image processing analysis in reconstructing fragmentation and transportation mechanisms of pyroclastic deposits. The case of Monte Pilato-Rocche Rosse eruptions, Lipari (Aeolian islands, Italy). Journal of Volcanology and Geothermal Research 71(1):13-29

Dellino P, Liotino G (2002) The fractal and multifractal dimension of volcanic ash particles contour: a test study on the utility and volcanological relevance. Journal of Volcanology and Geothermal Research 113(1-2):1-18

Dellino P, Mele D, Bonasia R, Braia G, La Volpe L, Sulpizio R (2005) The analysis of the influence of pumice shape on its terminal velocity. Geophysical Research Letters 32(21)

Durig T, Mele D, Dellino P, Zimanowski B (2012) Comparative analyses of glass fragments from brittle fracture experiments and volcanic ash particles. Bulletin of Volcanology 74(3):691-704

Durig T, Sonder I, Zimanowski B, Beyrichen H, Buttner R (2012) Generation of volcanic ash by basaltic volcanism. Journal of Geophysical Research-Solid Earth 117

Einarson EH, G. Larsen, S. Thorarinsson (1980) The Sólheimar tephra layer and the Katla eruption of 1357. Acta Naturalia Islandica 2:2-24

Engwell S, Sparks R, Aspinall W (2013) Quantifying uncertainties in the measurement of tephra fall thickness. Journal of Applied Volcanology 2(1):5

Engwell SL, Aspinall WP, Sparks RSJ (2015) An objective method for the production of isopach maps and implications for the estimation of tephra deposit volumes and their uncertainties. Bulletin of Volcanology 77(7)

Eychenne J, Le Pennec JL, Troncoso L, Gouhier M, Nedelec JM (2012) Causes and consequences of bimodal grain-size distribution of tephra fall deposited during the August 2006 Tungurahua eruption (Ecuador). Bulletin of Volcanology 74(1):187-205

Fierstein J, Nathenson M. (1992) Another look at the calculation of fallout tephra volume. Bull Volcanol 54

Fitch EP, Fagents SA, Thordarson T, Hamilton CW (2017) Fragmentation mechanisms associated with explosive lava–water interactions in a lacustrine environment. Bulletin of Volcanology 79(1):12

Folk RL, Ward WC, (1957) Brazos river bar: A study in the significance of grain size parameters. Journal of Sedimentary Petrology 27:3-26

Genareau K, Mulukutla GK, Proussevitch AA, Durant AJ, Rose WI, Sahagian DL (2013) The size range of bubbles that produce ash during explosive volcanic eruptions. Journal of Applied Volcanology 2(1):1-18

Genareau K, Proussevitch AA, Durant AJ, Mulukutla G, Sahagian DL (2012) Sizing up the bubbles that produce very fine ash during explosive volcanic eruptions. Geophysical Research Letters 39

Gislason SR, Hassenkam T, Nedel S, Bovet N, Eiriksdottir ES, Alfredsson HA, Hem CP, Balogh ZI, Dideriksen K, Oskarsson N, Sigfusson B, Larsen G, Stipp SLS (2011) Characterization of Eyjafjallajokull volcanic ash particles and a protocol for rapid risk assessment. Proceedings of the National Academy of Sciences of the United States of America 108(18):7307-7312

Gjerlow E, Hoeskuldsson A, Pedersen R-B (2015) The 1732 Surtseyan eruption of Eggoya, Jan Mayen, North Atlantic: deposits, distribution, chemistry and chronology. Bulletin of Volcanology 77(2)

Graettinger AH, Skilling I, McGarvie D, Hoskuldsson A (2013) Subaqueous basaltic magmatic explosions trigger phreatomagmatism: A case study from Askja, Iceland. Journal of Volcanology and Geothermal Research 264:17-35

Green RM, Bebbington MS, Jones G, Cronin SJ, Turner MB (2016) Estimation of tephra volumes from sparse and incompletely observed deposit thicknesses. Bulletin of Volcanology 78(4):25

Gudmundsdóttir ER, Larsen G, Björck S, Ingólfsson Ó, Striberger J (2016) A new high-resolution Holocene tephra stratigraphy in eastern Iceland: Improving the Icelandic and North Atlantic tephrochronology. Quaternary Science Reviews 150:234-249

Gudmundsson MT, Sigmundsson F, Bjornsson H (1997) Ice-volcano interaction of the 1996 Gjalp subglacial eruption, Vatnajokull, Iceland. Nature 389(6654):954-957

Gudmundsson MT, Thordarson T, Hoskuldsson A, Larsen G, Bjornsson H, Prata FJ, Oddsson B, Magnusson E, Hognadottir T, Petersen GN, Hayward CL, Stevenson JA, Jonsdottir I (2012) Ash generation and distribution from the April-May 2010 eruption of Eyjafjallajokull, Iceland. Scientific Reports 2

Gudmundsson MTL, G.; Höskuldsson, A.; Gylfason, A. G. (2008) Volcanic Hazards in Iceland. Jökull 58:251-268

Gudmundsson O, Brandsdottir B, Menke W, Sigvaldason GE (1994) The crustal magma chamber of the Katla volcano in South Iceland revealed by 2-D seismic undershooting. Geophysical Journal International 119(1):277-296

Gudnason J, Thordarson T, Houghton BF, Larsen G (2017) The opening subplinian phase of the Hekla 1991 eruption: properties of the tephra fall deposit. Bulletin of Volcanology 79(5):34

Hallgrímsson J (1870) Trettende udbrud 1755. In: De Islandske Vulkaner - Eldrit Jónasar Hallgrímssonar. pp 37v-39v

Hamilton CW, Fagents SA, Thordarson T (2010) Explosive lava-water interactions II: self-organization processes among volcanic rootless eruption sites in the 1783-1784 Laki lava flow, Iceland. Bulletin of Volcanology 72(4):469-485

Hamilton CW, Fitch EP, Fagents SA, Thordarson T (2017) Rootless tephra stratigraphy and emplacement processes. Bulletin of Volcanology 79(1):11

Hamilton CW, Thordarson T, Fagents SA (2010) Explosive lava-water interactions I: architecture and emplacement chronology of volcanic rootless cone groups in the 1783-1784 Laki lava flow, Iceland. Bulletin of Volcanology 72(4):449-467

Heap MJ, Xu T, Chen C-f (2014) The influence of porosity and vesicle size on the brittle strength of volcanic rocks and magma. Bulletin of Volcanology 76(9)

Heiken G (1972) Morphology and Petrography of Volcanic Ashes. Geological Society of America Bulletin 83(7):1961-&

Heiken G (1974) An Atlas of Volcanic Ash. Smithsonian Contributions to Earth Sciences 12:1-101

Honnorez J, Kirst P, (1975) Submarine basaltic volcanism: Morphometric parameters for discriminating hyaloclastites from hyalotuffs. Bulletin of Volcanology 39:441-465

Houghton BW, J. D. L.; Van Eaton, A. (2015) Phreatomagmatic and related eruption styles. In: Sigurdsson HH, B. McNutt, S.; Rymer, R.; Stix, J. (ed) Encyclopedia of Volcanoes. Academic Press,

Hreinsdottir S, Sigmundsson F, Roberts MJ, Bjornsson H, Grapenthin R, Arason P, Arnadottir T, Holmjarn J, Geirsson H, Bennett RA, Gudmundsson MT, Oddsson B, Ofeigsson BG, Villemin T, Jonsson T, Sturkell E, Hoskuldsson A, Larsen G, Thordarson T, Oladottir BA (2014) Volcanic plume height correlated with magma-pressure change at Grimsvotn Volcano, Iceland. Nature Geoscience 7(3):214-218

Inman DL (1952) Measures for describing the size distribution of sediments. Journal of Sedimentary Petrology 22:125-145

Jakobsson SP, Jonsson J, Shido F (1978) PETROLOGY OF THE WESTERN-REYKJANES-PENINSULA, ICELAND. Journal of Petrology 19(4):669-705

Johnson VE (2013) Revised standards for statistical evidence. Proceedings of the National Academy of Sciences of the United States of America 110(48):19313-19317

Jordan SC, Duerig T, Cas RAF, Zimanowski B (2014) Processes controlling the shape of ash particles: Results of statistical IPA. Journal of Volcanology and Geothermal Research 288:19-27

Jude-Eton TC, Thordarson T, Gudmundsson MT, Oddsson B (2012) Dynamics, stratigraphy and proximal dispersal of supraglacial tephra during the ice-confined 2004 eruption at Grimsvotn Volcano, Iceland. Bulletin of Volcanology 74(5):1057-1082

Jutzeler M, White JDL, Proussevitch AA, Gordee SM (2016) Vesiculation and fragmentation history in a submarine scoria cone-forming eruption, an example from Nishiizu (Izu Peninsula, Japan). Bulletin of Volcanology 78(2)

Kerminen VM, Niemi JV, Timonen H, Aurela M, Frey A, Carbone S, Saarikoski S, Teinila K, Hakkarainen J, Tamminen J, Vira J, Prank M, Sofiev M, Hillamo R (2011) Characterization of a volcanic ash episode in southern Finland caused by the Grimsvotn eruption in Iceland in May 2011. Atmospheric Chemistry and Physics 11(23):12227-12239

Klawonn M, Houghton BF, Swanson DA, Fagents SA, Wessel P, Wolfe CJ (2014) From field data to volumes: constraining uncertainties in pyroclastic eruption parameters. Bulletin of Volcanology 76(7):839

Klawonn M, Wolfe CJ, Frazer LN, Houghton BF (2012) Novel inversion approach to constrain plume sedimentation from tephra deposit data: Application to the 17 June 1996 eruption of Ruapehu volcano, New Zealand. Journal of Geophysical Research-Solid Earth 117

Kuehn SCP, S.; Wallace, K.; Bursik, M. I. (2014) Results of the Tephra 2014 Workshop on Maximizing the Potential of Tephra for Multidisciplinary Science. In: Conference: American Geophysical Union Fall Meeting. San Francisco, CA, USA

Lacasse C, Garbe-Schonberg CD (2001) Explosive silicic volcanism in Iceland and the Jan Mayen area during the last 6 Ma: sources and timing of major eruptions. Journal of Volcanology and Geothermal Research 107(1-3):113-147

Lacasse C, Sigurdsson H, Carey SN, Johannesson H, Thomas LE, Rogers NW (2007) Bimodal volcanism at the Katla subglacial caldera, Iceland: insight into the geochemistry and petrogenesis of rhyolitic magmas. Bulletin of Volcanology 69(4):373-399

Lacasse C, Sigurdsson H, Johannesson H, Paterne M, Carey S (1995) SOURCE OF ASH-ZONE-1 IN THE NORTH-ATLANTIC. Bulletin of Volcanology 57(1):18-32

Langmann B, Folch A, Hensch M, Matthias V (2012) Volcanic ash over Europe during the eruption of Eyjafjallajokull on Iceland, April-May 2010. Atmospheric Environment 48:1-8

Larsen C, Newton AJ, Dugmore AJ, Vilmundardottir EG (2001) Geochemistry, dispersal, volumes and chronology of Holocene from the Katla volcanic silicic tephra layers system, Iceland. Journal of Quaternary Science 16(2):119-132

Larsen G (2000) Holocene eruptions within the Katla volcanic system, south Iceland: Characteristics and environmental impact. Jökull 49:1-28

Larsen G (2010) Katla: Tephrochronology and Eruption History. Development in quaternary sciences 13:23-49

Larsen G, Dugmore A, Newton A (1999) Geochemistry of historical-age silicic tephras in Iceland. Holocene 9(4):463-471

Larsen G, Eiriksson J (2008) Late Quaternary terrestrial tephrochronology of Iceland - frequency of explosive eruptions, type and volume of tephra deposits. Journal of Quaternary Science 23(2):109-120

Larsen G, Eiriksson J (2008) Holocene tephra archives and tephrochronology in Iceland - a brief overview. Jokull 58:229-250

Lawson IT, Swindles GT, Plunkett G, Greenberg D (2012) The spatial distribution of Holocene cryptotephras in north-west Europe since 7 ka: implications for understanding ash fall events from Icelandic eruptions. Quaternary Science Reviews 41:57-66

Leibrandt SLP, JL (2015) Towards fast and routine analysis of volcanic ash morphometry for eruption surveillance applications. Journal of Volcanology and Geothermal Research 297:11-27

Liu EJ, Cashman KV, Rust AC, Gislason SR (2015) The role of bubbles in generating fine ash during hydromagmatic eruptions. Geology 43(3):239-242

Liu EJC, K.V.; Rust, A. C. (2015) Optimizing shape analysis to quantify volcanic ash morphology. GeoResJ 8:14-30

Lowe DJ (2011) Tephrochronology and its application: A review. Quaternary Geochronology 6(2):107-153

Magnússon T (1627) Relation om Jordskelff paa Island 1625. Kiøbenhaffn, p 14. Translated by Helvad, N

Mangan MT, Cashman KV (1996) The structure of basaltic scoria and reticulite and inferences for vesiculation, foam formation, and fragmentation in lava fountains. Journal of Volcanology and Geothermal Research 73(1-2):1-18

Maria A, Carey S (2002) Using fractal analysis to quantitatively characterize the shapes of volcanic particles. Journal of Geophysical Research-Solid Earth 107(B11)

Maria A, Carey S (2007) Quantitative discrimination of magma fragmentation and pyroclastic transport processes using the fractal spectrum technique. Journal of Volcanology and Geothermal Research 161(3):234-246

Mastin LG (2007) Generation of fine hydromagmatic ash by growth and disintegration of glassy rinds. Journal of Geophysical Research-Solid Earth 112(B2)

Mastin LG, Christiansen RL, Thornber C, Lowenstern J, Beeson M (2004) What makes hydromagmatic eruptions violent? Some insights from the Keanakako'i Ash, Kilauea Volcano, Hawai'i. Journal of Volcanology and Geothermal Research 137(1-3):15-31

Mastin LG, Guffanti M, Servranckx R, Webley P, Barsotti S, Dean K, Durant A, Ewert JW, Neri A, Rose WI, Schneider D, Siebert L, Stunder B, Swanson G, Tupper A, Volentik A, Waythomas CF (2009) A multidisciplinary effort to assign realistic source parameters to models of volcanic ash-cloud transport and dispersion during eruptions (vol 188, pg 1, 2009). Journal of Volcanology and Geothermal Research 186:10-21

Mastin LG, Spieler O, Downey WS (2009) An experimental study of hydromagmatic fragmentation through energetic, non-explosive magma-water mixing. Journal of Volcanology and Geothermal Research 180(2-4):161-170

Mastin LG, Van Eaton AR, Durant AJ (2016) Adjusting particle-size distributions to account for aggregation in tephra-deposit model forecasts. Atmospheric Chemistry and Physics 16(14):9399-9420

Mattsson HB (2010) Textural variation in juvenile pyroclasts from an emergent, Surtseyan-type, volcanic eruption: The Capelas tuff cone, Sao Miguel (Azores). Journal of Volcanology and Geothermal Research 189(1-2):81-91

Mattsson HB, Hoskuldsson A (2011) Contemporaneous phreatomagmatic and effusive activity along the Hverfjall eruptive fissure, north Iceland: Eruption chronology and resulting deposits. Journal of Volcanology and Geothermal Research 201(1-4):241-252

Mele D, Dellino P, Sulpizio R, Braia G (2011) A systematic investigation on the aerodynamics of ash particles. Journal of Volcanology and Geothermal Research 203(1-2):1-11

Miwa T, Shimano, T., Nishimura, T. (2015) Characterization of the luminance and shape of ash particles at Sakurajima volcano, Japan, using CCD camera images. Bulletin of Volcanology 77(5):1-24

Mueller SB, Ayris PM, Wadsworth FB, Kueppers U, Casas AS, Delmelle P, Taddeucci J, Jacob M, Dingwell DB (2017) Ash aggregation enhanced by deposition and redistribution of salt on the surface of volcanic ash in eruption plumes. Scientific Reports 7

Murtagh RM, White JDL (2013) Pyroclast characteristics of a subaqueous to emergent Surtseyan eruption, Black Point volcano, California. Journal of Volcanology and Geothermal Research 267:75-91

Nemeth K, Cronin SJ (2011) Drivers of explosivity and elevated hazard in basaltic fissure eruptions: The 1913 eruption of Ambrym Volcano, Vanuatu (SW-Pacific). Journal of Volcanology and Geothermal Research 201(1-4):194-209

Newhall CG, Self S (1982) The volcanic explosivity index (VEI) an estimate of explosive magnitude for historical volcanism. Journal of Geophysical Research: Oceans 87(C2):1231-1238

Oladottir BA, Larsen G, Sigmarsson O (2011) Holocene volcanic activity at Grimsvotn, Bardarbunga and Kverkfjoll subglacial centres beneath Vatnajokull, Iceland. Bulletin of Volcanology 73(9):1187-1208

Oladottir BA, Larsen G, Sigmarsson O (2014) Volume estimates of nine Katla tephra layers (similar to 1860 BC-870 AD). Jokull 64:23-40

Oladottir BA, Sigmarsson O, Larsen G, Devidal JL (2011) Provenance of basaltic tephra from Vatnajokull subglacial volcanoes, Iceland, as determined by major- and trace-element analyses. Holocene 21(7):1037-1048

Oladottir BA, Sigmarsson O, Larsen G, Thordarson T (2008) Katla volcano, Iceland: magma composition, dynamics and eruption frequency as recorded by Holocene tephra layers. Bulletin of Volcanology 70(4):475-493

Oladottir BAL, G.; Thordarson, T.; Sigmarsson, O. (2007) The Katla volcano S-Iceland: Holocene tephra stratigraphy and eruption frequency. Jökull (55):53-74

Owen J, Tuffen H, McGarvie DW (2013) Explosive subglacial rhyolitic eruptions in Iceland are fuelled by high magmatic H2O and closed-system degassing. Geology 41(2):251-254

Oxford-Economics (2010) The Economic Impacts of Air Travel Restrictions Due to Volcanic Ash Report for Airbus. In,

Pardini F, Spanu A, Vitturi MD, Salvetti MV, Neri A (2016) Grain size distribution uncertainty quantification in volcanic ash dispersal and deposition from weak plumes. Journal of Geophysical Research-Solid Earth 121(2):538-557

Parfitt EA, Wilson L (1995) Explosive volcanic eruptions – The transition between Hawaiian-style lava fountaining and Strombolian explosive activity. Geophysical Journal International 121(1):226-232

Parra R, Bernard B, Narváez D, Le Pennec J-L, Hasselle N, Folch A (2016) Eruption Source Parameters for forecasting ash dispersion and deposition from vulcanian eruptions at Tungurahua volcano: Insights from field data from the July 2013 eruption. Journal of Volcanology and Geothermal Research 309:1-13

Perugini D, Kueppers U (2012) Fractal analysis of experimentally generated pyroclasts: A tool for volcanic hazard assessment. Acta Geophysica 60(3):682-698

Proussevitch AA, Mulukutla GK, Sahagian DL (2011) A new 3D method of measuring bubble size distributions from vesicle fragments preserved on surfaces of volcanic ash particles. Geosphere 7(1):62-69

Pyle DM (1989) The thickness, volume and grainsize of tephra fall deposits. Bull Volcanol 51

Pyne-O'Donnell S (2011) The taphonomy of Last Glacial-Interglacial Transition (LGIT) distal volcanic ash in small Scottish lakes. Boreas 40(1):131-145

Riley CM, Rose WI, Bluth GJS (2003) Quantitative shape measurements of distal volcanic ash. Journal of Geophysical Research-Solid Earth 108(B10)

Sæmundsson K (1978) Fissure swarms and central volcanoes of the neovolcanic zones of Iceland. In: Laeke DRBaBE (ed) Crustal evolution in NW-Britain and adjacent regions. Geological Journal Spec., pp 415-432

Sammonds P, McGuire, W., Edwards, S. (2010) Volcanic hazard from Iceland: Analysis and Implication of the Eyjafjallajökull eruption. In: Sammonds P, McGuire, W., Edwards, S. (ed) UCL Institute for Risk and Disaster Reduction, London

Scaini C, Biass S, Galderisi A, Bonadonna C, Folch A, Smith K, Hoskuldsson A (2014) A multi-scale risk assessment for tephra fallout and airborne concentration from multiple Icelandic volcanoes - Part 2: Vulnerability and impact. Natural Hazards and Earth System Sciences 14(8):2289-2312

Schipper CI, White, J.D.L., Zimanowski, B., Büttner, R., Sonder, I., Schmid, A. (2011) Experimental interaction of magma and “dirty” coolants. Earth Planet. Sci. Lett. 203:323-336

Schipper CI, White JDL (2016) Magma-slurry interaction in Surtseyan eruptions. Geology 44(3):195-198

Schipper CI, White JDL, Houghton BF (2010) Syn- and post-fragmentation textures in submarine pyroclasts from Loihi Seamount, Hawaii. Journal of Volcanology and Geothermal Research 191(1-2):93-106

Schipper CI, White JDL, Houghton BF (2011) Textural, geochemical, and volatile evidence for a Strombolian-like eruption sequence at Lō`ihi Seamount, Hawai`i. Journal of Volcanology and Geothermal Research 207(1–2):16-32

Schipper CI, White JDL, Houghton BF, Shimizu N, Stewart RB (2010) "Poseidic" explosive eruptions at Loihi Seamount, Hawaii. Geology 38(4):291-294

Schmith J, Höskuldsson Á, Holm PM (2017) Grain shape of basaltic ash populations: implications for fragmentation. Bulletin of Volcanology 79(2):14

Schumann U, Weinzierl B, Reitebuch O, Schlager H, Minikin A, Forster C, Baumann R, Sailer T, Graf K, Mannstein H, Voigt C, Rahm S, Simmet R, Scheibe M, Lichtenstern M, Stock P, Ruba H, Schauble D, Tafferner A, Rautenhaus M, Gerz T, Ziereis H, Krautstrunk M, Mallaun C, Gayet JF, Lieke K, Kandler K, Ebert M, Weinbruch S, Stohl A, Gasteiger J, Gross S, Freudenthaler V, Wiegner M, Ansmann A, Tesche M, Olafsson H, Sturm K (2011) Airborne observations of the Eyjafjalla volcano ash cloud over Europe during air space closure in April and May 2010. Atmospheric Chemistry and Physics 11(5):2245-2279

SediGraph III 5120 Operator’s Manual (2010). In: Micromeritics Instrument Corporation, Norcross, GA p460

Det Kongelige Danske Videnskabernes Selskab (1758) Beskrivelse over det, i Island, den 11. September 1755 paakomne Jordskiælv og den derpaa, den 17de Oktober samme Aar, fulgte Ilds-Udbrydelse af den forbrændte Bierg-Kløfte Katlegiaa udi Is-Bjerget Myrdals-Jøkel; efter de sammesteds observerende Studenteres indsendte Beretninger. Skrifter som udi det Kiobenhavnske Selskab VII:185-196

Shea T, Houghton, B. F., Gurioli, L., Cashman, K. V., Hammer, J., E., Hobden, B. J (2010) Textural studies of vesicles in volcanic rocks: An integrated methodology. Journal of Volcanology and Geothermal Research 190:271-289

Sheridan MF, Marshall JR (1983) Interpretation of Pyroclast Surface-Features Using Sem Images. Journal of Volcanology and Geothermal Research 16(1-2):153-159
e
Sparks R (1986) The dimensions and dynamics of volcanic eruption columns. Bulletin of Volcanology 48(1):3-15

Sparks RSJ, Bursik MI, Ablay GJ, Thomas RME, Carey SN (1992) Sedimantation of tephra by volcanic plumes: Controls on thickness and grain-size variations of tephra fall deposits. Bulletin of Volcanology 54(8):685-695

Stevenson JA, Loughlin S, Rae C, Thordarson T, Milodowski AE, Gilbert JS, Harangi S, Lukacs R, Hojgaard B, Arting U, Pyne-O'Donnell S, MacLeod A, Whitney B, Cassidy M (2012) Distal deposition of tephra from the Eyjafjallajokull 2010 summit eruption. Journal of Geophysical Research-Solid Earth 117

Stovall WK, Houghton BF, Gonnermann H, Fagents SA, Swanson DA (2011) Eruption dynamics of Hawaiian-style fountains: the case study of episode 1 of the Kilauea Iki 1959 eruption. Bulletin of Volcanology 73(5):511-529

Sturkell E, Einarsson P, Roberts MJ, Geirsson H, Gudmundsson MT, Sigmundsson F, Pinel V, Guomundsson GB, Olafsson H, Stefansson R (2008) Seismic and geodetic insights into magma accumulation at Katla subglacial volcano, Iceland: 1999 to 2005. Journal of Geophysical Research-Solid Earth 113(B3)

Swindles GT, Lawson IT, Savov IP, Connor CB, Plunkett G (2011) A 7000 yr perspective on volcanic ash clouds affecting northern Europe. Geology 39(9):887-890

Thorarinsson S (1958) The Öræfajökull eruption of 1362. Acta Naturalia Islandica 2:1-100

Thorarinsson S (1967) The eruptions of Hekla in historical times. In: Einarsson TK, G.; Thorarinsson, S. (ed) The eruption of Hekla 1947-1948. Socíetas Scientarium Islandica, Reykjavík, pp 1-177

Thorarinsson S (1967) Surtsey – The new island in the North Atlantic. Penguin Group (USA), New York

Thorarinsson S (1975) Katla and annáll Kötlugosa (Katla and its historical eruptions). In: Árbók Ferdafélags Íslands 1975. Ferdafélags Íslands, Reykjavík, pp 125-149

Thorarinsson S (1981) GREETINGS FROM ICELAND - ASH-FALLS AND VOLCANIC AEROSOLS IN SCANDINAVIA. Geografiska Annaler Series a-Physical Geography 63(3-4):109-118

Thordarson T, Hoskuldsson A (2008) Postglacial volcanism in Iceland. Jokull 58:197-228

Thordarson T, Larsen G (2007) Volcanism in Iceland in historical time: Volcano types, eruption styles and eruptive history. Journal of Geodynamics 43(1):118-152

Valentine GA, Gregg TKP (2008) Continental basaltic volcanoes — Processes and problems. Journal of Volcanology and Geothermal Research 177(4):857-873

Van Eaton AR, Herzog M, Wilson CJN, McGregor J (2012) Ascent dynamics of large phreatomagmatic eruption clouds: The role of microphysics. Journal of Geophysical Research: Solid Earth 117(B3):n/a-n/a

Volentik ACM, Bonadonna C, Connor CB, Connor LJ, Rosi M (2010) Modeling tephra dispersal in absence of wind: Insights from the climactic phase of the 2450 BP Plinian eruption of Pululagua volcano (Ecuador). Journal of Volcanology and Geothermal Research 193(1-2):117-136

Watson EJ, Swindles GT, Lawson IT, Savov IP (2016) Do peatlands or lakes provide the most comprehensive distal tephra records? Quaternary Science Reviews 139:110-128

Watson EJ, Swindles GT, Savov IP, Lawson IT, Connor CB, Wilson JA (2017) Estimating the frequency of volcanic ash clouds over northern Europe. Earth Planet. Sci. Lett. 460:41-49

Watson EJ, Swindles GT, Stevenson JA, Savov I, Lawson IT (2016) The transport of Icelandic volcanic ash: Insights from northern European cryptotephra records. Journal of Geophysical Research-Solid Earth 121(10):7177-7192

White JT, Connor CB, Connor L, Hasenaka T (2017) Efficient inversion and uncertainty quantification of a tephra fallout model. Journal of Geophysical Research-Solid Earth 122(1):281-294

Wilkins KL, Western LM, Watson IM (2016) Simulating atmospheric transport of the 2011 Grimsvotn ash cloud using a data insertion update scheme. Atmospheric Environment 141:48-59

Wohletz K (1986) Explosive magma-water interactions: Thermodynamics, explosion mechanisms, and field studies. Bulletin of Volcanology 48:245-264

Wohletz K, Orsi G, Devita S (1995) ERUPTIVE MECHANISMS OF THE NEAPOLITAN-YELLOW-TUFF INTERPRETED FROM STRATIGRAPHIC, CHEMICAL, AND GRANULOMETRIC DATA. Journal of Volcanology and Geothermal Research 67(4):263-290

Wohletz KH (1983) MECHANISMS OF HYDROVOLCANIC PYROCLAST FORMATION - GRAIN-SIZE, SCANNING ELECTRON-MICROSCOPY, AND EXPERIMENTAL STUDIES. Journal of Volcanology and Geothermal Research 17(1-4):31-63

Wohletz KH, Sheridan MF, Brown WK (1989) Particle size distributions and the sequential fragmentation/transport theory applied to volcanic ash. Journal of Geophysical Research: Solid Earth 94(B11):15703-15721

Wohletz KK, D. (1982) Scanning electron microscopy of basaltic hydromagmatic ash. In: Los Alamos National Laboratory Report. Los Alamos National Laboratory, p 26

Woodcock DC, Gilbert JS, Lane SJ (2012) Particle-water heat transfer during explosive volcanic eruptions. Journal of Geophysical Research-Solid Earth 117

Yang Q, Bursik M (2016) A new interpolation method to model thickness, isopachs, extent, and volume of tephra fall deposits. Bulletin of Volcanology 78(10):68

Zimanowski B, Buttner R, Lorenz V (1997) Premixing of magma and water in MFCI experiments. Bulletin of Volcanology 58(6):491-495

Zimanowski B, Buttner R, Lorenz V, Hafele HG (1997) Fragmentation of basaltic melt in the course of explosive volcanism. Journal of Geophysical Research-Solid Earth 102(B1):803-814

Appendices

Appendix A – soil sections

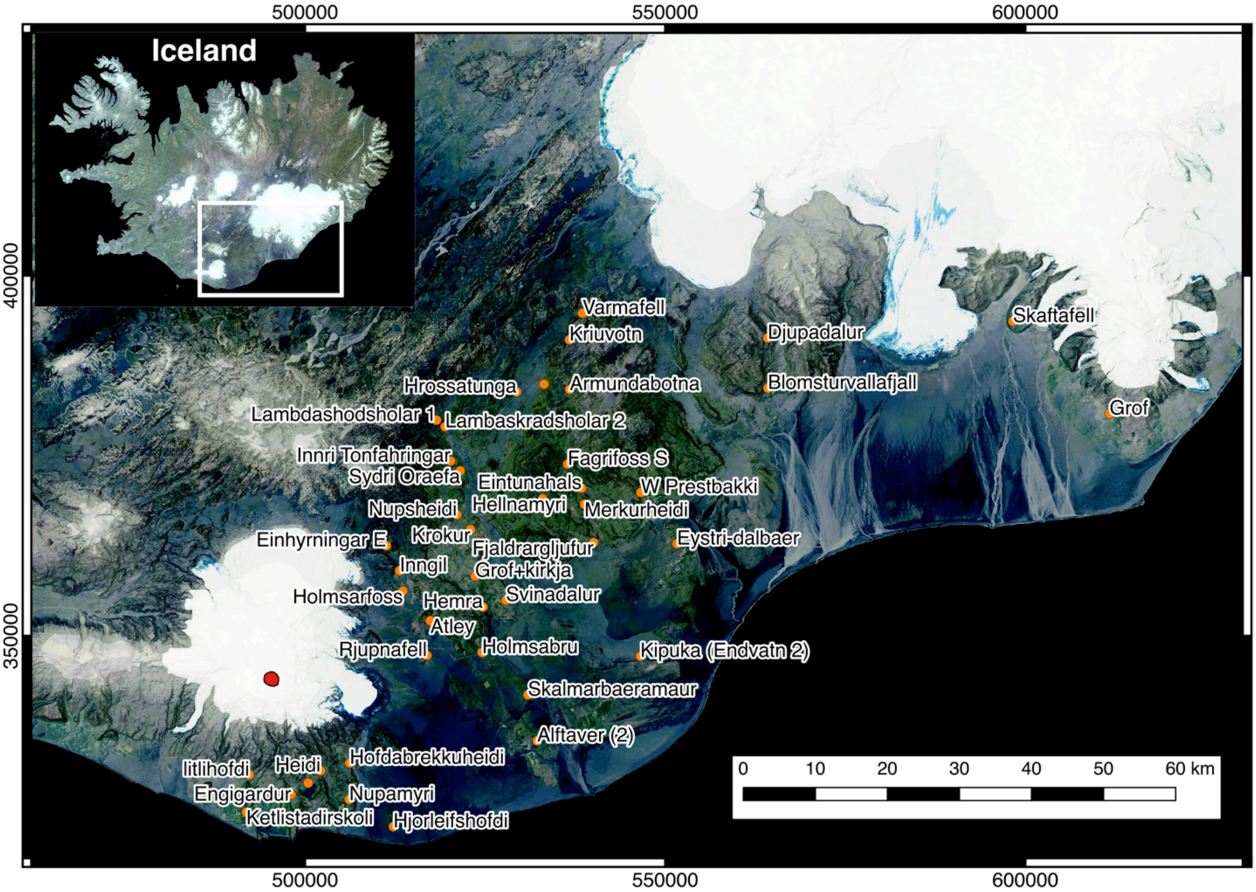

Map of soil sections with section names. All sections are listed alphabetically below.

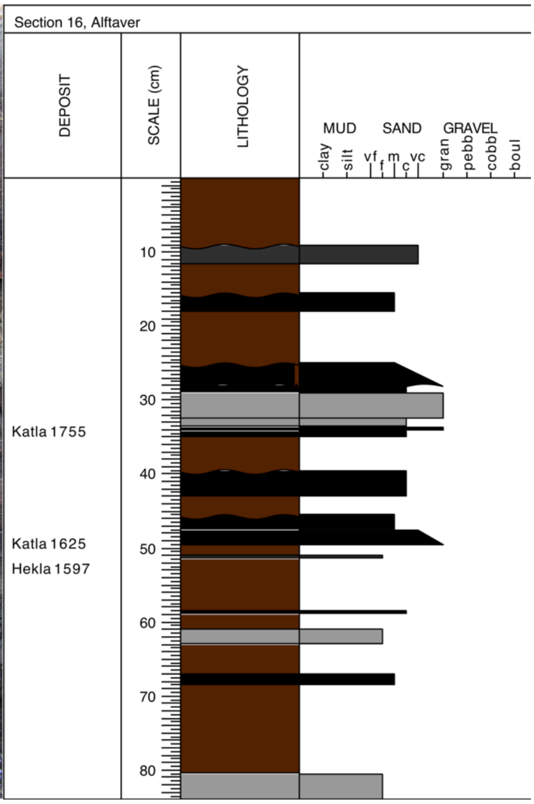

Appendix A – soil sections

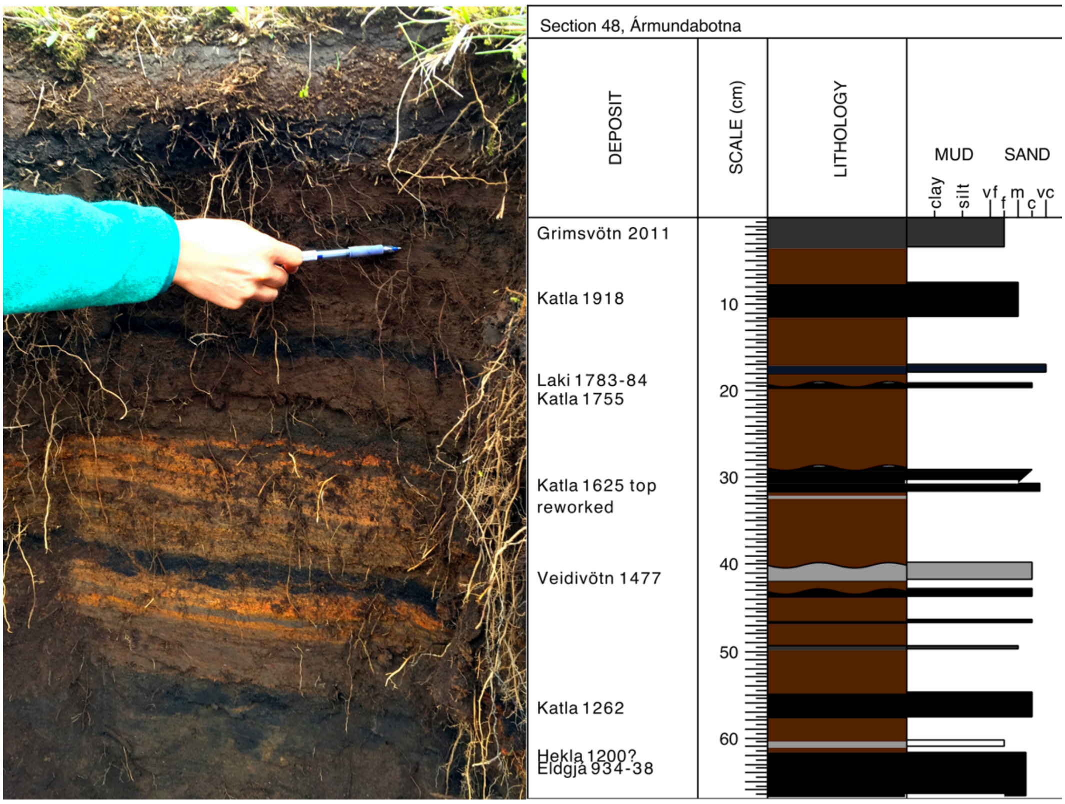

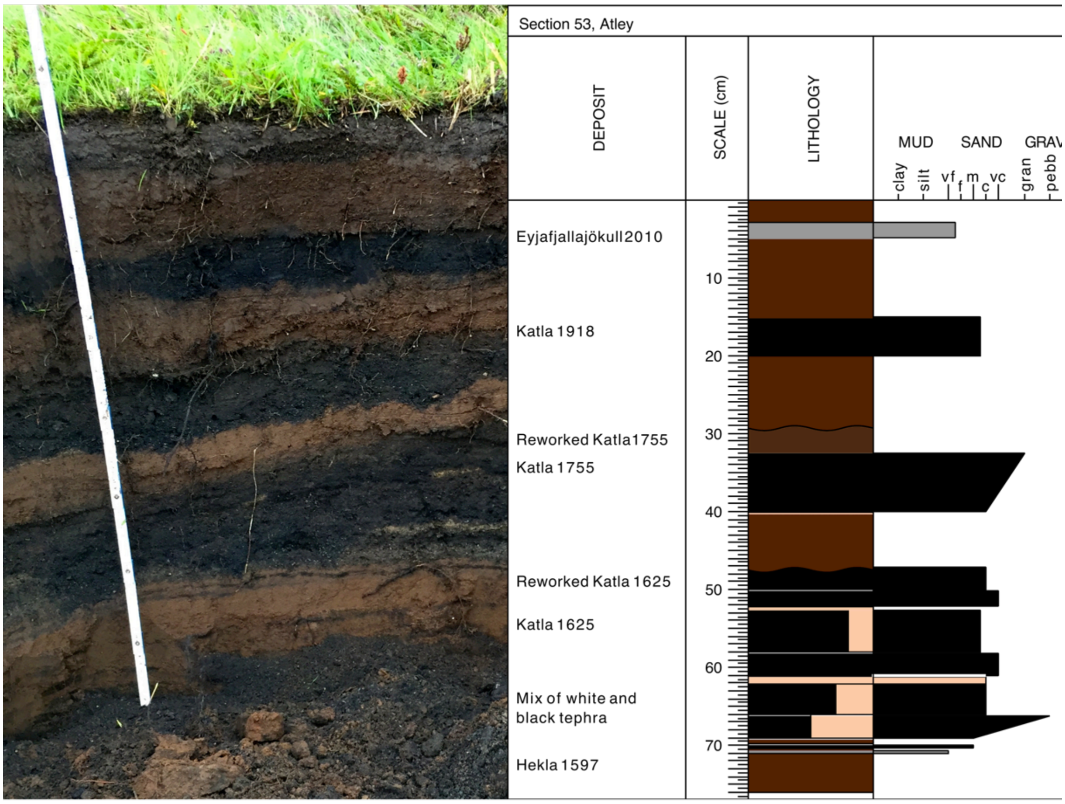

Appendix A – soil sections

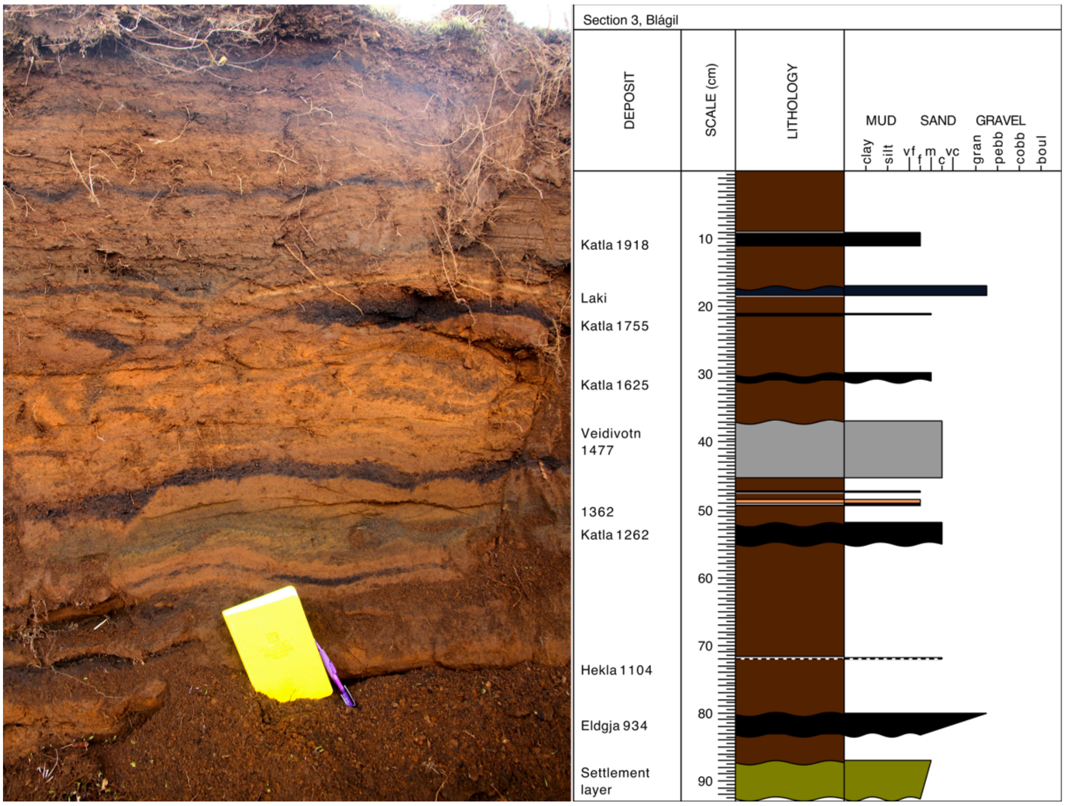

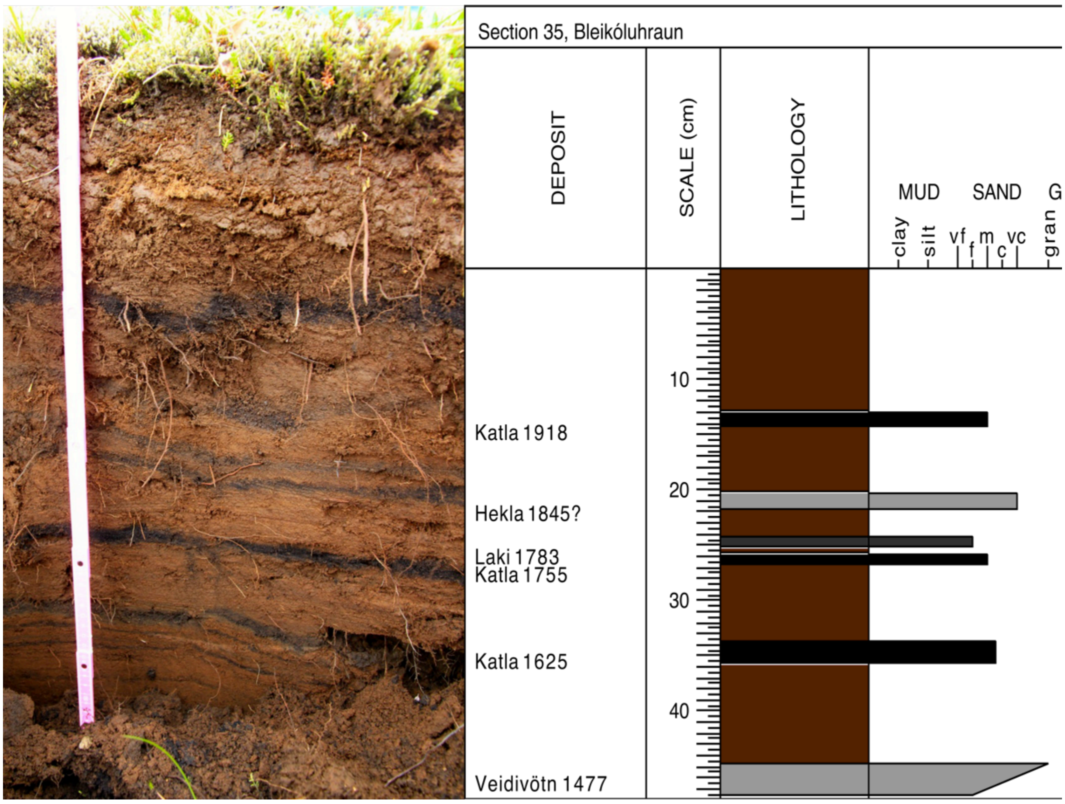

Appendix A – soil sections

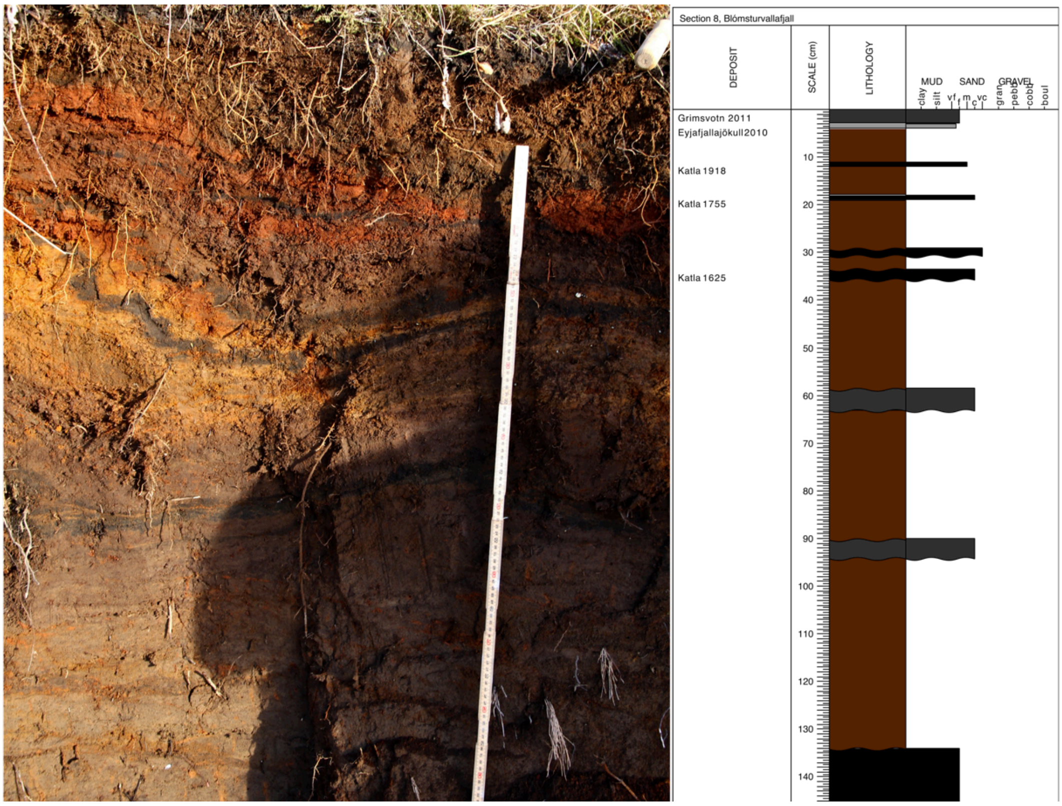

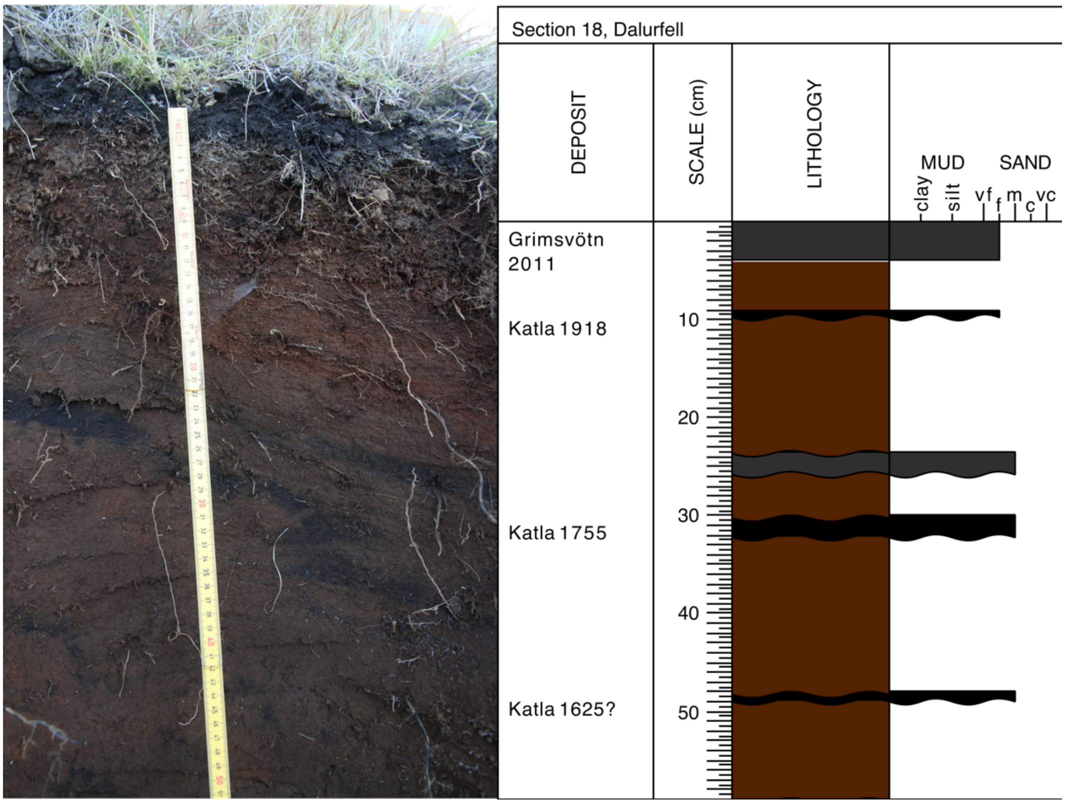

Appendix A – soil sections

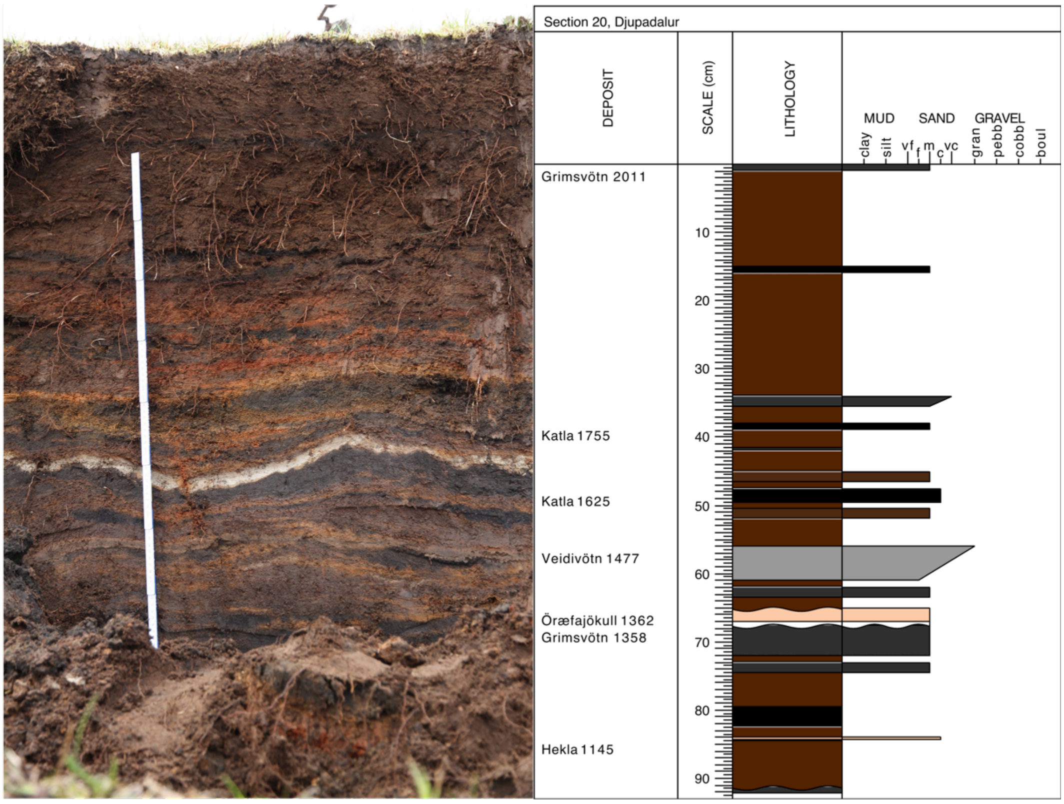

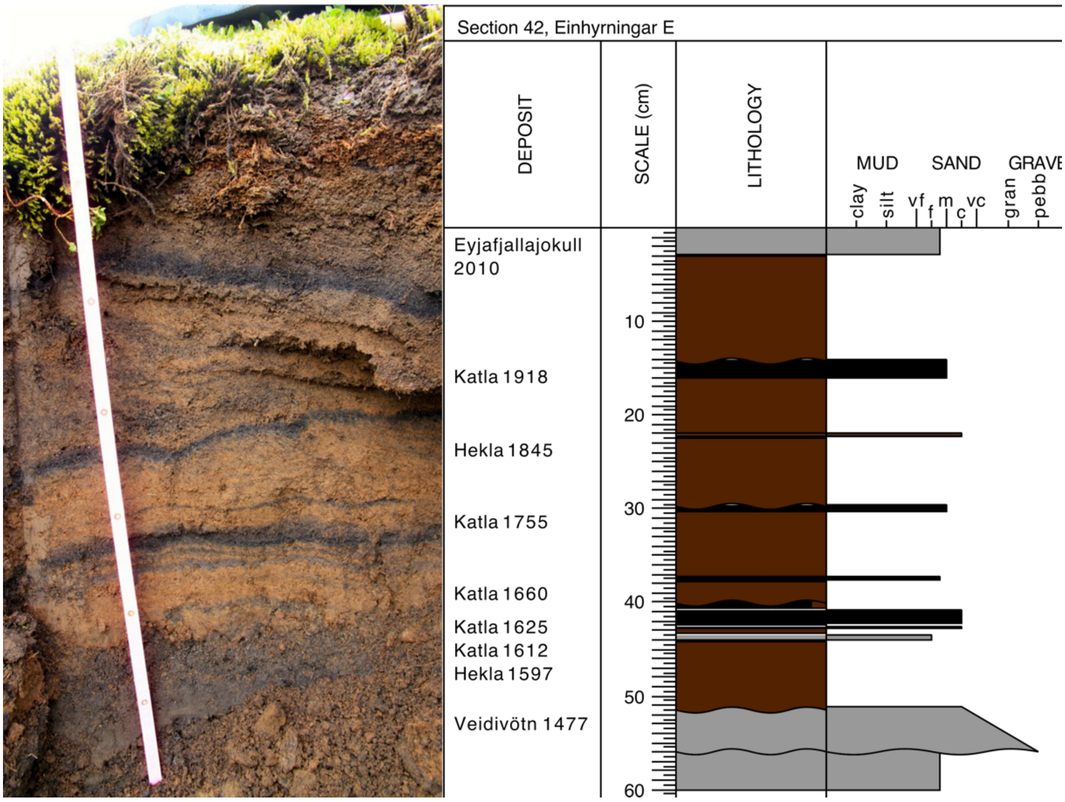

Appendix A – soil sections

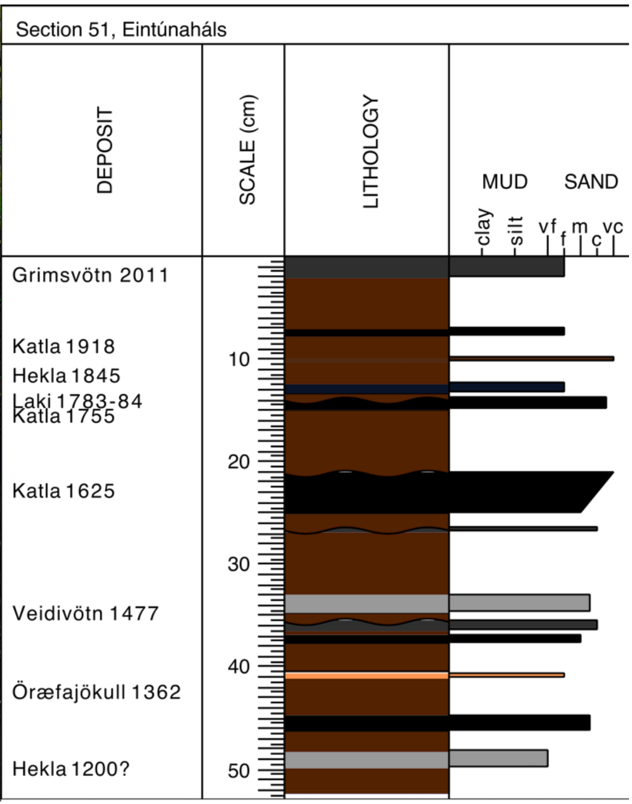

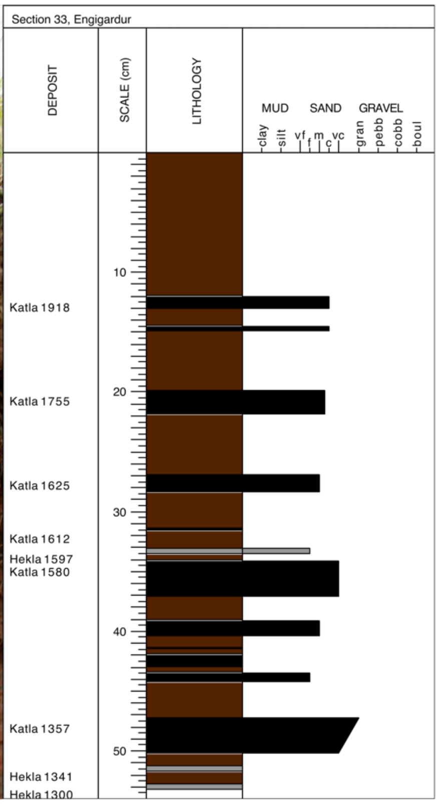

Appendix A – soil sections

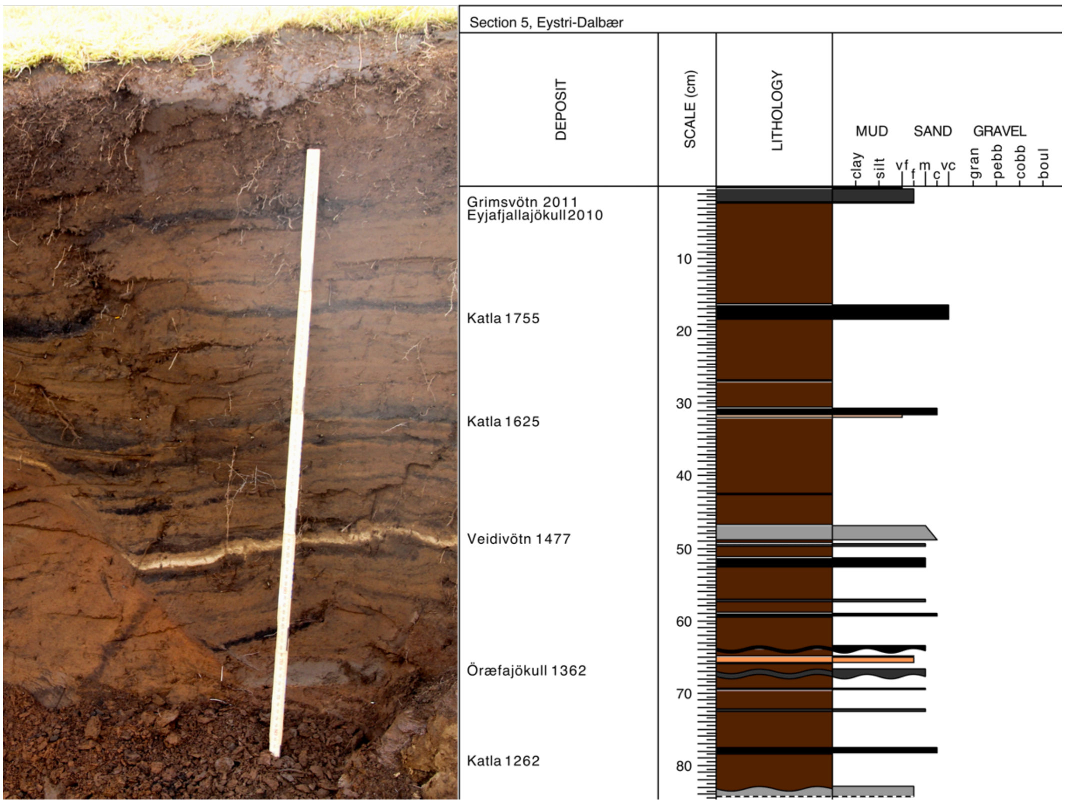

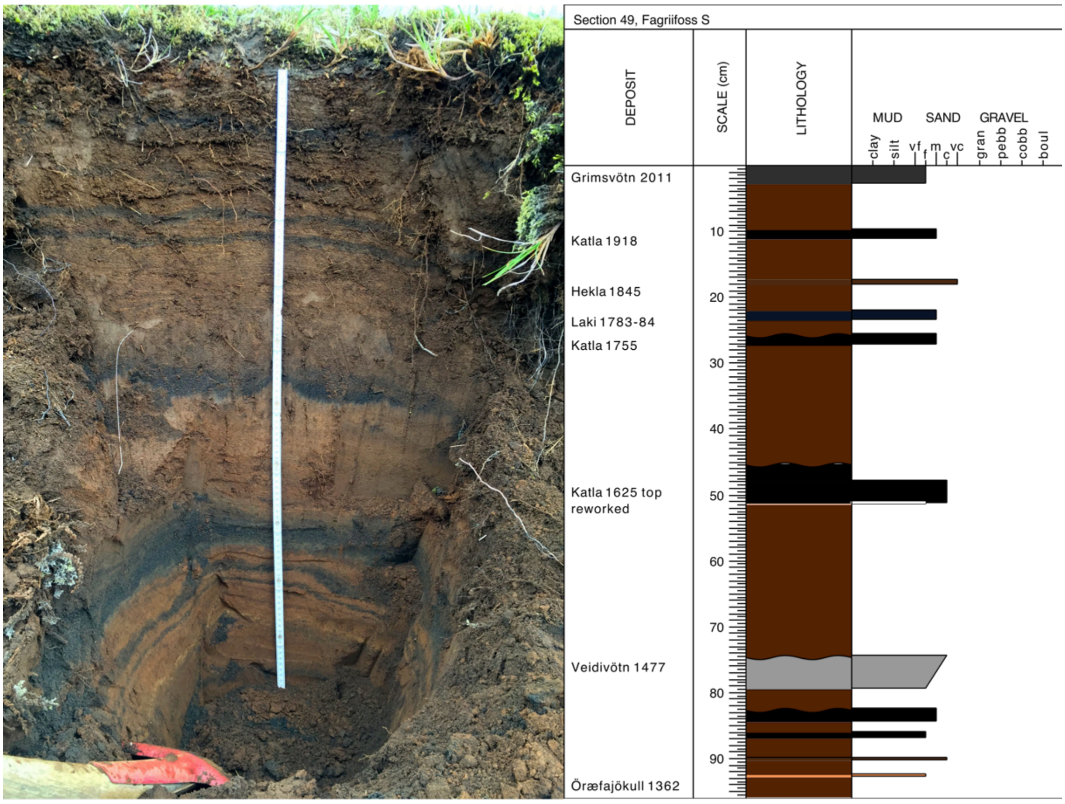

Appendix A – soil sections

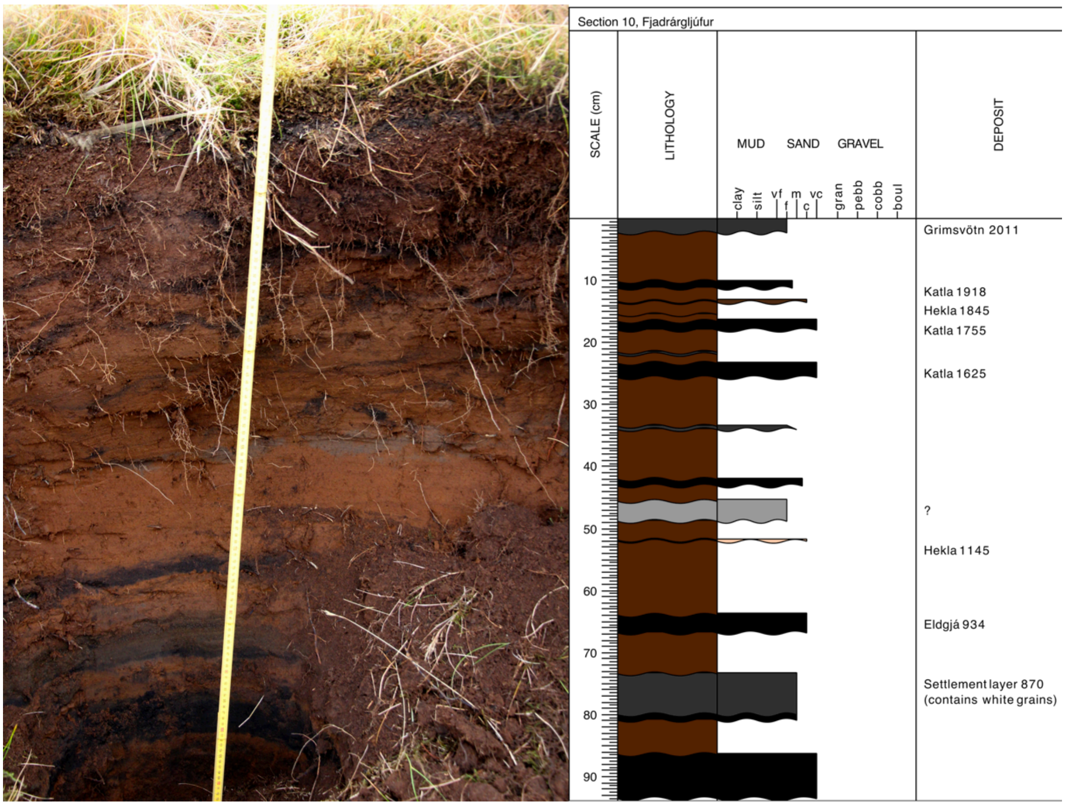

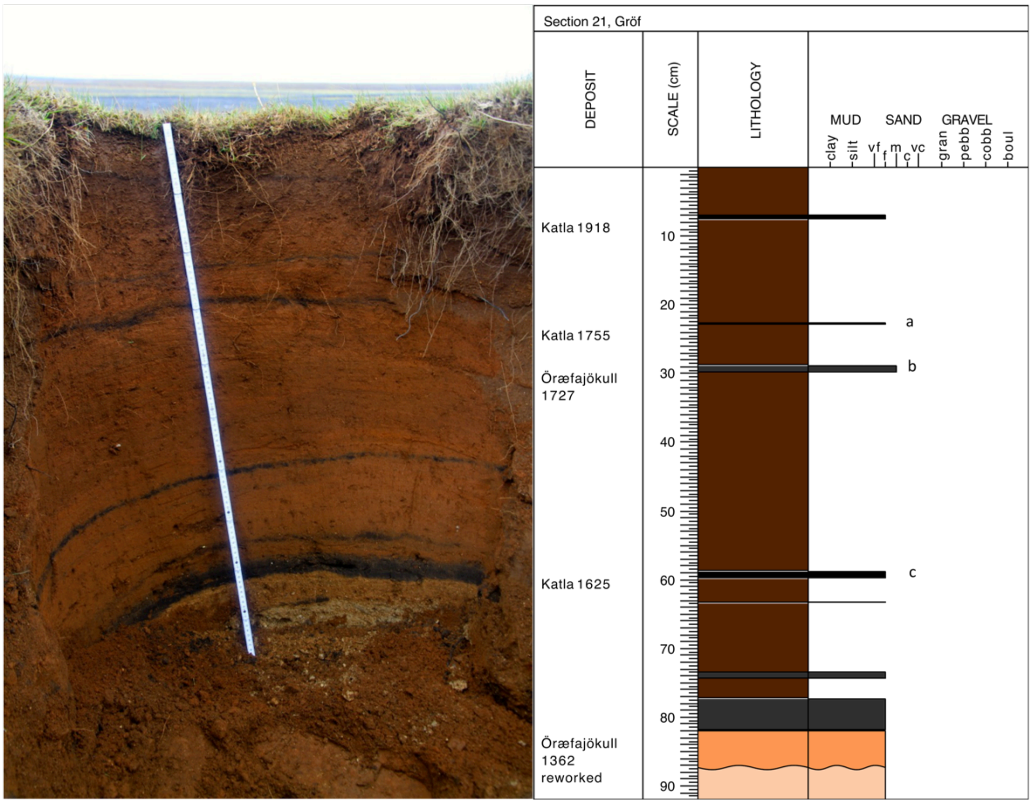

Appendix A – soil sections

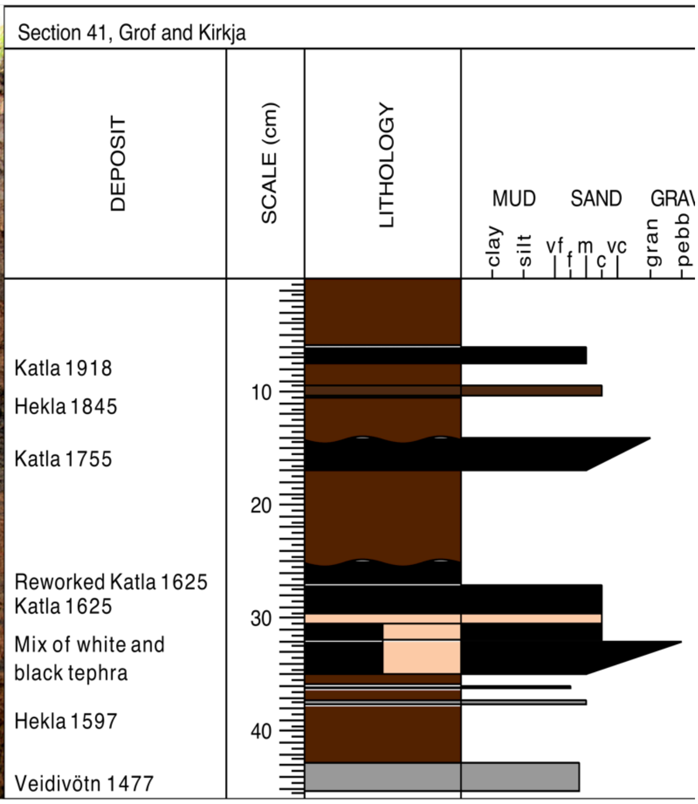

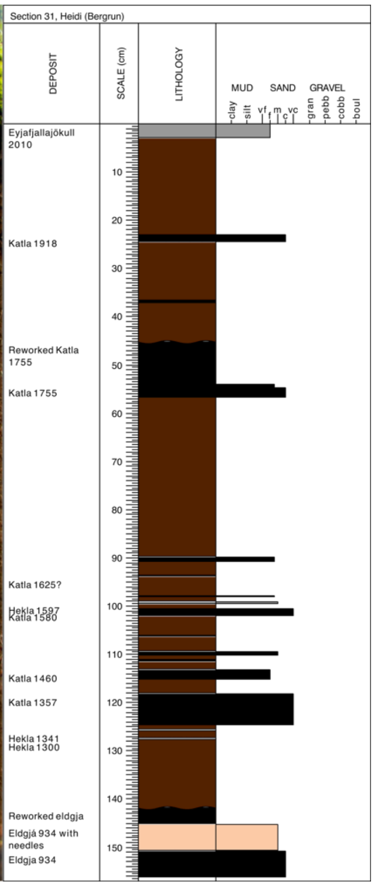

Appendix A – soil sections

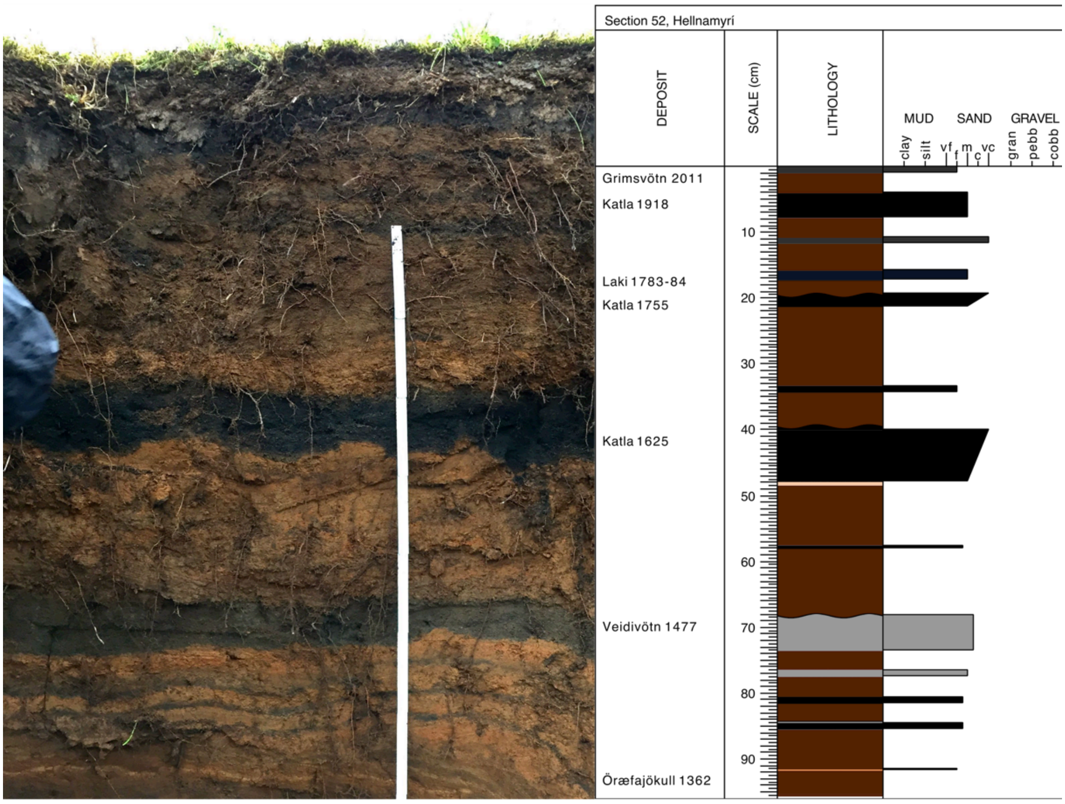

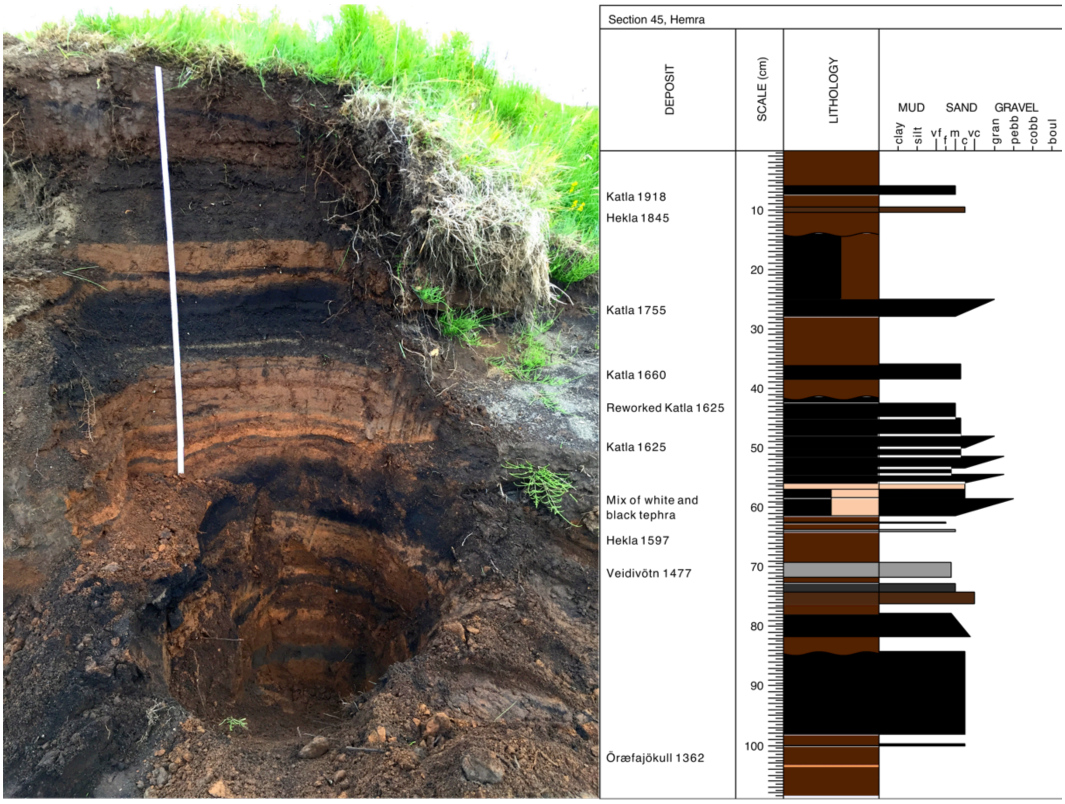

Appendix A – soil sections

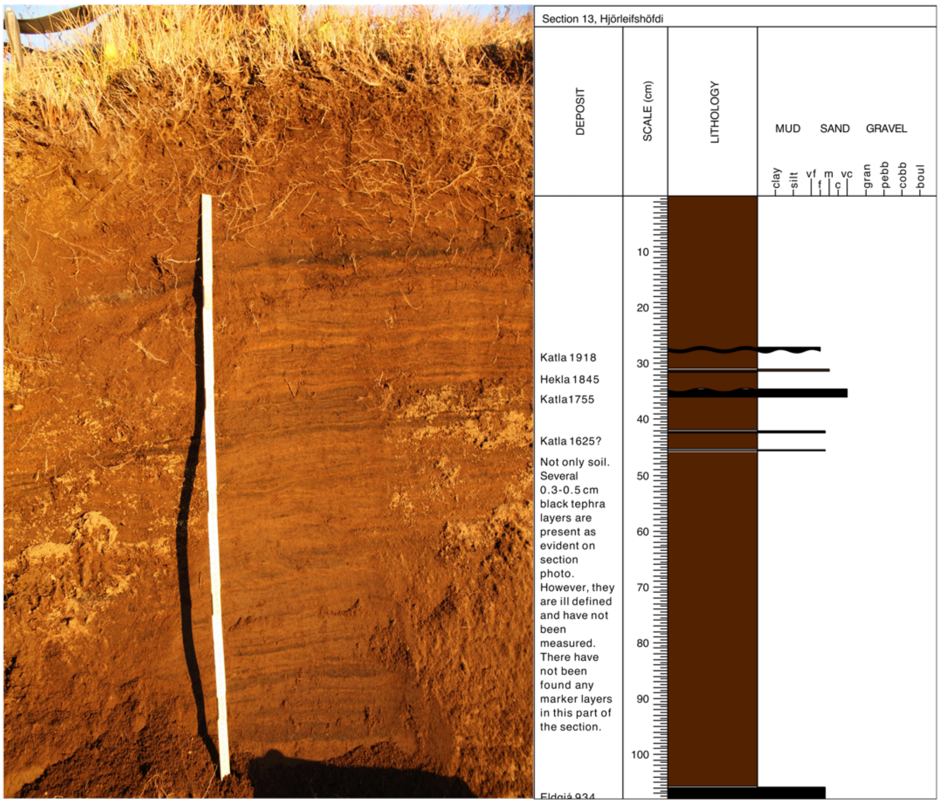

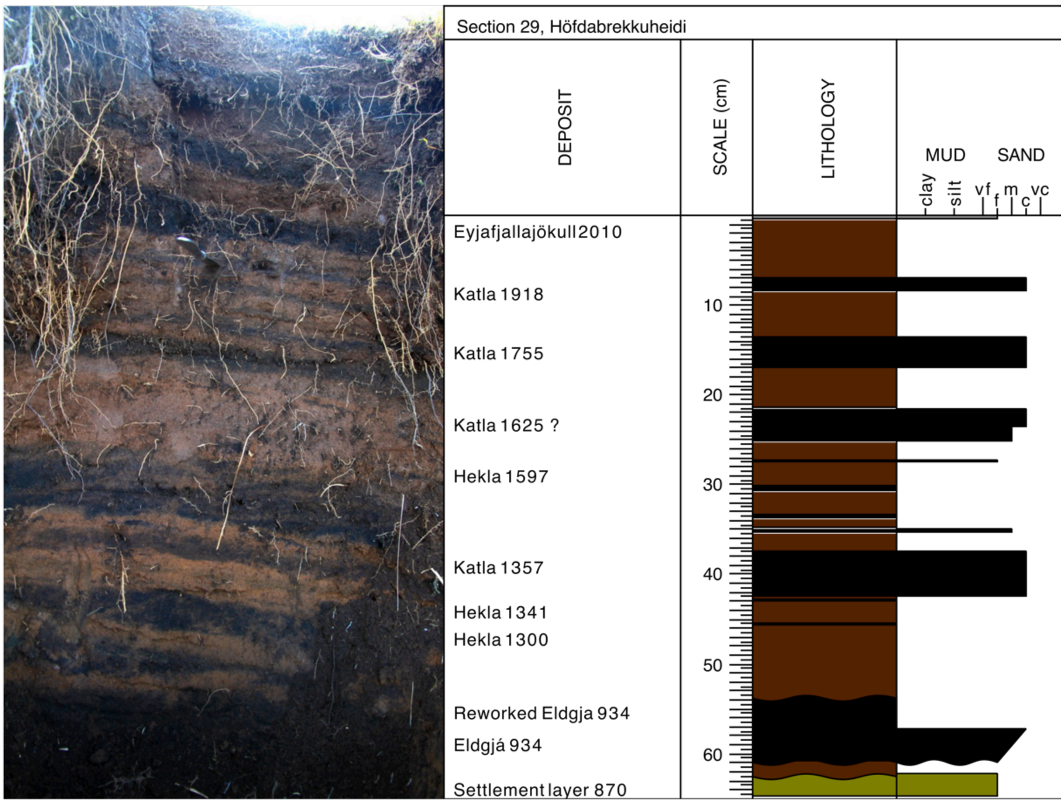

Appendix A – soil sections

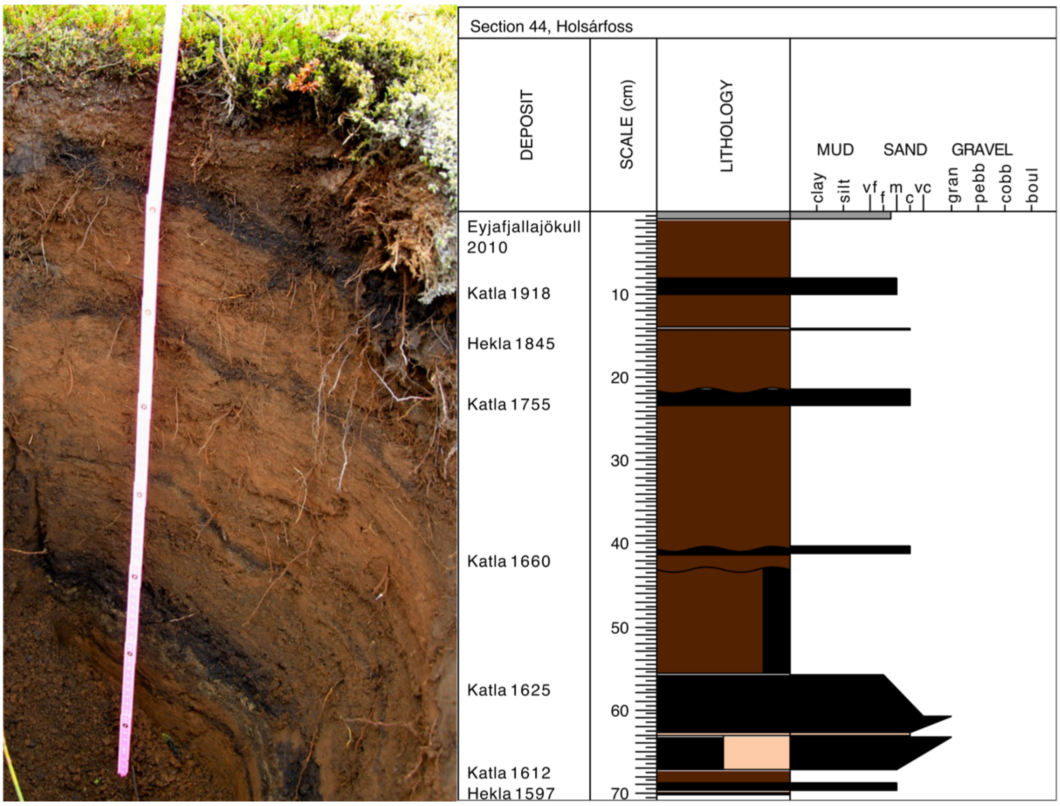

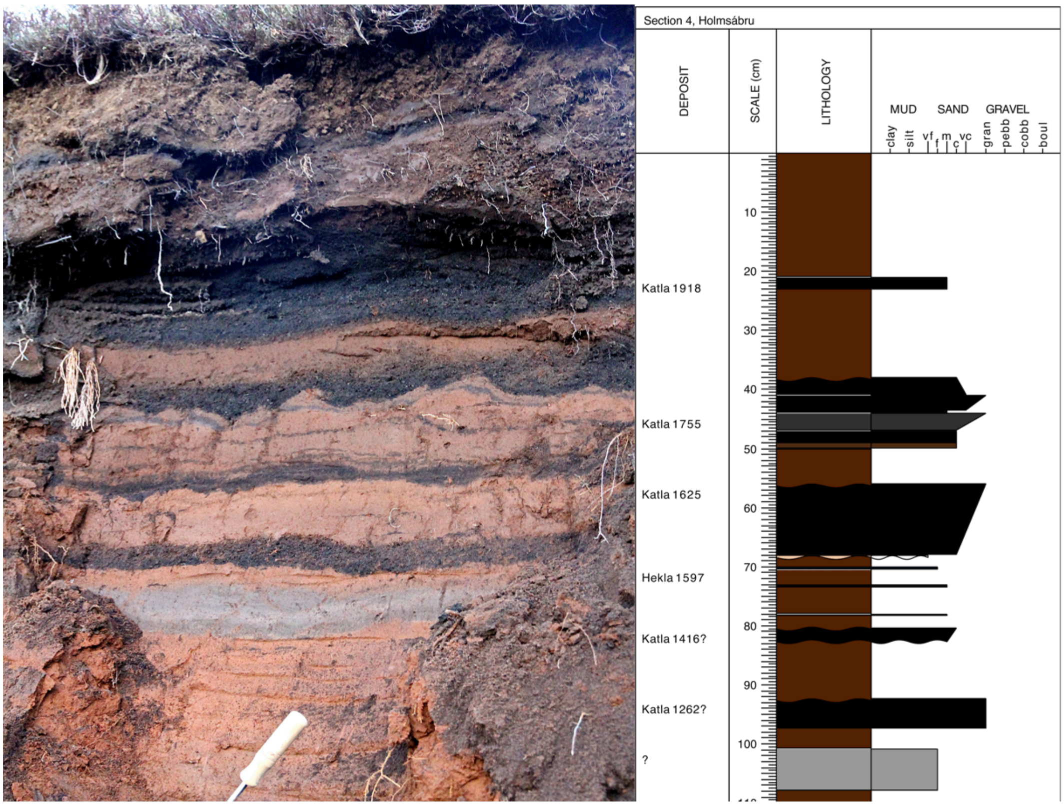

Appendix A – soil sections

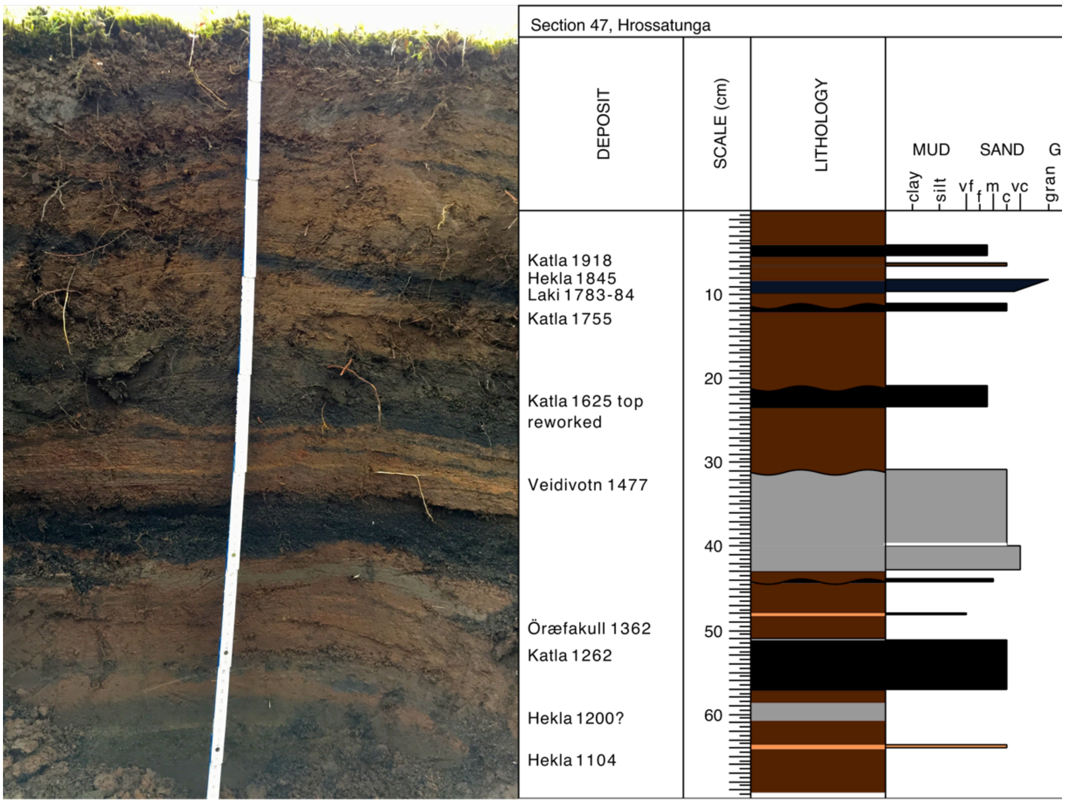

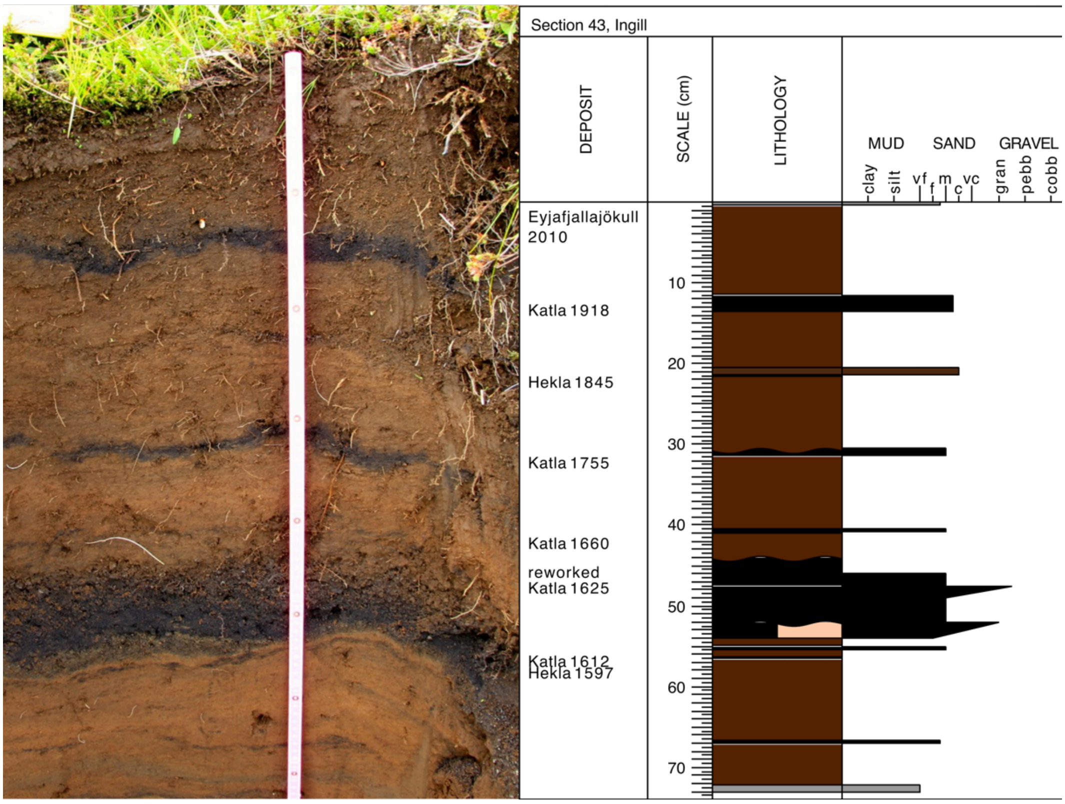

Appendix A – soil sections

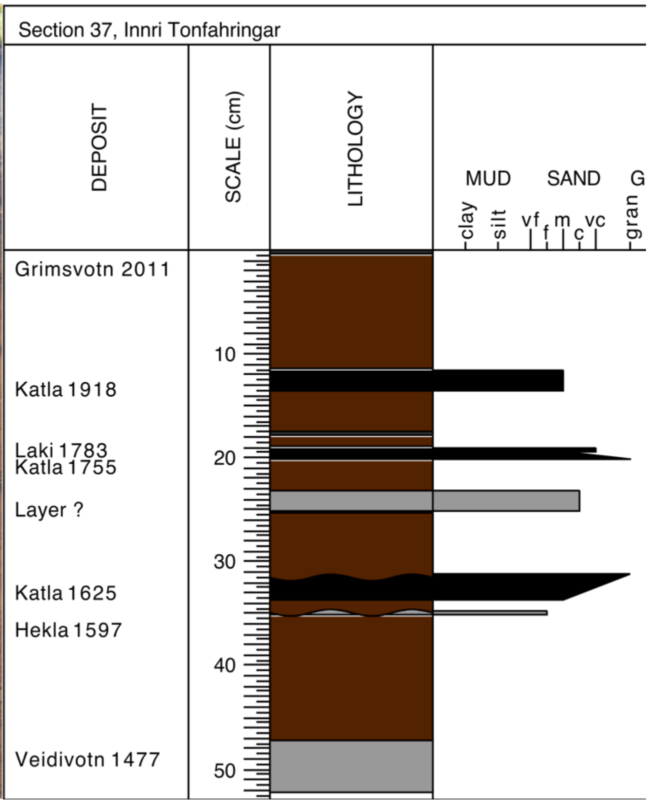

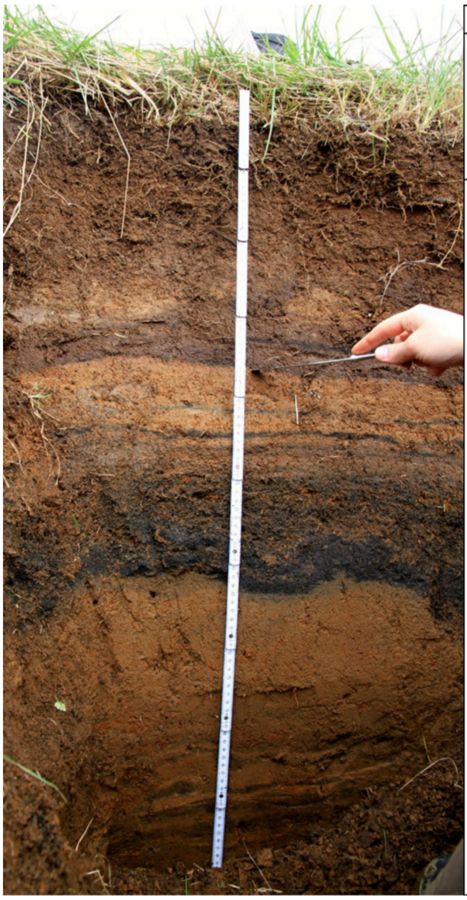

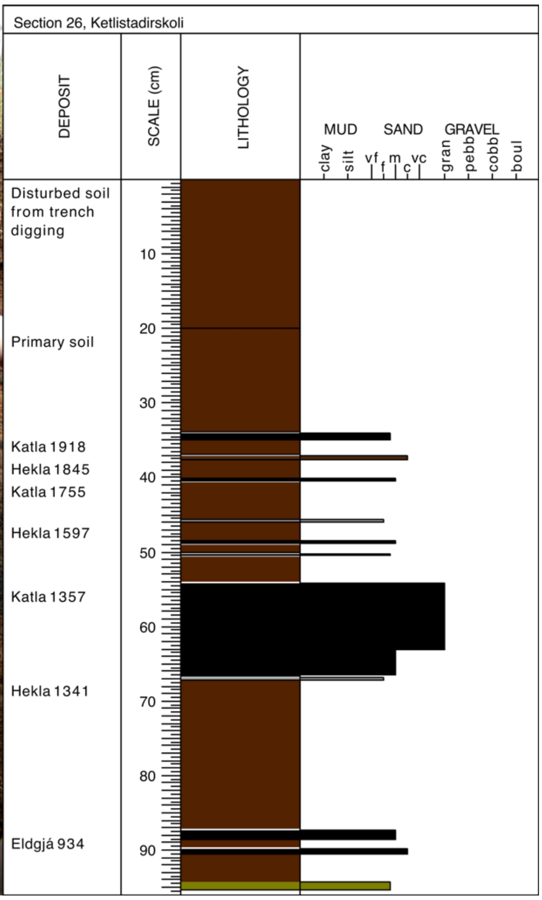

Appendix A – soil sections

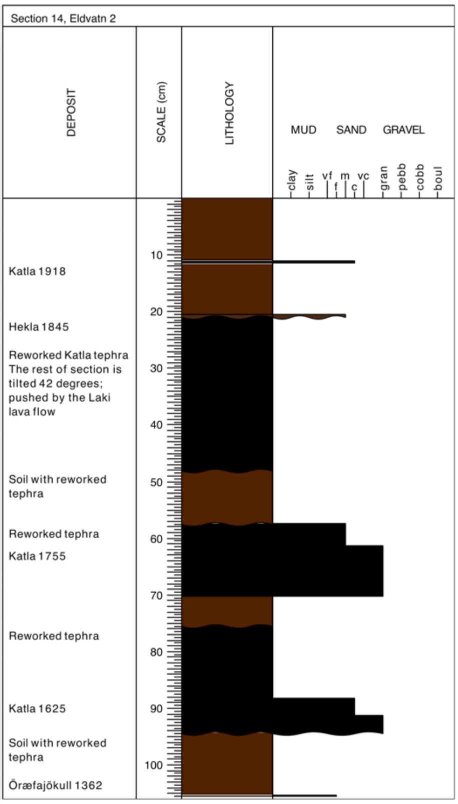

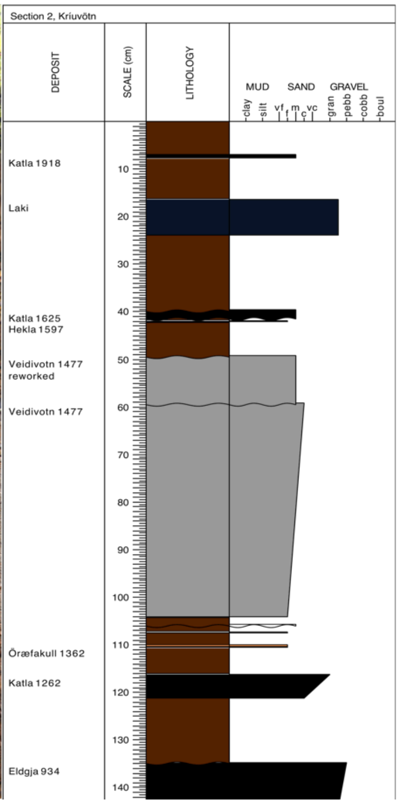

Appendix A – soil sections

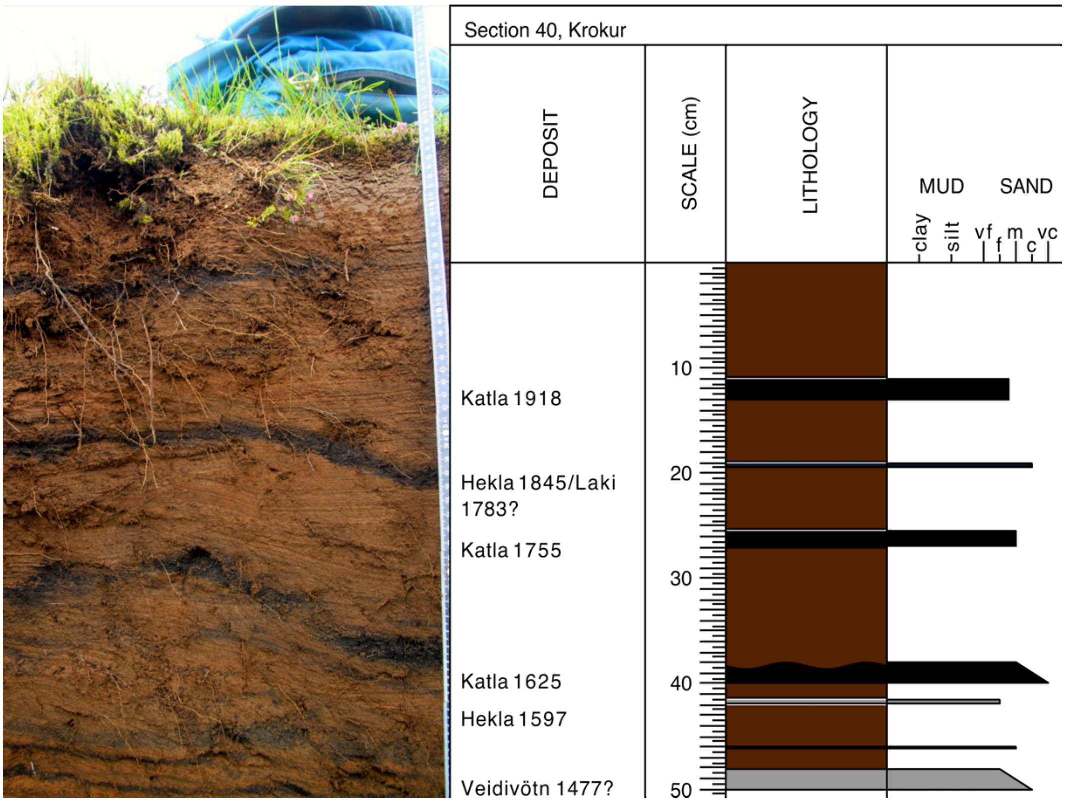

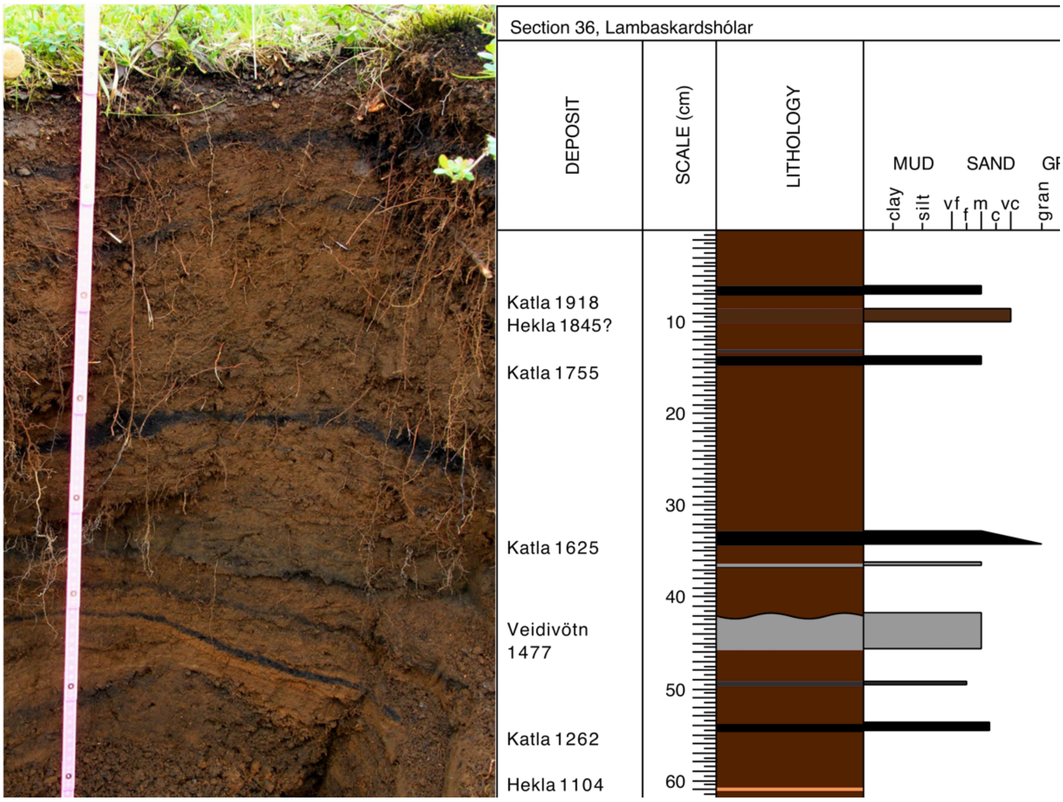

Appendix A – soil sections

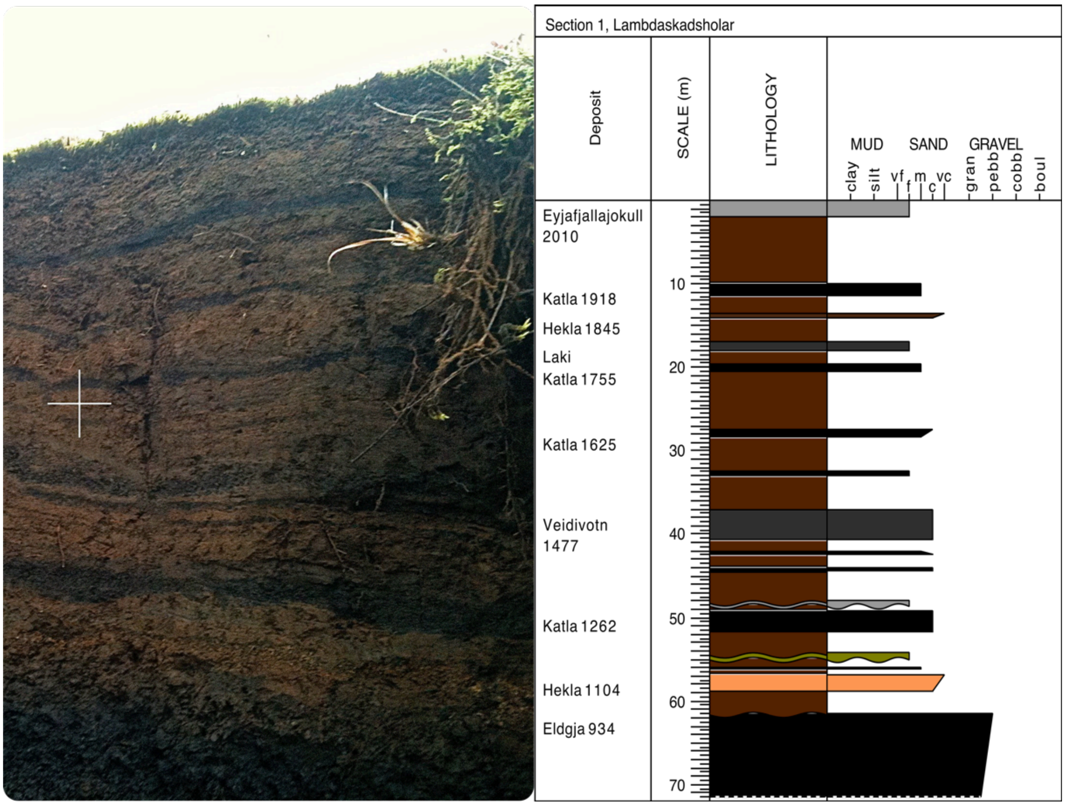

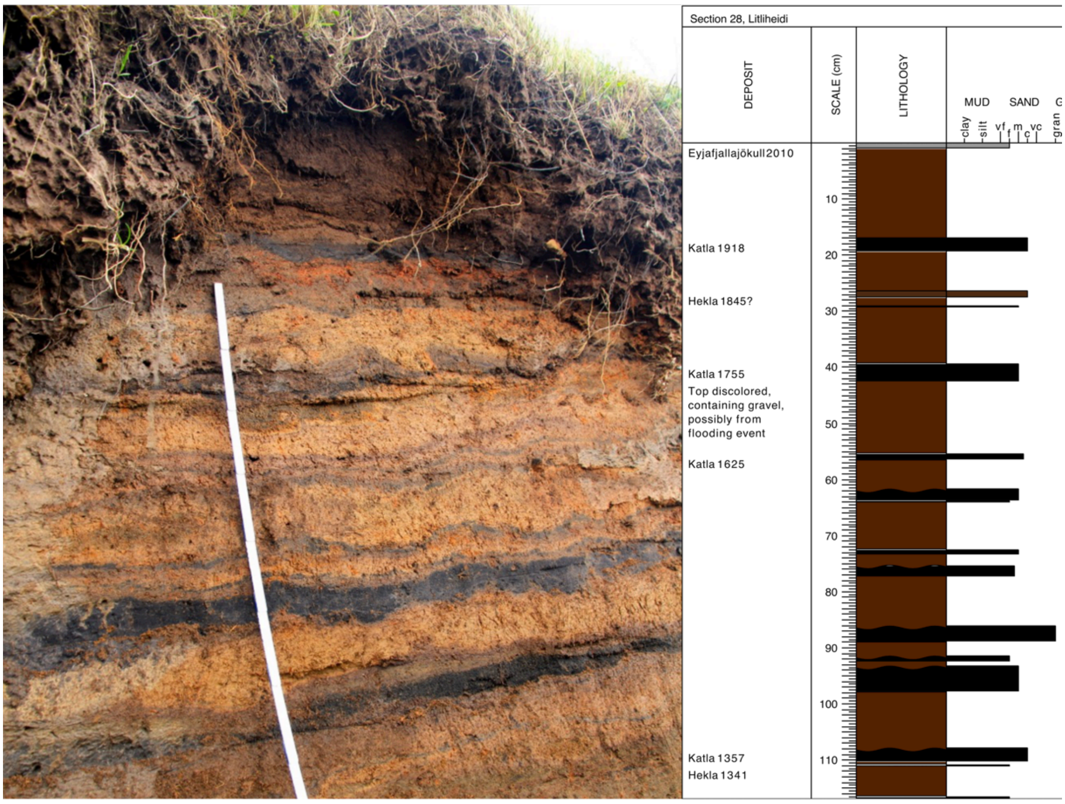

Appendix A – soil sections

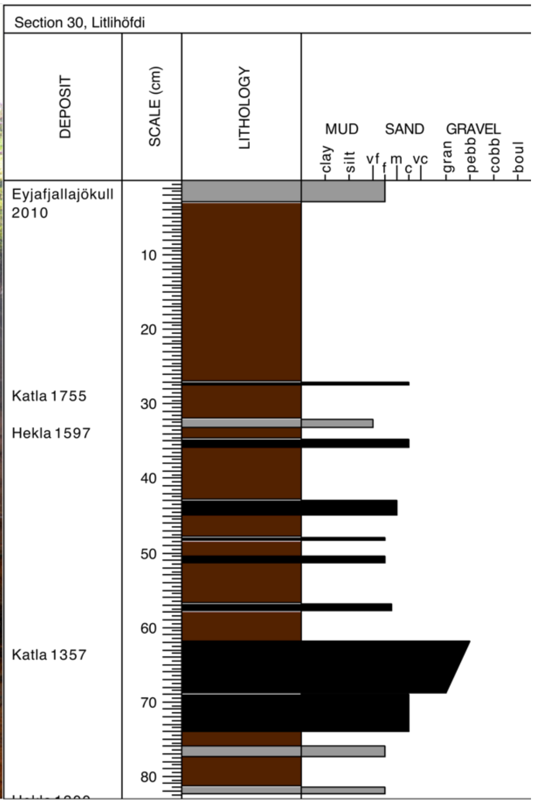

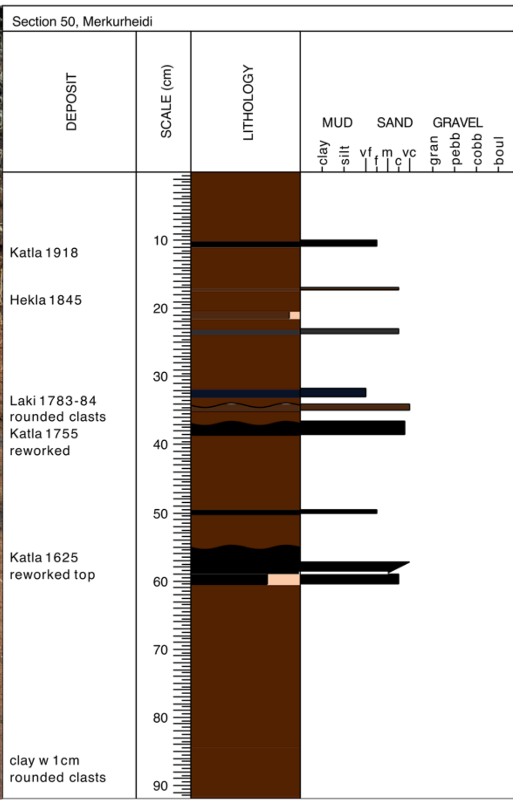

Appendix A – soil sections

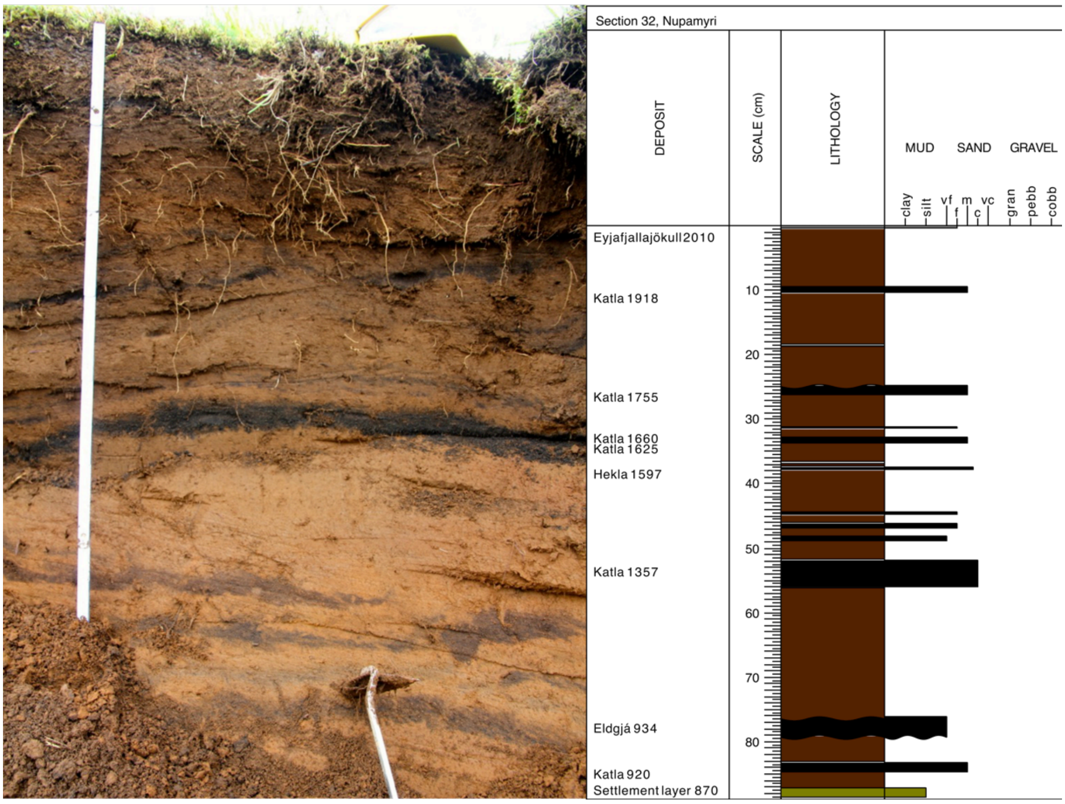

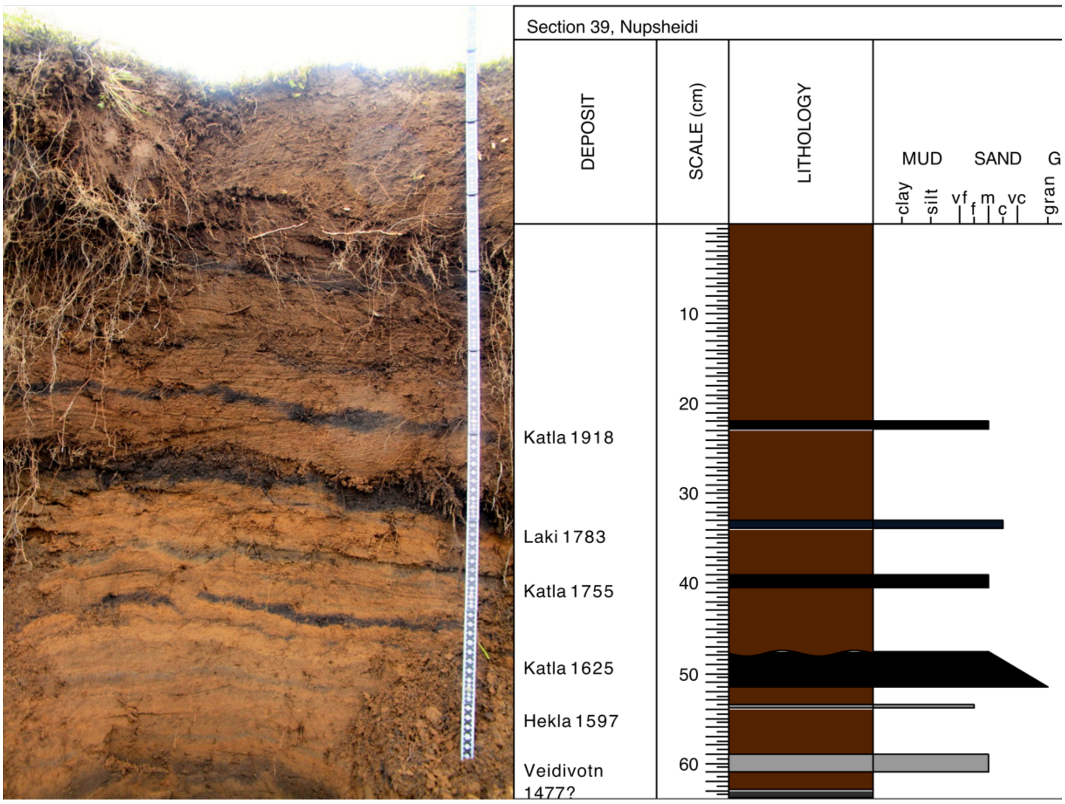

Appendix A – soil sections

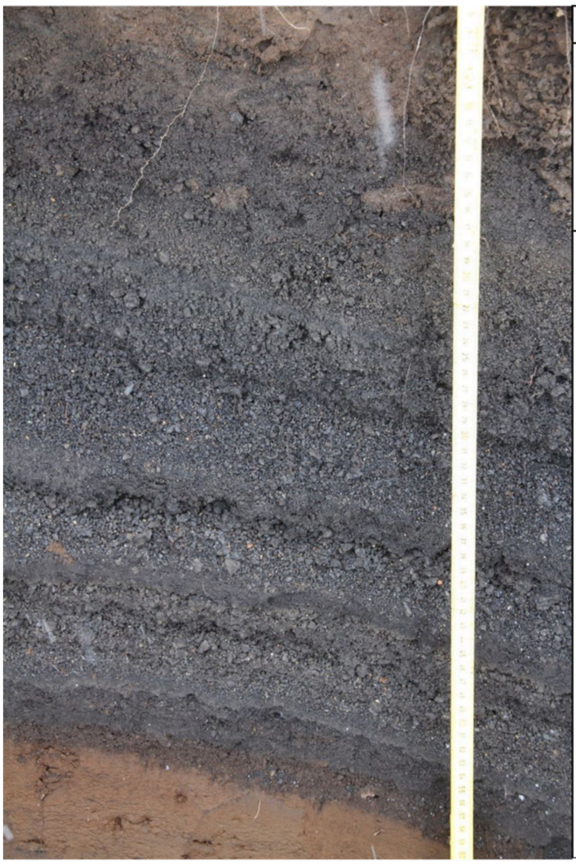

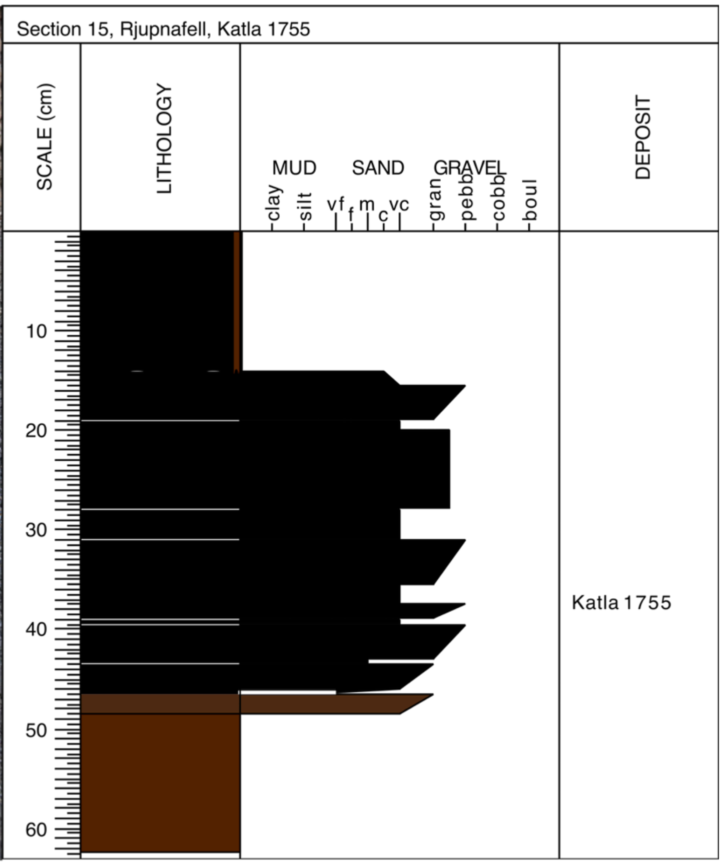

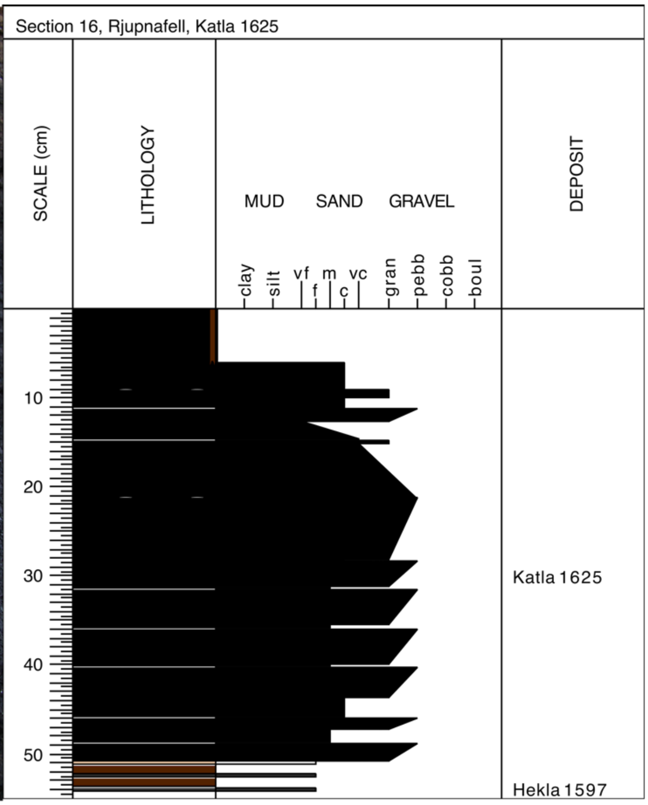

Appendix A – soil sections

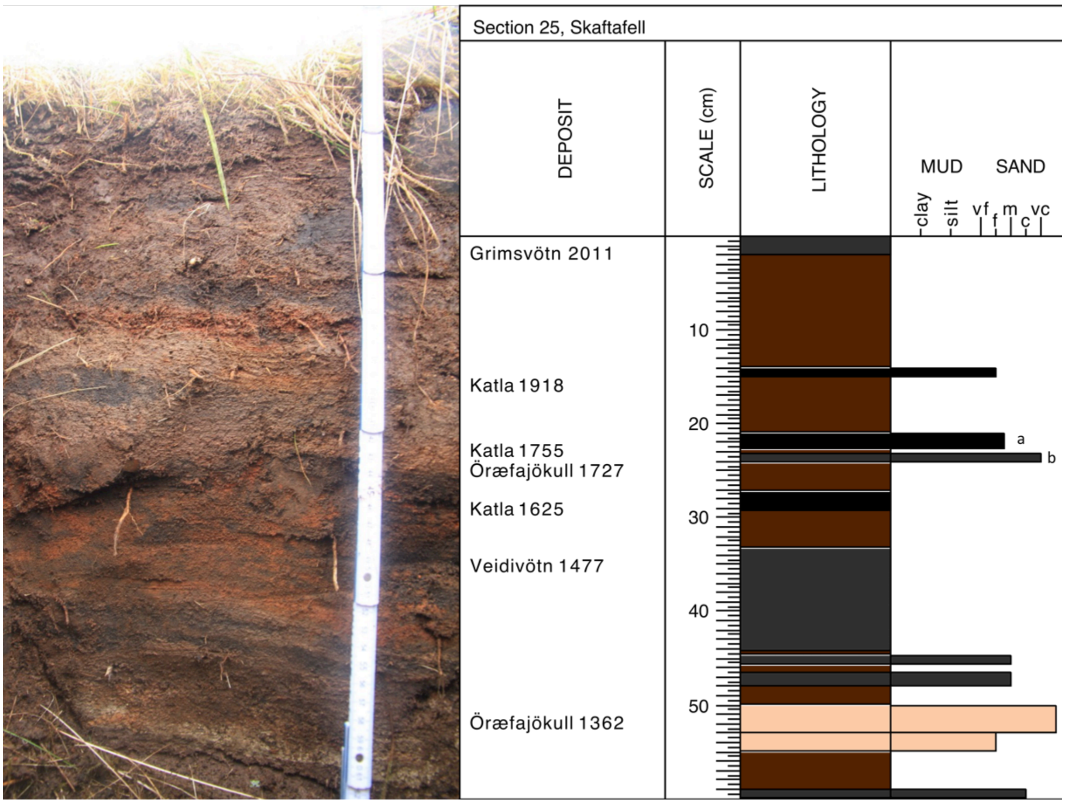

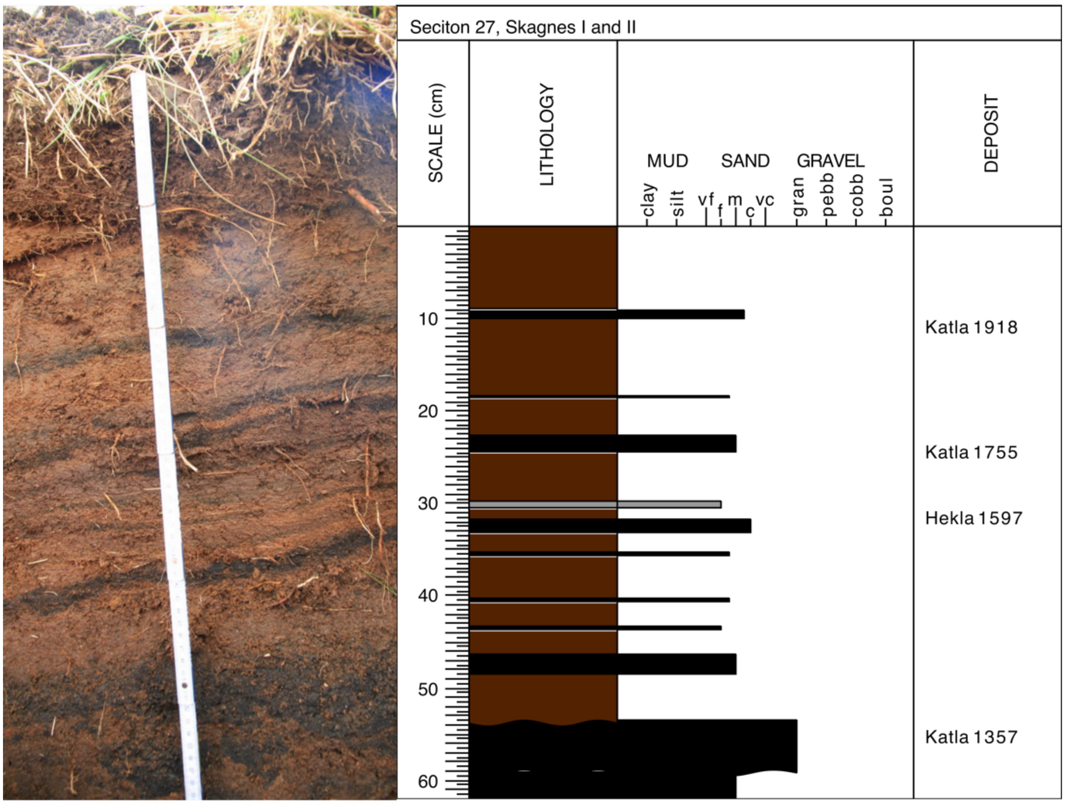

Appendix A – soil sections

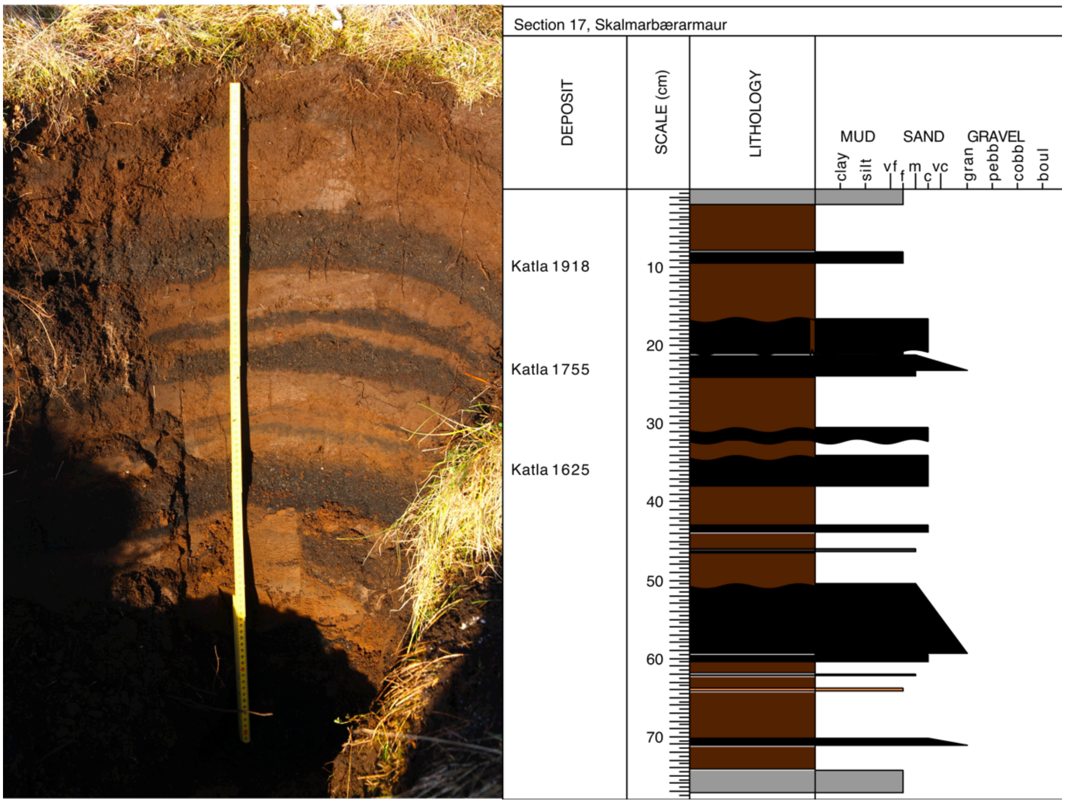

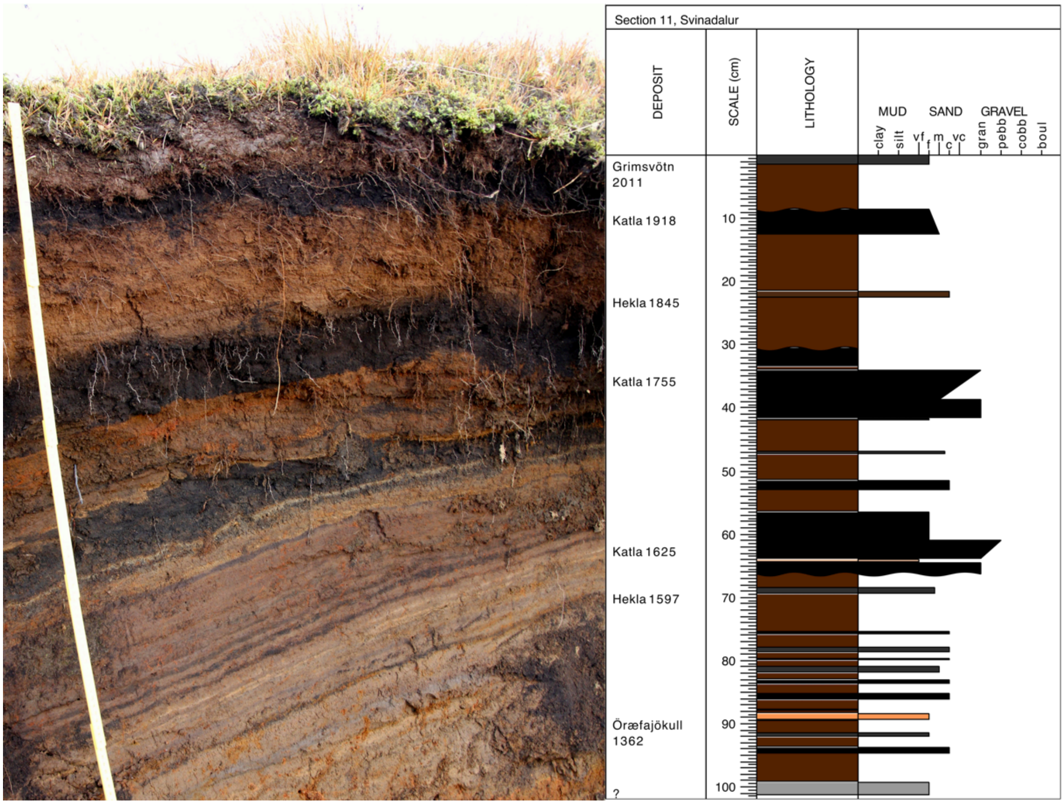

Appendix A – soil sections

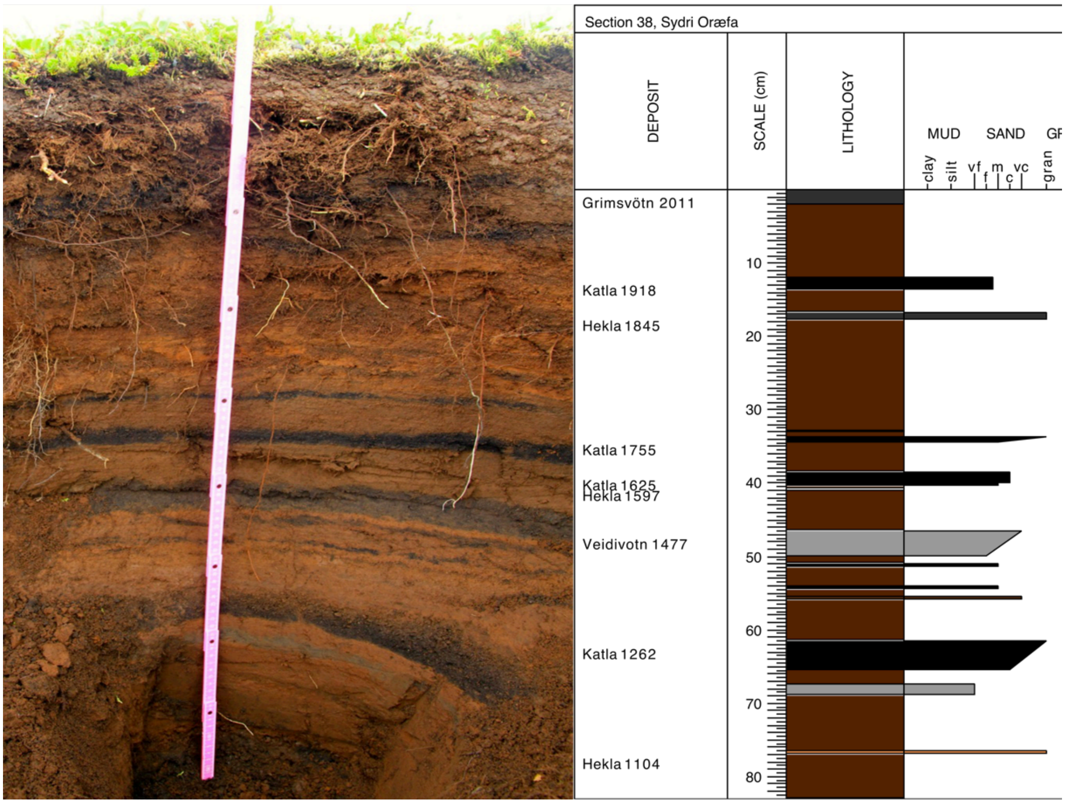

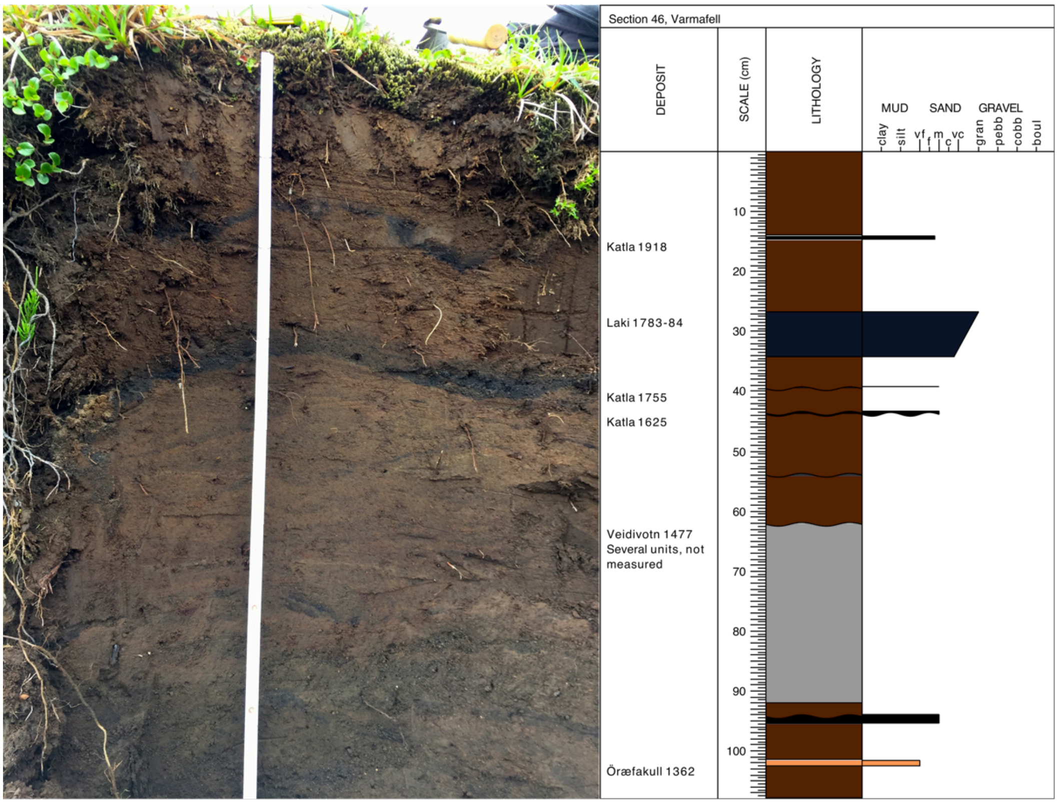

Appendix A – soil sections

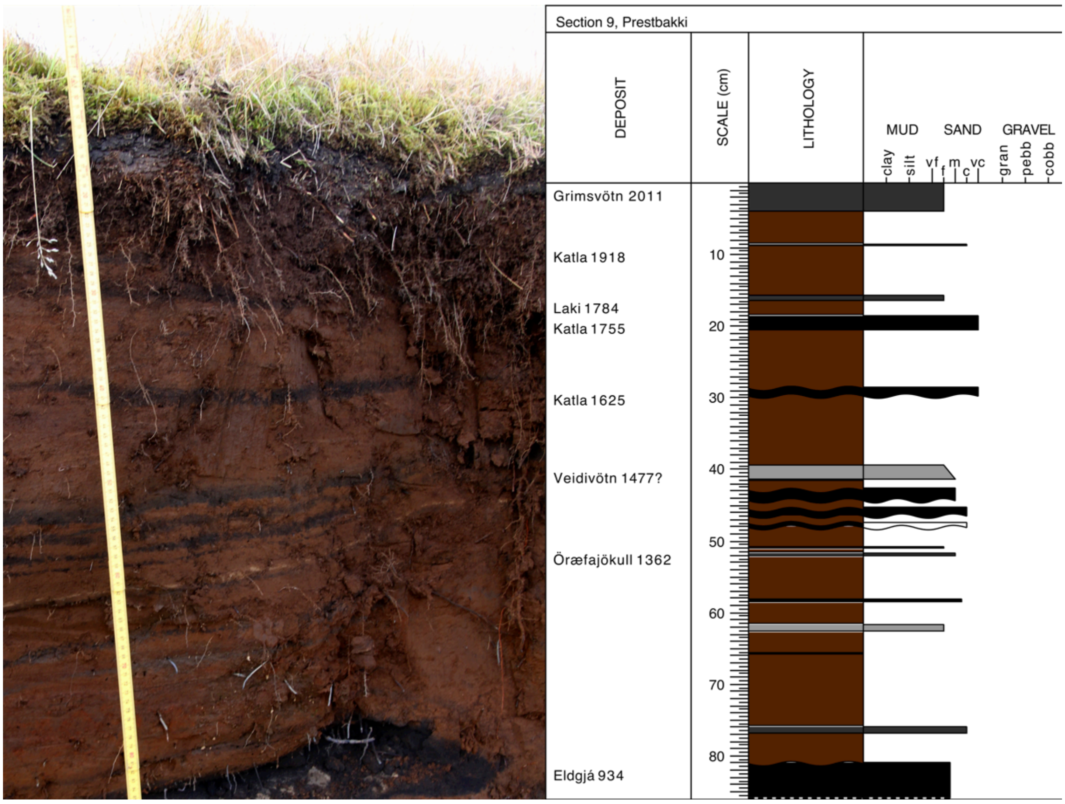

Appendix A – soil sections

Discarded sections

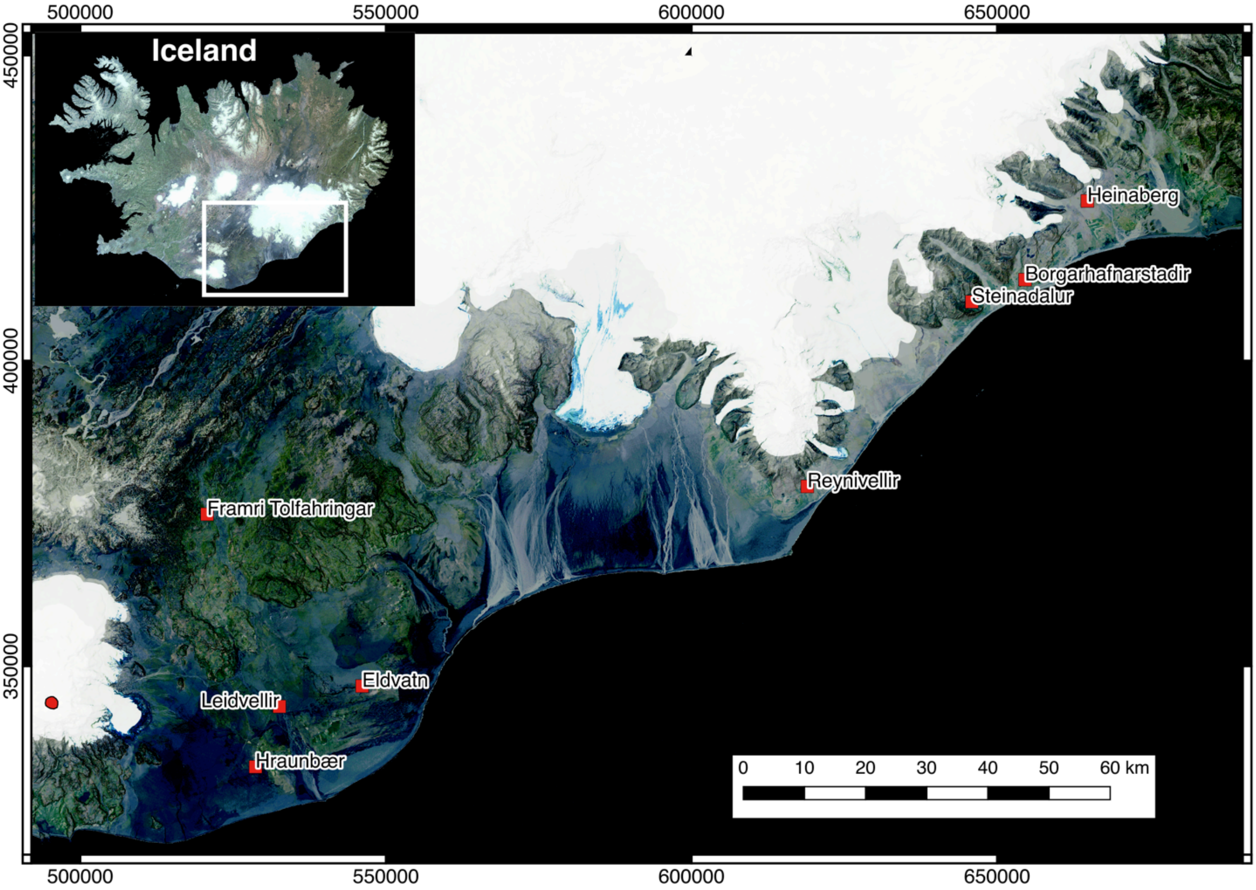

Map of discarded sections. Discarded sections are listed alphabetically below.

Discarded section. Eldvatn, section 6. Flow deposits

Discarded section. Leidvellir section 7, prehistoric layers

Appendix A – soil sections

Discarded section. Hraunbær, section 12. Flow deposits.

Appendix A – soil sections

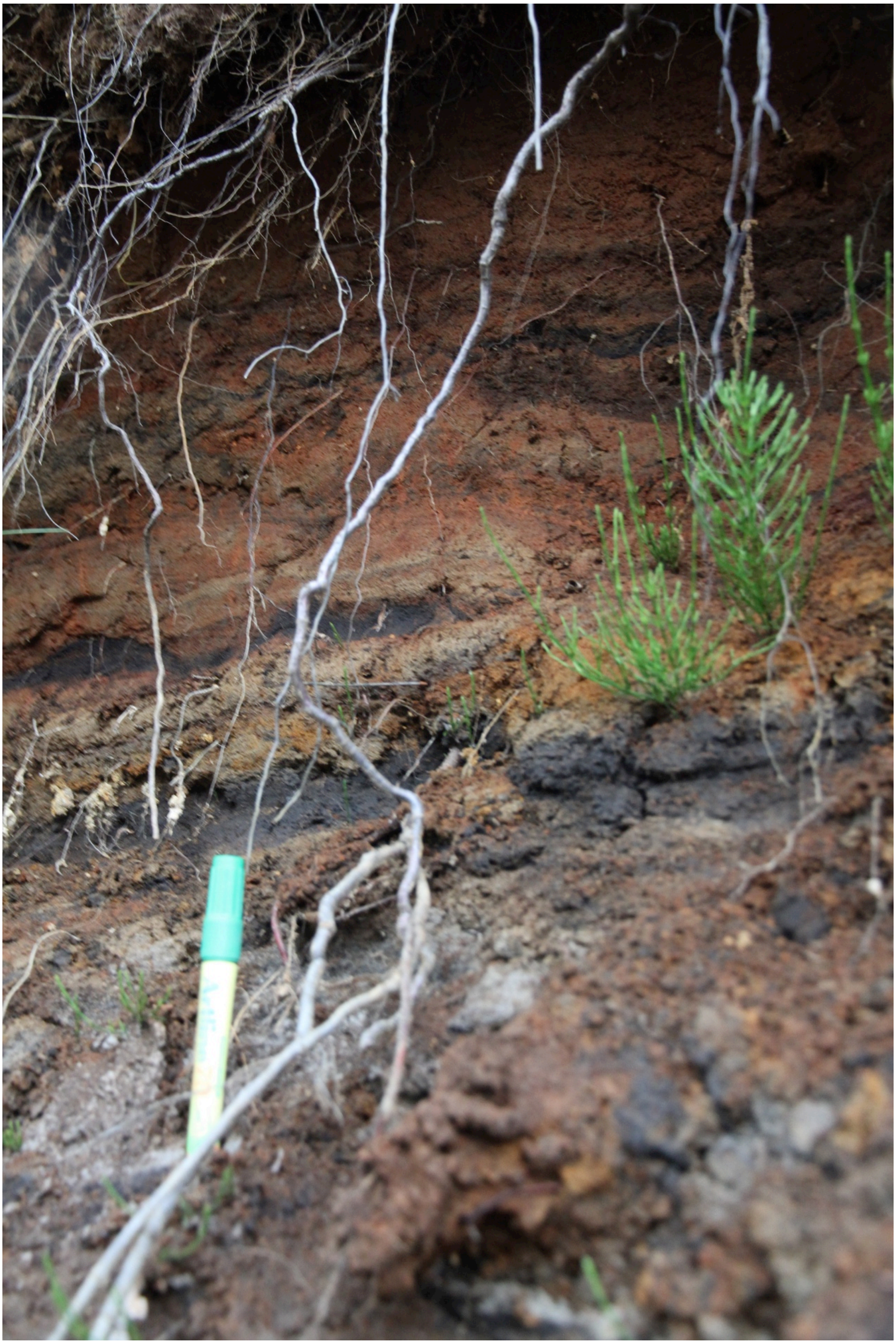

Discarded section. Steinadalur, section 19. Poor stratigraphic control.

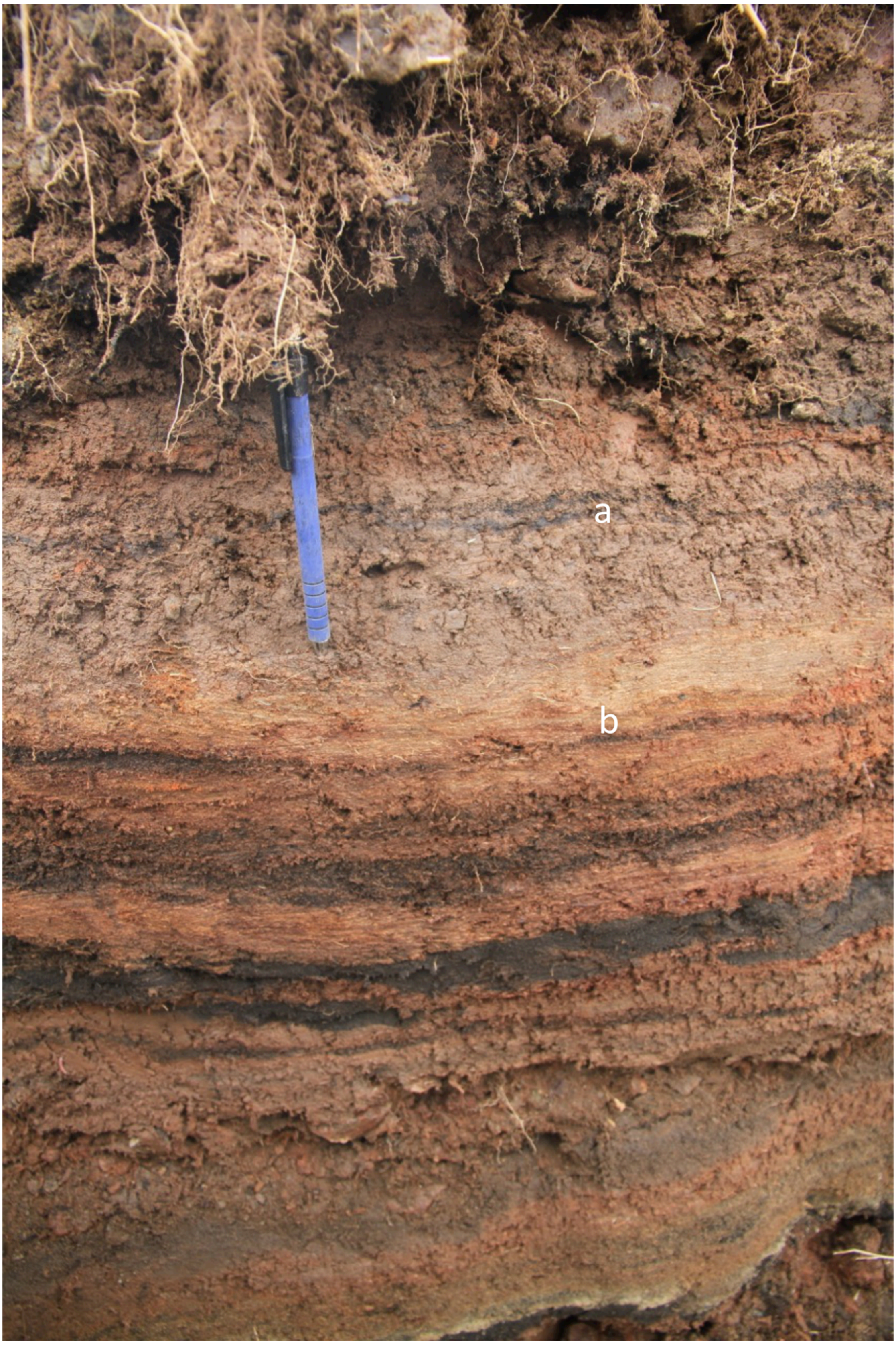

Discarded section. Reynivellir, section 22. Discarded based on geochemical analyses.

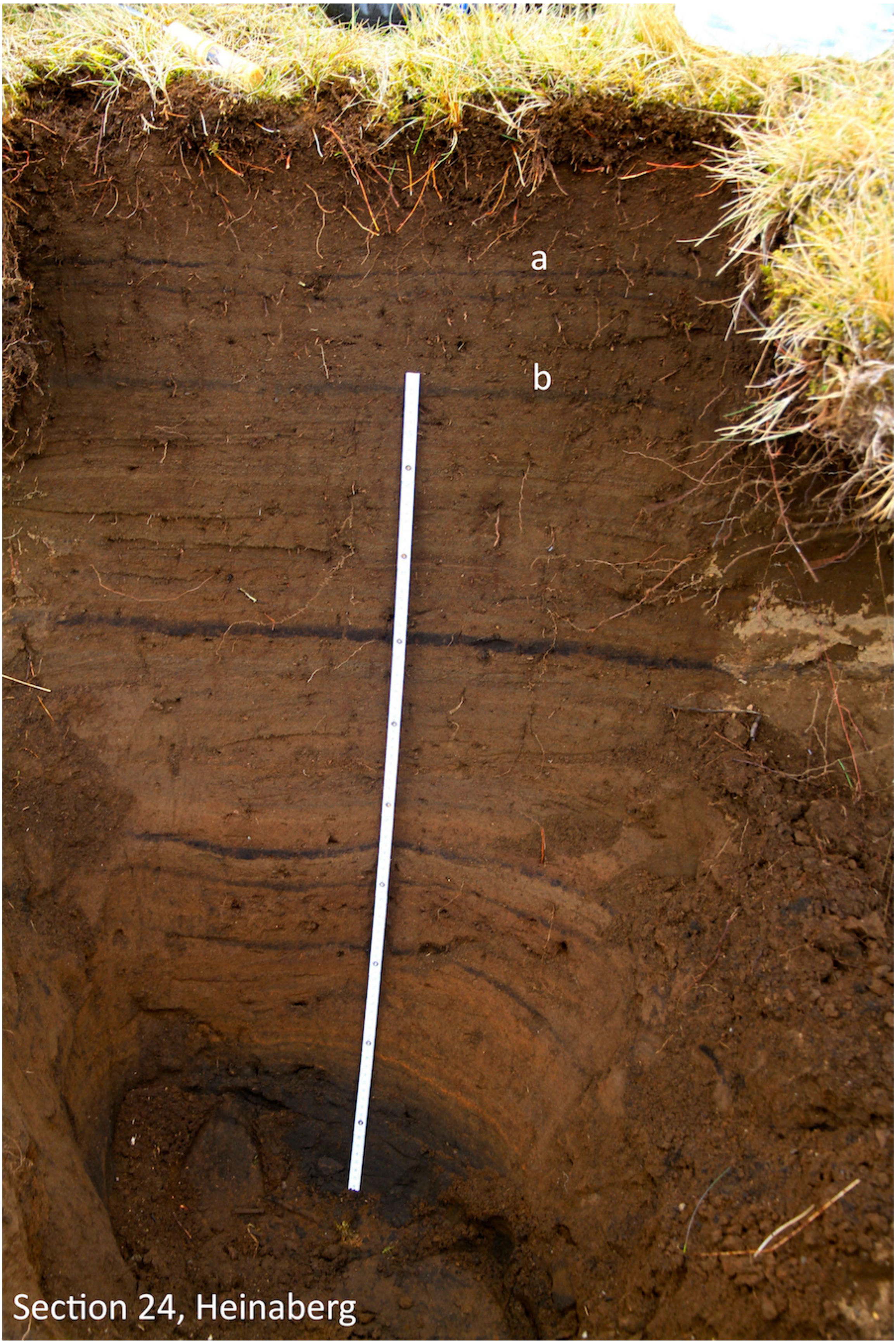

Discarded section. Heinaberg, section 24. Discarded based on geochemical analyses.

Appendix A – soil sections

Discarded section. Framri Tolfahringar, section 34. Poor preservation compared to nearby section.

Appendix B – soil section coordinates

Locality	Gps-coordinates (wgs 84)		Sec no.	Locality	Gps-coordinates (wgs 84)		Sec no.
Alftaver (2)	63.5224	-18.3528	16	Hrossatunga	63.9571	-18.4008	47
Armundabotna	63.9594	-18.2504	48	Inngil	63.7353	-18.7344	43
Atlay	63.6729	-18.6489	53	Innri Tónfahringar	63.8716	-18.5890	37
Blagil	63.9663	-18.3229	3	Ketlistadirskóli	63.4351	-19.1635	26
Bleikóluhraun	63.8777	-18.5738	35	Kipuka, Endvatn 2	63.6261	-18.0613	14
Blómsturvallafjall	63.9569	-17.6889	8	Kríuvötn	64.0211	-18.2494	2
Dalurfell	63.9139	22.7301	18	Krókur	63.7861	-18.5344	40
Djupadalur	64.0193	-17.6866	20	Lambaskradshólar	63.9144	-18.6038	36
Einhyrningar E	63.7666	-18.7713	42	Lambdashodsholar	63.9226	-18.6284	1
Eintunahals	63.8362	-18.2199	51	Litliheidi	63.4713	-18.9914	28
Engigardur	63.4571	-19.0387	33	litlihöfdi	63.4814	-19.1552	30
Eystri-dalbær	63.7653	-17.9537	5	Merkurheidi	63.8162	-18.2126	50
Fagrifoss S	63.8664	-18.2588	49	Nupamyri	63.4508	-18.8772	32
Fjaldrárgljúfur	63.7684	-18.1882	10	Nupsheidi	63.8045	-18.5722	39
Gröf	63.9130	-16.7243	21	Rjúpnafell	63.6299	-18.6588	15
Gröf + kirkja	63.7282	-18.5224	41	Skaftafell	64.0321	-16.9893	25
Heidi	63.4866	-18.9568	31	Skagnes I and II	63.4569	-19.1352	27
Hellnamyri	63.8237	-18.3305	52	Skalmarbæramaur	63.5797	-18.3772	17
Hemra	63.6896	-18.5010	45	Svinadalur	63.6978	-18.4363	11
Hjörleifshöfdi	63.4169	-18.7547	13	Sydri Oræfa	63.8593	-18.5621	38
Höfdabrekkuheidi	63.4962	-18.8756	29	Varmafell	64.0540	-18.2117	46
Holmsárfoss	63.7101	-18.7253	44	W Prestbakki	63.8300	-18.0533	9
Hrifunes	63.6330	-18.5042	4				

Table B1. Sections included in the study. Locality names refer to place names in the vicinity of the section site.

Locality	Gps-coordinates (wgs 84)		Sec no.	Comments
Eldvatn	63.6223	-18.0703	6	Mixed with flooding deposits
Leidvellir	63.5938	-18.3438	7	Prehistoric layers
Hraunbær	63.50557	-18.42432	12	Flooding deposit
Steinadalur	64.15862	-16.00111	19	Sampled primarily for Öræfakjökull 1362 and strategraphic control not good enough
Reynivellir	63.89807	-16.57772	22	Layers were not from Katla (geochemistry)
Borgarhafnarstadir	64.1872	-15.81861	23	Layers were not from Katla (geochemistry)
Heinaberg	64.298	-15.59486	24	Layers were not from Katla (geochemistry)
Framri Tólfahringar	63.87702	-18.57784	34	Poor preservation and a better section was found at Bleikóluhraun (35)

Table B2. Sections discarded from study. The reason for discarding each section is described in the comments.

Appendix C – Geochemical analyses of tephra grains

Katla 1755	SiO2	FeO	K2O	TiO2	Na2O	Al2O3	MnO	CaO	Cr2O3	F	P2O5	MgO	O	Total
	47,35	15,01	0,76	4,77	3,18	12,52	0,28	9,54	0,00	0,10	0,74	4,78	0,00	99,03
	47,25	14,58	0,73	4,97	3,14	12,75	0,26	9,70	0,00	0,00	0,75	5,00	0,00	99,13
	47,88	15,65	0,69	5,08	3,01	12,72	0,20	9,86	0,00	0,06	0,68	5,17	0,00	100,99
	47,83	15,13	0,74	5,07	2,85	12,81	0,24	9,75	0,00	0,02	0,68	5,08	0,00	100,20
	46,06	15,62	0,77	4,79	3,28	11,97	0,26	9,32	0,02	0,01	0,78	4,60	0,00	97,48
	47,17	15,13	0,74	4,80	3,17	12,25	0,19	9,62	0,02	0,01	0,80	5,03	0,00	98,94
	46,92	15,54	0,78	4,75	3,12	12,40	0,24	9,61	0,01	0,06	0,64	4,88	0,00	98,95
	47,25	14,78	0,74	4,68	3,14	12,66	0,22	9,49	0,00	0,00	0,70	4,95	0,00	98,60
	47,14	14,76	0,78	4,76	3,16	12,76	0,23	9,52	0,04	0,10	0,72	5,10	0,00	99,06
	47,52	14,68	0,71	4,72	3,29	12,62	0,16	9,53	0,00	0,03	0,67	5,03	0,00	98,96
Avg.	**47,24**	**15,09**	**0,74**	**4,84**	**3,13**	**12,55**	**0,23**	**9,59**	**0,01**	**0,04**	**0,72**	**4,96**	**0,00**	**99,13**
SD	**0,49**	**0,38**	**0,03**	**0,14**	**0,12**	**0,25**	**0,03**	**0,14**	**0,01**	**0,04**	**0,05**	**0,16**	**0,00**	**0,88**

Katla 1625	SiO2	FeO	K2O	TiO2	Na2O	Al2O3	MnO	CaO	Cr2O3	F	P2O5	MgO	O	Total
	47,01	15,25	0,74	4,84	3,22	12,32	0,22	9,36	0,00	0,00	0,78	4,97	0,00	98,71
	46,72	15,18	0,78	4,86	3,30	12,26	0,19	9,49	0,01	0,03	0,77	4,97	0,00	98,56
	47,10	14,55	0,65	4,62	3,19	12,40	0,26	9,60	0,02	0,13	0,78	4,99	0,00	98,30
	47,24	14,91	0,82	4,68	3,25	12,37	0,26	9,38	0,00	0,08	0,76	4,94	0,00	98,69
	46,76	14,63	0,70	4,66	3,29	12,71	0,18	9,60	0,03	0,01	0,78	5,05	0,00	98,40
	46,07	14,74	0,78	4,71	3,33	12,35	0,18	9,40	0,00	0,06	0,69	5,12	0,00	97,42
	47,38	14,89	0,75	4,66	3,29	12,48	0,31	9,72	0,00	0,11	0,69	5,02	0,00	99,29
	47,01	14,55	0,69	4,76	3,32	12,46	0,21	9,61	0,01	0,03	0,76	4,97	0,00	98,38
	46,80	15,15	0,72	4,85	3,19	12,26	0,21	9,57	0,00	0,01	0,77	4,92	0,00	98,44
	47,04	14,65	0,72	4,97	3,27	12,43	0,18	9,46	0,00	0,05	0,73	4,97	0,00	98,47
Avg.	**46,91**	**14,85**	**0,73**	**4,76**	**3,27**	**12,40**	**0,22**	**9,52**	**0,01**	**0,05**	**0,75**	**4,99**	**0,00**	**98,47**
SD	**0,34**	**0,25**	**0,05**	**0,11**	**0,05**	**0,12**	**0,04**	**0,11**	**0,01**	**0,04**	**0,03**	**0,06**	**0,00**	**0,44**

Section 21a	SiO2	FeO	K2O	TiO2	Na2O	Al2O3	MnO	CaO	Cr2O3	F	P2O5	MgO	O	Total
	47,71	13,02	0,23	1,92	2,54	12,86	0,18	11,35	0,04	0,00	0,24	6,45	0,00	96,54
	48,95	13,02	0,23	1,84	2,51	13,50	0,26	11,60	0,02	0,06	0,15	6,44	0,00	98,57
	48,96	12,65	0,22	1,89	2,52	13,17	0,23	11,53	0,00	0,00	0,15	6,56	0,00	97,87
	49,88	9,38	0,00	1,32	0,30	3,84	0,24	19,10	0,29	0,00	0,04	15,80	0,00	100,19
	50,78	9,28	0,00	0,94	0,25	2,68	0,23	18,94	0,16	0,00	0,02	16,78	0,00	100,07
	52,67	10,04	0,01	0,68	0,23	1,76	0,35	16,21	0,14	0,00	0,02	18,58	0,00	100,69
	50,29	15,12	0,28	3,09	3,37	13,29	0,29	9,64	0,02	0,05	0,37	5,09	0,00	100,90
	50,51	13,95	0,27	2,98	3,09	13,31	0,24	9,82	0,05	0,00	0,22	5,68	0,00	100,12
	50,68	13,35	0,29	3,20	2,93	13,28	0,18	10,42	0,00	0,00	0,35	6,22	0,00	100,90
	50,05	12,20	0,17	1,98	1,97	9,74	0,24	13,18	0,08	0,01	0,17	9,73	0,00	99,54
Avg.	**1,33**	**1,99**	**0,12**	**0,88**	**1,24**	**4,96**	**0,05**	**3,61**	**0,09**	**0,02**	**0,13**	**5,24**	**0,00**	**1,45**
SD	**47,71**	**13,02**	**0,23**	**1,92**	**2,54**	**12,86**	**0,18**	**11,35**	**0,04**	**0,00**	**0,24**	**6,45**	**0,00**	**96,54**

Section 21b	SiO2	FeO	K2O	TiO2	Na2O	Al2O3	MnO	CaO	Cr2O3	F	P2O5	MgO	O	Total
	46,86	14,85	0,79	4,81	3,27	12,58	0,18	9,52	0,00	0,09	0,74	5,05	0,00	98,74
	46,55	14,83	0,70	4,86	3,20	12,44	0,26	9,75	0,01	0,08	0,72	5,12	0,00	98,53
	46,24	15,73	0,73	4,81	3,18	12,21	0,16	9,63	0,02	0,10	0,69	5,02	0,00	98,52
	46,47	15,18	0,75	4,55	3,07	12,41	0,15	9,84	0,00	0,05	0,65	4,92	0,00	98,04
	47,19	14,81	0,67	4,79	3,29	12,41	0,30	9,63	0,00	0,02	0,68	5,12	0,00	98,91
	47,25	15,08	0,71	4,94	3,26	12,63	0,34	9,51	0,04	0,00	0,70	5,12	0,00	99,58
	46,70	14,78	0,70	4,76	3,20	12,59	0,24	9,65	0,00	0,08	0,77	5,11	0,00	98,58
	46,69	15,02	0,79	4,85	3,26	12,49	0,26	9,72	0,03	0,01	0,75	5,11	0,00	98,98
	46,82	15,12	0,71	4,94	3,29	12,54	0,16	9,61	0,00	0,08	0,71	5,11	0,00	99,10
	47,01	15,22	0,69	4,63	3,20	12,59	0,22	9,71	0,00	0,06	0,56	5,12	0,00	99,01
Avg.	**46,78**	**15,06**	**0,72**	**4,79**	**3,22**	**12,49**	**0,23**	**9,66**	**0,01**	**0,06**	**0,70**	**5,08**	**0,00**	**98,80**
SD	**0,30**	**0,27**	**0,04**	**0,12**	**0,06**	**0,12**	**0,06**	**0,10**	**0,01**	**0,03**	**0,06**	**0,06**	**0,00**	**0,40**

Appendix C – Geochemical analyses of tephra grains

Section 21c	SiO2	FeO	K2O	TiO2	Na2O	Al2O3	MnO	CaO	Cr2O3	F	P2O5	MgO	O	Total
	46,89	15,29	0,78	5,03	2,68	12,45	0,26	9,73	0,00	0,06	0,90	5,14	0,00	99,20
	47,24	14,85	0,80	4,84	2,75	12,80	0,23	9,67	0,05	0,09	0,75	5,16	0,00	99,23
	46,80	14,74	0,74	4,53	3,33	12,56	0,14	9,67	0,00	0,08	0,79	5,00	0,00	98,38
	46,73	15,08	0,76	4,84	3,34	12,61	0,23	9,47	0,01	0,08	0,70	5,11	0,00	98,95
	47,09	14,99	0,72	4,83	3,36	12,49	0,23	9,54	0,00	0,09	0,76	5,10	0,00	99,20
	47,05	14,99	0,80	4,82	3,23	12,46	0,21	9,60	0,00	0,05	0,82	5,17	0,00	99,20
	46,81	15,45	0,68	4,93	3,33	12,26	0,24	9,58	0,00	0,06	0,67	5,05	0,00	99,07
	46,76	14,74	0,70	4,76	3,34	12,54	0,27	9,53	0,01	0,00	0,67	5,10	0,00	98,42
	46,45	15,10	0,75	4,67	3,33	12,34	0,19	9,42	0,00	0,06	0,75	5,04	0,00	98,10
	46,81	14,98	0,67	4,80	3,23	12,28	0,16	9,26	0,02	0,02	0,73	5,02	0,00	97,99
Avg.	**46,86**	**15,02**	**0,74**	**4,81**	**3,19**	**12,48**	**0,21**	**9,55**	**0,01**	**0,06**	**0,75**	**5,09**	**0,00**	**98,78**
SD	**0,21**	**0,21**	**0,04**	**0,13**	**0,24**	**0,15**	**0,04**	**0,13**	**0,02**	**0,03**	**0,07**	**0,06**	**0,00**	**0,47**

Section 22a	SiO2	FeO	K2O	TiO2	Na2O	Al2O3	MnO	CaO	Cr2O3	F	P2O5	MgO	O	Total
	49,71	14,21	0,49	3,20	3,03	12,61	0,28	9,45	0,00	0,00	0,40	5,25	0,00	98,63
	49,84	14,11	0,43	3,29	3,12	12,51	0,18	9,58	0,00	0,07	0,36	5,33	0,00	98,82
	49,50	14,28	0,50	3,20	3,13	12,69	0,20	9,58	0,02	0,00	0,42	5,25	0,00	98,77
	49,99	14,40	0,48	3,20	3,13	12,65	0,21	9,64	0,03	0,04	0,35	5,48	0,00	99,60
	49,23	14,08	0,49	3,10	3,12	12,62	0,25	9,48	0,03	0,05	0,33	5,26	0,00	98,04
	49,65	14,52	0,40	3,01	3,10	12,65	0,26	9,55	0,00	0,02	0,38	5,26	0,00	98,80
	49,83	14,43	0,45	3,22	3,04	12,68	0,23	9,35	0,01	0,02	0,28	5,25	0,00	98,80
	47,17	14,32	0,64	4,56	3,31	12,79	0,24	9,71	0,00	0,09	0,51	5,25	0,00	98,60
	49,34	12,91	0,38	2,58	2,81	13,24	0,23	10,67	0,00	0,01	0,25	6,26	0,00	98,69
	49,73	12,66	0,44	2,63	2,71	13,30	0,13	10,42	0,02	0,04	0,25	6,13	0,00	98,46
Avg.	**49,40**	**13,99**	**0,47**	**3,20**	**3,05**	**12,77**	**0,22**	**9,74**	**0,01**	**0,04**	**0,35**	**5,47**	**0,00**	**98,72**
SD	**0,78**	**0,62**	**0,07**	**0,51**	**0,16**	**0,26**	**0,04**	**0,42**	**0,01**	**0,03**	**0,08**	**0,37**	**0,00**	**0,37**

Section 22b	SiO2	FeO	K2O	TiO2	Na2O	Al2O3	MnO	CaO	Cr2O3	F	P2O5	MgO	O	Total
	50,26	13,73	0,54	3,10	3,00	13,00	0,26	9,73	0,01	0,00	0,33	5,35	0,00	99,31
	49,86	14,01	0,48	2,95	3,06	12,99	0,18	9,63	0,01	0,01	0,32	5,45	0,00	98,95
	49,89	14,07	0,50	3,13	2,98	13,12	0,26	9,63	0,01	0,01	0,27	5,51	0,00	99,38
	50,37	14,30	0,46	3,16	3,00	12,91	0,22	9,51	0,02	0,02	0,37	5,40	0,00	99,74
	50,25	14,62	0,16	2,57	2,66	13,45	0,24	10,65	0,02	0,00	0,29	6,40	0,00	101,30
	49,83	13,79	0,41	3,13	3,36	12,97	0,21	9,79	0,06	0,01	0,33	5,10	0,00	98,98
	50,15	15,69	0,54	3,07	3,21	13,37	0,25	8,36	0,02	0,03	0,33	3,82	0,00	98,85
	50,09	14,32	0,44	3,02	3,04	13,12	0,23	9,61	0,02	0,01	0,32	5,29	0,00	99,50
	0,21	0,63	0,12	0,19	0,20	0,20	0,03	0,62	0,02	0,01	0,03	0,71	0,00	0,79
	50,26	13,73	0,54	3,10	3,00	13,00	0,26	9,73	0,01	0,00	0,33	5,35	0,00	99,31
Avg.	**49,86**	**14,01**	**0,48**	**2,95**	**3,06**	**12,99**	**0,18**	**9,63**	**0,01**	**0,01**	**0,32**	**5,45**	**0,00**	**98,95**
SD	**49,89**	**14,07**	**0,50**	**3,13**	**2,98**	**13,12**	**0,26**	**9,63**	**0,01**	**0,01**	**0,27**	**5,51**	**0,00**	**99,38**

Section 24a	SiO2	FeO	K2O	TiO2	Na2O	Al2O3	MnO	CaO	Cr2O3	F	P2O5	MgO	O	Total
	48,73	15,56	0,53	3,57	3,14	12,25	0,24	8,93	0,00	0,00	0,42	4,56	0,00	97,93
	49,85	15,25	0,55	3,38	3,10	12,60	0,29	8,79	0,00	0,00	0,37	4,56	0,00	98,75
	49,65	13,22	0,34	2,43	2,15	14,18	0,15	10,57	0,02	0,05	0,29	6,36	0,00	99,41
	49,38	12,73	0,36	2,54	2,11	14,19	0,20	11,42	0,00	0,05	0,29	6,55	0,00	99,83
	50,21	14,04	0,48	3,14	3,10	12,89	0,16	9,80	0,01	0,04	0,33	5,40	0,00	99,61
	49,95	14,12	0,56	3,04	3,07	13,03	0,28	9,56	0,00	0,02	0,31	5,24	0,00	99,18
	47,79	16,14	0,89	4,80	3,45	12,41	0,21	8,74	0,00	0,12	0,88	4,24	0,00	99,67
	47,30	15,05	0,68	4,92	3,16	12,74	0,31	10,08	0,00	0,01	0,67	5,24	0,00	100,17
	50,79	12,72	0,50	3,23	2,63	12,70	0,28	10,43	0,03	0,00	0,37	6,15	0,00	99,83
	51,38	13,46	0,52	3,14	2,89	13,02	0,23	10,05	0,00	0,00	0,29	5,69	0,00	100,68
Avg.	**49,50**	**14,23**	**0,54**	**3,42**	**2,88**	**13,00**	**0,24**	**9,84**	**0,01**	**0,03**	**0,42**	**5,40**	**0,00**	**99,50**
SD	**1,20**	**1,15**	**0,15**	**0,79**	**0,42**	**0,64**	**0,05**	**0,82**	**0,01**	**0,04**	**0,19**	**0,75**	**0,00**	**0,72**

Appendix C – Geochemical analyses of tephra grains

Section 24b	SiO2	FeO	K2O	TiO2	Na2O	Al2O3	MnO	CaO	Cr2O3	F	P2O5	MgO	O	Total
	49,97	12,66	0,24	1,96	2,76	13,47	0,25	11,08	0,03	0,01	0,15	6,45	0,00	99,03
	50,37	12,79	0,28	1,93	2,66	13,72	0,20	10,95	0,00	0,01	0,18	6,45	0,00	99,54
	50,19	12,38	0,27	1,86	2,61	13,31	0,24	11,05	0,00	0,00	0,18	6,33	0,00	98,42
	52,42	7,10	0,02	0,60	0,20	2,57	0,25	20,16	0,19	0,00	0,02	17,02	0,00	100,54
	52,42	6,81	0,02	0,59	0,22	3,08	0,21	20,32	0,27	0,00	0,00	16,71	0,00	100,65
	49,56	12,74	0,20	2,23	2,60	13,44	0,29	11,85	0,04	0,00	0,24	6,56	0,00	99,75
	49,59	11,98	0,13	2,32	2,60	13,34	0,20	12,12	0,05	0,04	0,22	7,46	0,00	100,05
	48,74	12,01	0,21	1,85	2,37	13,77	0,25	12,22	0,02	0,01	0,12	7,47	0,00	99,04
	49,33	11,88	0,19	1,90	2,27	13,89	0,20	12,34	0,01	0,01	0,15	7,54	0,00	99,70
	49,67	11,52	0,17	1,72	2,28	13,94	0,18	12,26	0,05	0,02	0,18	7,57	0,00	99,56
Avg.	**50,23**	**11,19**	**0,17**	**1,70**	**2,06**	**11,45**	**0,23**	**13,44**	**0,07**	**0,01**	**0,14**	**8,96**	**0,00**	**99,63**
SD	**1,18**	**2,15**	**0,09**	**0,58**	**0,94**	**4,32**	**0,03**	**3,44**	**0,09**	**0,01**	**0,07**	**3,98**	**0,00**	**0,65**

Section 25a	SiO2	FeO	K2O	TiO2	Na2O	Al2O3	MnO	CaO	Cr2O3	F	P2O5	MgO	O	Total
	47,35	15,38	0,71	4,90	3,19	12,51	0,28	9,53	0,01	0,08	0,67	4,94	0,00	99,54
	47,34	15,18	0,74	4,95	3,36	12,70	0,29	9,59	0,00	0,09	0,66	4,96	0,00	99,86
	46,81	15,02	0,74	4,79	3,13	12,60	0,22	9,56	0,00	0,06	0,72	4,98	0,00	98,63
	47,25	15,27	0,75	4,84	3,16	12,73	0,27	9,76	0,01	0,04	0,78	4,94	0,00	99,79
	47,24	15,13	1,01	4,80	3,19	12,91	0,27	9,92	0,03	0,03	0,58	4,96	0,00	100,08
	46,60	15,49	0,99	4,60	2,99	12,93	0,15	9,51	0,00	0,04	0,46	4,95	0,00	98,71
	43,95	14,81	0,72	4,55	3,15	11,89	0,23	9,57	0,00	0,05	0,65	4,72	0,00	94,29
	46,79	15,00	0,69	4,73	3,18	12,62	0,20	9,65	0,01	0,00	0,70	4,94	0,00	98,50
	46,89	14,96	0,72	4,92	3,32	12,76	0,25	9,56	0,02	0,03	0,72	4,93	0,00	99,07
	46,89	14,66	0,71	4,85	3,11	12,51	0,21	9,56	0,00	0,04	0,74	4,96	0,00	98,24
Avg.	**46,71**	**15,09**	**0,78**	**4,79**	**3,18**	**12,62**	**0,24**	**9,62**	**0,01**	**0,05**	**0,67**	**4,93**	**0,00**	**98,67**
SD	**0,95**	**0,24**	**0,11**	**0,13**	**0,10**	**0,28**	**0,04**	**0,12**	**0,01**	**0,02**	**0,09**	**0,07**	**0,00**	**1,58**

Section 25b	SiO2	FeO	K2O	TiO2	Na2O	Al2O3	MnO	CaO	Cr2O3	F	P2O5	MgO	O	Total
	57,11	13,23	1,59	1,44	4,76	13,48	0,38	5,37	0,00	0,00	0,64	1,43	0,00	99,42
	57,55	13,16	1,59	1,57	4,80	13,65	0,39	5,43	0,00	0,09	0,62	1,36	0,00	100,20
	57,64	12,68	1,65	1,38	4,77	13,67	0,37	5,18	0,00	0,10	0,40	1,24	0,00	99,07
	56,58	13,21	1,60	1,46	4,60	13,52	0,34	5,06	0,00	0,09	0,44	1,27	0,00	98,17
	56,89	13,80	2,00	1,76	4,39	11,66	0,44	4,95	0,04	0,11	0,75	1,28	0,00	98,06
	56,94	14,74	2,00	1,74	4,40	11,78	0,37	4,90	0,03	0,07	0,67	1,31	0,00	98,94
Avg.	**57,12**	**13,47**	**1,74**	**1,56**	**4,62**	**12,96**	**0,38**	**5,15**	**0,01**	**0,08**	**0,58**	**1,32**	**0,00**	**98,98**
SD	**0,37**	**0,65**	**0,19**	**0,15**	**0,17**	**0,88**	**0,03**	**0,20**	**0,01**	**0,04**	**0,12**	**0,06**	**0,00**	**0,73**

Section 31	SiO2	FeO	K2O	TiO2	Na2O	Al2O3	MnO	CaO	Cr2O3	F	P2O5	MgO	O	Total
	60,66	9,07	1,67	1,00	4,47	15,11	0,28	4,77	0,02	0,10	0,45	1,31	0,00	98,92
	60,56	9,33	1,76	1,05	4,44	15,10	0,34	4,71	0,02	0,09	0,33	1,33	0,00	99,06
	59,36	9,66	1,39	1,14	4,39	15,09	0,25	5,27	0,00	0,09	0,49	1,68	0,00	98,81
	59,65	9,43	1,54	1,21	4,27	15,04	0,31	5,16	0,00	0,09	0,51	1,73	0,00	98,93
	57,94	9,68	1,60	1,23	4,20	14,57	0,21	5,05	0,00	0,13	0,57	1,70	0,00	96,88
	58,91	9,70	1,67	1,21	4,28	14,91	0,34	5,10	0,00	0,14	0,58	1,71	0,00	98,55
Avg.	**59,51**	**9,48**	**1,61**	**1,14**	**4,34**	**14,97**	**0,29**	**5,01**	**0,01**	**0,11**	**0,49**	**1,58**	**0,00**	**98,52**
SD	**0,94**	**0,23**	**0,12**	**0,09**	**0,10**	**0,19**	**0,05**	**0,20**	**0,01**	**0,02**	**0,09**	**0,18**	**0,00**	**0,75**

Appendix D – SediGraph setup experiments

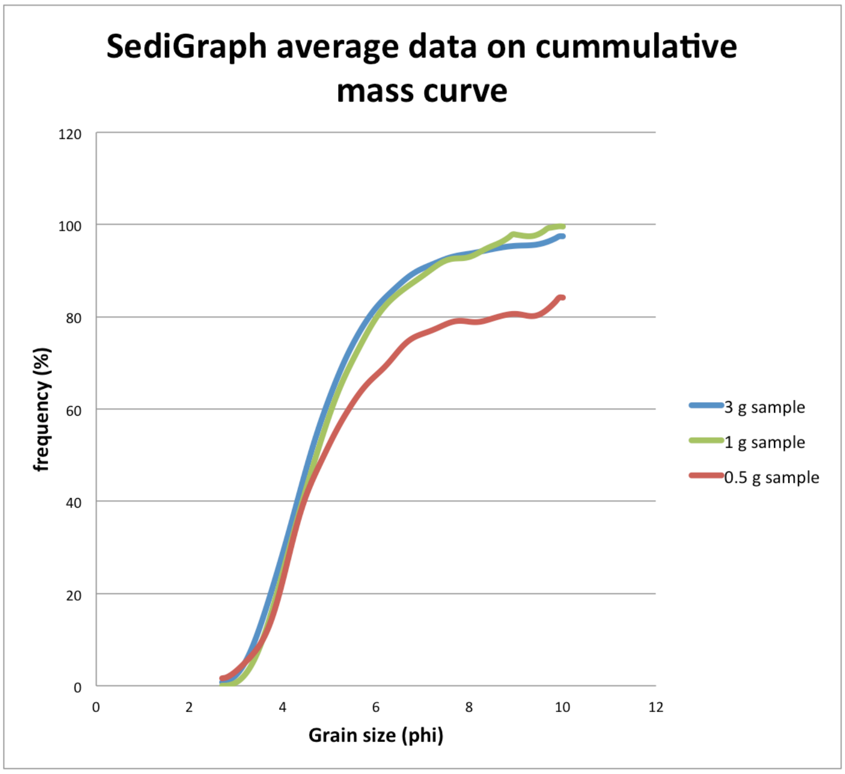

Figure D1. Cumulative grain size curves from measurements with different ash concentration of the same sample. All samples were run from the Mastertech with ash dispersed in 60 ml 50% glycerol liquid. All curves show averages of 3 consecutive runs with the same ash concentration. The 3 g curve is smooth showing well-defined data detection, whereas the low concentrations in the 1 g sample make the detection of the fine particles below ~7φ less reliable as seen by the kinks on the curve, but still within 95% cumulative mass. At 50% lower concentrations (0.5 g sample) detection becomes difficult around 5-6 φ and the average data are unsatisfactory with a total cumulative sum of 84 %.

Amount of sample	Sedigraph x-ray intensity feedback
4 g	79/142 kCnts/s **good** 44-45% baseline
3 g	85/145 kCnts/s **good** 41-42% baseline
2 g	102/145 kCnts/s **good/low** 29-30 % baseline
1 g	121/145 kCnts/s **concentration is low** 16-17 % baseline
0.5 g	130/145 kCnts/s **concentration is low** 9-10% baseline

Table D1. Feedback about x-ray intensity reduction as a function of grain concentration. Baseline x-ray intensity was 145.000 counts/s and intensity feedback is given as measured counts and the percentage of intensity reduction. Intensity reduction between 30-75 % is acceptable, whereas intensity reductions below 30 % are too low for reliable measurements and intensity reductions above 75% are too high (Sedigraph III 5120 Operator's Manual, 2010). Sample sizes of 2.5-3.5 g are sufficiently large to safely meet the x-ray intensity reduction criterion.

Appendix E – SEM images of ash > 3φ

Blomsturvallafjall, distal 1755 deposit

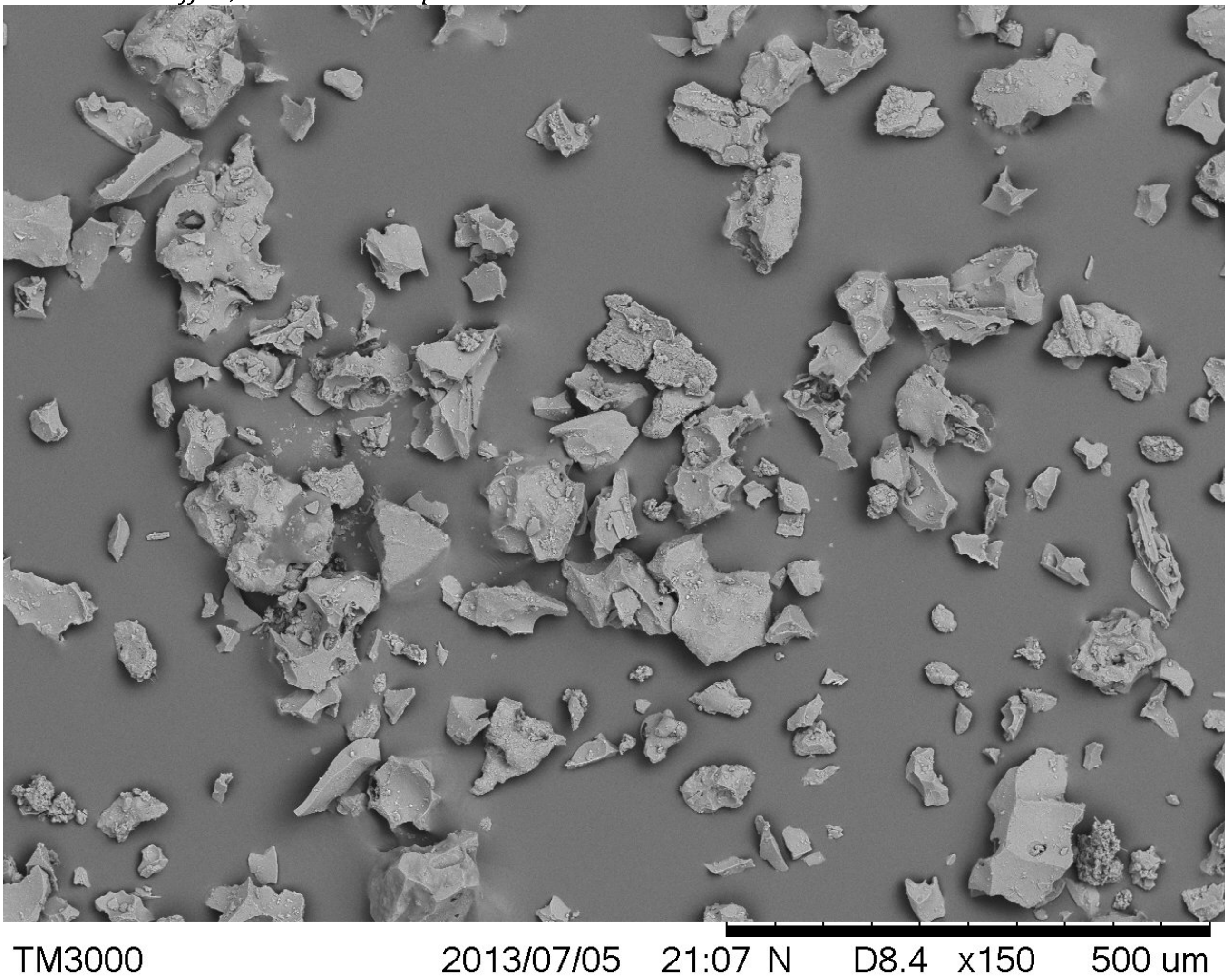

Appendix E – SEM images of ash > 3φ

Rjupnafell 1755, unit 5, coarse part

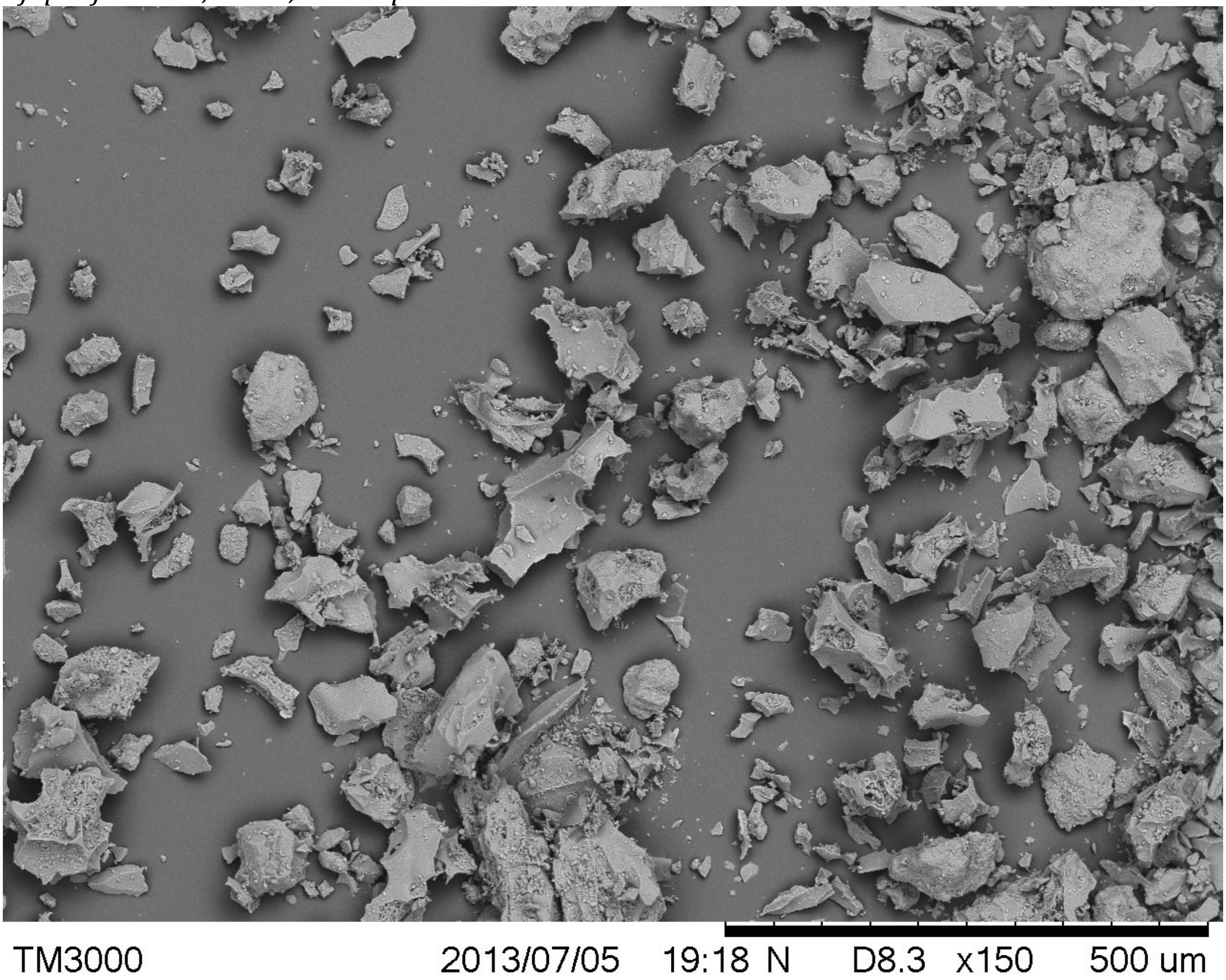

Appendix E – SEM images of ash > 3φ

Rjupnafell, 1755 unit 4, coarse part

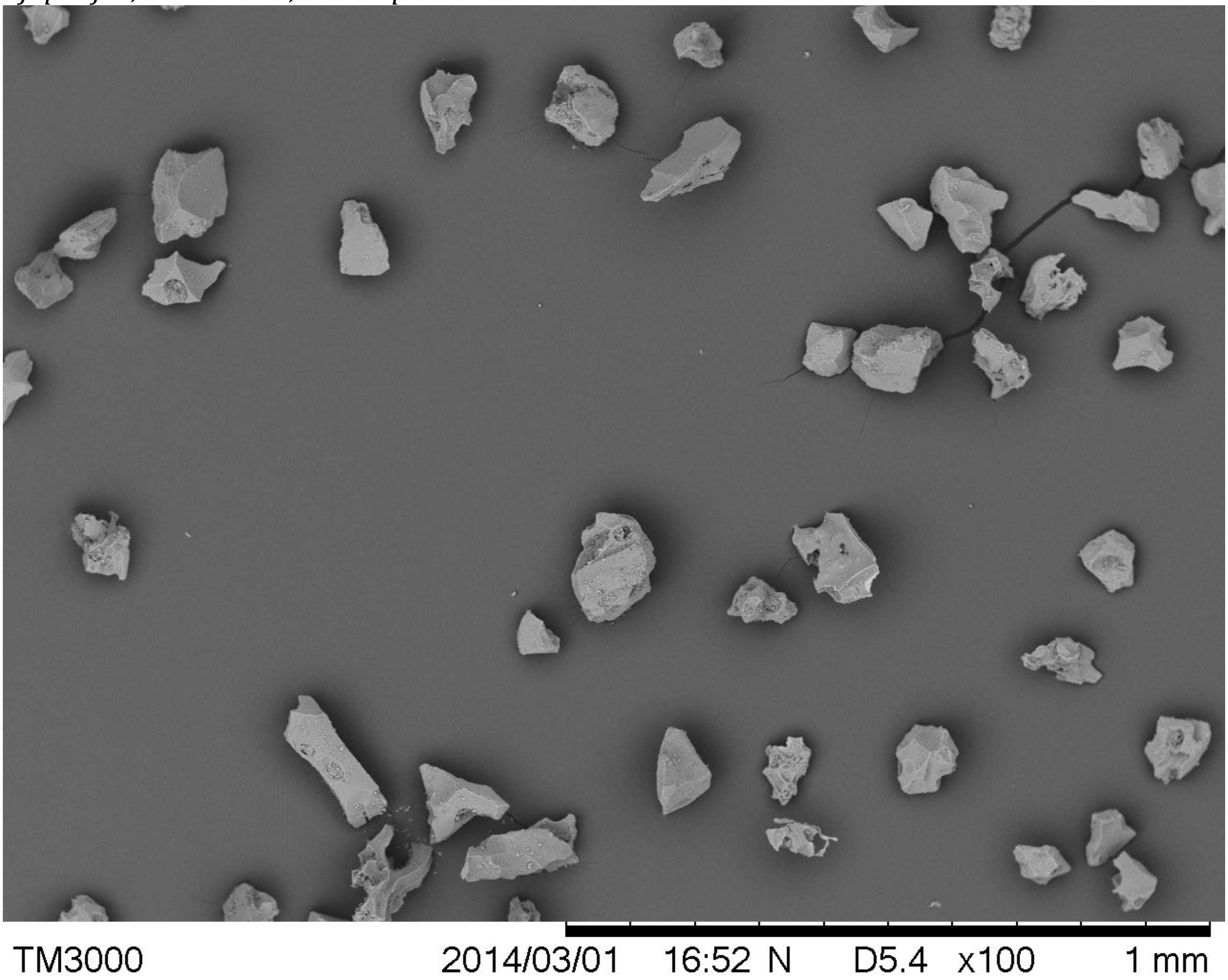

Appendix E – SEM images of ash > 3φ

Rjupnafell, 1755, unit 4 fine part

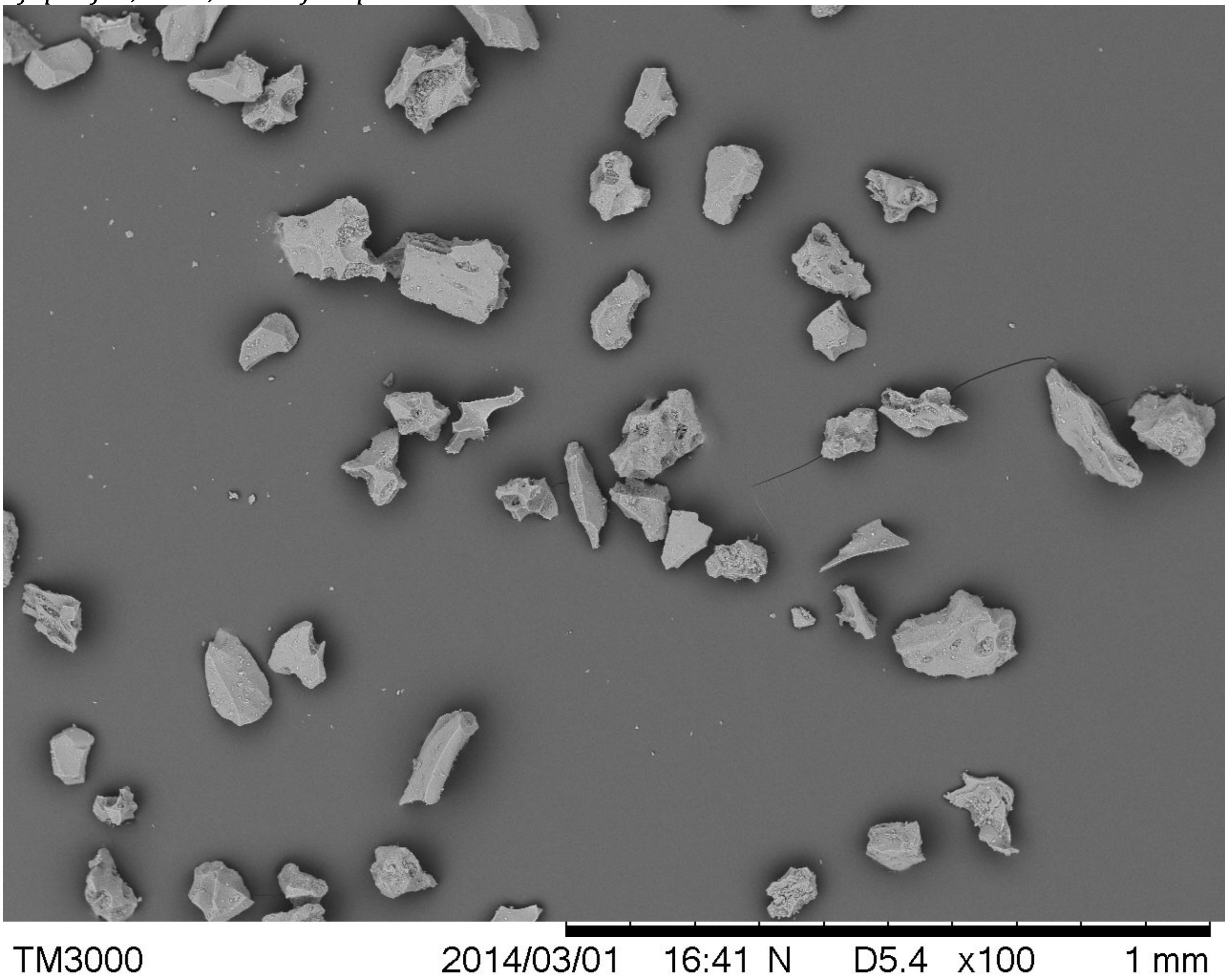

Appendix E – SEM images of ash > 3φ

Rjupnafell, 1755 unit 2

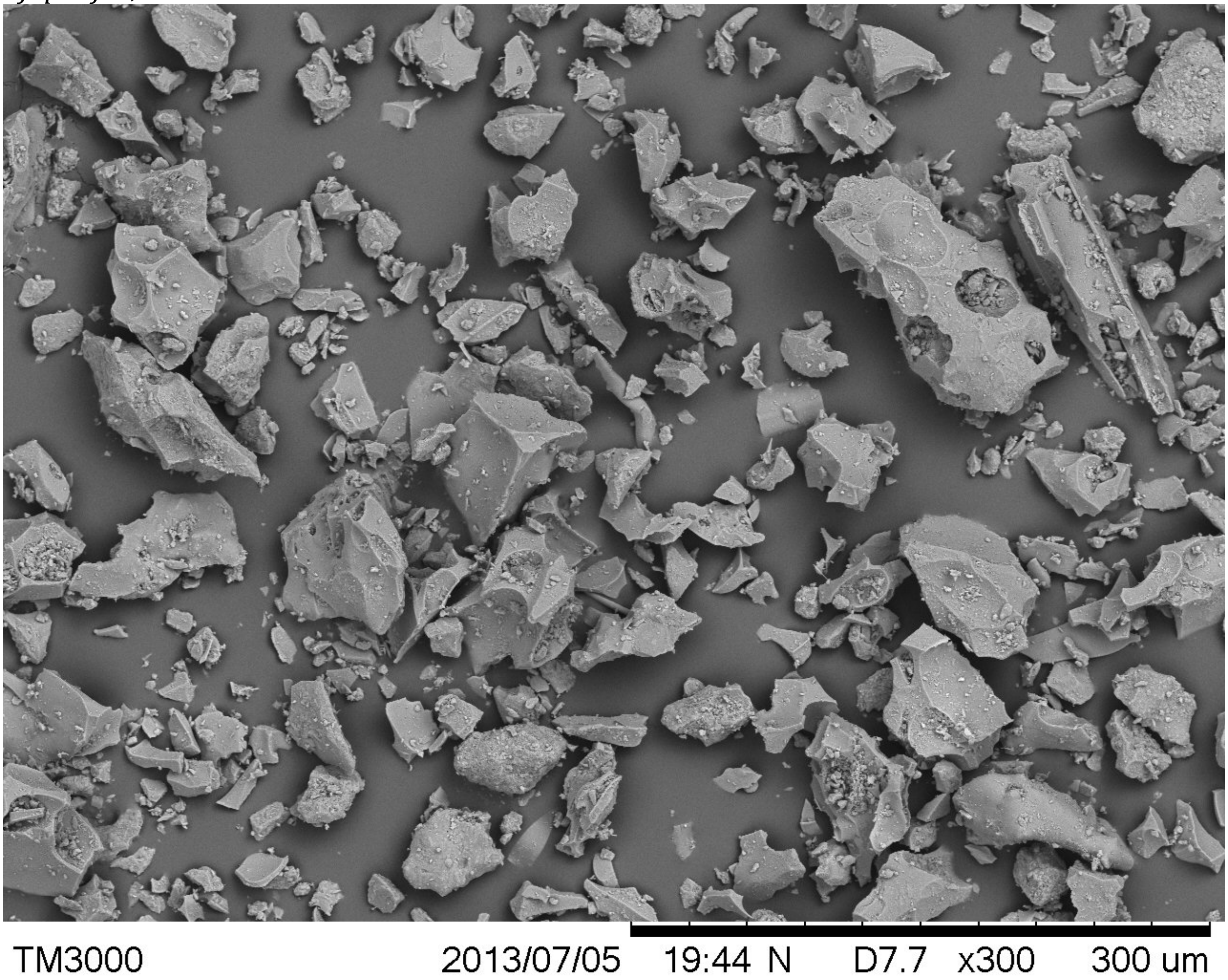

Appendix E – SEM images of ash > 3φ

Blomsturvallafjall, 1625, distal deposit

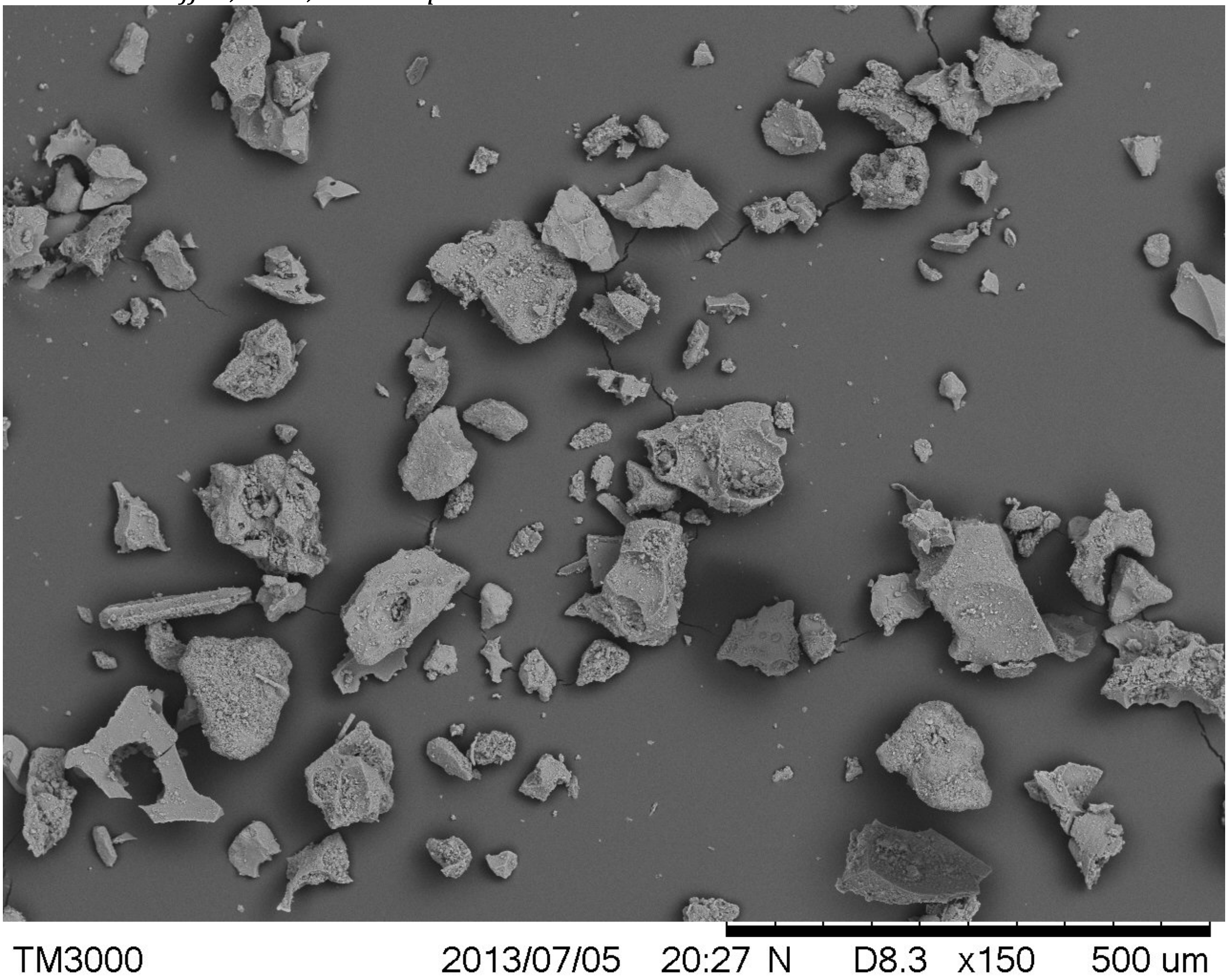

Appendix F – Shape parameters of reference grains

Dataset of reference grains

Please find the electronic appendix F by following the link. The dataset is in read-only excel format as it was too spacious to print in full.

Appendix G – grain size distribution

1755

Grain size (mm) in 1φ intervals

Locality	16	8	4	2	1	0.5	0.25	0.125	0.0625	0.03125	0.01563	0.00781	0.0039	0.00195	0.00098
Alftaver (2)	0.00	0.00	1.50	9.09	19.40	19.97	14.17	12.93	11.97	6.28	3.06	0.91	0.53	0.16	0.04
Bleikóluhraun	0.00	0.00	0.00	0.05	1.67	8.42	19.29	20.86	20.45	18.07	7.86	2.26	0.67	0.36	0.04
Blómsturvallafjall	0.00	0.00	0.00	0.72	2.10	2.94	6.54	24.48	30.23	19.89	9.78	2.09	0.47	0.43	0.33
Dalurfell	0.00	0.00	0.00	0.03	1.06	4.75	6.02	20.48	39.10	21.43	5.66	1.03	0.22	0.05	0.16
Djupadalur	0.00	0.00	0.00	0.16	0.54	3.26	12.93	28.54	33.78	11.81	5.26	2.84	0.62	0.26	0.00
Einhyrningar E	0.00	0.00	0.34	2.28	4.87	12.92	23.05	20.43	19.16	11.58	3.95	0.96	0.22	0.22	0.03
Eintunahals	0.00	0.00	0.00	1.63	15.62	17.59	11.98	13.65	16.82	11.75	7.62	2.50	0.25	0.04	0.56
Engigardur	0.00	0.00	0.00	0.50	5.30	18.08	29.02	26.15	13.75	4.43	1.60	0.63	0.34	0.12	0.08
Eystri-dalbær	0.00	0.00	0.20	1.62	8.75	17.15	12.70	15.97	9.45	23.32	8.27	1.57	0.52	0.41	0.07
Fagrifoss S	0.00	0.00	0.00	0.11	2.60	5.97	17.80	27.51	25.95	11.53	5.22	2.02	0.28	0.24	0.77
Fjaldrárgljúfur	0.00	0.00	0.00	0.87	9.25	22.87	13.36	12.23	17.92	14.88	6.72	1.48	0.17	0.24	0.00
Gröf	0.00	0.00	0.00	0.29	0.54	4.60	22.72	30.24	22.96	9.50	5.43	2.32	0.43	0.46	0.50
Gröf + kirkja	0.00	0.00	0.57	3.37	15.79	16.64	10.70	12.55	16.74	12.09	7.48	3.18	0.54	0.36	0.00
Heidi	0.00	0.00	0.05	0.16	3.01	15.47	26.63	18.52	16.00	10.82	5.73	2.52	0.76	0.33	0.00
Hellnamyri	0.00	0.00	0.00	1.45	8.15	11.24	13.60	20.31	21.01	14.70	6.92	2.04	0.27	0.14	0.18
Hemra	0.00	0.49	2.51	6.06	14.00	11.01	10.98	13.85	16.88	10.83	8.13	3.81	0.77	0.12	0.58
Hjörleifshöfdi	0.00	0.00	0.22	0.25	3.06	12.17	23.67	20.60	21.49	10.74	5.29	1.36	0.60	0.35	0.19
Höfdabrekkuheidi	0.00	0.00	2.79	6.09	8.75	10.99	17.61	18.54	16.22	10.96	4.87	2.34	0.47	0.37	0.00
Hólmsábrú	0.00	0.00	0.59	2.23	9.06	20.08	19.83	15.62	19.25	9.80	2.86	0.55	0.14	0.00	0.00
Holmsárfoss	0.00	1.65	0.59	3.76	10.89	14.78	11.70	11.54	19.10	14.86	7.36	2.61	0.87	0.29	0.00
Hrossatunga	0.00	0.00	0.00	0.43	0.58	5.63	15.44	24.24	30.19	14.04	4.98	2.11	0.38	0.10	1.87
Inngil	0.00	0.00	0.00	0.54	1.75	5.41	18.94	17.86	23.95	19.20	9.26	2.32	0.46	0.26	0.05
Kipuka. Endvatn 2	0.00	0.00	0.00	1.48	15.54	13.64	47.98	19.85	1.16	0.27	0.07	0.00	0.00	0.00	0.00
Krókur	0.00	0.00	0.00	1.27	2.71	8.53	26.55	21.91	19.20	11.45	6.06	1.71	0.48	0.13	0.00
Litliheidi	0.00	0.00	0.00	0.03	0.88	8.93	26.65	12.43	22.48	15.04	8.15	4.13	0.95	0.32	0.00
litlihöfdi	0.00	0.00	3.59	3.59	4.88	6.10	12.98	28.48	28.85	6.00	2.16	1.69	0.79	0.64	0.26
Nupamyri	0.00	0.00	0.35	0.09	1.05	5.69	28.87	22.66	20.40	11.97	6.10	1.81	0.73	0.25	0.04
Nupsheidi	0.00	0.00	0.00	0.02	0.89	11.38	25.53	21.98	17.96	12.89	6.54	2.18	0.36	0.27	0.00
Rjúpnafell	0.11	3.05	7.77	18.63	25.41	12.99	5.66	6.15	8.98	5.60	3.52	1.42	0.43	0.24	0.04
Skalmarbæramaur	0.00	0.13	2.94	10.57	28.52	24.70	9.82	8.24	6.82	4.67	2.43	0.53	0.10	0.17	0.38
Svinadalur	0.00	0.00	0.53	2.34	8.25	14.29	17.00	18.29	22.00	12.48	3.76	0.97	0.08	0.00	0.00
Sydri Oræfa	0.00	0.00	0.00	0.33	2.85	12.39	18.17	18.09	18.75	16.60	8.48	3.49	0.54	0.30	0.00
Varmafell	0.00	0.00	0.00	0.00	1.69	3.39	13.56	23.73	19.40	17.25	2.82	9.70	1.35	0.00	7.10
W Prestbakki	0.00	0.00	0.00	0.36	4.12	16.69	16.66	22.64	22.62	11.14	3.84	0.91	0.45	0.57	0.00

1625

Grain size (mm) in φ intervals

Locality	16	8	4	2	1	0.5	0.25	0.125	0.0625	0.03125	0.01563	0.00781	0.0039	0.00195	0.00098
Alftaver (2)	0.00	0.00	0.36	1.59	7.32	20.77	23.33	14.61	13.70	10.90	5.61	1.25	0.31	0.21	0.03
Armundabotna	0.00	0.00	0.00	0.44	3.15	13.56	21.79	15.71	23.44	11.91	6.68	2.17	0.29	0.07	0.79
Blagil	0.00	0.00	0.00	0.13	1.08	7.63	23.71	20.68	22.16	10.57	8.07	4.37	1.05	0.14	0.41
Bleikóluhraun	0.00	0.00	0.00	0.00	0.84	9.16	24.19	22.24	22.21	11.66	6.90	2.23	0.42	0.15	0.00
Blómsturvallafjall	0.00	0.00	0.00	0.99	2.70	11.29	9.70	21.64	35.30	12.09	3.97	0.98	0.53	0.46	0.35
Djupadalur	0.00	0.00	0.00	0.10	1.10	14.10	33.89	25.85	14.47	6.24	1.83	0.55	0.16	1.16	0.54
Einhyrningar E	0.00	0.00	0.49	2.93	12.12	14.64	10.63	16.26	23.54	11.53	4.90	2.07	0.51	0.38	0.00
Eintunahals	0.00	0.00	0.32	1.23	10.00	19.87	18.98	14.76	17.48	10.12	5.14	1.90	0.20	0.00	0.00
Eystri-dalbær	0.00	0.00	0.09	1.33	6.62	19.08	23.91	15.58	15.24	8.62	3.73	0.68	0.36	2.62	2.14
Fagrifoss S	0.00	0.00	0.15	1.35	6.36	15.08	17.87	19.07	18.24	11.64	6.64	2.52	0.15	0.26	0.67
Fjaldrárgljúfur	0.00	0.00	0.00	1.10	11.61	21.25	10.60	11.99	17.83	14.44	7.78	2.20	0.54	0.36	0.29
Gröf	0.00	0.00	0.00	0.07	0.09	1.42	18.33	30.76	23.98	15.30	6.69	2.50	0.63	0.24	0.00
Gröf + kirkja	0.00	0.00	3.30	10.87	17.23	10.75	8.46	10.07	15.32	12.71	7.65	2.51	0.70	0.31	0.11
Hellnamyri	0.00	0.00	0.28	2.25	11.00	18.63	18.03	12.01	13.32	10.20	8.92	4.01	0.64	0.07	0.64
Höfdabrekkuheidi	0.00	0.00	0.55	2.00	5.57	15.19	24.67	25.15	16.87	6.93	2.14	0.63	0.18	0.11	0.00
Hólmsábrú	0.32	1.33	4.91	11.22	21.20	21.08	12.27	8.41	8.74	6.05	3.17	0.99	0.31	0.00	0.00
Holmsárfoss	0.00	0.47	4.16	9.14	13.43	14.00	11.68	12.01	15.19	9.81	6.37	2.41	0.81	0.41	0.11
Hrossatunga	0.00	0.00	0.00	0.02	0.25	4.00	19.54	21.79	23.87	15.32	9.31	3.51	0.64	0.16	1.60
Inngil	0.00	0.13	2.93	9.96	16.79	12.75	10.73	11.45	14.57	10.76	6.82	2.34	0.55	0.22	0.00
Kipuka. Endvatn 2	0.00	0.00	0.43	2.11	10.45	22.62	26.93	14.60	11.43	6.31	3.44	1.22	0.45	0.00	0.00
Kríuvötn	0.00	0.00	0.00	0.00	0.18	2.63	19.03	23.19	30.24	19.66	4.20	0.18	0.14	0.37	0.18
Krókur	0.00	0.00	0.94	5.79	12.40	13.76	14.92	15.17	16.02	12.38	6.19	1.83	0.45	0.15	0.00
Lambaskradshólar	0.00	0.00	1.12	0.50	0.93	9.24	20.37	17.36	19.30	14.12	10.09	5.07	1.04	0.73	0.12
Lambdashodsholar	0.00	0.00	0.00	0.44	6.50	31.72	13.29	13.09	19.84	11.29	2.82	0.46	0.30	0.16	0.08
Litliheidi	0.00	0.00	0.00	0.00	1.43	4.47	6.63	11.39	33.76	25.19	10.70	4.28	1.10	0.69	0.35
Nupsheidi	0.00	0.00	2.41	6.64	16.15	17.39	8.67	11.39	18.10	10.72	5.68	2.14	0.48	0.24	0.00
Rjúpnafell	0.90	3.72	7.50	12.49	18.46	13.72	9.36	9.74	11.15	6.44	3.91	1.67	0.59	0.34	0.01
Skalmarbæramaur	0.00	0.41	3.48	7.52	17.63	17.94	9.73	10.82	14.14	11.94	5.14	0.94	0.22	0.08	0.00
Svinadalur	0.00	0.44	1.99	6.27	17.22	18.67	12.55	12.24	14.58	8.45	4.85	1.69	0.66	0.27	0.13
Sydri Oræfa	0.00	0.00	0.25	0.46	3.67	14.70	19.30	17.84	19.67	13.25	7.41	2.47	0.87	0.11	0.00
Varmafell	0.00	0.00	1.36	0.00	0.68	2.04	13.61	19.05	16.33	30.17	9.89	3.87	0.77	0.69	1.55
W Prestbakki	0.00	0.00	0.00	0.14	4.08	18.33	18.14	16.36	19.57	14.23	5.99	1.58	1.09	0.49	0.00

Appendix H – Isopach area

Isopach (cm)	Area (km)
1755	
100	70
50	137
20	264
10	626
5	1910
2	6684
1	18601
0.1	45010
0.01	125998
1625	
50	91
30	171
20	278
10	594
5	1344
3	3194
1	9271
0.5	16476
0.01	46114

Appendix I – mass loading data

Locality	Section no	Mass loading (kg/m^2)	Thickness (cm)
Alftaver (2)	16	66.19172068	12
Bleikóluhraun	35	7.4175	1
Dalurfell	18	13.30555556	2
Einhyrningar E	42	11.73543307	1
Eintunahals	51	10.78055556	0.8
Engigardur	33	13.33333333	2
Fagrifoss S	49	12.2671875	1.5
Gröf	21	8.897402597	1
Gröf + kirkja	41	29.54888889	3
Heidi	31	27.94285714	3.5
Hellnamyri	52	7.366666667	1.5
Hemra	45	86.61694431	9
Holmsárfoss	44	17.37142857	2
Kipuka, Endvatn 2	14	128.2785714	12
Krókur	40	12.3225	1.5
Nupamyri	32	4.795833333	1.5
Rjupnafell	15	179.9675116	35
Skalmarbæramaur	17	40.75359643	7
Svinadalur	11	49.068125	11
W Prestbakki	9	12.03166667	2

Table I1. Mass loading and thickness data for the 1755 deposit

Appendix I – mass loading data

Locality	Section no	Mass loading (kg/m^2)	Thickness (cm)
Alftaver (2)	16	58.4459032	4
Armundabotna	48	20.7064148	2.5
Blagil	3	7.919480519	0.8
Bleikóluhraun	35	13.3	2
Djupadalur	20	33.58333333	2
Einhyrningar E	42	17.29913043	2.5
Eintunahals	51	19.03846154	2.7
Fagrifoss S	49	28.46933333	4
Gröf+kirkja	41	86.31777778	8
Hellnamyri	52	95.37200651	7.8
Holmsárfoss	44	91.944	11
Hrossatunga	47	19.15306122	2
Inngil	43	53.05357143	11
Kipuka, Endvatn 2	14	40.51923077	20
Krókur	40	19.49230769	2.5
Lambaskradshólar	36	9.665079365	1
Nupsheidi	39	28.9025	4
Rjúpnafell	15	335.096242	35
Skalmarbæramaur	17	26.27142857	4
Svinadalur	11	36.44	6.5
Sydri Öræfa	38	19.15324675	2

Table I2. Mass loading and thickness data for the 1625 deposit

Appendix J – Supplementary figure 1, chapter 3

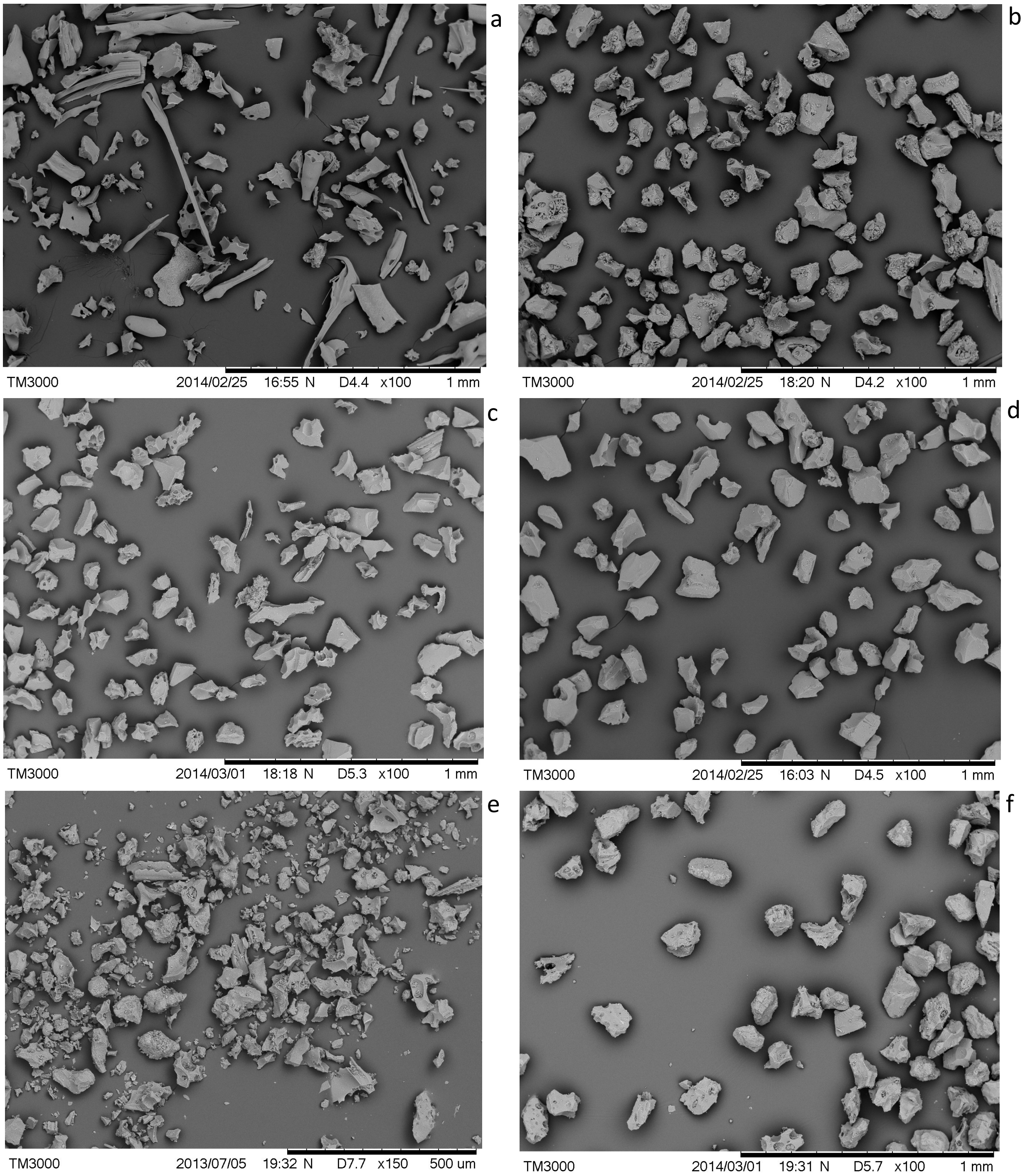

Supplementary Fig 1.
SEM-images showing bulk grain population of the six eruption deposits used for this study. a) Fimmvörduhals Hawaiian deposit dominated by achneliths and irregular grains b) Karl Surtseyan fall deposit dominated by angular blocky grains c) Grimsvötn subplinian fall deposit showing a mix of blocky and vesicular grains d) Hverfjall Surtseyan fall deposit dominated by angular blocky grains e) Katla subplinian fall deposit showing both angular blocky grains, vesicular grains and fluidal grains f) Eggoya Surtseyan fall deposit dominated by angular blocky grains.
Please note that the shown grains are not the ones that have been run on the PIdsa, but taken from the same sample bag by the same random sampling method used to sample subsamples for the PIdsa.

Appendix K – Supplementary figure 2, chapter 3

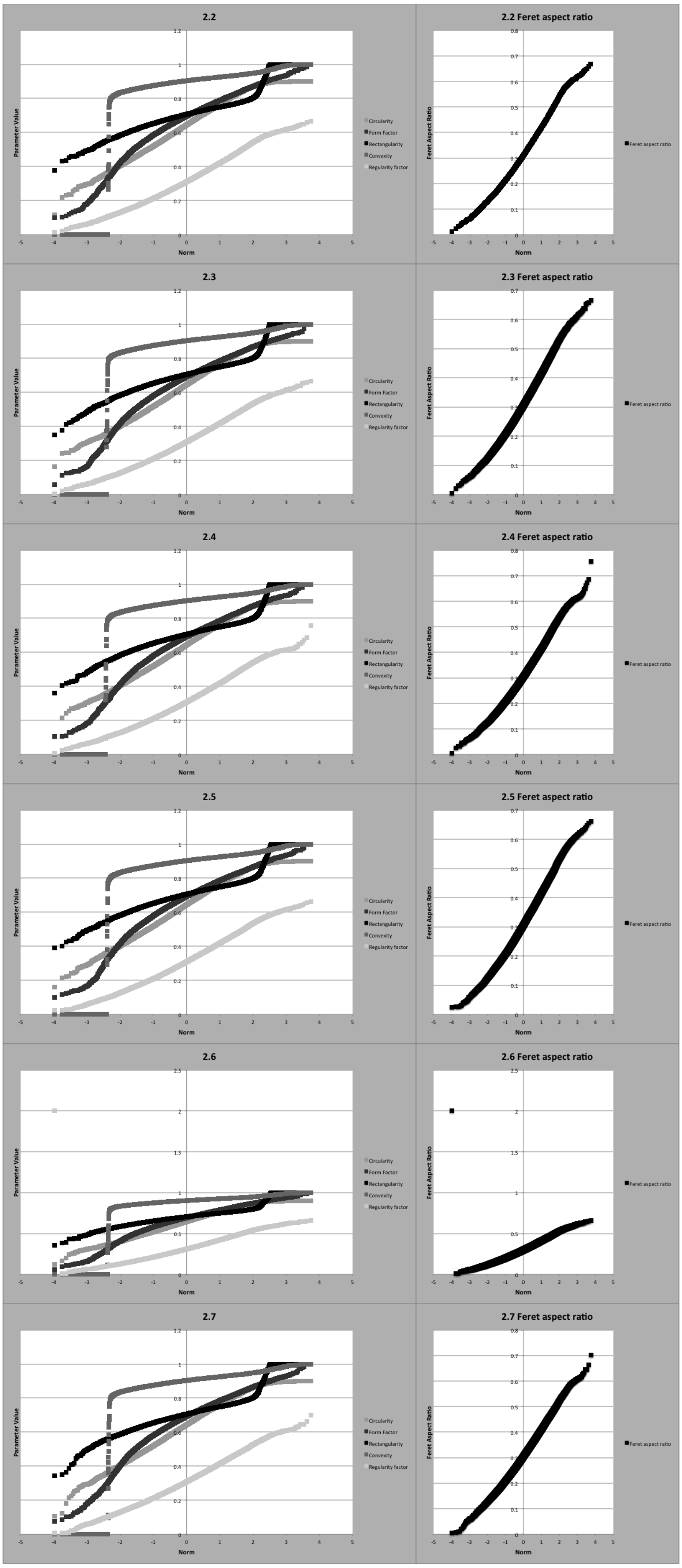

Appendix L – Supplementary figure 3, chapter 3